Morphology of polymer solar cells

Böttiger, Arvid P.L.; Andreasen, Jens Wenzel; Krebs, Frederik C; Yang, Xiaoniu

Publication date:
2013

Document Version
Publisher's PDF, also known as Version of record

Citation (APA):
Böttiger, A. P. L., Andreasen, J. W., Krebs, F. C., & Yang, X. (2013). Morphology of polymer solar cells. Department of Energy Conversion and Storage, Technical University of Denmark.

Morphology of polymer solar cells

Arvid P. L. Böttiger

Risø Campus 2013

Technical University of Denmark
DTU Energy Conversion
Frederiksborgvej 399, DK-4000 Roskilde, Denmark
Phone +45 4677 5800 , Fax +45 4677 5858
ecs.dtu.dk PhD-2013

Summary (English)

Organic electronic devices are an intense area of research. While some devices, such as organic light emitting diodes (OLED) have matured and are found in a vast amount of consumer electronic devices, their energy producing counterpart, organic photovoltaics (OPV), are still in the process of making the transition from the laboratory into the commercial market. One of the biggest challenges in this process is upscaling the production.

The object of this thesis is to investigate the morphology of OPV devices produced from pilot scale roll to roll (R2R) coaters. OPV devices still struggle with low performance, and the morphology is known to have a critical impact on the performance of a device. Several studies have tried to identify the optimal morphology of OPV devices and how to achieve it. Most work has been focused on OPVs produced by spin coating in a small laboratory scale. Devices produced by R2R coating, which works fundamentally different, have not been studied.

Traditional production of OPV has required the use of toxic solvents. A new environmentally friendly approach using water based inks, made of nanoparticles, is now being tested. However, nothing is known about the morphology of the active layer of the solar cells when produced with water based inks using R2R coating.

Using a broad range of scattering and imaging techniques, cells coated with water based inks were investigated, and compared to their spin coated counterpart. Two challenges to be addressed were small domain size to be studied, in the nanometer regime, and the poor contrast due to the similarity of the organic materials.

The physical impact of the ink and the process of coating it, was investigated by electron microscopy, X-ray scattering, hard X-ray ptychography and soft X-ray transmission imaging.

Utilizing the robustness and high resolution of transmission electron microscopy, different preparations of inks were studied. Electron microscopy offers good visualization, but lacks contrast to distinguish similar organic materials, such as P3HT and PCBM, two components of the active layer.

Electron diffraction yields information about the crystal structure of the samples but have a coarse spot size.

X-ray scattering is a well known technique for measuring shapes, sizes, crystal structures and orientation. Both small- and wide-angle scattering were used to measure the crystallinity of the layers as a function of polymer, type of ink, annealing etc.

Ptychography is a new state of the art X-ray imaging technique based on coherent scattering. Together with Scanning X-ray Transmission Microscopy (STXM) it has been used in this study to inspect the morphology of the active layer taken from working solar cells. Ptychography offers desirable properties such as potentially high resolution, quantitative contrast and possibility for tomography. Both these X-ray imaging techniques were used to measure the samples with high spatial and chemical resolution. In addition, these experiments explored and reviewed the viability of ptychography as a characterization technique for OPVs evaluated.

The ink studies showed that the nanoparticles in the active layer were disrupted. Dense parts of the nanoparticles could be observed surrounded by a bulk of less dense material. The same pattern was seen in preparations made by both coating methods.

A difference, observed between the two methods was that the layer produced by R2R consisted of aggregates of particles. The particles in the spin coated samples were uniformly distributed.

Furthermore, this thesis focuseds on developing, and testing, a new method for high throughput characterization of OPV devices. An advantage with R2R coating is the continuous production of layers and the possibility to change production parameters continuously during the process. It would therefore be an advantage if the characterization could also be done continuously. For this purpose a small film winder-underwinder was tested.

The crystalline structure was measured using small angle X-ray scattering on three samples. The high spatial resolution obtained, made it possible to see the changes in crystalline structure as a function of coating paramters. These changes would not have been possible to see using a series of spin coated samples.

Resume (Dansk)

Organisk elektronik er et felt hvor der forskes intensivt. Mens nogle områder, som OLEDs, har modnet og findes i et utal af elektroniske enheder der sælger til almindelige forbrugere er deres energiproducerende modstykke, organiske solceller, stadig i færd med at gennemgå forandringen fra forskning og ind i der kommercielle marked. En af de største, hvis ikke den største, udfordring i processen er at kunne opskalere produktionen.

Målet med denne afhandling er at undersøge morfologien af organiske solceller produceret fra ktmmercielle rulle-til-rulle (R2R) trykkere. Organiske solceller kæmper stadigvæk med lav effektivitet, og det er velkendt af morfologien har kritisk indflydelse for effektiviteten af en celle. Der er lavet meget forskning på hvordan en optimal morfologi skal se ud, og hvordan man kan opnå den, men stort set ingen fokuserer på celler fra R2R trykkere der fungerer fundamentalt anderledes end laboratorieskala spin coating.

At producere organiske solceller har traditionelt krævet brugen af giftige opløsningsmidler, men en ny miljøvenlig fremgangsmåde, der bruger en vandbaseret blæk med nanopartikler bliver i øjeblikket testet. Intet er imidlertid kendt omkring morfologien af disse celler når de trykkes med R2R metoden.

Ved brug af en lang række sprednings- og billeddannelsesmetoder undersøger vi celler trykt med vandbaseret blæk, og sammenligner dem med deres spincoatede modstykke. Størrelsesskalaen for morfologien er i nanometerregimet og kontrasten er meget dårlig mellem de forskellige organiske materialer. Den fysiske karakterisering af blækken bliver foretaget vha. elektron mikroskopi, røntgenspredning, transmissionsbilleder med blød røntgen og ptychografi. Ved brug af nævnte metoder undersøges den fysiske påvirkning af R2R tryk på den vandbaserede blæk.

Røntgenspredning er en robust og gennemprøvet teknik til at måle formfaktorer, størrelser, krystalstrukturer og orienteringer. Da polymererne, der bruges i solcellerne, danner semikrystalinske strukturer når de trykkes bliver både små- og vid-vinkelspredning brugt til at måle krystalstrukturer af film som funktion af polymer, blæktype, varmebehandling etc.

Elektronmikroskopi bliver også brugt til at tage billeder af blækken. Ved at udnytte robustheden og den meget høje opløsning af transmissions electronmikroskopi bliver der taget billeder af forskellige blække, der er fremstillet på forskellige måder og dernæst sammenlignes de med hinanden. Elektronmikroskopi er den letteste måde at få gode visuelle billeder, men teknikken mangler god kontrast til at skelne de forskellige materialer fra hinanden. Elektronmikroskopi kan dog give information om krystalstrukturer i prøven, men kun over et stort område.

Ptychografi er en af, om ikke den, nyeste metode til at danne røntgenbilleder ved brug af coherent spredning. Sammen med transmissionsbilleder fra blød røntgen bliver den brugt til at undersøge morfologien af det aktive lag fra færdige solceller. Ptychografi tilbyder adskillige attraktive egenskaber så som potentielt meget høj opløsning, kvantitativ kontrast og muligheden for tomografi. Begge røntgenteknikker bliver brugt til at måle prøverne med høj rumlig og kemisk opløsning. Ved hjælp af røntgenbillederne og tomogrammerne, undersøger vi morfologien af cellerne. Desuden udforsker og gennemgår vi mulighederne for ptychografi som karakteriseringsteknik for organiske solceller fremadrettet: fordele, ulemper, praktiske problemer og fremtidsmuligheder.

Afhandlingen fokuserer også på udvikling og testing af en ny metode til hurtig karakterisering af organiske solceller. R2R trykning lover høj volumen produktion, dog har vores tidligere eksperimenter vist at morfologien er anderledes i forhold til spincoatede celler. R2R tryk tillader også at hurtigt producere celler med kontinuerligt ændrede parametre for at teste nye produktionsparametre, men der er endnu ingen karakteriseringsmuligheder for nanostrukturen der kan følge med det høje antal prøver.

Publications on which this thesis is based

Publiction I (Published)

Arvid P. L. Böttiger, Mikkel Jørgensen, Andreas Menzel, Frederik C. Krebs and Jens W. Andreasen

High-throughput roll-to-roll X-ray characterization of polymer solar cell active layers

Publiction II (Manuscript)

Arvid P. L. Böttiger, Thue T. Larsen-Olsen, Thomas R. Andersen, Ana Diaz, Jostein B. Fløystad, Morteza Esmaeili, Karl Thyden, Dag Breiby, Frederik C. Krebs, Jens W. Andreasen

Influence of Roll to Roll coating on the morphology of polymer solar cells coated using nano-particle dispersions

Publiction III (Published)

Morten V. Madsen, Thomas Tromholt, Arvid Böttiger, Jens W. Andreasen, Kion Norrman, Frederik C. Krebs

Influence of processing and intrinsic polymer parameters on photochemical stability of polythiophene thin films

Publiction IV (Published)

Thue T. Larsen-Olsen, Birgitta Andreasen, Thomas R. Andersen, Arvid P.L. Böttiger, Eva Bundgaard, Kion Norrman, Jens W. Andreasen, Mikkel Jørgensen, Frederik C. Krebs

Simultaneous multilayer formation of the polymer solar cell stack using roll-to-roll double slot-die coating from water

Publiction V (Published)

Thue T. Larsen-Olsen, Thomas R. Andersen, Birgitta Andreasen, Arvid P.L. Böttiger, Eva Bundgaard, Kion Norrman, Jens W. Andreasen, Mikkel Jørgensen, Frederik C. Krebs

Roll-to-roll processed polymer tandem solar cells partially processed from water

Publiction VI (Published)

Thomas R. Andersen, Thue T. Larsen-Olsen, Birgitta Andreasen, Arvid P. L. Böttiger, Jon E. Carle, Martin Helgesen, Eva Bundgaard, Kion Norrman, Jens W. Andreasen, Mikkel Jørgensen, and Frederik C. Krebs

Aqueous Processing of Low-Band-Gap Polymer Solar Cells Using Roll-to-Roll Methods

Publiction VII (Published)

Jørgensen, Mikkel; Carlé, Jon Eggert; Søndergaard, Roar R.; Lauritzen, Marie; Dagnæs-Hansen, Nikolaj Aleksander; Byskov, Sedi Louise; Andersen, Thomas Rieks; Larsen-Olsen, Thue Trofod; Böttiger, Arvid P.L.; Andreasen, Birgitta; Fu, Lei; Zuo, Lijian; Liu, Yao; Bundgaard, Eva; Zhan, Xiaowei; Chen, Hongzheng; Krebs, Frederik C. Krebs

The state of organic solar cells-A meta analysis.

Contents

Chapter 1

Introduction

Today the world's energy consumption is 10 gigatons of oil equivalent (Gtoe) per year and it is rapidly increasing. *World Energy Technology Outlook* expected in 2005 the global demand to rise to 22 Gtoe in 2050[2]. With fossil fuels being a limited resource, the prices are constantly increasing. Furthermore, the fossil fuels have a significant impact on the environment due to its large carbon footprint. Therefore, a sustainable energy production in the future will be dependant on sources of clean and renewable energy.

Different sustainable energy sources like solar energy, wind power, hydro power and biomass exist, but they have in common that they are ultimately a proxy for solar energy. Wind power harvests the winds that are created by the sun heating the earth surface. Likewise, hydro power utilizes water that is evaporated from the seas and later condensates back into water in mountains or other areas with high potential energy. Biomass uses energy stored in biomaterial that also needs the sun to grow.

Due to the inherent loss caused by using a proxy for harvesting solar energy, the potential of solar energy is much larger than any of the other sources[4]. With constantly decreasing prices, solar cells are currently getting deployed rapidly. *Renewable Energy Policy Network for the 21st Century* (REN21) concludes in their 2012 report[6] that solar power was not only the fastest growing renewable energy source, but also experienced the highest growth rate acceleration with a 74% growth in 2011 compared to an average growth of 54% over the last 5 years. The second fastest growing renewable energy source was wind power with a 20% growth in 2011 which is a decline compared to the preceeding 5 year average growth of 26%.

From the REN21 report it is clear that solar energy currently is adopted on a larger scale.

1.0.1 Organic photovoltaics

Today the vast majority of all solar cells are made of silicon. An alternative to the classical silicon based cells are organic solar cells, or organic photovoltaic (OPV). OPVs are typically divided into two main groups, dye sensitized solar cells (DSSC) and heterojunction cells. The heterojunction cells can be made of small molecules and polymers, respectively. The small molecules have a broad absorption spectrum, are easy to design and have had great success in the, closely related and more mature, organic light emitting diode (OLED) industry[5]. However, polymers are currently promising in the field of OPV due to high charge carrier mobility and better morphology control[7].

While not as efficient as traditional solar cells made of silicon, polymer solar cells can be made in high volumes, fast and cheap. However, they have not so far made the transition from research projects to a viable commercial product.

1.1 Hypothesis

The topic of this thesis is the investigation of the morphology of the nanostructure in OPVs. The morphology of the active layer in OPVs is known to have a critical importance for its performance[8]

To improve OPVs one of the problems that must be addressed is the morphology on the nanoscale level. Lots of research have been conducted on traditional OPVs created from spin coating[3] but it is well known that in the transition from spin coating to R2R coating a lot of parameters are reset.

The scope of this thesis is to study whether the transition from spin coating to R2R coating impacts the morphology of OPVs on a nanoscale level, and in case it does, understand the impact of R2R coating as well as understanding the processing of new types of inks developed at DTU. The primary system will be a water based ink developed at DTU, based on nanoparticles in dispersion.

Furthermore we wish, if possible, to study the internal structure of the nanoparticles and see if their internal morphology is suitable as an optimal heterojunction or if morphology control on a individual particle level also needs to be achieved in the future in order to move OPVs into a commercial product.

Several techniques can be used to study the morphology, but since no technique can provide a complete picture they have to complement each other. To investigate the morphology of both the active layer and the nanoparticles several techniques like electron microscopy, X-ray scattering, Scanning Transmission X-ray Microscopy and ptychography were applied. Each of them offering one or more valuable features.

Ptychography is a new technique for high resolution X-ray imaging. It offers many attractive qualitites but requires moving the sample a lot. If the sample during this process drifts relative to the sample holder tomographic reconstruction will not be possible. This thesis proposes a new method of aligning a drifting sample in order to perform a tomographic reconstruction. In contrast to the many existing methods optimized for medical tomography this algorithm focuses on being robust for large drifts rather than being able to deliver results in near real time.

Secondly, when switching production method from spin coating to R2R coating a lot of parameters are reset and needs to be optimized by empirical methods again[1]. However, one of the large advantages with R2R coating, in contrast to spin coating, is the possibility to vary the coating parameters while coating. There is not believed to be a simple relation between the coating parameters and the nanostructure of the cells thus making empirical optimizations essential. Part of this thesis explores the possibilities of a new mechanical setup for coating parameter optimization with high resolution in the parameter space. The goal is to be able to understand the formations of crystal structures during the coating process and create a setup which in a later stage can be applied in a laboratory setup

1.2 Thesis outline

The structure of this thesis is divided into 10 chapters.

Chapter 1-2 Introduces the subject and the basic textbook theory for OPVs.

Chapter 3 Explains the the sample preparation process, including the various pitfalls one should be aware of when repeating the experiments.

Chapter 4 Outlines a range of well known lab scale X-ray characterization techniques and how they relate to the characterization of OPVs. The Chapter also includes examples of how these techniques are used in a practical context and used to gain knowledge nessecary to fully understand various steps in the processing and/or analysis of the OPVs. Furthermore the chapters explains the implementation of the Bayesian Inverse Fourier Transform for calculating the size distribution of a polydisperse system.

Chapter 5 Explores the physical morphology of the bulk heterojunctions of cells fabricated at DTU with various inks and post-process treatments.

Chapter 6 Explores the morphology with chemical contrast using absorption of soft X-rays.

Chapter 7 Aims to introduce the reader to the theory, current state and applications of the new X-ray based imaging technique, called ptychography, by summarizing the currently known and published information. Furthermore a new image alignment algorithm for aligning a drifting sample is introduced.

Chapter 8 Presents the results obtained from ptychographic tomography including the challenges in reconstructing the tomograms. The chapter briefly explains the well known steps in the reconstruction process and continues to investigate the results of ptychography.

Chapter 9 Introduces a new technique for high spatial X-ray scattering measurements of R2R coated samples.

Chapter 10 Summarizes and evaluates the results obtained from the various chapters and concludes the thesis.

References

[1] Jan Alstrup, Mikkel Jørgensen, Andrew J. Medford, and Frederik C. Krebs. Ultra fast and parsimonious materials screening for polymer solar cells using differentially pumped slot-die coating. *ACS Applied Materials & Interfaces*, 2(10):2819–2827, 2010.

[2] European Commission Directorate-General for Research Information and Communication Unit. World energy technologyoutlook-2050. Technical report, European Union, 2006.

[3] Rajiv Giridharagopal and David S Ginger. Characterizing morphology in bulk heterojunction organic photovoltaic systems. *The Journal of Physical Chemistry Letters*, 1(7):1160–1169, 2010.

[4] F.C. Krebs. *Polymer Photovoltaics a Practical Approach*. Press Monographs. Society of Photo Optical, 2008.

[5] Oskar Nuyken, Steffen Jungermann, Valerie Wiederhirn, Erwin Bacher, and Klaus Meerholz. Modern trends in organic light-emitting devices (OLEDs). *MONATSHEFTE FUR CHEMIE*, 137(7):811–824, JUL 2006. 7th Austrian Polymer Meeting, Graz, AUSTRIA, JUL, 2005.

[6] REN21. Renewables global status report 2012. Technical report, REN21, 2012.

[7] M. Riede, T. Mueller, W. Tress, R. Schueppel, and K. Leo. Small-molecule solar cells - status and perspectives. *NANOTECHNOLOGY*, 19(42), OCT 22 2008.

[8] G Yu, J Gao, JC Hummelen, F Wudl, and AJ Heeger. Polymer photovoltaic cells: enhanced efficiencies via a network of internal donor-acceptor heterojunctions. *Science-AAAS-Weekly Paper Edition*, 270(5243):1789–1790, 1995.

Chapter 2

Polymer solar cells

2.1 Polymer solar cells

Polymer solar cells are OPVs made with polymers as the active layer. Compared to the common commercially available inorganic photovoltaics (IPV) made of silicon, cells made of polymers are produced of cheap materials, have a low energy payback time and can be printed in high volumes on flexible substrate using existing roll to roll (R2R) printing technology, figure 2.1. The largest obstacles have been a lower efficiency than PVs. In addition, stability and production cost need to be further optimized before polymer solar cells become financially viable. In comparison, inorganic PV, made from polycrystalline silicon, and sold commercially have an efficiency of 15% while good organic cells efficiency is approximately 3%[10].

2.1.1 Design and materials

The textbook version of a polymer solar cell consists of an active layer, a hole transporting layer, an electron transporting layer, two electrodes and a substrate. The materials and geometry vary, but the most common type uses poly(3-hexylthiophene) (P3HT) and [6,6]-phenyl-C61-butyric acid methyl ester (PCBM) as the active layer. The hole transporting layer is poly3,4-ethylenedioxythiophene:polystyrene sulfonate (PEDOT:PSS) and the electron transporting layer consists of zink oxide (ZnO). Finally, the electrodes are made of indium tin oxide (ITO) and silver (Ag). The substrate is either glass in small scale cells or poly(ethylene terephthalate) (PET) in large scale R2R coated cells.

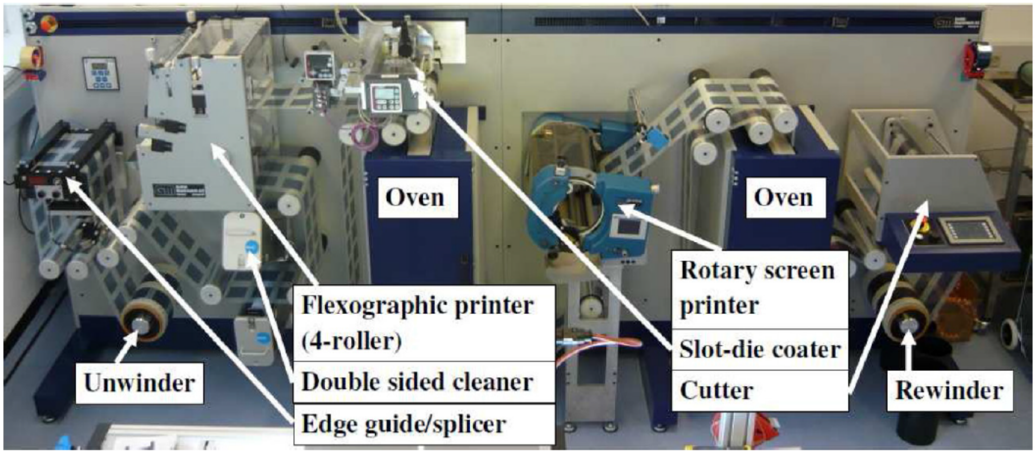

Figure 2.1: *R2R coater found at DTU.*

2.1.2 Fundamental physics

The cells are designed with the metal-insulator-metal approach. Here, the mixture of two components can be viewed as a single semiconductor material with the LUMO level of the acceptor and the HOMO level of the conductor as the virtual valence and conducting band, respectively. The energy difference between the two energy levels is the effective band gap.

The active layer of a cell consists of an electron donor and an electron acceptor. When a photon is absorbed by the electron donor material an electron enters an excited state where it is bound to the corresponding hole by the Coulomb force, but still moves freely within the donor material. The electron in this state is called an exciton. If the exciton reaches the interface between the donor and acceptor material, the electron will move into the acceptor material, and the exciton will separate into a free electron and hole.

To extract a current it is necessary for the various layers to have well-chosen HOMO and LUMO levels and well-chosen band gaps. In the active layer the electron acceptor material has both a lower HOMO and LUMO energy than the donor, to make the exciton separate into two free charges. The cell can deliver a higher potential if the energy difference is smaller, but if the energy difference is too small the risk of recombination occurs.

While it is important to prevent the free electrons from recombining with the hole they are separated from, it is also important to isolate them from the environment outside the cell, where they will find a hole to recombine with.

This isolation is achieved by creating a sandwich with two layers of semiconductors surrounding the active layer. As illustrated in in figure 2.2 semiconductors will have energy levels which will attract electrons (or holes)

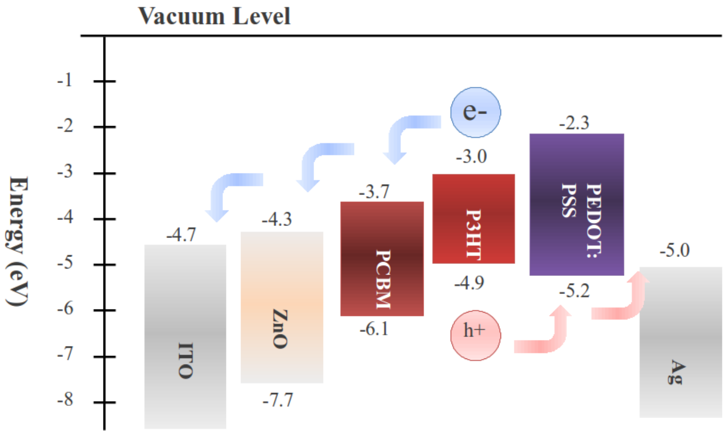

Figure 2.2: *Schematic representation of the energy levels of the layers of an inverted cell. The two charges are transported through the respective materials and collected by the electrodes. As the anode a layer of PEDOT:PSS deposited on top of ITO was used, while on top of the active layer ZnO and aluminum.*

from the active layer but prevent holes (or electrons) from the outside entering the system and interfering.

By creating this potential slope towards the electrodes the free charges are guided out of the cell. The final potential of the cell depends on the final potential difference between the electrodes as indicated on figure 2.2.

2.1.2.1 Band gap

A high band gap of the electron donor may seem preferable, because of the high potential the cell is able to produce. However, the sun emits black body radiation, and the majority of the flux is thereby in the low energy spectrum, and not able to produce excitons in a high band gap electron donor. As a result low band gap materials are also an active area of research. Another topic of research is tandem cells which combine the advantages of high band gap cells and low band gap cells at the cost of a much more complex cell design.

2.1.3 Efficiency

While OPVs are behind IPV with regard to efficiency, they have been considerably improved in the recent years. Efficiency has increased and has been reported close to 9%[5] albeit only on devices smaller than 1 cm^2. On large scale devices the efficiency is still around 3%[10].

2.1.4 Stability

All organic solar cells are subject to degradation due to a slow but constantly changing state[8,9].The degradation is mainly caused by the presence of oxygen and water. Isolation of the cell by encapsulation, will therefore improve its lifetime significantly. However, temperature and irradiation also degrades the cell and may require more robust materials.

Today, encapsulated cells have a longer and acceptable operating lifetime of more than 1 year[8]. However, to penetrate into the commercial market lifetimes up to 10 years need to be achieved[19].

2.1.5 Fabrication

OPV is an area of intensive research and almost all cells are created in a lab by either evaporation or spin coating the various layers on top of each other.

However, if OPVs are going to be transferred from the laboratories to commercial production, it must be possible to produce the cells in high volumes. The current most promising solution is R2R printing, where cells can be printed at over 100 m/ min and with 1 m wide substrate for wet coating[4].

The price can be dramatically reduced if the cells are printed in high volumes, but the large scale printing does raise problems regarding keeping the various layers homogeneous. In addition, there are other restrictions on the coating conditions. For example, due to the size of a R2R coater a protected atmosphere is unpractical.

Furthermore, almost all the knowledge we have about morphology of OPV is based on cells made on a small scale. It is doubtful whether this knowledge can be transferred to R2R coated cells.

The best cells produced by R2R coating today have an efficiency of 4.2%[10].

2.2 The importance of morphology

The external quantum efficiency is often written as

$$\eta_{EQE} = \eta_A \cdot \eta_{ED} \cdot \eta_{CC} \tag{2.1}$$

where the η's are probabilities between 0 and 1. η_A is the probability of absorption, η_{ED} is the probability of the exciton reaching an interface and η_{CC} is the probability for the electron/hole to reach an electrode[14].

The diffusion length of the exciton is uncertain, but from the exciton lifetime it has been estimated to be between 4 and 20 nm[6,18]. The goal is to have a domain size in the active material of the same length scale to secure that all excitons reach an interface before decay and thus can be converted into current. Unnecessary loss of efficiency can thus be prevented, e.g. a high η_{ED}. It is also important that all the donor/acceptor domains are connected to the electron/hole transport layers encapsulating the active layer. If a donor layer is isolated from the transport layer inside the acceptor layer it will not be possible for the hole to be extracted if the exciton separates. This will lead to a recombination and also loss of performance, e.g. a low η_{CC}.

To have both a sufficient small domain size and an active layer thick enough to absorb enough light it is not enough to just have two thin layers of donor and acceptor material on top of each other. The donor and acceptor materials need to be approximately 100 nm thick, and to fulfil the requirement of small domain sizes it normally consists of a sponge-like interpenetrating network of donor-acceptor material.

Mixing the two active materials before coating has proven to result in a good morphology with a small domain size. However, albeit the structures are fine they are believed to contain many isolated domains. To optimize the domain size, and get a more connected network, the coated active layers are often annealed. This has shown to grow the domains (lower η_{ED}) thus making the network more connected (higher η_{CC})[16]. The ratio between η_{ED} and η_{CC} by annealing has been optimized by empirical methods.

2.2.0.1 Controlled growth heterojunctions

Due to the random nature of the way a bulk heterojunction forms itself it is tempting to try to optimize it manually. A designed morphology would be able to provide both a high η_{ED} and η_{CC}, and this has been done with success[20]. Controlled grown heterojunctions are being investigated, but they are today not possible to grow on a large scale and almost always yield inferior results compared to the randomly generated heterojunction.

2.2.1 Water dispersed nanoparticles

P3HT and PCBM are not soluble in water. Chlorobenzene (CB) is the most widely used solvent, but like other organic solvents it is toxic and the use of it in production is actively discouraged by the EU[15].

Getting chlorobenzene out of the production of organic solar cells has therefore been an area of interest. A solution was proposed by Landfester[11] who suggested to create nanoparticles containing the active materials, thus making each particles functioning as a small independent minicell. The particles are created as a miniemulsion where the two immiscible liquid

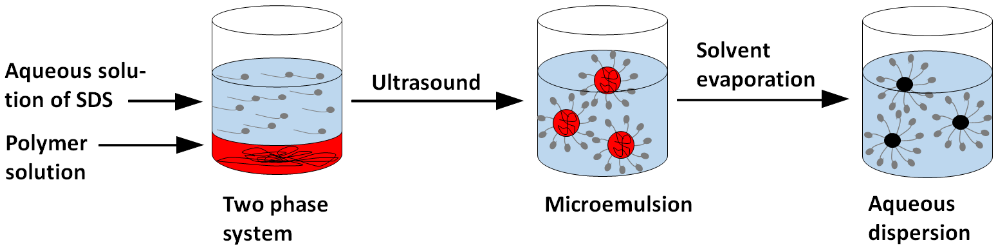

Figure 2.3: *Schematic overview of the preparation of polymer nanoparticles dispersed in water. First a solution of polymer and/or PCBM is mixed with an aqueous solution of SDS. After a pre-emulsion by stirring, a micro-emulsion is formed upon ultrasonic treatment, and finally the solvent is removed by evaporation resulting in the nanoparticle dispersion.*

phases are mixed and sheared by ultrasound treatment. The method has the advantage of creating particles of a few hundred nanometers reliably and in a parallel fashion, making it possible to create large amounts.

By utilizing the method above it has been possible to create working organic cells by mixing the active materials with an aqueous solution of sodium dodecylsulphate (SDS). After ultrasound treatment the particles are dialysed and concentrated and can thereafter be coated on the substrate by spin or R2R coating without the use of chlorobenzene[1].

2.3 X-ray interaction with matter

When doing imaging one needs to have some physical quantities which changes when a sample is put in front of a detector. X-rays are electromagnetic waves which can interact in different ways. The sample can either be imaged by use of absorption, refraction or scattering of the waves. All three phenomena are known from optical light.

2.3.1 Absorption

When X-rays passes through matter some photons will be absorbed by transferring their energy to an electron. The electron is freed and the atom is ionized. The intensity attenuation coefficient, μ, describes the extent to which the intensity of an X-ray beam is reduced as it passes through a specific material.

μ has the dimension of reciprocal length, and the change of X-ray intensity can be expressed as

$$-\,\mathrm{dI} = I(z)\mu\,\mathrm{dz} \tag{2.2}$$

Solving this equation for I leads to an expression for the intensity at a depth z inside the material. This is known as the Beer-Lambert law:

$$I(z) = I_0 e^{-\mu z} \tag{2.3}$$

Since the absorption is due to electrons, the attenuation coefficient is proportional to the electron density, ρ_a. The proportionality factor is called the electron absorption cross section, σ_a, and the attenuation coefficient can be expressed as $\mu = \rho_a \sigma_a$,[7].

2.3.2 Refraction

A quantitative description of the refraction is traditionally given by the refractive index n.

When W. C. Röntgen in 1895 discovered X-rays he suspected they were waves but he had no success in trying to reflect, refract or focus them[17]. This was because the refractive index for X-rays in all materials is very close to unity and the angle of total reflection is very low. The refractive index is therefore often written as $n = 1 - \delta$, where δ is a very small quantity. Knowing the energy of the incoming X-rays and the density of the samples, δ can be calculated from the following expression.[12]:

$$\delta = \frac{r_0 \lambda^2}{2\pi} \sum_l N_l (Z_l + f_l^r) \tag{2.4}$$

λ is the wavelength of the incoming X-rays, Z denotes the atomic number of the element l, N_l is the atomic number density and where r_0 is the Thomson scattering length, often called the classical electron radius. f_l^r is the real part of the dispersion correction,[7]. The dispersion correction is frequency dependent and only significant when one is close to the absorption edge of the electrons, otherwise it can be neglected.

2.3.2.1 Phase shifts

The phase of a wave is commonly written as $e^{\imath\Phi}$. The phase shift of a photon in an object with refraction index n, can be calculated as the difference in phase between moving the distance z inside and outside the object:

$$e^{\imath\Phi} = e^{\imath kz} - e^{\imath nkz} = e^{\imath kz(1-n)} = e^{\imath kz\delta} \Rightarrow \Phi = \delta kz \tag{2.5}$$

Therefore the phase shift of an X-ray passing through an object with the $\delta(x, y, z)$ can be written as:

$$\Phi(x, y) = k \int \delta(x, y, z)\,\mathrm{dz} \tag{2.6}$$

Combining this with equation (2.4) $\Phi(x, y)$ can be rewritten as:

$$\Phi(x, y) = \int \sum_{l} N_l(x, y, z) p_l\,\mathrm{dz} \tag{2.7}$$

where p_l is defined as:

$$p_l \equiv r_0 \lambda (Z_l + f_l^r) \tag{2.8}$$

p_l is called the phase shift cross section for reasons which will be obvious in a moment.

2.3.2.2 Size of δ

We can estimate the size of δ. Knowing that $r_0 = 2.82 \cdot 10^{-5}$ Å, the order of magnitude of N is 1 electron/ Å^3 and λ has the order of magnitude 1 Å^{-1}. δ normally lies somewhere around 10^{-6}, which means the real part of the refractive index very close to unity for X-rays. The general trend of the refractive index as a function of energy can be seen on figure 2.4^2.

For visible light, the refraction index for different kinds of glass lies somewhere between 1.4 and 1.9. This means that if we consider a ray of light moving from glass ($n = 1.4$) to air ($n = 1$) with an angle of incidence of 15° , the angle of refraction can be found using Snells law:

$$\frac{\sin\theta_1}{\sin\theta_2} = \frac{n_2}{n_1} \Rightarrow \theta_1 = \arcsin\left(\frac{n_2}{n_1}\sin\theta_2\right) = 21.2^\circ \tag{2.9}$$

The angle of the refracted ray is around 30% larger than the angle of the incident ray.

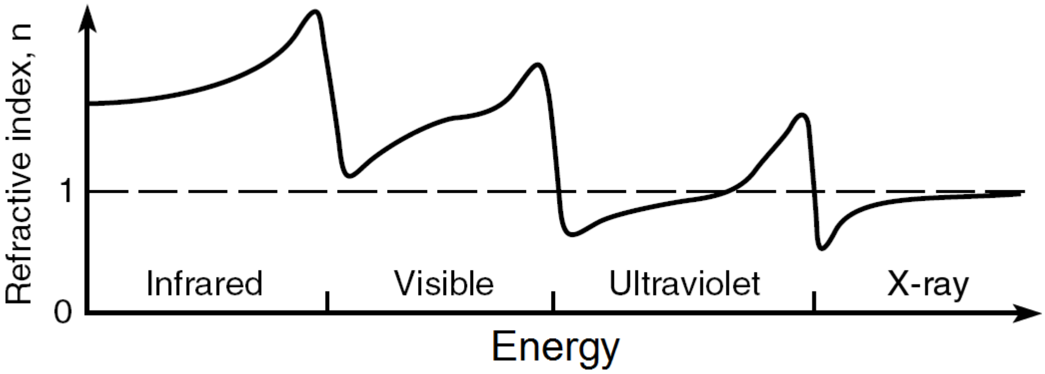

Figure 2.4: *The general trend of the energy of photons af a function the refractive index. It is worth noting that the refractive index of X-rays is close to unity. The figure is reproduced with permission from* Soft X-Rays and Extreme Ultraviolet Radiation [2].

2.4 Relation between refraction and absorption

In order to account for the absorption of X-rays an additional complex term is often added to the refractive index.

$$n = 1 - \delta + \imath\beta \tag{2.10}$$

where β can be expressed as[12].

$$\beta = \frac{r_0\lambda^2}{2\pi}\sum_l N_l f_l^i \tag{2.11}$$

With f_l^i denoting the imaginary part of the dispersion correction.

Inserting the full expression for n into the wave function.

$$\Psi(\mathbf{r}) = E_0 e^{\imath n\mathbf{k}\cdot\mathbf{r}} = E_0 e^{\imath(1-\delta)\mathbf{k}\cdot\mathbf{r}} e^{-\beta\mathbf{k}\cdot\mathbf{r}} \tag{2.12}$$

It becomes clear that extending the refraction index with β makes the amplitude proportional to $\exp[-\beta kz]$. Since the intensity is the amplitude squared the intensity will behave like:

$$I \propto \exp[-2\beta kz] \tag{2.13}$$

Looking back at equation (2.3), β can be related to the attenuation coefficient μ:

$$\beta = \frac{\mu}{2k} \tag{2.14}$$

Therefore the transmission of an object can be written as

$$\begin{aligned} T(x,y) &= \int \mu \, \mathrm{dz} \\ &= \int 2k \cdot \beta \, \mathrm{dz} \\ &= \int \sum_l N_l f_l^i 2\pi r_0 \lambda \, \mathrm{dz} \\ &= \int \sum_l N_l \sigma_a \, \mathrm{dz} \end{aligned} \tag{2.15}$$

2.4.0.3 Relation between δ and β

Comparing the expression for the phase shift (2.7) and transmission (2.15) caused by an object, σ_a for the transmission corresponds to p for the phase shift, and thus we name p for the phase shift cross section.

The absorption cross section, σ_a, can be approximated by,[3]

$$\sigma_a = 0.02[\mathrm{barn}] \left(\frac{k_0}{k}\right)^3 Z^4 \tag{2.16}$$

Where k is the wave number, k_0 is the wave number for an X-ray photon with a wavelength of 1 Å, and Z is the atomic number.

Calculating σ_a and p for a 1 Å X-ray in a light medium with $Z = 10$ one gets.

$$\sigma_a = 0.02[\mathrm{barn}]10^4 = 200\mathrm{barn} = 2 \cdot 10^{-22}\ \mathrm{cm}^2 \tag{2.17}$$

$$p = 2.82 \cdot 10^{-5}\ \text{Å} \cdot 1\ \text{Å} \cdot 10 = 2.82 \cdot 10^{-20}\ \mathrm{cm}^2 \tag{2.18}$$

Which shows that p is two orders of magnitude larger than σ_a. The interpretation of this is that even though δ is a very small number and the real part of the refraction index is very close to unity and thus hard to measure, it is still a very sensitive quantity. It will be two orders of magnitude more sensitive to changes in the electron density of the sample for $\lambda = 1$ Å and $Z = 10$.

To get a better picture of the relation between δ and β we look at the growth of them as a function of k and Z. From equation (2.4) it is clear that δ behaves like:

$$\delta \propto \frac{Z}{k^2} \tag{2.19}$$

Likewise equation (2.15) shows a relation between β and σ_a (2.16).

$$2k\beta = \sum_l N_l \sigma_a \Rightarrow 2k\beta \propto \frac{Z^4}{k^3} \Rightarrow \beta \propto \frac{Z^4}{k^4} \tag{2.20}$$

Finally we can establish a relation between δ and β.

$$\frac{\delta}{\beta} \propto \frac{k^2}{Z^3} \tag{2.21}$$

Looking at equation (2.21) it becomes clear that the advantages of δ compared to β will increase when going to high energies and low atomic number.

2.4.1 Absorption and phase shift cross section

Figure 2.5 shows the relationship between the absorption cross section and the phase shift cross section. Going to atomic numbers below 20 makes the phase shift cross section between three and four orders of magnitude larger than the absorption cross section. At high atomic numbers it is still an order of magnitude or two larger than σ_a.

Since organic samples are mostly made of light materials, taking images using the refraction of X-rays becomes a very effective for looking at organic samples. Taking images using the refraction of X-rays are called phase contrast imaging.

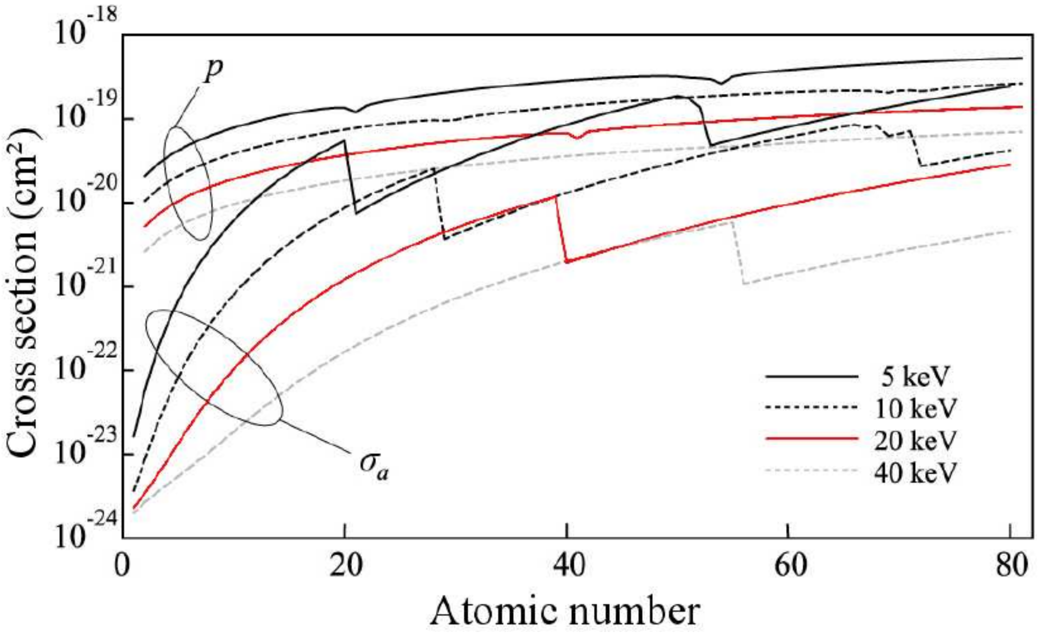

Figure 2.5: *The phase shift cross section, p, and the absorption cross section, σ_a, plotted as a function of the atomic number Z at the energies 5, 10, 20 and 40 keV. For atomic numbers below 20 p is three or four orders of magnitude larger than σ_a. The sudden drop of σ_a between 20 and 40 is due to the passing of the K edge. Figure by momose* et al.[13]. *Copyright 2006-2013 The Japan Society of Applied Physics*

2.5 Summary

This chapter is written as an introduction to the field of polymer solar cells. It introduces the key concepts which will be used in this thesis such as the fundemental design of OPV, the challenges OPV faces as well as the solutions which are being tested.

It also introduces the basic physics for X-ray transmission, refraction and scattering which is the basis for most of the imaging techniques in the thesis.

References

[1] Thomas R. Andersen, Thue T. Larsen-Olsen, Birgitta Andreasen, Arvid P. L. Böttiger, Jon E. Carlé, Martin Helgesen, Eva Bundgaard, Kion Norrman, Jens W. Andreasen, Mikkel Jørgensen, and Frederik C. Krebs. Aqueous processing of low-band-gap polymer solar cells using roll-to-roll methods. *ACS Nano*, 5(5):4188–4196, 2011.

[2] David Attwood. *Soft X-Rays and Extreme Ultraviolet Radiation: Principles and Applications.* Cambridge University Press, 2007.

[3] Martin Bech. *X-ray imaging with a grating interferometer.* PhD thesis, University of Copenhagen, 2009.

[4] Lars Blankenburg, Karin Schultheis, Hannes Schache, Steffi Sensfuss, and Mario Schrödner. Reel-to-reel wet coating as an efficient up-scaling technique for the production of bulk-heterojunction polymer solar cells. *Solar Energy Materials and Solar Cells*, 93(4):476–483, 2009.

[5] Hyosung Choi, Jung-Pil Lee, Seo-Jin Ko, Jae-Woo Jung, Hyungmin Park, Seungmin Yoo, Okji Park, Jong-Ryul Jeong, Soojin Park, and Jin Young Kim. Multipositional silica-coated silver nanoparticles for high-performance polymer solar cells. *Nano Letters*, 13(5):2204–2208, 2013.

[6] JJM Halls, K Pichler, RH Friend, SC Moratti, and AB Holmes. Exciton diffusion and dissociation in a poly (p-phenylenevinylene)/c 60 heterojunction photovoltaic cell. *Applied Physics Letters*, 68(22):3120–3122, 1996.

[7] Des McMorrow Jens Als-Nielsen. *Elements of Modern X-ray Physics*. John Wiley and Son, Ltd, 2001.

[8] Mikkel Jørgensen, Kion Norrman, Suren A Gevorgyan, Thomas Tromholt, Birgitta Andreasen, and Frederik C Krebs. Stability of polymer solar cells. *Advanced Materials*, 24(5):580–612, 2012.

[9] Mikkel Jørgensen, Kion Norrman, and Frederik C Krebs. Stability/degradation of polymer solar cells. *Solar Energy Materials and Solar Cells*, 92(7):686–714, 2008.

[10] Mikkel Jørgensen, Jon Eggert Carle, Roar R. Søndergaard, Marie Lauritzen, Nikolaj Aleksander Dagnæs-Hansen, Sedi Louise Byskov, Thomas Rieks Andersen, Thue Trofod Larsen-Olsen, Arvid P.L. Bøttiger, Birgitta Andreasen, Lei Fu, Lijian Zuo, Yao Liu, Eva Bundgaard, Xiaowei Zhan, Hongzheng Chen, and Frederik C Krebs. The state of organic solar cells-a meta analysis. *Solar Energy Materials & Solar Cells*, 2013.

[11] K. Landfester. The generation of nanoparticles in miniemulsions. *Advanced Materials*, 13(10):765–768, 2001.

[12] Atsushi Momose and Jun Fukuda. Phase-contrast radiographs of nonstained rat cerebellar specimen. *Medical Physics*, 22(4):375–379, 1995.

[13] Atsushi Momose, Wataru Yashiro, Yoshihiro Takeda, Yoshio Suzuki, and Tadashi Hattori. Phase tomography by x-ray talbot interferometry for biological imaging. *Japanese journal of applied physics*, 45:5254, 2006.

[14] F. Padinger, R.S. Rittberger, and N.S. Sariciftci. Effects of postproduction treatment on plastic solar cells. *Advanced Functional Materials*, 13(1):85–88, 2003.

[15] European Parliament and of the Council. Directive 2010/75/eu of the european parliament and of the council of 24 november 2010 on industrial emissions (integrated pollution prevention and control, 2010.

[16] P Peumans, S Uchida, and SR Forrest. Efficient bulk heterojunction photovoltaic cells using small-molecular-weight organic thin films. *NATURE*, 425(6954):158–162, SEP 11 2003.

[17] Wilhelm Conrad Röntgen. Über eine neue art von strahle. *Physical-Medical Society*, 1895.

[18] Paul E Shaw, Arvydas Ruseckas, and Ifor DW Samuel. Exciton diffusion measurements in poly (3-hexylthiophene). *Advanced Materials*, 20(18):3516–3520, 2008.

[19] Roar Søndergaard, Markus Hösel, Dechan Angmo, Thue T Larsen-Olsen, and Frederik C Krebs. Roll-to-roll fabrication of polymer solar cells. *Materials Today*, 15(1):36–49, 2012.

[20] F Yang, M Shtein, and SR Forrest. Controlled growth of a molecular bulk heterojunction photovoltaic cell. *NATURE MATERIALS*, 4(1):37–41, JAN 2005.

Chapter 3

Samples & Preparation

While the characterization techniques used in this thesis are very different, the sample preparation often had a lot in common. In this chapter all the preparation methods will be introduced without going into detail with the experiments. Throughout this thesis the most important samples are nanoparticles made of P3HT, P3HT:PCBM and P3:PCBM, where P3 is a low band gap polymer first published by Andersson *et al*[5]. This section explains the preparation of the samples for the various techniques used to characterize them.

3.1 Materials & Ink preparation

P3HT (Sepiolid P-200 from BASF) was employed as the donor polymer and technical grade PCBM was employed as the acceptor material (Solenne BV). PEDOT:PSS was based on an aqueous dispersion (2:1 w/w) of Orgacon EL-P 5010 from Agfa that was used directly as received. The substrate, acquired from IST, was a 130 μm PET substrate with a patterned ITO layer (nominally 60 Ω square^{-1}). The low band gap polymer P3 were prepared as described in the literature[5].

The ink was prepared using the procedure proposed by Landfester *et al*[3] with the minor variations described by Andersen *et al*[2]. The P3HT and/or PCBM were dissolved in chloroform or chlorobenzene, and mixed with an aqueous sodium dodecyl sulfate (SDS) solution in a tall beaker. The mixture was stirred vigorously for 1 hour and then subjected to ultrasound (0.65 kW) using an UIP 1000 hd transducer from Hielscher ultrasound technology fitted with a booster head. The mixture was stirred on a hot plate, at a temperature suitable, until the solvent had evaporated. Excess of SDS was removed from the aqueous dispersions by dialysis against pure water using dialysis tubes

(Milipore) or using a labscale dialysis system. In the final step the dispersions were concentrated to approximately 60 mg/mL. The full specifications for the inks are shown in table 3.1.

Sample	Polymer [g]	PCBM [g]	Chloroform [mL]	Chlorobenzene [mL]	SDS [g/L]	SDS [mL]	Ultrasound [min]
P3HT:PCBM	0.3	0.3	15	0	30	50	4
P3HT	0.3	0	10	0	30	25	6
PCBM	0	0.2	5	0	40	20	6
P3:PCBM	0.3	0.3	5	0	40	20	6

Table 3.1: *Production specifications for the materials used for the samples. Ink consists of a mixture of polymer-material (P3HT or P3) and PBCM material. Inks were added* 5 mg/ mL *FSO*

Prior to coating, the dispersions was added a wetting agent, typically FSO. In the rest of this thesis we will refer to a solution mixed with a wetting agent as an *ink*, while a solution without a wetting agent will be refered to as *material*. The distinction is used because several expeirments are performed on identical samples with and without wetting agent. A *nano-particle dispersion* is used as a common name for both inks and materials.

3.1.1 Spin coating

Spin coating was always performed on a small glass slide or silicon wafer of 1×1 cm^2. In case of problems with too low wettability the slides were treated with 10 minutes of ozone before coating. The spin coater was set to 800 RPM unless otherwise noted.

3.2 Samples for X-ray scattering experiments

Small angle scattering of a nano-particle dispersion was performed on the dispersion in a sealed 1 mm capillary made of borosilicate. The capillary was sealed with epoxy glue.

Grazing incidence small angle X-ray scattering (GISAXS) was performed either from films spin coated on glass, or R2R coated samples on PET.

3.3 Samples for TEM

TEM sample holders are a 3 mm diameter ring with a mesh grid for support. The type of grid used and the method of transfering the sample to the grid varied depending on the sample.

3.3.1 Nano-particle dispersions

The nano-particle dispersion was drop casted on a TEM grid with a hexagonal grid structure, 150 holes per inch and coated with a holey carbon film. The ink was only dropped on half of the grid and a small tissue was used to absorb most of it, leaving only a thin layer. The remaining layer is not a monolayer but a bi- or tri-layer. At the border of the ink however, the particles will form a monolayer or even a submonolayer.

3.3.2 Spin coated samples

For the lift off, the films were slowly slid into a beaker of water, with the film floating onto the water surface. A piece of film with the desired size was then transferred to a TEM grid by directly catching it with the grid in the water. Since the spin coated films are large and strong the TEM grids with only 50 holes per inch and without a supporting carbon film was used.

3.3.3 R2R coated samples

The nanoparticles from a working device was prepared by delaminating the cell. This creates a very clean separation between the PEDOT:PSS and the active layer[4]. The remaining cell was then submerged into a solution of potassium hydroxide. After 4-5 hours the active layer can be remove from the substrate by scraping it off the surface with a blunt object. The small films of active layer are then transferred to the sample holder, in this case a TEM grid as shown on figure 3.1.

With this method it is not possible to remove a piece of film much larger than a few hundred microns since it creates small pieces with a broad size distribution. The size distribution makes it very usefull as a general sample preparation technique. Figure 3.2 shows an optical microscopy image of a piece of active layer removed from a working cell. The diameter of the films starts below the resolution of optical microscopy and up to around 100 μm. The TEM grids for films from devices were not coated by a carbon film and used a mesh of 150 holes pr inch.

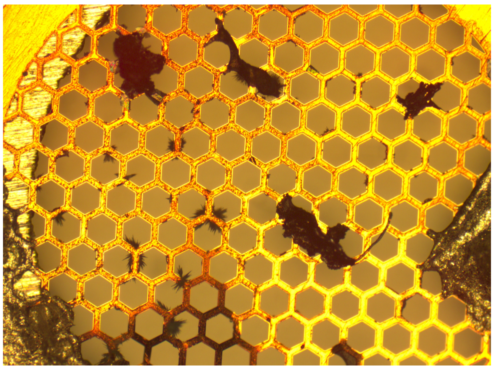

Figure 3.1: *A TEM grid with a several pieces of film from a R2R coated sample*

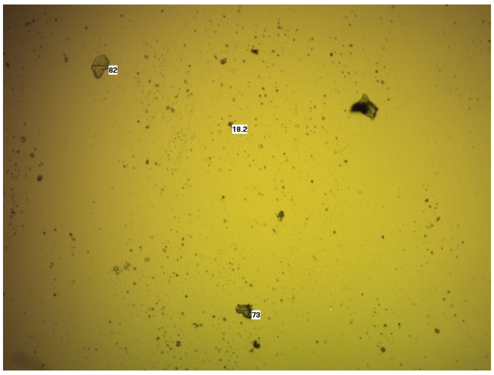

Figure 3.2: *Small pieces of film removed from a working R2R coated device. The pieces were scraped of using a blunt tool. The size of the films are anywhere from 1* µm*to 100* µm

3.4 Soft X-rays

For experiments with soft X-ray most samples were prepared identically to the ones used in the electron microscopy experiments.

In addition some of the samples were spin coated directly on silicon nitride membranes in order to avoid transferring the film to grids. The membranes were standard SiN membranes from Silson.com with a frame of 5 × 5 mm, a membrane width of 1.5 mm and a window thickness of 100 nm. A 50 nm window was too fragile for spin coating.

3.5 Hard X-rays

The samples for ptychography are required to be mounted upright and to be rotated 180° around itself. In our experiments the ptychographic images have a field of view around 20 µm and it is nessecary that the sample stays in the field of view from all angles.

We used two different approaches to mount the sample. One where the sample is welded to a needle using a FIB-SEM and one where the sample is placed in a microcapillary.

3.5.1 Mounting the sample on a needle

After the R2R coated sample has been delaminated and the active layer was removed from the substrate by the same procedure as previously described, the films were examined in a FIB-SEM. The conductance of the polymers made it possible to omit the sample coating sometimes used for SEM measurements. Albeit the contrast of the SEM does not make it possible to distinguish polymers from ITO or other pieces of contamination this was easily accomplished using EDS.

After locating a film of polymer of the right size the FIB was used to weld the piece of film to a thin needle. One problem with this approach was that pieces larger than 5 µm was sticking too hard to the sample holder inside the FIB-SEM and would break when trying to lift the needle with sample, limiting the maximum size of the sample.

3.5.2 Mounting the sample in a microcapillary

Another approach was to use microcapillaries to hold small pieces of film. The microcapillaries were produced by pulling a heated regular capillary of borosilicate under low pressure.

The microcapillaries were pulled on a Sutter P-97 Flaming/Brown Micropipette Puller (Sutter Co, Novato, CA, U.S.A.) to a few microns in diameter at the tip. They were all produced by pulling them at 590 °C and 0.1 atm pressure. This produced capillaries with a tip around 10 µm while simultaneously keept them as short as possible. A short tip is preferable because it is less fragile and because it is easier to get a piece of film placed at the very end of the microcapillary.

The borosilicate has a mass density of 2.23 g/cm^3 which translates into an electron density of $1.3\,\mathrm{e}/\mathrm{Å}^3$.

After producing a microcapillary, the sample was either spin coated on a piece of glass or, in case of R2R coated cells, delaminated between the PEDOT:PSS layer and the active layer[4]. The thick end of the capillary was then used to scrape against the sample in order to get small pieces of film into the capillary. A nitrogen airflow is then used to blow the material into the tip of the microcapillaries.

Mounting the samples in microcapillaries became the most commonly used method for mounting samples because it did not require any high end equipment such as the FIB-SEM.

3.6 Unwinder unit

A part of this thesis explores the possibilities of characterizing long foils with R2R coated samples with continually changing parameters. This is done by mounting the foil on a custom foil winder-unwinder unit resembling a large casette tape.

The samples for the unwinder unit were coated on PET in a 13 mm side band by using R2R coating technology. The 5 m long foil was then cut by a R2R cutting machine in 3 cm wide bands in order to fit the device. Furthermore the foil was labeled with a barcode every 10 cm in order to be able to uniquely identify a position on the foil.

Prior to coating all solutions were stirred at 70 °C and filtered through a 0.45 micro Teflon filter.

3.6.1 Thickness

The film with varying thickness was coated with P3HT and PCBM, both 20 mg/ mL in chlorobenzene. The film was coated with a wet film thickness of 10 mm, which from similar experiments, is known to correspond to a dry film thickness of 400 nm[1]. The dry thickness of the measured film varied from 150 nm to 400 nm.

3.6.2 Ratio

The film with the varying ratio of P3HT and PCBM was coated with one pump containing P3HT (20 mg/ mL) in chlorobenzene and another pump containing PCBM (20 mg/ mL) in chlorobenzene. The film started with 100% P3HT and 0% PCBM and changed linearly to 100% PCBM and 0% P3HT.

3.6.3 Additive

The film with varying amount of 1-chloronaphthalene pump A contained P3HT and PCBM, both 20 mg/ mL in chlorobenzene. Pump B contained P3HT and PCBM, both 20 mg/ mL in chlorobenzene with 1-chloronaphthalene (5% v/v). The final film gradually, and linearly, changes from 0% additive to 5% additive.

References

[1] Jan Alstrup, Mikkel Jørgensen, Andrew J. Medford, and Frederik C. Krebs. Ultra fast and parsimonious materials screening for polymer solar cells using differentially pumped slot-die coating. *ACS Applied Materials & Interfaces*, 2(10):2819–2827, 2010.

[2] Thomas R. Andersen, Thue T. Larsen-Olsen, Birgitta Andreasen, Arvid P. L. Böttiger, Jon E. Carlé, Martin Helgesen, Eva Bundgaard, Kion Norrman, Jens W. Andreasen, Mikkel Jørgensen, and Frederik C. Krebs.

Aqueous processing of low-band-gap polymer solar cells using roll-to-roll methods. *ACS Nano*, 5(5):4188–4196, 2011.

[3] K. Landfester. The generation of nanoparticles in miniemulsions. *Advanced Materials*, 13(10):765–768, 2001.

[4] Thue T. Larsen-Olsen, Birgitta Andreasen, Thomas R. Andersen, Arvid P.L. Böttiger, Eva Bundgaard, Kion Norrman, Jens W. Andreasen, Mikkel Jørgensen, and Frederik C. Krebs. Simultaneous multilayer formation of the polymer solar cell stack using roll-to-roll double slot-die coating from water. *Solar Energy Materials and Solar Cells*, 97(0):22 – 27, 2012.

[5] Ergang Wang, Lintao Hou, Zhongqiang Wang, Stefan Hellström, Fengling Zhang, Olle Inganäs, and Mats R Andersson. An easily synthesized blue polymer for high-performance polymer solar cells. *Advanced Materials*, 22(46):5240–5244, 2010.

Chapter 4

X-ray scattering and diffraction

This chapter aims to give the reader a basic understanding of how various X-ray scattering techniques, such as small angle scattering, wide angle scattering, scattering from grazing incidence, reflectrometry and rocking curves work. First section 4.1.1 to 4.1.3 will explain how the techniques work, when they can be used and what they measure. The details about the excact mathematical relationship between the experimental geometry and aquired data will be ommitted.

Secondly, section 4.2 explains an implementation of the inverse Fourier transform aimed at finding particle size distributions from small angle scattering data.

Section 4.4.1 to 4.4.4 will demonstrate how X-ray scattering can and have been applied to polymer solar cells in various forms.

4.1 Experimental techniques & setups

4.1.1 Small Angle X-ray Scattering

Small Angle X-ray Scattering (SAXS) from particles in solution is a commonly used technique for determining the shape or size of the scattering particles. SAXS is used on samples with domain sizes in the range from 1 nm and up to 1 µm. Due to the inverse relationship between the domain size and the scattering angle, samples with domains smaller than 1 nm will scatter at large angles and be regarded as Wide Angle X-ray Scattering (WAXS) and samples with domain sizes larger than 1 µm will scatter at angles too small for a regular SAXS setup to resolve. Ultra Small Angle Scattering (USAXS) is designed to go to even smaller angles than regular SAXS.

The advantages of SAXS compared to other techniques, such as AFM, is the ability to measure samples in solution and in contrast to electron microscopy there is no risk of causing beam damage to the sample.

4.1.1.1 Experimental setup

The SAXS setup at DTU Risø Campus, see figure 4.1, is a rotating copper anode, used in fine focus mode. The copper K_α line delivers an X-ray energy of 8.046 keV (1.5418 Å).

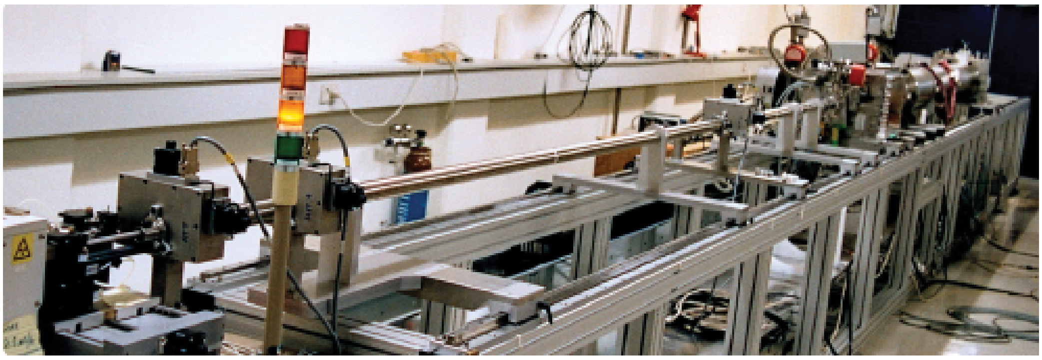

Figure 4.1: *The SAXS setup at DTU Risø Campus operating in its long geometry. The rotating anode can be seen at the far left. The sample chamber, the flight tube and the detector can be seen to the far right.*

The setup is a 12 m pinhole camera and the collimation of the beam is achieved by three sets of circular pinholes. The fine focus anode gives a small source size, which is focused. Two sets of slits are enough to define the beam but due to slit scattering from the second slit a third pinhole is used. The detector is an 18 × 18 cm active area 2D position sensitive multi wire gas detector with a pixel size of 208 × 218 μm^3.

The sample to detector can be adjusted from 15 cm to 460 cm. With the energy from the Cu K_α line this translate into a $\mathbf{q}$-range between $2 \cdot 10^{-2}\,\mathrm{nm}^{-1}$ and $20\,\mathrm{nm}^{-1}$. In the long geometry, the distance from sample to detector is only 4.5 m and not 12 m because of the need for collimation. When using the short gemometry a more divergent beam is acceptable and less strict collimate of the beam is required. However when usign the long gemometry, the beam needs to have a low divergence which impacts the flux. A 4 mm cylindrical and highly absorbing material is used as a beamstop to protect the detector.

4.1.2 Grazing incidence small angle X-ray scattering

Small Angle X-ray Scattering under grazing incident angles (GISAXS) is used to measure on coated samples[17]. Compared to liquids, thin films are often coated on a substrate which is too thick to penetrate with the X-ray beam, or scatters too much compared to the sample.

By orienting the substrate surface at or just below the critical angle for total reflection with respect to the incoming X-ray beam ($\approx 0.2°$), the beam will be scattering from the deposited film and can be used to investigate the nanostructure similiary to regular SAXS.

GISAXS have become a valuable tool in thin film characterization but the data analysis is complex. The primary reason for this is that in addition to normal scattering events, some X-rays will first reflect from the substrate and then scatter. Some X-rays will be scattered from the samples and the be reflected by the substrate. Some will even be reflected from the substrate, scattered by the sample and reflected a second time. This diffuse scattering requires a good understanding of the nanostructure of the sample in advance to be analysed. However, when the incident angle is close to the critical angle a dynamic feature called the Yoneda Peak[20] emerges.

The peak is a dynamic scattering process and arises because of interference between the incoming X-rays and the reflected X-ray. If the incomming X-ray hits the sample at an incident angle, α_i, the specular peak will be located at the angle $2\alpha_f$. The Yoneda peak will be located below the specular peak, but above the sample horizon at α_f, where the exit angle equals the critical angle: $\alpha_f + \alpha_c$.

The scattering intensity of the $\mathbf{q}_y$ axis corresponds to a transmission SAXS measurement. Due to the high intensity at the Yoneda line it is often used as an effective method of performing regular SAXS measurements on thin films.

All the GISAXS measurements were performed on the same setup as used for the SAXS experiments.

4.1.3 Wide angle X-ray scattering

Due to the reciprocal relationship between scattering angle and domain size WAXS is used to measure structure on the molecular level inside particles instead of domain sizes in the particle regime.

The wide angle X-ray scattering (WAXS) is performed similiarily to the small angle scattering but the sample is placed much closer to the detector thus measuring scattering at much larger angles ($> 5\ °$). The major difference in the setup is the use of an offline photostimulable image plate detector which is scanned after each measurement. In addition the setup is using a high-flux collimation and a more divergent beam.

The source is a rotating Cu-anode (Rigaku 18 kW) operating at 50 kV/200mA focused, and monochromatized (Cu K_α, $\lambda = 1.5418$ Å) by a 1D multilayer.

4.2 Data Analysis

4.2.1 SAXS data using the bayesian inverse fourier transform

SAXS can be used for determining a lot of different size or shape parameters depending on the experiment and prior knowledge about the sample. In the case of nanoparticles in solution the most important data parameter is the particle size distribution.

One of the most commonly calculated properties is the pair correlation function, $g(r)$, describing how the sample density varies as a function of distance from a given position.

The pair correlation function is the inverse Fourier transform of the scattering form factor, $P(Q)$. Since the dispersion is dilute, the particles act as individual scatterers. In this case $P(Q)$ is the only significant contribution to the scattering. $P(Q)$ depends on the size and shape of the particles so if we assume a shape the size can be determined.

In order to calculate $P(Q)$ the inverse Fourier transform is used. Traditionally this has been done by the method proposed by Glatter[8] where the user needs to estimate a smoothness parameter, α, and the largest particle size, D_{max}, manually by various rule of thumb guidelines.

A more modern approach by S. Hansen[9] is to iterate through a large set of α and D_{max} values, perform the inverse fourier transform and fit the calculated result to the original data. Scattering patterns are often not unique, and have more than one solution, but by this method one can identify the most probable solution. In most cases this approach will converge without any user interaction. This apporoach is called the Bayesian Inverse Fourier Transform (BIFT).

4.2.2 Particle size distribution

An implementation of BIFT is provided in the MATLAB package SAXSGUI[4] which calculates the pair correlation function. Albeit related the pair correlation function is not directly related to the size distribution function.

A variation of BIFT which instead of calculating the pair correlation function, calculates the size distribution function for a polydispers system. To calculate the size distribution of the nanoparticles the polydispers BIFT variation was implemented in SAXSGUI for future use. The function was added as option in the GUI as seen on figure 4.2.

The theory for the implementation can be found in another paper by S. Hansen.[18]

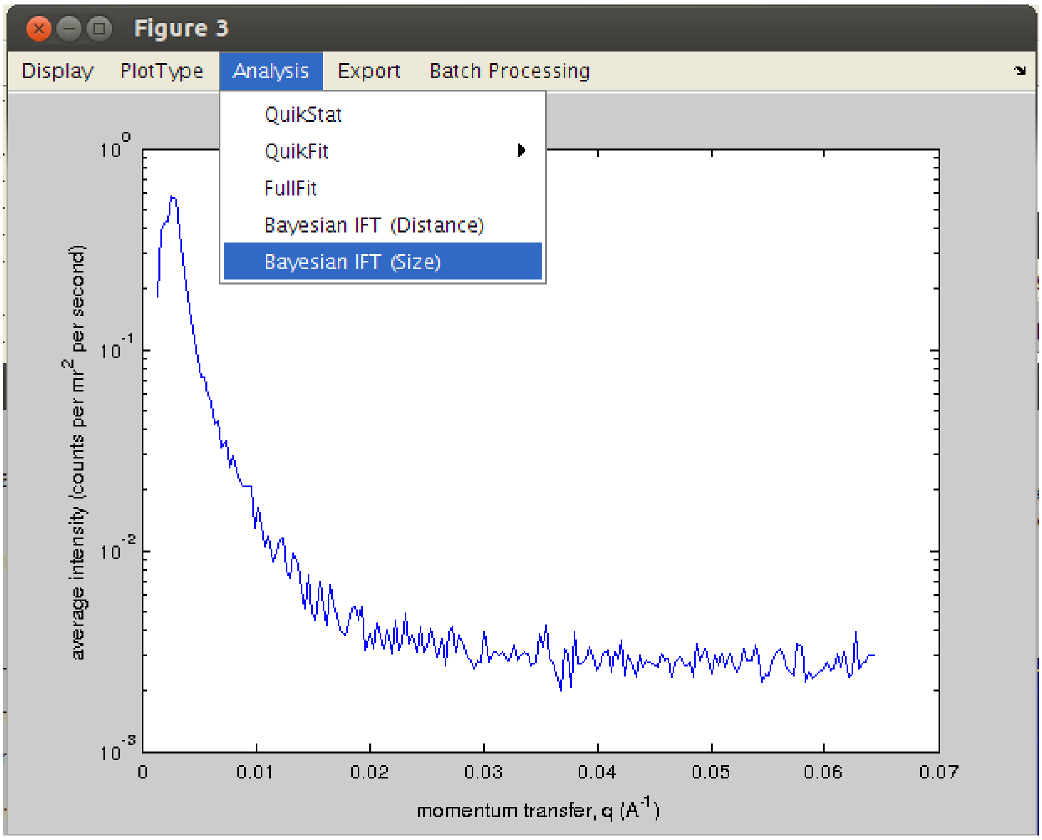

Figure 4.2: *The SAXSGUI 1D scattering intensity processing dialog. The option of calculating particle size distributions is highligted.*

4.2.3 Azimuthal and q_r integration

For quantitative comparison between different samples the 2D scattering data are often integrated along either the azimuthal direction, or in a narrow Δq_r band.

4.3 WAXS - scattering from R2R coated cells

Spin coated P3HT is known to form a semicrystalline structure on the substrate. Figure 4.3 shows the crystallite structure in P3HT. The (h00) is the lamellar stacking direction, the (0k0) direction is the π-π stacking direction and the (00l) direction is the conjugation direction.

When the π-π stacking in the substrate plane is often referred to as *edge-on* while π-π stacking out of the substrate are referred to as *head-on*.

When P3HT is spin coated the out of plane lammllear stacking is always highly textured and will cause a strong reflection in the $\mathbf{q}_z$ direction.

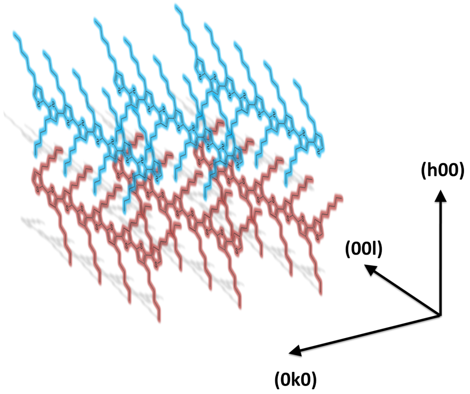

Figure 4.3: *edge-on stacking for the P3HT. P3HT are highly textured out of plane, with the lammellar-stacking repeat direction lying out of the plane of the substrate and the resulting (h00) reflections*

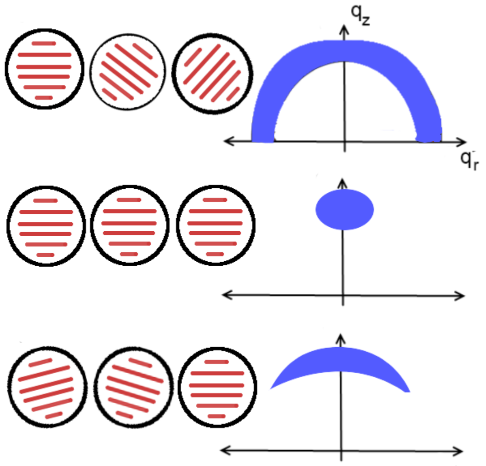

Figure 4.4: *Scattering as a function of texture.* top*: randomly oriented crystals creates a diffraction ring.* center*: highly textured crystals will diffract in a single direction.* bottom*: Semi-textured crystals diffract in a half circle.*

Figure 4.5, displays the wide angle scattering of a film with P3HT, a film with PCBM as well as a film of with P3HT:PCBM coated on PET by R2R coating. For the pure P3HT, see figure 4.5a, the bright diffraction ring corresponds to the scattering in the out of plane direction with a d-spacing of 0.39 nm^{-1}. The second order reflection is also present.

From the diffraction pattern, the orientation of the crystallites can also be determined since the direction of the reciprocal lattice vectors depend on that of crystallographic planes. As shown in figure 4.4: *top*, a film with isotropic crystallites orientation the diffraction pattern will form a uniform ring on the 2D detector. For a film with a preferred out of plane orientation where the crystallographic planes stack parallel to the surface, the diffraction pattern will consist of spots for each crystallographic plane. *center*, the diffraction peak will resemble arcs instead of a spot. *bottom*, semi-textured crystallites will scatter in an arc where the width depends on the degree of texture.

We observe that the P3HT is textured in the plane of the substrate. It is worth noting that the same aligning, out of the substrate plane, happens to P3HT during R2R coating, which works fundamentally different from spin coating.

While we know that the P3HT and PCBM will form a bulk heterojunction which consists of a complex network, figure 4.5c shows that there are no changes in the semicrystal formation of the two materials when mixed together in a heterojunction.

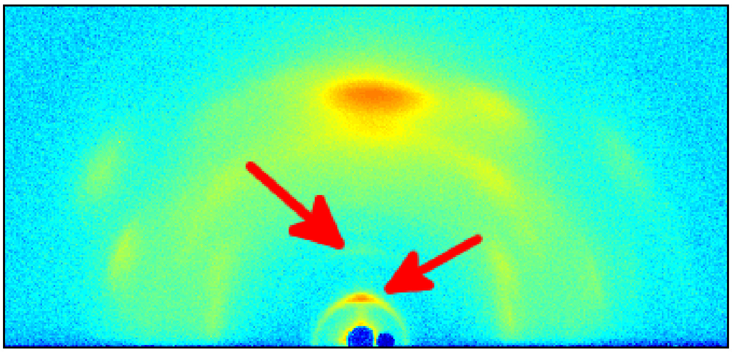

(a) *P3HT from chlorobenzene R2R coated on PET. The red arrows mark the 100 and the 200 diffraction peaks. It is worth noting that the P3HT diffraction is highly directional meaning that the crystals are ordered in the substrate plane. All the scattering at higher angles is from PET.*

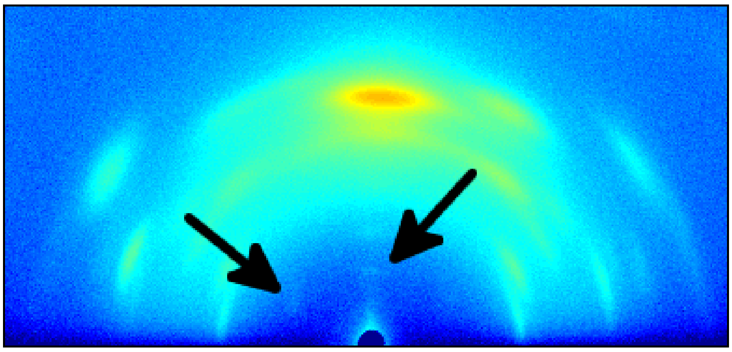

(b) *PCBM from chlorobenzene R2R coated on PET. The black arrow marks the PCBM diffraction peaks.*

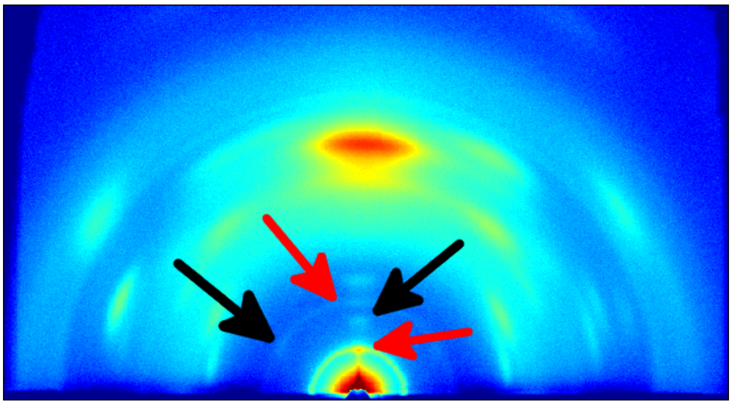

(c) *A solution of P3HT and PCBM R2R coated on PET. The red arrows mark the P3HT 100 and 200 diffraction peaks and the black arrows mark the PCBM diffraction peaks.*

Figure 4.5: *Wide angle scattering of R2R coated solutions with P3HT (fig. 4.5a), PCBM (fig. 4.5b) and P3HT:PCBM (fig. 4.5c). The diffraction peaks from P3HT are marked with red arrows while PCBM is marked with black arrows. It is clear that the solution with P3HT:PCBM is just a sum of the two individual components.*

4.4 Applications of X-ray scattering

The decribed X-ray techniques are used in a broad range of characterization studieds. The rest of the chapter will briefly describe a few eksperiments were each of the various X-ray characterization techniques was used to investigate different types of cells.

4.4.1 Low band gap nanoparticles

In addition to nanoparticles using P3HT as the electron donors, the same approach was tested with three low band gap polymers. Low band gap polymers are attractive as electron donors since the majority of the suns radiation is emitted below the P3HT band gap.

The low band gap polymers used are just referred to as **P1**[5], **P2**[10] and **P3**[19]. The structure is shown on figure 4.6 and systematic names are listed in table 4.1. The polymer P3 is also known by the name TQ1 and is used repeatedly through this thesis.

Polymer	Systematic name
P1[5]	poly[4,8-bis(2-ethylhexyloxy)benzo(1,2-b:4,5-b0)dithio-phene-alt-5,6-bis(octyloxy)-4,7-di(thiophen-2-yl)(2,1,3-benzothiadiazole)-5,50-diyl]
P2[10]	poly[(4,40 -bis(2-ethyl-hexyl)-dithieno[3,2-b:2 0 ,3 0 -d]silole)-2,6-diyl-alt-(2,1,3-benzothiadiazole)-4,7-diyl]
P3[19]	poly[2,3-bis-(3-octyloxyphenyl)-quinoxaline-5,8-diyl-alt-thiophene-2,5-diyl]

Table 4.1: *The systematic names for the low band gap polymers P1, P2 and P3*

The size distribution of the low band gap polymer particles was measured using SAXS in solution and AFM and GISAXS after being coated. The measured sizes can be seen in table 4.2.

The SAXS samples were prepared as previously described and measured for 1 hour. In addition a 1 hour background scan with a waterfilled capillary and a 24 hour dark current measurement was performed.

The dark current was subtracted from the 2D scattering image which was azimuthally averaged into 1D scattering data. The data was then corrected for the water scattering using the background measurement before being processed using the BIFT implementation in SAXSGUI[4] for calculating the size distribution of the particles.

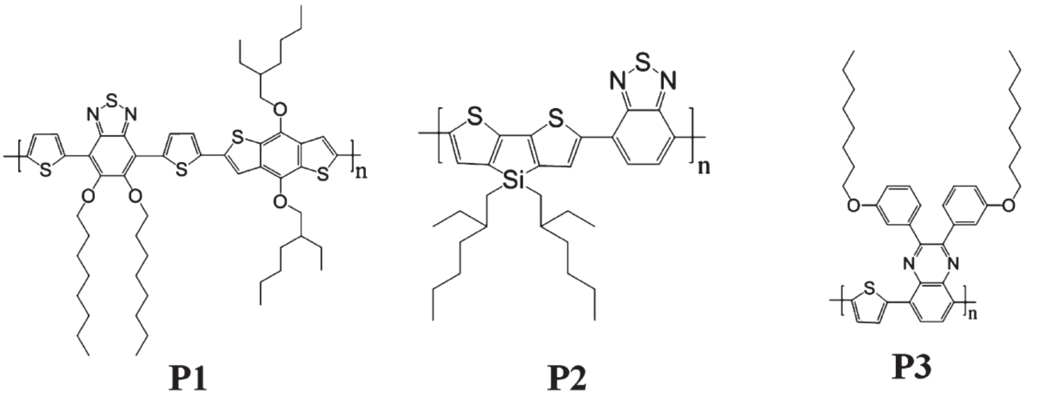

Figure 4.6: The chemical structure of the three low band gap polymers: P1, P2 and P3. Figure from Andersen et al.[2]

The size distribtion measured of the particles coated on PET was done by GISAXS and the intensity distribution along the Yoneda line was treated as SAXS transmission data.

Polymer	SAXS (dispersion)	AFM (films)	GISAXS (films)
P1[5]	130 (38) nm	n/a	n/a
P2[10]	32 (10) nm	69 (47) nm	32 (22) nm
P3[19]	87 (21) nm	120 (82) nm	107 (72) nm

Table 4.2: *The average particle diameter of the inks made of P1, P2 and P3 measured with SAXS, AFM and GISAXS. The brackets denotes the standard deviation. P1 could not be measured after the coating process due to aggregations of the particles.*

Comparing the PCE of the water based devices to their counterpart coated with use of organic solvents, it was clear that the ink with smaller particles performed better. While each particle contains a separate small bulk heterojunction one could think that larger particles would perform better due to the possibility of the donor and acceptor having greater opportunity to create a similliar nanostructure, as in a regular bulk heterojunction. However, the fact that smaller particles perform better suggests that the donor and acceptor does not mix inside the particles, or that they mix very poorly.

The GIWAXS scattering was perform from polymers spin coated on glass. In contrast to the P3HT:PCBM nanoparticles the low band gap particles had very little to no crystal structure. P1 did not show any scattering from the polymer and P2 and P3 only had a weak 100 reflection corresponding to a d-spacing of the lamellar stack of 18.2 Å^{-1} and 24.0 Å^{-1} respectively.

4.4.2 Tandem cells

One of the fundamental problems with polymer solar cells is the narrow absorption bands of the chromophores that constitute the photoactive layer of the solar cells. This makes it impossible to harvest most of the energy emitted by the suns. A tandem cell is a popular, and thoroughly studied[1,12,16] solution to the problem and utilizes two electron donors with different absorption spektra in a single cell. This increases the cells absorption band and effeciencies up to 15% have been reported[6]. The largest obstacle with tandem cells is the large and complex structure of the stack and the many points of failure due to the many layers.

TT Larsen-Olsen *et al.*[13] demonstrated the first tandem cell coated with R2R from water based inks. One ink, used for the front active layer, was based on P3HT and the ink used for the back was based on P3 used in the previous low band gap cells. We measured the front and back cell using WAXS

Figure 4.7 displays three different WAXS patterns for a R2R coated tandem cell from an aqueous solution of nanoparticles. The semi-crystal structure of P3HT and PCBM looks identical to films on figure 4.5 coated from CB. The orientation of the 100 peaks is still present as well. While it is reasonable to believe that P3HT and PCBM creates the same heterojunction inside a particle as they do in a regular cell, the hypothesis about the particles is that they should be independent. Recalling how the scattering direction depends on the texture, figure 4.4, the only way the orientation of the 100 diffraction can be explained is to assume that all the particles during the coating process align up with respect to the orientation of the P3HT inside of them. This explanation however, is far fetched and the problem will be investigated later.

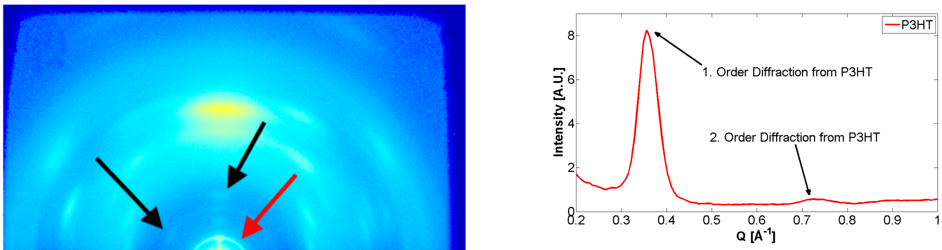

(a) *The P3HT:PCBM front active layer of the tandem cell. The diffraction peaks from P3HT is marked by the red arrow, and the features from PCBM is marked with black arrows.*

(b) *The 1D, azimuthally averaged, scattering profile of the GIWAXS image to the left, figure 4.7a. The First and second order diffraction peak from P3HT is marked at* 0.38 Å *and* 0.76 Å *respectively.*

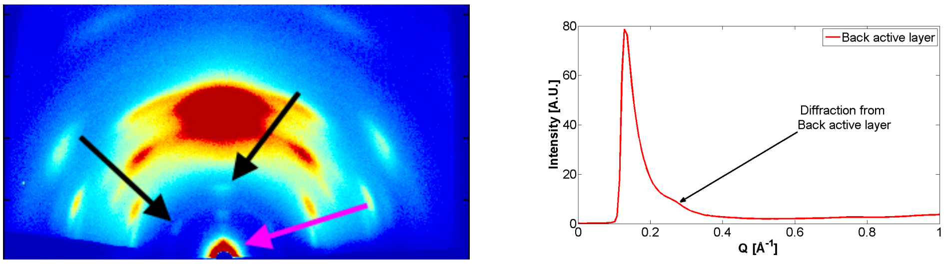

(c) *The, P3, back active layer of the tandem cell. The diffraction peaks from P3 is marked by the purple arrow, but is not clear on the GIWAXS image.*

(d) *The 1D, azimuthally averaged, scattering profile of the GIWAXS image to the left, figure 4.7c. The First order diffraction peak from P3 is marked at* 0.27 Å.

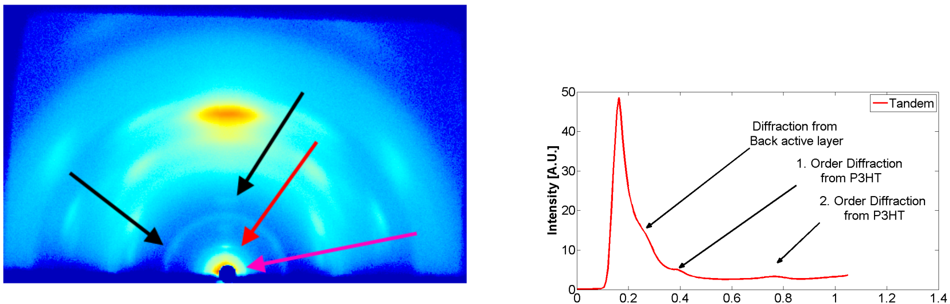

(e) *The entire tandem cell. Shows the features from both figure 4.7a and figure 4.7c combined in a single GIWAXS image. The diffraction peaks from P3HT is marked by the red arrow, the diffraction peaks from P3 is marked by the purple arrow and the features from PCBM is marked with black arrows.*

(f) *The 1D, azimuthally averaged, scattering profile of the GIWAXS image to the left, figure 4.7e. Both the first and order diffraction peak from P3HT is visible as well as the first order diffraction peak from P3.*

Figure 4.7: *GIWAXS diffraction patterns from the front and back electrode of the tandem cell from section 4.4.2.* Left*: Scattering pattern marked with features.* Right*: 1D azimuthal averaged intensity profile, displaying the diffraction peaks and their position.*

4.4.3 Double slot-die coating

Double slot-die coating is the simultaneous coating of multiple layers in the solar cell stack. The advantages are much faster processing time and less damage to the layers due to the reduced number of passthroughs of the processing equipment.

From a cell coated using double slot-die coating for both the PEDOT:PSS layer simultaneous with the active layer based on P3HT:PCBM nanoparticles we investigated the particles prior and anterior to the coating process[14].

The size distribution of the P3HT:PCBM particles was measured with SAXS and TEM and can be seen on figure 4.8 and 4.9 respectively. Furthermore reflectrometry was used in order to measure the coated film in order to validate that the PEDOT:PSS and P3HT:PCBM ink did not mix during the coating.

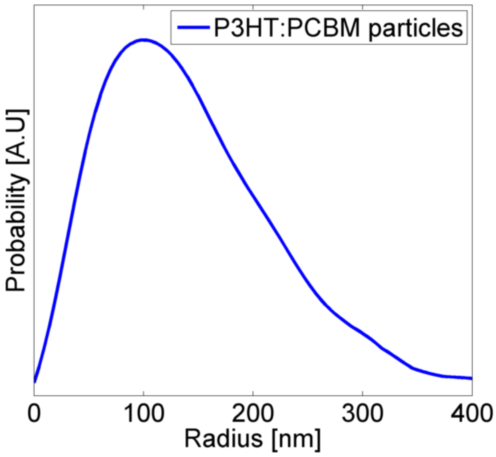

Figure 4.8: *The size distribution of the P3HT:PCBM nanoparticles in dispersion measured by SAXS and calculated using BIFT.*

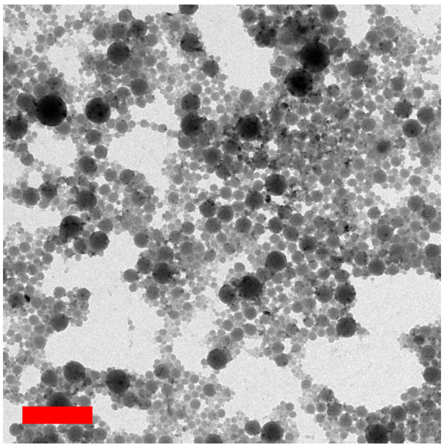

Figure 4.9: *Small pieces of film removed from a working R2R coated device. The pieces were scraped of using a blunt tool. The size of the films are anywhere from* 1 µm *to* 100 µm*.*

4.4.4 Polymer crystallinity

When coated P3HT crystals become textured in plane, but there will also be randomly oriented crystallites. When investigating the total amount of crystallites in a film, as a function of some other parameter, it becomes important to include the randomly oriented crystallites as well.

In order to quantify the total amount of scatterers one performs a omega scan also called a rocking curve. By first performing an *omega - two theta* scan and then locating a Bragg point of the out of plane crystals. The detector is then placed at the Bragg peak and the sample is independently rotated. The width of the measured curve is used to measure the texture of the crystals, and the area of the curve provides a relative number of scatteres one can compare with similar samples.

It is well known that the crystallinity of both P3HT and PCBM is drastically increased upon annealing[21].

In a study on the photochemical stability[15] of P3HT we measured the integrated amount of P3HT scatterers using rocking curves. The samples were regio-regular P3HT (rrP3HT) and regio-random P3HT (rraP3HT) both spin coated and annealed at 120°C and 140°C respectively, as well as a pristine sample.

The theory proposed by Dupuis *et al*[7] claims that the degradation rate of P3HT depends on the how fast oxygen can diffuse through the polymer. A more crystalline phase will be denser and harder to penetrate, while an amorphous phase will leave more space for other elements.

Due to the uniform structure the rrP3HT crystalises much more readily than rraP3HT. The rocking curves shows an increased crystallinity of the rrP3HT when annealed while the rraP3HT did not scatter and was concludede to be amorphous as expected[11].

It became clear that the annealing at both 120°C and 140°C had increased the crystallinity of the polymers as well as reduced the degradation of them.

The degradation rate of the polymer has been shown to scale with the number of kinks. It is believed that annealing relaxes the polymer, leading to an increased conjugation length. Consequently, annealing P3HT will improve the photo-chemical stability because the kinks created during spin coating are relaxed.

4.5 Summary

In this chapter we have introduced well known lab scale X-ray scattering techniques such as small- and wide-angle scattering and how they are implemented at DTU, Risø Campus. The basic methods for data processing have been introduced, including how the Bayesian inverse Fourier transform works and how it been implemented in SAXSGUI.

This chapter focused on the application of the various techniques in the context of polymer solar cells and it showed how the various techniques are used in order to characterize the nanostructure cells. SAXS and GISAXS was used in multiple instances to measure the size of the nanoparticles in solution and on film, and compare it with images from both AFM and TEM. WAXS was used to measure the crystalline structure of the polymers after being coated. In addition, rocking curves around Bragg peaks were used to measure the relative amount of P3HT crystallites in different types of P3HT and annealing temperatures. This helped understand the process of photodegradation.

References

[1] Tayebeh Ameri, Gilles Dennler, Christoph Lungenschmied, and Christoph J Brabec. Organic tandem solar cells: a review. *Energy & Environmental Science*, 2(4):347–363, 2009.

[2] Thomas R. Andersen, Thue T. Larsen-Olsen, Birgitta Andreasen, Arvid P. L. Böttiger, Jon E. Carlé, Martin Helgesen, Eva Bundgaard, Kion Norrman, Jens W. Andreasen, Mikkel Jørgensen, and Frederik C. Krebs. Aqueous processing of low-band-gap polymer solar cells using roll-to-roll methods. *ACS Nano*, 5(5):4188–4196, 2011.

[3] D Apitz, RP Bertram, N Benter, W Hieringer, JW Andreasen, MM Nielsen, PM Johansen, and K Buse. Investigation of chromophore-chromophore interaction by electro-optic measurements, linear dichroism, x-ray scattering, and density-functional calculations. *Physical Review E*, 72(3):036610, 2005.

[4] JJ X-Ray Systems ApS. *Saxsgui v2.08.03 SAXSLAB*, 2011.

[5] Eva Bundgaard, Ole Hagemann, Mikkel Jørgensen, and Frederik C Krebs. Low band gap polymers for roll-to-roll coated organic photovoltaics – design, synthesis and characterization. *Green*, 1(1):55–64, 2011.

[6] Gilles Dennler, Markus C Scharber, Tayebeh Ameri, Patrick Denk, Karen Forberich, Christoph Waldauf, and Christoph J Brabec. Design rules for donors in bulk-heterojunction tandem solar cells towards 15% energy-conversion efficiency. *Advanced Materials*, 20(3):579–583, 2008.

[7] Aurélie Dupuis, Pascal Wong-Wah-Chung, Agnès Rivaton, and Jean-Luc Gardette. Influence of the microstructure on the photooxidative degradation of poly (3-hexylthiophene). *Polymer Degradation and Stability*, 97(3):366–374, 2012.

[8] O. Glatter and O. Kratky. *Small Angle X-ray Scattering.* Academic Press, 1982.

[9] Steen Hansen. Bayesian estimation of hyperparameters for indirect fourier transformation in small-angle scattering. *Journal of applied crystallography*, 33(6):1415–1421, 2000.

[10] Jianhui Hou, Hsiang-Yu Chen, Shaoqing Zhang, Gang Li, and Yang Yang. Synthesis, characterization, and photovoltaic properties of a low band gap polymer based on silole-containing polythiophenes and 2, 1, 3-benzothiadiazole. *Journal of the American Chemical Society*, 130(48):16144–16145, 2008.

[11] S Hugger, R Thomann, T Heinzel, and T Thurn-Albrecht. Semicrystalline morphology in thin films of poly (3-hexylthiophene). *Colloid and Polymer Science*, 282(8):932–938, 2004.

[12] JD Kotlarski and PWM Blom. Ultimate performance of polymer: fullerene bulk heterojunction tandem solar cells. *Applied Physics Letters*, 98:053301, 2011.

[13] Thue T. Larsen-Olsen, Thomas R. Andersen, Birgitta Andreasen, Arvid P.L. Böttiger, Eva Bundgaard, Kion Norrman, Jens W. Andreasen, Mikkel Jørgensen, and Frederik C. Krebs. Roll-to-roll processed polymer tandem solar cells partially processed from water. *Solar Energy Materials and Solar Cells*, 97(0):43 – 49, 2012.

[14] Thue T. Larsen-Olsen, Birgitta Andreasen, Thomas R. Andersen, Arvid P.L. Böttiger, Eva Bundgaard, Kion Norrman, Jens W. Andreasen, Mikkel Jørgensen, and Frederik C. Krebs. Simultaneous multilayer formation of the polymer solar cell stack using roll-to-roll double slot-die coating from water. *Solar Energy Materials and Solar Cells*, 97(0):22 – 27, 2012.

[15] Morten V. Madsen, Thomas Tromholt, Arvid Böttiger, Jens W. Andreasen, Kion Norrman, and Frederik C. Krebs. Influence of processing and intrinsic polymer parameters on photochemical stability of polythiophene thin films. *Polymer Degradation and Stability*, 97(11):2412 – 2417, 2012.

[16] Young Min Nam, June Huh, and Won Ho Jo. A computational study on optimal design for organic tandem solar cells. *Solar Energy Materials and Solar Cells*, 95(4):1095–1101, 2011.

[17] Gilles Renaud, Rémi Lazzari, and Frédéric Leroy. Probing surface and interface morphology with grazing incidence small angle x-ray scattering. *Surface Science Reports*, 64(8):255–380, 2009.

[18] Bente Vestergaard and Steen Hansen. Application of bayesian analysis to indirect fourier transformation in small-angle scattering. *Journal of applied crystallography*, 39(6):797–804, 2006.

[19] Ergang Wang, Lintao Hou, Zhongqiang Wang, Stefan Hellström, Fengling Zhang, Olle Inganäs, and Mats R Andersson. An easily synthesized blue polymer for high-performance polymer solar cells. *Advanced Materials*, 22(46):5240–5244, 2010.

[20] Y. Yoneda. Anomalous Surface Reflection of X Rays. *Physical Review*, 131:2010–2013, September 1963.

[21] Uladzimir Zhokhavets, Tobias Erb, Harald Hoppe, Gerhard Gobsch, and N Serdar Sariciftci. Effect of annealing of poly (3-hexylthiophene)/fullerene bulk heterojunction composites on structural and optical properties. *Thin Solid Films*, 496(2):679–682, 2006.

Chapter 5

Electron microscopy

Electron microscopy is often considered the default choice for imaging samples, where the resolution of optical microscopy is too coarse due, to its high reliability, availability and superior resolution. Since electron microscopy has been a common technique for studying the morphology of OPV the initial characterization of the nanoparticles in this work was done using TEM.

The experiments were performed several times at DTU Center for Electron Nanoscopy (CEN), DTU Risø Campus and the Changchun Institute of Applied Technology (CIAC).

This chapter describes using transmission electron microscopy (TEM) for the initial characterization of the nanoparticles as well as how the particles react to annealing, physically and chemically.

5.0.1 Measurements at DTU

The initial measurements were performed in April 2011 at DTU CEN using their FEI Tecnai T20 G^2 microscope and measured at 300 keV. Two samples worth noting were the dropcasted P3HT:PCBM nanoparticles and the same nanoparticles used as the active layer in working cell, coated by R2R coating.

Figure 5.1a shows the nanoparticles immediately after treatment with ultrasound and upconcentration. Figure 5.1b shows the same batch of particles having been through all the steps by R2R coating, including the following delamination process .

In figure 5.1a shows the same batch of particles having been through all the steps by R2R coating, including the delamination process.

In contrast figure 5.1b a much less coherent image can be seen. There are structures clearly resembling the particles in figure 5.1a but the shape is more like grains than spheres. Furthermore, the particles are connected by a bulk of unknowns substance.

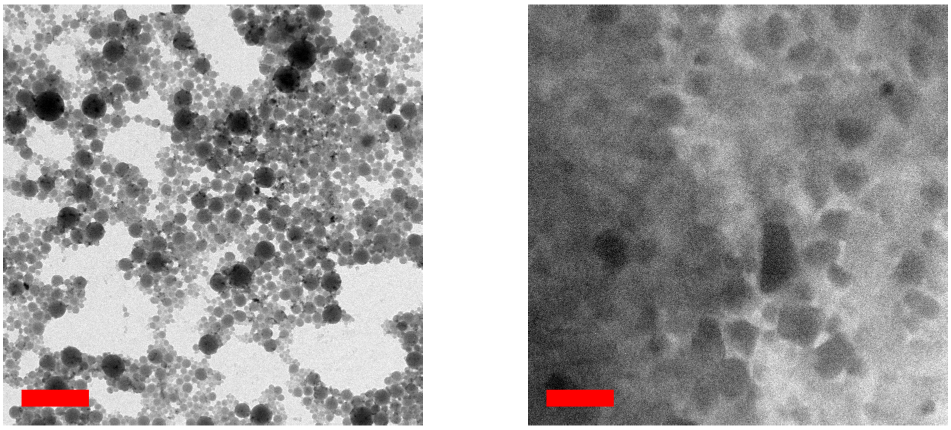

(a) P3HT:PCBM nanoparticles dropcasted on a TEM grid. All the particles are spheres and the size distribution matches the one measured with SAXS.

(b) The active layer of the same P3HT:PCBM nanoparticles from a R2R coated device. The particles are no longer spheres but have a more grain-like structure. There is also an unknown substance connecting the particles.

Figure 5.1: *Dropcasted and R2R coated nanoparticles measured with TEM at DTU CEN at 300 keV. The image are both* $5 \times 5\,\mu\mathrm{m}$ *and the scalebar is* $1\,\mu\mathrm{m}$

5.1 Annealing experiments performed in Changchun, China

There are several steps in the coating process that can affect the nanoparticles and it is unknown which steps that causes the morphological changes. The changes could be caused by the addition of FSO-100 (Sigma-Aldrich), the diffusion between the ink and the surrounding layers in the cell, the annealing of the cells, the delamination or a combination of two or more of these steps. At the CIAC we performed an experiment to study what affect the annealing had on the morphology of the nanoparticles. Using the P3HT:PCBM nanoparticle ink, as well as an ink based on P3, 6 samples were spin-coated with each of the two ink types and were annealed at 140° C for 0, 1, 3, 5, 10 and 15 minutes, respectively. The results for the P3HT:PCBM particles are shown in figure 5.2 and the results of P3 are shown in figure 5.3.

The ink based on P3HT, figure 5.2, shows a large collection of grain like particles, similar to the previously observed in the R2R coated active layer, figure 5.1b. The bulk is more homogenious and less noisy but the morphology does not seem to be affected by the annealing time. However, what does seem to change is the contrast between the particles and the surrounding

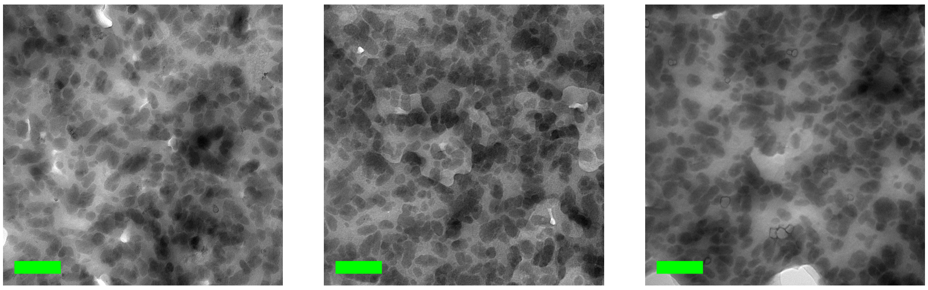

(a) *Pristine* ***(b)*** *1 minute* ***(c)*** *3 minutes*

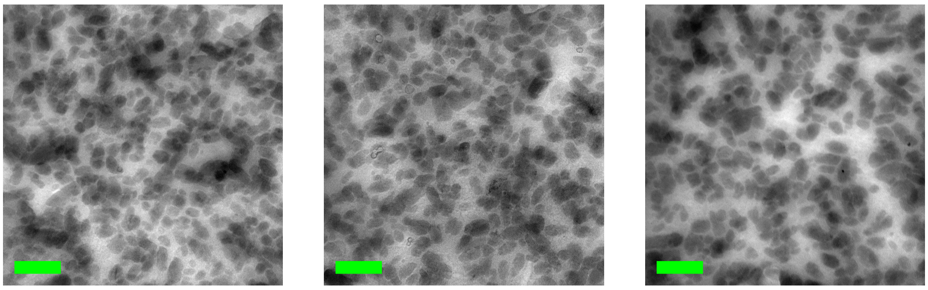

(d) *5 minutes* ***(e)*** *10 minute* ***(f)*** *15 minutes*

Figure 5.2: *P3HT:PCBM nanoparticles spincoated at a silicon wafer at 800 RPM and annealed at 140° C. The samples were annealed for: a: pristine, b: 1 minute, c: 3 minutes, d: 5 minutes, e: 10 minutes, f 15 minutes. After annleaing the films were floated of the wafer and to a TEM grid in a water beaker. There are no obvious physical changes in the morphology. The scalebar is* 1 µm

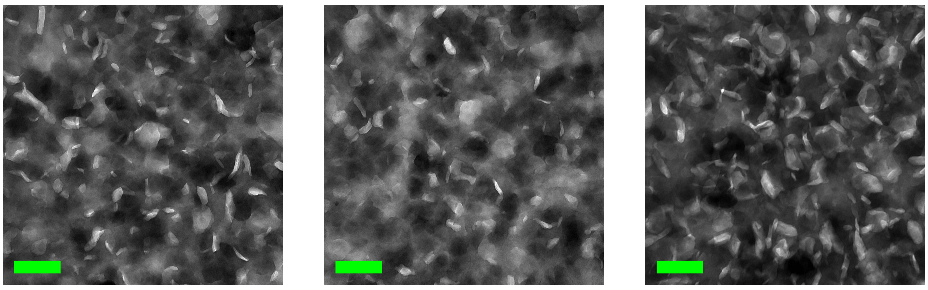

(g) *Pristine* ***(h)*** *1 minute* ***(i)*** *3 minutes*

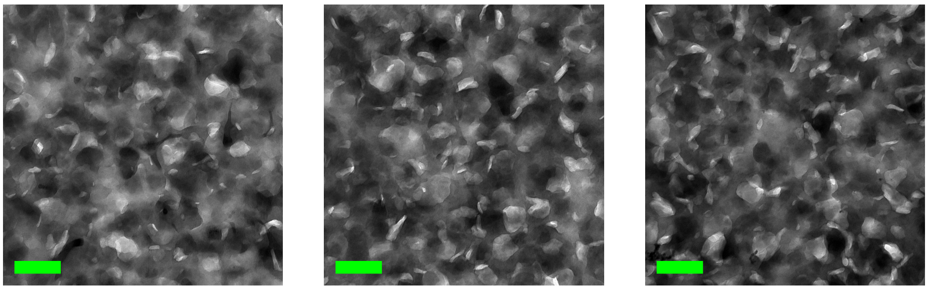

(j) *5 minutes* ***(k)*** *10 minute* ***(l)*** *15 minutes*

Figure 5.3: *P3:PCBM nanoparticles spincoated at a silicon wafer at 800 RPM and annealed at 140° C. The samples was annealed for: g: pristine, h: 1 minute, i: 3 minutes, j: 5 minutes, k: 10 minutes, l: 15 minutes. After annleaing the films were floated of the wafer and to a TEM grid in a water beaker. Just as with the P3HT:PCBM particles there are no obvious physical changes in the morphology The scalebar is* 1 µm

matrix. Knowing how both P3HT and PCBM crystallizes during annealing is it reasonably to expect this is due to the formation of denser crystal structures in the particles compared to the surrounding matrix.

The images of particles based on P3 are difficult to interpret. The images are cloudy with lots of white areas with sharp edges and large dark blurry spheres. The white areas are likely holes in the film due to pores. Recalling the size distribution of P3 (table 4.2, page 38) the particles should have an average size of 100 nm, making the dark blurry areas far too large to be single particles. However, they could be aggregates of several particles, or just density variations in the film.

The measurement of P3 was repeated several times using dropcasting and different speeds on the spin coater, but we were never able to see any particles clearly or any meaningful structures.

5.1.1 Wetting agents

To investigate if the morphological changes was caused by the wetting agent FSO-100, another batch of samples was prepared using the wetting agent TWEEN 80 (Sigma-Aldrich). In addition, we measured particles without the addition of a wetting Agent. They were dropcasted directly on the TEM grid as spin coating was not possible. The sample without any wetting agent was measured at DTU, Risø campus at 100kV. The result can be seen in figure 5.4. The spin coated samples with FSO-100 and TWEEN80, figure 5.4a and 5.4b, are completely identical. The dropcasted nanoparticles without any wetting agent, figure 5.4c, are more densely packed which could be expected since they were not spin coated. More important is the fact that the matrix connecting the particles is still present. Because of this finding we concluded that the matrix could not be a product of the coating or the wetting agent, but must come from the particles themselves.

5.1.2 Watershed based segmentation

The size distribution of the particles was analyzed in MATLAB . The watershed based segmentation[2] is a often used technique for segmentation of separate, and also overlapping, objects.

The idea of the watershed segmentation is easy to understand. The image is regarded as a topological landscape which is being flooded. The water sources are the local minimas in the image which is marked in advance. Each of the sources floods the image at the same rate and when two lakes meet the image is partitioned at that point.

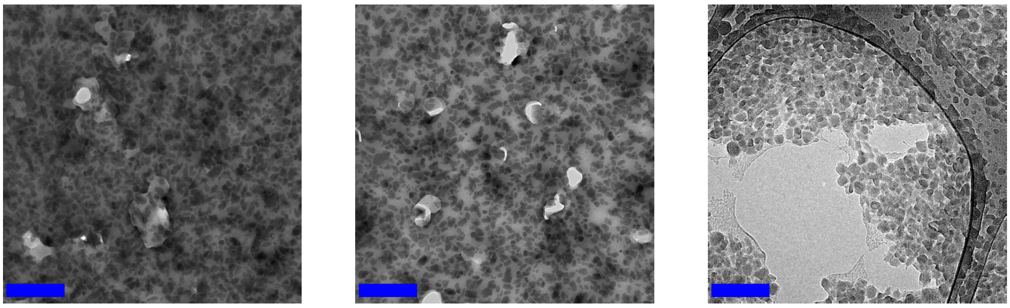

(a) *TEM image of P3HT:PCBM nanoparticles spin coated with FSO-100 as wetting agent*

(b) *TEM image of P3HT:PCBM nanoparticles spin coated with TWEEN80 as wetting agent*

(c) *TEM image P3HT:PCBM nanoparticles dropcasted without the addition of any wetting agent*

Figure 5.4: *Comparison of the P3HT:PCBM nanoparticle dispersion with the itself after the addition of two different wetting agents, FSO-100 and TWEEN80. The dispersion without any wetting agent was drop casted on the TEM grid. The spin coated particles (a, b) were measured at CIAC at* 100 *kV. The drop casted nanoparticles (c) were measured at DTU, Risø Campus at* 300 *kV. The scalebars are* 2 µm

The core algorithm is built into MATLABs image processing toolbox. The core algorithm is only able to segmentate with help of a precomputed image describing the objects to be segmented and another image including some rough boundaries.

5.1.2.1 Identification of particle markers

In the TEM images the nanoparticles were visually clear, but due to the inhomogenous film thickness some parts of the images were darker, and a simple threshold is not enough to segmentate the particles from the background. To perform the segmentation the images were processed with a high-pass filter to remove the low frequency background. The period of the background was estimated to be approximately 1 µm. After using the high-pass filter the particles could be identified by tresholding the image, but a lot of high frequency shot-noise remained. The shot noise was further reduced by using a median filter with a 5×5 kernel. The result of each step is shown on figure 5.8.

5.1.2.2 Segmentation

The threshold image on figure 5.8 was used as marker for the particles and its inverse image as the boundaries[3,1].

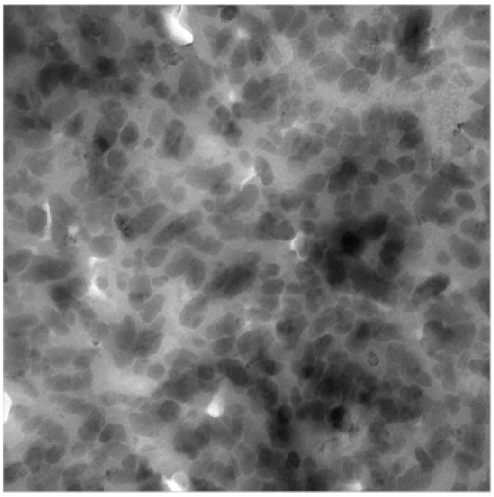

Figure 5.5: *The initial TEM image of P3HT:PCBM nanoparticles.*

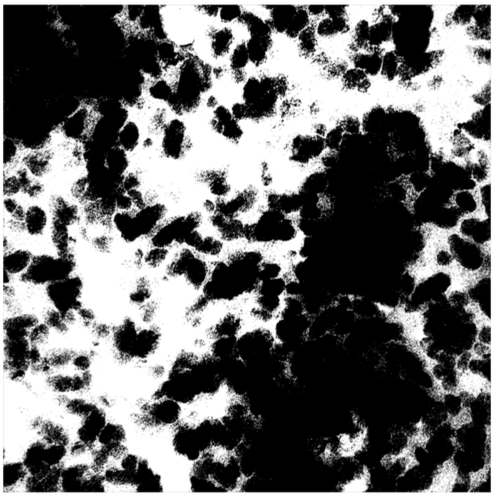

Figure 5.6: *A simple threshold segmentation is applied to the raw image from figure 5.5. It is possible to resolve a few particles but due to the inhomogenious film thickness most of the particles will fall outside the threshold.*

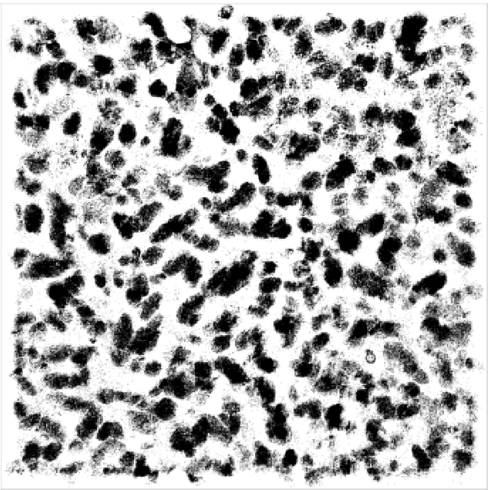

Figure 5.7: *By using a high pass filter the low frequency of the film is removed and all the particles can be segmented with a simple threshold*

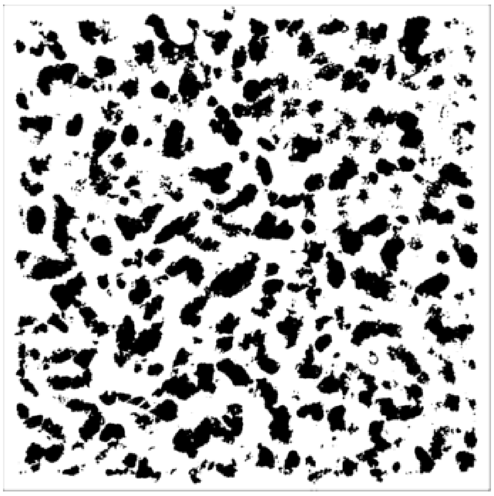

Figure 5.8: *By further using a median filter, with a* 5×5 *kernel on figure 5.7 a lot of the shot noise is also removed*

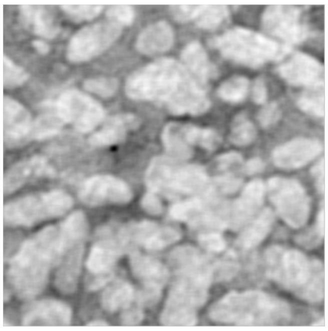

Figure 5.9: *A TEM image cropped to* $2 \times 2\,\mu\mathrm{m}$ *for clarity*

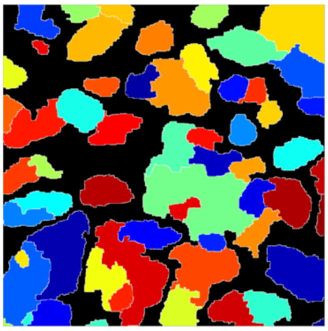

Figure 5.10: *The watershed segmentation of figure 5.9. Individual particles are found and identified very well. Adjacent particles are often resolved into seperate particles as one would do manually. The algorithm is not able to resolve large aggregates of particles*

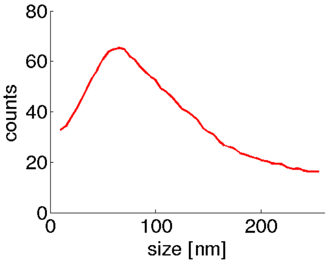

Figure 5.11: *The size distribution found in the TEM images. The size is defined as half the average between the largest and smallest axis length. The distribution has a maximum at* 70 nm.

This allowed the particles to be segmented reasonably well in areas where the particles were not too densely packed as seen on figure 5.10. Single and adjacent particles were found and segmented but larger clusters were identified as a single particle.

However, this was not a large problem since particles larger than a manually fixed threshold were exluded from further analysis.

Since the particles were not spheres an alternative definition of size was needed. The size was defined as the average between the length of the major and minor axis. The size distribution is shown on figure 5.11. Any correlation between size and annealing could not be seen but it is worth noting that the average particle size is approximately 30 nm smaller compared to the size distribution measured previously with SAXS.

5.1.3 Diffraction

For each sample at least two diffraction patterns were acquired. One diffraction pattern from an area with particles and one from the bulk material in between. However, the samples turned out to be too particle dense to acquire diffraction patterns without including at least a few particles.

Common for these diffraction patterns was a diffuse ring from P3HT and several Bragg points caused by PCBM crystals.

However, the diffraction patterns from the bulk material did show less

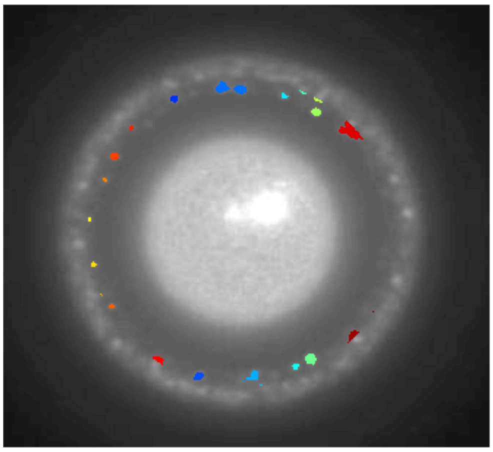

Figure 5.12: *A diffraction pattern from the P3HT:PCBM particles. The homogenious ring is P3HT. The Small brigth dots are PCBM crystals. All the crystals diffractions points with twice the intensity of the P3HT intensity have been colored.*

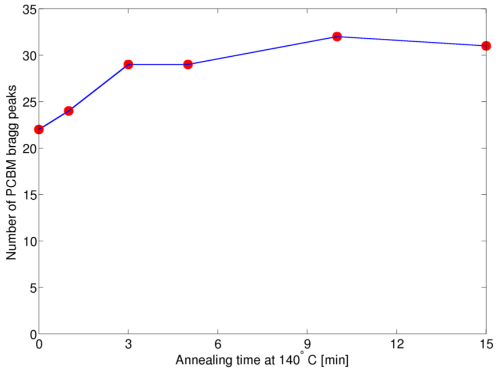

Figure 5.13: *The number of large PCBM crystals from figure 5.12 as a function of annleaing time. The crystals seems to grow rapidly for the first 3 minutes, then the growth stagnates*

PCBM crystals, suggesting the PCBM was mostly, perhaps only, located inside the particles.

Using the intensity of the P3HT diffraction ring as a reference the number of diffracting PCBM crystals with an intensity above a certain threshold can be counted. If the chosen threshold is too low most diffraction peaks will be difficult to separate. A threshold too high will filter out more diffraction peaks than necessary. An intensity about two times the intentisy of the P3HT ring was found as a good value. Counting the PCBM diffraction peaks showed an increase in the number PCBM crystals larger than the threshold. This suggested the PCBM crystals are growing as expected from the annealing.

5.2 Conclusion

A fundamentally different morphology was observed in particles after being coated with spin coating or R2R coating compared to un-treated particles. We initially suspected the annealing to be the cause of this difference. However, further experiments testing different annealing length were not able to detect any physical morphological changes of the particles and therefore this suspicion was discarded.

The bulk surrounding the particles was then believed to be FSO. The TEM measurements were repeated on the same particles but with the addition of another wetting agent as well as without wetting agent. The results showed that the bulk was not influenced by the wetting agent. Due to the lack of any other possibility our conclusion was that the bulk must be a physical change in the particles, rather than the presence of any substance added later in the coating process.

From the electron diffraction tests we observed an increasing amount of large PCBM crystalites during the annealing process, which was expected. However, the PCBM seemed to be concentrated inside the particles. This finding suggested the surrounding bulk is not particles too small to be resolved. Therefore the bulk must, by the lack of alternatives, be the P3HT previously inside the particles. It was not possible to compare the P3HT:PCBM particles with particles made of P3:PCBM due to difficulties interpreting the P3:PCBM TEM images.

The nanoparticles did not show any significant difference in shape or size as a function of coating or annealing, but were slightly smaller than prior to coating.

References

[1] David Legland. Region adjacency graph (rag). `http://www.mathworks.com/matlabcentral/fileexchange/16938-region-adjacency-graph-rag`, 2007. [Online; accessed 2013].

[2] Fernand Meyer. Topographic distance and watershed lines. *Signal processing*, 38(1):113–125, 1994.

[3] E. Preteux. Watershed and skeleton by influence zones: A distance-based approach. *Journal of Mathematical Imaging and Vision*, 1(3):239–255, 1992.

Chapter 6

Soft X-rays 2D imaging

Although electron microscopy does provide superior resolution compared to any other method of imaging it can sometimes be difficult to know what the objects on an image are. A solution to this problem is to measure the sample at different energies. Since each element has a unique absorption spectrum several images at several well chosen energies will make it possible to distinguish different elements due to the change in contrast. This approach has been adopted by both X-ray and electron microscopy. The main difference is that electrons offer superior resolution but also a larger interaction cross section. The large interaction cross section constrains the sample thickness to below 100 nm for most materials[2].

Scanning Transmission X-ray Microscopy (STXM) on the other hand is able to measure samples up to 1 µm thick and the reduced cross section also reduces beam damage[5].

In this chapter we will utilize STXM to map the active layer of R2R coated devices in order to investigate the chemical composition.

6.1 Soft X-ray imaging

Scanning Transmission X-ray Microscopy (STXM), combined with Near Edge X-ray Absorption Fine structure Spectroscopy (NEXAFS) provides an excellent technique for achieving strong chemical contrast. The contrast comes from the differences in NEXAFS spectra that are observed at the carbon 1s absorption edge. This allows direct imaging of the chemical composition of the P3HT:PCBM nanoparticles.

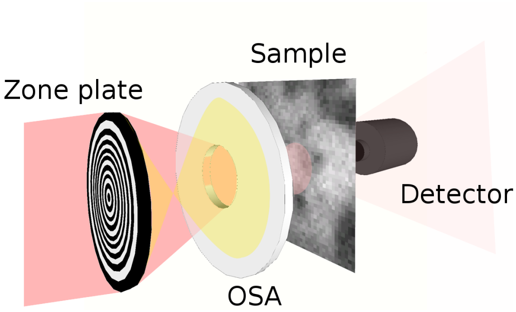

Figure 6.1: *A rendering of the experimental setup. The zone plate focuses the beam down to a spot size of* 31 nm*. The order sorting aperture removes higher order diffracted X-rays (yellow). The X-rays penetrates the sample and the detector measures the remaining intensity*

6.1.1 Scanning Transmission X-ray Spectroscopy (STXM)

Two types of transmission X-ray microscopy systems are routinely used today:

1. The full field transmission X-ray microscope (TXM)
2. The scanning transmission X-ray microscope (STXM)

In the TXM, the specimen is illuminated by a condenser lens and a magnified image is formed by an objective lens on a two dimensional X-ray detector. In the STXM, the X-rays are focused by an objective lens to a small spot which forms the scanning probe. The X-ray transmission through the specimen is measured point by point in a scanning process. In the rendering on figure 6.1, it is illustrated how the order sorting aperture (OSA) select only the first order focused radiation to reach the specimen.

6.1.2 Near-Edge X-ray Absorption Spectroscopy (NEXAFS)

The intensity of X-rays transmitted through a sample decreases due to absorption. Depending on the energy of X-rays, the absorbed X-rays can excite core electrons from different levels in an atom or a molecule. Based on the origin of the excited electron, the absorption edge can be classified as K-edge (corresponding to the excitation of a $1s$ electron.), L-edge (L_1-, L_2-, and L_3-edge corresponds to the excitation of a $2s$, $2p_{1/2}$, and $2p_{3/2}$ electron, respectively), and so on. Figure 6.2 presents a typical X-ray absorption spectrum as a function of the X-ray energy around the carbon edge[8].

With the increase of photon energy, the X-ray absorption cross section that describes the probability of absorption decreases. However, when the

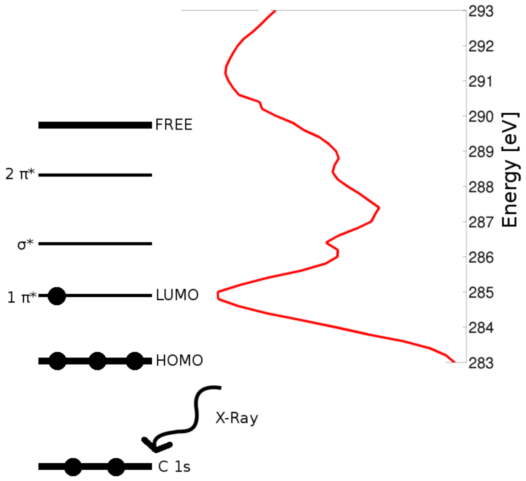

Figure 6.2: *Schematic representation of the energy levels around the carbon edge.*

photon energy corresponds to the binding energy of a core electron, the X-ray absorption cross section increases abruptly, and then decreases monotonically above the core edge. Thus an edge-like structure is observed in the absorption spectrum.

6.2 Experimental details

The experiments were carried out at the MAXYMUS scanning transmission X-ray microscope (STXM) at BESSY II, Berlin, using a 31 nm Fresnel zone plate. The energy could be tuned from 250 eV to 320 eV in steps of 0.2 eV which covered the carbon K-shell to molecular orbital transitions. Compositional maps were derived from images collected at energies that maximized the X-ray intensity contrast between the two components. Any lateral drift between the images was corrected for in post-processing by laterally shifting the images to maximize the image correlation function. Further data analysis of the STXM data was done using using MATLAB and Axis2000[6].

Axis2000 is an IDL-based package for analyzing STXM data using a graphical interface. Axis2000 together with documentation of how to load, view and export datasets are available from the authors website (`http://unicorn.mcmaster.ca/aXis2000.html`).

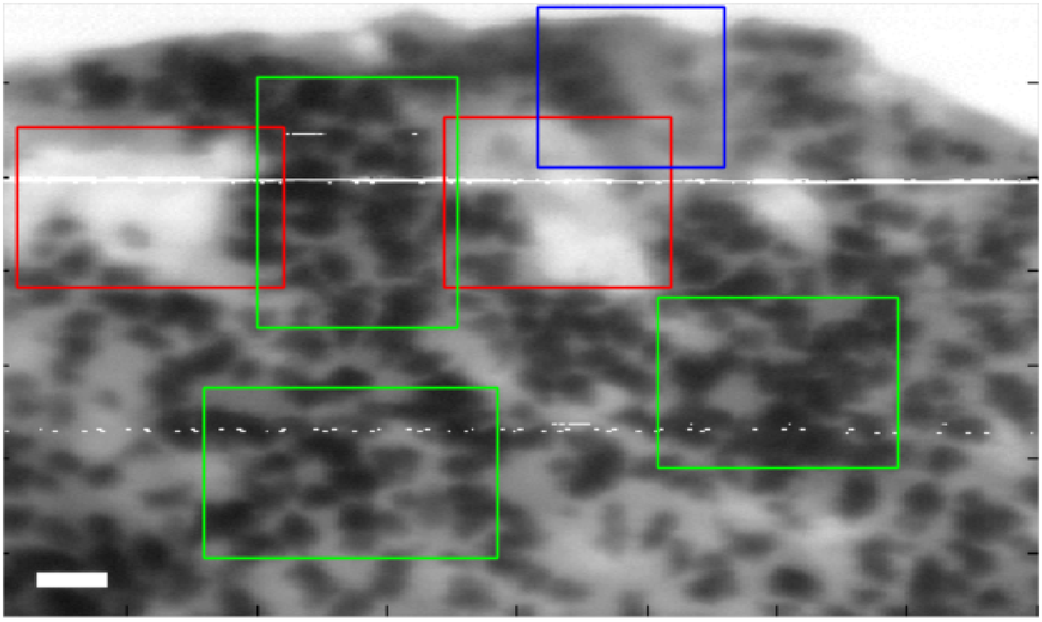

Figure 6.3: 6 × 4 µm *area scan of R2R coated P3HT:PCBM nanoparticles at 285 eV. Green areas mark clusters or particles while red mark empty regions. The white lines are noise created by the beamline. The scale bar is* 500 µm.

6.3 Imaging

Figure 6.3 shows a high resolution image of the R2R coated P3HT:PCBM nanoparticles. The field of view is 6 × 4 µm with a step size of 15 µm at 285 eV. A rough estimate of the resolution was done by comparing the 1D transition profile from particle to film (not shown) with our TEM images. The resolution was estimated to be around 40 µm.

It was apparent that the morphology was similar to the grainy particles observed with the TEM. The particles were also a lot harder to seperate. Partly because of the inferior resolution compared to TEM but also because they seemed to aggregate into larger clusters, leaving other areas empty. In figure 6.3 the clusters have been annotated with a green rectangle, and the empty areas with red ones.

The blue area was chosen for further investigation. This area, located close to a border, contained a typical cluster, separate particles and bulk material. The empty region outside the border was used for beam intensity calibration.

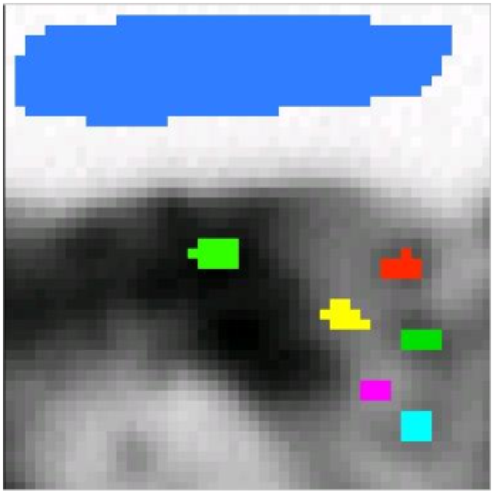

Figure 6.4: *The STXM image of a* $1 \times 1\,\mu\mathrm{m}$ *region at* 286 eV*. Red, dark green and cyan mark three areas with particles. Yellow and magenta mark bulk in between. Light green marks a large cluster. Blue is void and used for calibrating the intensities.*

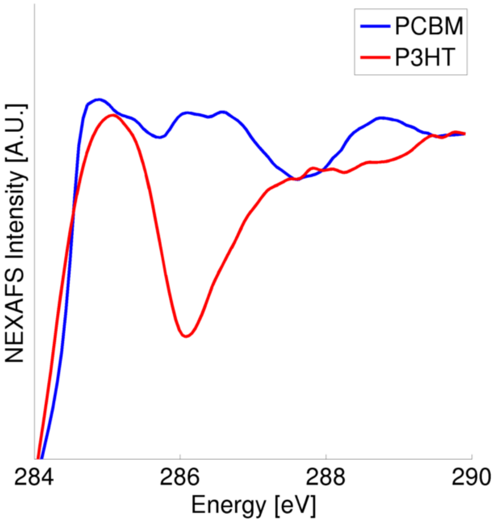

Figure 6.5: *The NEXAS spektra of P3HT and PCBM measured at the beamtime with* 0.2 eV *energy steps. The most important feature is that the PCBM absorption edge is located* 284.7 eV *and P3HT is located at* 285.3 eV

6.4 Energy scans

P3HT and PCBM are both materials with well known absorption edges. The NEXAFS intensity is dominated by resonances arising from transitions from the 1s core level to unfilled molecular orbitals of π^* and σ^* character, which are specific to the bonding within different functional groups. The most significant absorption peaks at 284.6 eV and 285.7 eV are C=C π^* resonances from PCBM, and the peak at 285.3 eV is the C=C π^* resonance from P3HT. However, the peaks will shift depending on the blend ratio[3]. The broad features at higher energies are transitions to σ^* orbitals[4].

Scanning samples made from pure P3HT and PCBM from 280 eV to 300 eV with a energy resolution of 0.25 eV reveals the expected spectrum with P3HT having its maximum absorption at 285 eV and PCBM 284.5 eV, see figure 6.5.

6.4.1 2D scans

Prior to performing 2D energy scans of the sample a few degradation tests were made. The results showed serious beam damage during a full scan with 0.2 eV energy resolution. This was mitigated by increasing the energy steps

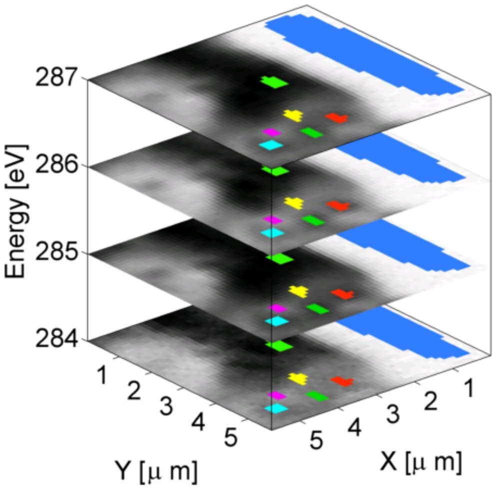

Figure 6.6: *A overview of how the NEXAFS images varies as a function of energy. The particles marked by red, green and cyan have maximum contrast at* 285 eV *but are hardly visible at* 284 eV

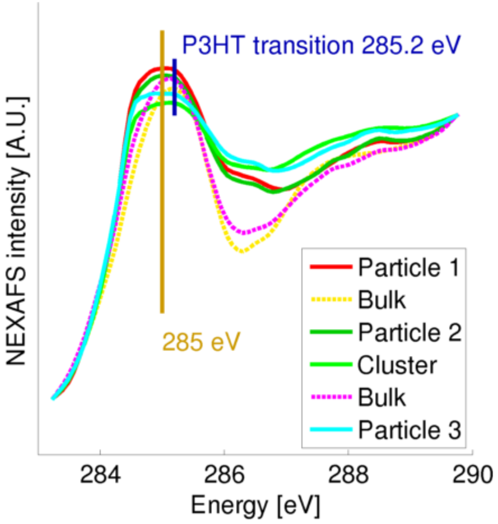

Figure 6.7: *The spectra from the areas on figure 6.6. The Yellow and Magenta areas, not located on a particle or cluster, absorps at* 285.2 eV*, the P3HT carbon edge. The other areas start absorpting at* 285 eV*.*

to 0.5 eV in some scans or only measuring certain key energies instead of performing a full scan from 280 eV to 300 eV.

Using energy steps of 0.5 eV we scanned a 1 × 1 µm area from 280 eV to 300 eV with a 15 µm step size. Due to the energy steps of 0.5 eV a lot of details in the absorption spectra were lost. It was no longer possible to resolve the two π^* transitions for PCBM but it was still possible to distinguish P3HT and PCBM due to the width and position of the π^* peaks.

In figure 6.4 the image at 286 eV is shown. The particles are visible in the right side of the image, and a dark homogenous region region fills up the center-left side of the image. The top of the image does not contain any sample and is used for calibrating the intensity of the beam since the decreasing current in the storage ring on the synchrotron cannot be ignored over the time span of a 2D energy scan which takes 2-4 hours.

Figure 6.7 displays the energy absorption spectra for the homogenous area and the particles (located under the red, green and blue marker). From the different π^* peak positions it was concluded that the particles, contrary to the bulk area, contained PCBM. Figure 6.6 shows the 2D image at four different energies.

6.5 Scanning for other elements

While the NEXAFS spectra showed an absorption edge at the P3HT π^* resonance it was worth testing for other carbon based materials as well.

The nanoparticle ink consisted of nanoparticles dispersed in water with a small amount of FSO as wetting agent. The only materials to get in contact with the active layer besides P3HT and PCBM themselves were water, FSO, SDS, PEDOT:PSS and ZnO.

Depending on their chemical composition some of the materials could be tested more easily than others. The instrument was not able to go to the sulfur absorption edge at 2.4 keV but was able to tune the energy to sodium at 821 eV, present in SDS. However, we were not able to observe any amount.

6.6 P3:PCBM nanoparticles

Spin coated nanoparticles of P3:PCBM were also measured, but on a SiN membrane. Performing a NEXAFS scan around the carbon edge revealed PCBM particles identical to the ones measured in the sample with P3HT:PCBM. However, we did not observe any signs of the P3 polymer. This was initially believed to be a limitation of the energy resolution of the instrument, but after analysing the P3HT:PCBM particles it is now believed the P3:PCBM particles behave similarly. Contrary to not observing any P3 in the STXM images it is believed that there is a large bulk of P3 covering the membrane. Any features from P3 then gets removed when the signal is normalized with the membrane spectrum.

While the literature shows several experiments with P3, even NEXAFS studies, any NEXAFS spectra of P3 has to our knowledge not been published.

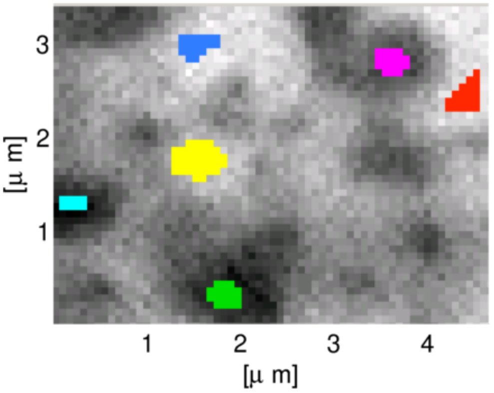

Figure 6.8: *P3:PCBM particles on a membrane at* 289 eV *where the particle constrast was maximum*

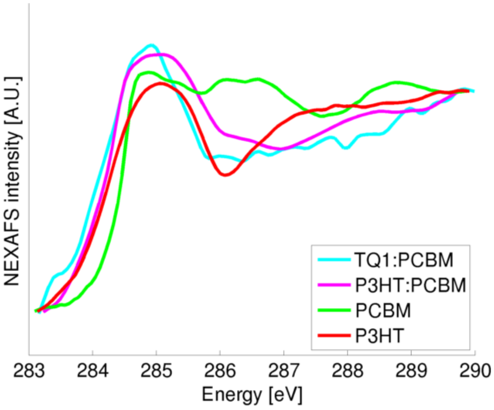

Figure 6.9: *The spectrums of the areas marked on figure 6.8. Blue is used for normalisation. Yellow gets completly removed by the normalisation. Red, Magenta, Green and Light Blue all show a clear absorption edge at* 284.8 eV *indicating PCBM.*

6.7 Discussion

The data from SAXS confirmed the existance of particles as small as 20 nm but there were not enough small particles to explain the bulk we saw in the STXM images. Neither did the STXM show any existance of PCBM in the bulk. The morphology in the STXM images looked identical to what was measured with TEM which have a superior resolution and would be able to resolve tiny particles.

Recalling the previous results from the TEM images, the NEXAFS scans confirmed that the coated ink had transformed from P3HT:PCBM nanoparticles into PCBM nanoparticles in a thin film of P3HT. We were confident that the layer must be P3HT, party because the absorption edge matched the P3HT absorption edge, and partly due to the lack of alternatives.

Since we did not observe any physical changes in the individual PCBM particles during annealing or R2R coating we believe they were representative of how the PCBM half of the particle was shaped.

The only difference in the preparation of the round particles observed initially and the later observed disrupted particles was different SDS dialysing methods. Because the method of dialysing the SDS is the only parameter varying in the preparation method between the batches of nanoparticles, we believe this explains the observed difference in morphology. As illustrated on figure 6.10 we speculate that the slow dialysis of the first batch, B1, caused the hydrolysis to create a more rigid structure, keeping the nanoparticles

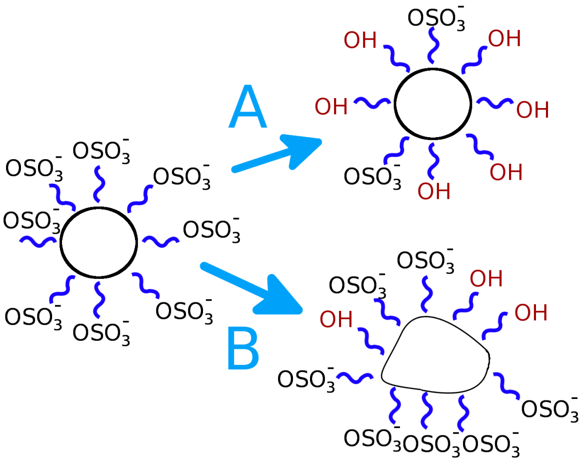

Figure 6.10: A: *The hydrolysis of the SDS chains creates a more rigid particle.* B: *The particles where the sulphate groups are preserved will leak the P3HT when coated.*

spherical. In the second batch, B2, the dialysis was carried out using a labscale dialysis system (tff) for SDS-removal. The hydrolysis of the sulfuric groups is accelerated in acidic environments. This presumably causes a higher degree of hydrolysis of the sulphate groups on the surface of the B1 micelles[7]. In the solid, the flexible SDS chains form an oil-like layer on the B2 particle surface, through which the polymer may diffuse, causing widespread phase separation. Through hydrolysis, a more rigid shell of dodecanol groups is formed on the B1 particles[1], which apparently contain and preserve the polymer particulate structure.

6.8 Conclusion

By performing NEXAFS scans on active layers from R2R coated devices we have observed the same morphology as we previously did with the TEM. We are confident that the particles have separated into PCBM particles in a film of P3HT. This also explains how the P3HT crystals could be ordered in the WAXS data. The reason is not that the particles are interacting but that the P3HT and PCBM phase separates and the P3HT forms the same semicrystaline structure as usual. The reason for the phase separation is believed to be a result of the dialysis in the preparation phase.

We also observed P3:PCBM nanoparticles similar to the ones of P3HT:PCBM, which may have phase separated as well. At last we observed R2R coating, in contrast to spin coating, seemed to cause clustering of the particles on micrometer scale. This clustering is definitely causing a significant hit on the

PCE of the R2R coated cells.

References

[1] Brian D Casson, Rüdiger Braun, and Colin D Bain. Phase transitions in monolayers of medium-chain alcohols on water studied by sum-frequency spectroscopy and ellipsometry. *Faraday Discussions*, 104:209–229, 1996.

[2] Emiel de Smit, J Fredrik Creemer, Henny W Zandbergen, Bert M Weckhuysen, and Frank MF de Groot. In-situ scanning transmission x-ray microscopy of catalytic materials under reaction conditions. In *Journal of Physics: Conference Series*, volume 190, page 012161. IOP Publishing, 2009.

[3] David S. Germack, Calvin K. Chan, Behrang H. Hamadani, Lee J. Richter, Daniel A. Fischer, David J. Gundlach, and Dean M. DeLongchamp. Substrate-dependent interface composition and charge transport in films for organic photovoltaics. *Applied Physics Letters*, 94(23):233303, 2009.

[4] David S. Germack, Calvin K. Chan, Behrang H. Hamadani, Lee J. Richter, Daniel A. Fischer, David J. Gundlach, and Dean M. DeLongchamp. Substrate-dependent interface composition and charge transport in films for organic photovoltaics. *Applied Physics Letters*, 94(23):233303, 2009.

[5] Adam P Hitchcock, James J Dynes, Göran Johansson, Jian Wang, and Gianluigi Botton. Comparison of nexafs microscopy and tem-eels for studies of soft matter. *Micron*, 39(3):311–319, 2008.

[6] AP Hitchcock. axis2000 is written in interactive data language (idl). *It is available free for noncommercial use from http://unicorn. mcmaster. ca/aXis2000. html*, 2008.

[7] Masayuki Nakagaki and Shoko Yokoyama. Acid-catalyzed hydrolysis of sodium dodecyl sulfate. *Journal of pharmaceutical sciences*, 74(10):1047–1052, 1985.

[8] B.K. Teo. *EXAFS: basic principles and data analysis*. Inorganic chemistry concepts. Springer-Verlag, 1986.

Chapter 7

Ptychography

7.1 Coherent diffractive imaging

Coherent Diffractive Imaging (CDI) is an X-ray imaging technique based on scattering from a coherent X-ray beam. In contrast to STXM where the data are directly acquired by directly measuring a pixel or image for each exposure, CDI normally measures the scattering of the sample several times and needs a lot of computer processing power in order to produce a real space image of the sample.

All photons are defined by an amplitude and a phase, however, detectors can only measure the amplitude. The phase is often just as important as the amplitude, but the limitation of detectors is often referred to as the *phase problem.* A central part of CDI is solving the phase problem by oversampling.

This chapter will explain the history and theory of CDI in general as well as a new CDI technique called ptychographic. The theory for tomography will also be outlined.

7.2 History of coherent diffractive imaging

The theory for coherent diffractive imaging was originally pioneered by David Sayre who was the first to propose methods to the phase problem by oversampling in crystallography[15]. Later in 1969 Walter Hoppe proposed the first theoretical solution to the problem, but lack of computing power prevented him from ever performing the experiments. Hoppe both provided a solution to the problem with periodic crystalline samples[6], and later expanded his theory to include non-periodic samples[8,7].

When computer processing power caught on John Rodenburg took Hoppes work and demonstrated the first proof of concept measurement using electron microscopy with a crystalline sample[11,13]. Later in 2007 he, as the first, demonstrated ptychography using hard X-rays[12].

CDI is still a relatively new technique but is currently rapidly being deployed at synchrotrons around the world.

7.3 Phase retrieval

The phase retrieval process uses an iterative algorithm where the object is transformed back and forth between real space and frequency space applying known constraints.

The basic concept of the algorithm is to use a series of measurements and a initial arbitrary guess of the electron distribution in the sample. Using the initial, and presumably wrong, electron distribution the interference pattern between the probe and the scattered beam is calculated. The wave front is then converted into intensities on the detector, but are applied various constrains dictated by the experimental setup. The calculated detector intensity is then compared and corrected by the actual measured intensity and the sample electron distribution is the corrected accordingly. The process is the repeated iteratively until the calculated and measured intensities match.

In practical setups more advanced algorithms are used which applies more sophisticated constraints, but the basic iterative constraining loop remains the same. A modern approach to the reconstruction was demonstrated by Dierolf *et al.*[3] who demonstrated the first practical 3D ptychographic measurement.

Because ptychography aims to reconstruct the wave front after the illuminated object, both the change in amplitude and phase is measured. This results in two images where the phase image often shows strong contrast, with the highest peak signal to noise ratio, for soft materials. Since the phase change in the wavefield is directly related to the X-ray refractive index without any major uncertainties it easy to quantify the contrast.

7.3.1 Gerchberg-Saxton algorithm

The Gerchberg-Saxton algorithm[5] tried to determine the phase of an object despite only having measured the amplitude. This can be done from the relation between a function, $f(x)$, describing and object and its Fourier transform, $F(u)$:

$$F(u) = \mathcal{F}[f(x)] = |F(u)| \exp[\imath\psi(u)] \tag{7.1}$$

$$f(x) = |f(x)| \exp[\imath\eta(x)] \tag{7.2}$$

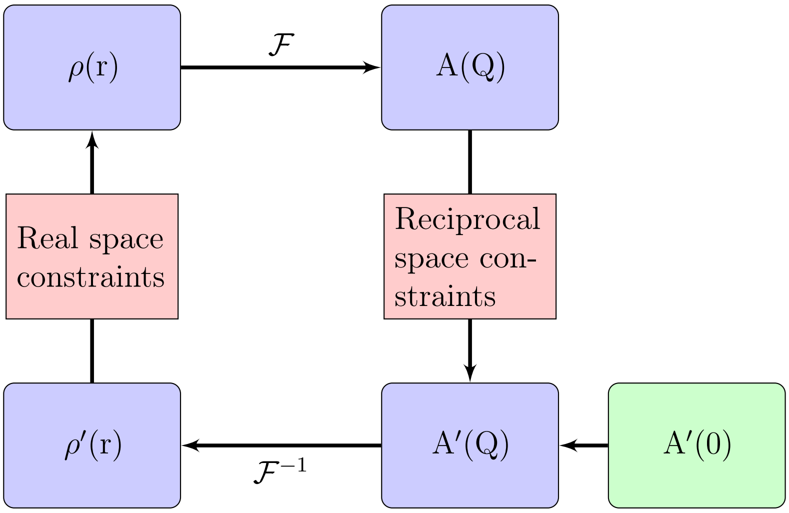

Figure 7.1: *Block diagram illustrating the iterative approach used to reconstruct the real space images.* ***A'(0)*** *is the initial measured amplitude, added a random phase.* ***A'(Q)*** *is the measured amplitude with the best estimated phase.* $\boldsymbol{\rho'(r)}$ *is the electron density calculated from A'(Q).* $\boldsymbol{\rho(r)}$ *is* $\rho'(r)$ *added some real space constrains such as "no negative densities".* ***A(Q)*** *is* $\rho(r)$ *in reciprocal space. The "Reciprocal space constraints" is often the measured intensity only. The "Real space constraints" is often that the densities should be real and non-negative.*

The task can thus be reformulated as finding $\eta(x)$ from a measurement of $|F(u)|$ and $|f(x)|$ and some fundamental prior knowledge about $f(x)$ as support. In the case of imaging where $f(x)$ might describe an electron density the fact that $f(x)$ is real and non-negative is often used as a prior.

The algorithm is iterative and consists of four steps.

1. Inverse Fourier transform the amplitude into to real space
2. Apply physical constraints to the real space image if any
3. Fourier transform an estimated object
4. Replace the modulus of the estimated Fourier transform with the measured modulus

The Gerchberg-Saxton algorithm is illustrated on figure 7.1 and often referred to as the *error reduction algorithm.*

The contraints applied in step 2 are surprisingly simple. Typically fundamental physical constraints like "the electron densities must be positive" and “the electron densities must be real” are enough. The iterative process continues until it converges and the modeled object matches all the constraints within a certain threshold. The algorithm normally converge fast in the first few iterations but the speed decreases rapidly hereafter. Figure 7.2 shows a reconstruction using 20 iterations.

The Gerchberg-Saxton algorithm is still basis of many phase reconstruction algorithms today. The largest problem, beyond speed, is the risk of being caught in a local minimum which will prevent the algorithm from terminating.

7.3.2 Fienup phase retrieval algorithm

To solve the stagnation problem in a local minimum the most common solution used today is called “Hybrid input output” and was proposed by Fienup[4] in 1982.

The purpose of the Fienup extension of the error-reduction algorithm is to introduce an extra parameter, β, with the property of always forcing the algorithm to deliver an output different from the input - thus avoiding stagnation at a fixed set of parameters.

This is implemented in the real space domain by considering step 3, 4 and 1 in the error-reduction algorithm as a combined function, $g(x)$, transforming the object $f(x)$ to another object, $f'(x)$:

$$g(f(x)) = f'(x) \tag{7.3}$$

From the nature of the error-reduction algorithm $f'(x)$ does by definition satisfy the constraints in the fourier space. If one can design $g(x)$ to also make $f'(x)$ satisfy the real space constraints $f'(x)$ will be a solution.

A small change in the input of g in general will lead to a change in the output in the same direction. I.e. if you increase the density of an area, the density after one additional iteration of the error-reduction algorithm will in more often than not be higher, compared to if you did not changed the density.

g is not linear but if one aims for a change in value by Δg, a crude approximation would be to change the input of g with $\beta\Delta g$. Where β is a constant. Since g is non-linear a linear change in input will not yield the correct output. However, since $g(x)$ changes in the direction of x the value of $g(x)$ can be pushed in the desired direction by modifying x appropriately.

When reconstructing images a common constrain is positive values. In this case the n'th iteration of g can be written in many different ways, but the most straight forward one is:

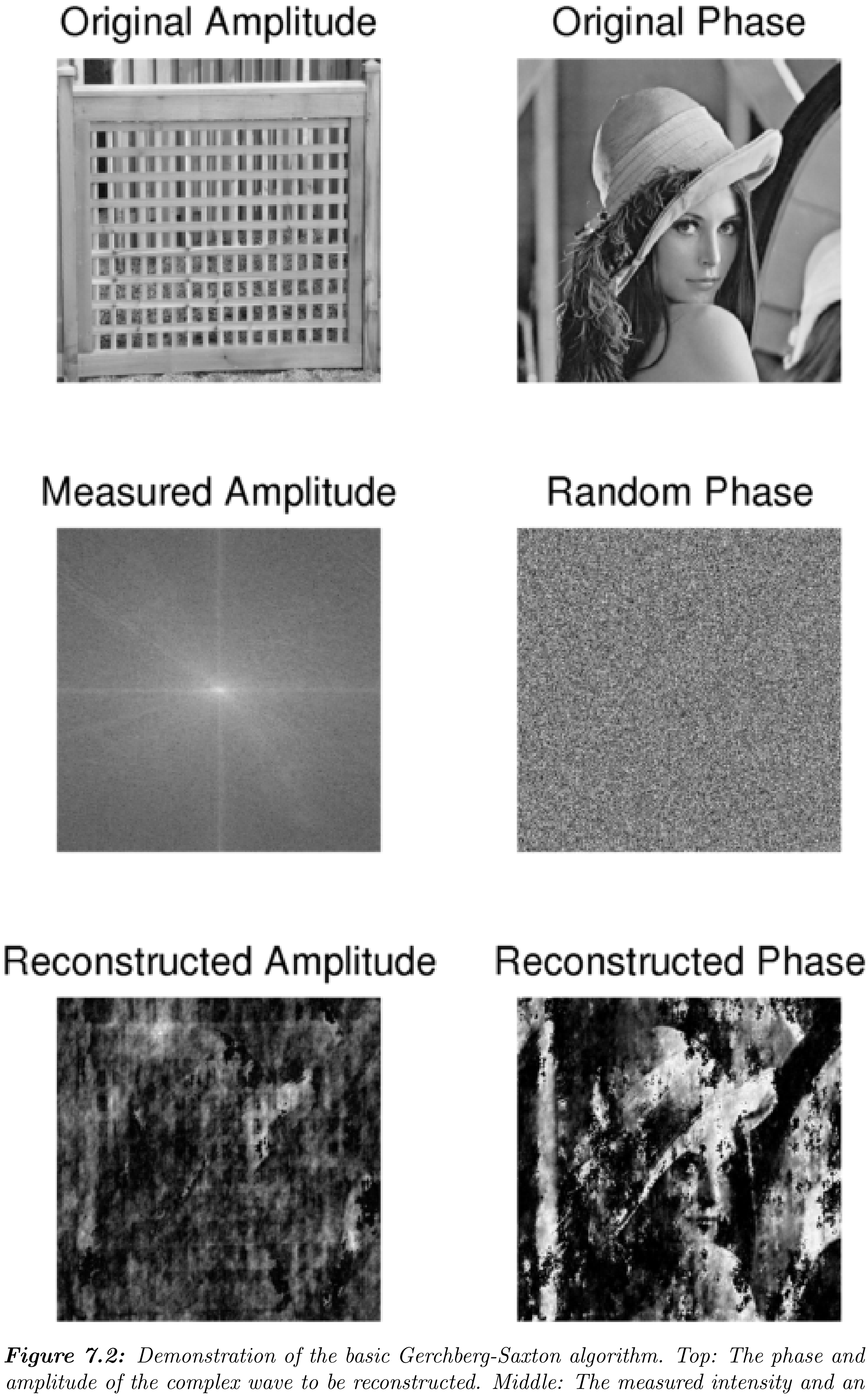

Figure 7.2: *Demonstration of the basic Gerchberg-Saxton algorithm. Top: The phase and amplitude of the complex wave to be reconstructed. Middle: The measured intensity and an initial random phase. Bottom: The reconstructed phase and amplitude.*

$$g_n(x) = \begin{cases} g_{n-1}(x) & \text{if } x > 0 \\ g_{n-1}(x) - \beta g_{n-1}(x) & \text{otherwise} \end{cases} \tag{7.4}$$

From equation (7.4) it is clear that if a parameter x satisfy the physical conditions we require, we let it stay constant. If it violates the constraints we change it in the desired direction. This change will continue until x satisfy our conditions. It is worth noting that in the case of $\beta = 1$ the output-output algorithm becomes the error-reduction algorithm again.

Another definition of g, called the hybrid input-output algorithm is:

$$g_n(x) = \begin{cases} g'_{n-1}(x) & \text{if } x > 0 \\ g_{n-1}(x) - \beta g'_{n-1}(x) & \text{otherwise} \end{cases} \tag{7.5}$$

The main advantage of this implementation is if x is negative for more than one iteration the value will increase more and more for every forthcoming iteration. (7.5) is used in a wide range of different phase reconstruction algorithms because it prevents stagnation.

7.4 Ptychography

Ptychography extends the approach of the iterative phase reconstruction loop but adds redundancy by performing several oversampling measurements. The reconstruction can be achieved by letting the function $O(\mathbf{r})$ describe the transmission function of the sample and the function $P(\mathbf{r})$ the complex wave function of the incoming beam. If the sample is thinner than the coherence length, the exit wave can be written as a product of $O(\mathbf{r})$ and $P(\mathbf{r})$

$$\psi(\mathbf{r}_1, \mathbf{r}_2) = O(\mathbf{r}_1)P(\mathbf{r}_2) \tag{7.6}$$

From equation 7.6 the phase retrieval problem can be restated as “we want to find $O(\mathbf{r})$ assuming we know $P(\mathbf{r})$ and measure $\psi(\mathbf{r}_1, \mathbf{r}_2)$”.

The function for the initial real space object , $O(\mathbf{r})$, is initially a random guess. The subscript g represent a guessed function and the subscript n represent the n’th iteration.

At a given position the illumination function is $\mathbf{R}$, $P(\mathbf{r} - \mathbf{R})$. The current guessed object is multiplied by the illumination function, producing a guessed exit wave.

$$\psi_{g,n}(\mathbf{r}, \mathbf{R}) = O(\mathbf{r}) \cdot P(\mathbf{r} - \mathbf{R}) \tag{7.7}$$

By transforming $O(\mathbf{r})$ the corresponding wave function in the diffraction space plane for the position $\mathbf{R}$ is obtained

$$\Psi_{g,n}(\mathbf{k},\mathbf{R}) = \mathcal{F}[\psi_{g,n}(\mathbf{r},\mathbf{R})] \tag{7.8}$$

k denotes the coordinates in the reciprocal space. $\Psi_{g,n}(\mathbf{k},\mathbf{R})$ is calculated from a random guess of the real space object. However, as described with the previous algorithms successive iterations will, in order to satisfy the constrains, produce increasingly accurate wavefunctions.

$\Psi_{g,n}(\mathbf{k},\mathbf{R})$ can be rewritten as:

$$\Psi_{g,n}(\mathbf{k},\mathbf{R}) = |\Psi_{g,n}(\mathbf{k},\mathbf{R})| e^{\imath\theta_{g,n}(\mathbf{k},\mathbf{R})} \tag{7.9}$$

By replacing the amplitude of $\Psi_{g,n}(\mathbf{k},\mathbf{R})$ with the one measured it becomes:

$$\Psi_{c,n}(\mathbf{k},\mathbf{R}) = |\Psi(\mathbf{k},\mathbf{R})| e^{\imath\theta_{g,n}(\mathbf{k},\mathbf{R})} \tag{7.10}$$

The improved wave function is the transformed back to real space.

$$\psi_{c,n}(\mathbf{k},\mathbf{R}) = \mathcal{F}^{-1}[\Psi_{c,n}(\mathbf{r},\mathbf{R})] \tag{7.11}$$

At last the guessed object is updated in the overlapping area.

$${}_{g,n+1}(\mathbf{r}) = {}_{g,n}(\mathbf{r}) + \frac{|P(\mathbf{r}-\mathbf{R})|}{P_{max}(\mathbf{r}-\mathbf{R})} \cdot \frac{P*(\mathbf{r}-\mathbf{R})}{|(P\mathbf{r}-\mathbf{R})|^2+\alpha} \cdot (\beta(\psi_{c,n}(\mathbf{r},\mathbf{R}) - \psi_{g,n}(\mathbf{r},\mathbf{R}) \tag{7.12}$$

β and α are appropriately chosen. $P_{max}(\mathbf{r}-\mathbf{R})$ is the maximum value of the amplitude of $P(\mathbf{r})$. β should be between 0.5 and 1.

The approach above describes one iteration of a loop which runs until the sum squared error (SSE) is small enough. It was first published by Rodenburg & Faulkner[14] in 2004 and dubbed *The ptychographic engine* (PIE). The use of overlapping areas have prooven to be a critical part in making the deconvolution fast and accurate.

It is worth nothing that setting $\beta = 1$ and $\alpha = 0$ reduces the algorithm to Fienup phase retrieval algorithm.

7.5 Quantitative measurements

For X-rays the refractive index of materials, $n \equiv 1 - \delta + \imath\beta$, where the real part δ is directly related to the refraction, or phase shift, caused by the sample whereas the imaginary part $\imath\beta$ is related to X-ray absorption in the material. Absorption, and thus β, is relatively easy to measure and has been the conventional contrast mechanism exploited in X-ray imaging.

The real part of the refraction index, δ is however usually about two orders of magnitude larger than β and offers a much better contrast mechanism, especially for samples with a low mean atomic number and for X-rays with high energy. The relation between the material density and δ is straight forward and can be derived by combining the relation between δ and the electron density, with the relation between bulk material density and electron density:

$$\rho = \frac{2\pi\delta A}{\lambda r_0 N_A Z} \tag{7.13}$$

The accuracy in resolution of the densities is reported to be within 1%[2]. Ptychography is very well suited for imaging soft materials. It provides high contrast which can be quantified and converted into electron densities. Furthermore the sensitivity for density variations is also very high making it well suited for organic materials which are otherwise very difficult to distinguish with other imaging techniques, and the high penetration depth of hard X-rays makes it possible to penetrate samples with would otherwise be opaque to electrons and soft X-rays. The complicated reconstruction process has been automated and can be processed on an average computer. This leaves spatial resolution as the primary focus for improvements, and although very good today it is expected to improve significantly in the near future due to technical improvements in the setups.

7.5.1 Requirements

CDI covers various different techniques for reconstructing the phase of the scattered x-rays. Ptychography has the advantage of not requiring a specially crafted sample with a known reference structure or a reference beam.

7.6 Tomography

7.6.1 Tomographic reconstruction

The techniques previously explained can be used to image two dimensional objects. This works well for thin samples but for thick samples with features along the third dimension the image will only be a projection of the three dimensional object, where is will be impossible to resolve where inside the object a specific feature is.

Computed Tomography (CT) is a nondestructive imaging technique used to create three-dimensional images of the inside of the sample. CT has since

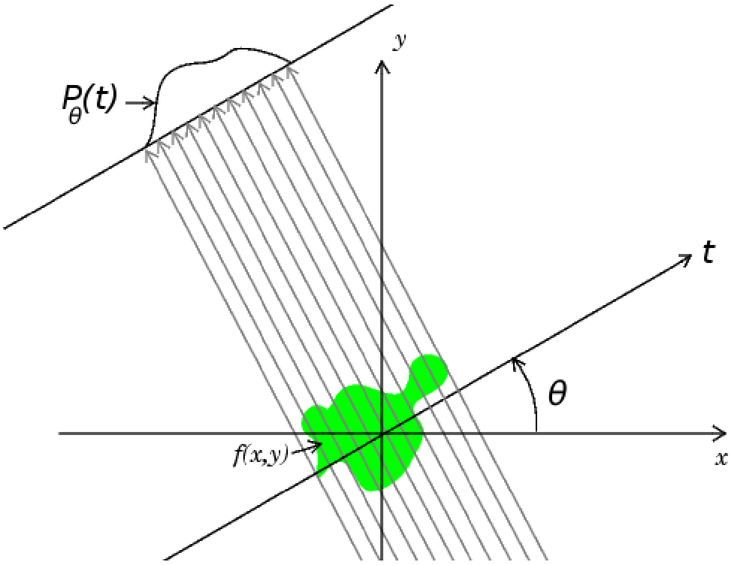

Figure 7.3: *The projection, $P_\theta(t)$, of the function $f(x,y)$ along the line t*

the 1970's been a standard technique for medical images at hospitals, however, CT is also used in a wide range of other fields for nondestructive material testing and analysis.

CT works by taking a series of two-dimensional images of the object and reconstruct the full 3D object by backtracking the images using the Fourier Slice Theorem and applying some normalization filters. This process is called Filtered Back Projection (FBP).

If we have an two-dimensional object, where a function $f(x,y)$ describes the density of the object, and shine X-rays onto it, we can record a projection image, figure 7.3. The projection of $f(x,y)$ along the line t angle θ to the x-axis can be calculated as

$$P_\theta(t) = \int_{(\theta,t)line} f(x,y)\,\mathrm{ds} \tag{7.14}$$

The equation can be rewritten with the help of a delta function.

$$P_\theta(t) = \int_{-\infty}^{\infty}\int_{-\infty}^{\infty} f(x,y)\delta(x\cos\theta + y\sin\theta - t)\,\mathrm{dx}\,\mathrm{dy} \tag{7.15}$$

The function, $P_\theta(t)$, is mathematically known as the Radon Transformation for $f(x,y)$.

Going back from a number of projections, $P_0(t), P_1(t)\ldots P_N(t)$, to the function $f(x,y)$ is not quite as straight forward but can be done by using the Fourier slice theorem.

7.6.2 Fourier slice theorem

By Fourier transforming both $f(x, y)$ and $P_\theta(t)$ one gets:

$$F(u, v) = \int_{-\infty}^{\infty} \int_{-\infty}^{\infty} f(x, y) e^{-\imath 2\pi(ux+vy)} \,\mathrm{dx}\,\mathrm{dy} \tag{7.16}$$

$$S_\theta(w) = \int_{-\infty}^{\infty} P_\theta(t) e^{-\imath 2\pi wt} \,\mathrm{dt} \tag{7.17}$$

The simplest projection of an object must be the projection at $\theta = 0$. Furthermore we arbitral choose to only look at the Fourier transformation along the line $v = 0$ in the frequency domain. Equation 7.16 can then be rewritten as:

$$\begin{aligned} F(u, 0) &= \int_{-\infty}^{\infty} \int_{-\infty}^{\infty} f(x, y) e^{-\imath 2\pi ux} \,\mathrm{dx}\,\mathrm{dy} \\ &= \int_{-\infty}^{\infty} \left[\int_{-\infty}^{\infty} f(x, y) \,\mathrm{dy} \right] e^{-\imath 2\pi ux} \,\mathrm{dx} \\ &= \int_{-\infty}^{\infty} \left[P_{\theta=0}(t) \right] e^{-\imath 2\pi ux} \,\mathrm{dx} \end{aligned} \tag{7.18}$$

By recognizing the right hand side of equation (7.17) and (7.18) we can establish the following relationship between them.

$$F(u, 0) = S_{\theta=0}(w) \tag{7.19}$$

Although the equation is only valid for $\theta = 0$, we never made any assumption of the coordinate system, and the result must be independent of the coordinate system and can therefore be generalized to any value of θ.

This is really the *Fourier Slice Theorem* in it's simplest form.

> The Fourier transform of a parallel projection of an image $f(x, y)$ taken at angle θ gives a slice of the two-dimensional transform, $F(u, v)$, subtending an angle θ with the u-axis. In other words, the Fourier transform of $P_\theta(t)$ gives the values of $F(u, v)$ along line BB in Figure 7.4.[9]

By measuring a projection of an object at an angle θ we thereby get the values of F along a line. Measuring at an infinite amount of angles will thereby give us the values of F for all the points in the (v, u) space. Because F is just the fourier transform of f, one can apply the inverse fourier transform to F in order to get back to the original function f.

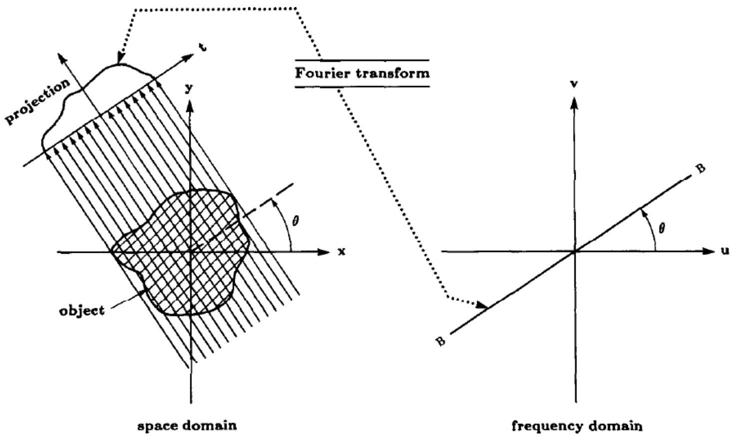

Figure 7.4: *The Fourier slice theorem relates the Fourier transform of a projection to the Fourier transform of the object along a radial line. Figure reproduced with permission from* A. C. Kak and Malcolm[10]

$$f(x,y) = \int_{-\infty}^{\infty} F(u,v)e^{i2\pi(ux+vy)}\,\mathrm{du}\,\mathrm{dv} \tag{7.20}$$

In practice however, one can only make a finite amount of projections. This results in that only some of points in the reciprocal space are known. The rest has to be interpolated as shown in figure 7.5.

Since the data points are much closer together at origo in the (u,v) space, one will typically take that into account by applying a filter to the back projection, hence the name - filtered back projection. The most common filter is a linear one, called a Ram-Lak filter, but a lot of other filters exist, which is used depending on the specific context. For instance, if one wants to suppress high frequencies one might choose a Hamming filter for the back projection. Four common types of filters are shown in figure 7.6.

The amount of angles you need in order to make a good reconstruction of an image is hard to define. But empirical evidence has shown that in order to reconstruct a 1024x1024 pixel image you need approximately 700 projections. In everyday talk the resolution, in pixels, is said to be $\pi/2 \times$ [Number of projections]:

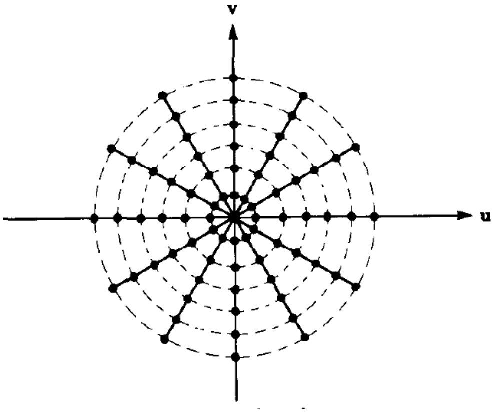

Figure 7.5: *The data points of 6 projections plotted in the frequency space. The values between the lines has to be interpolated. Figure reproduced with permission from* A. C. Kak and Malcolm[10].

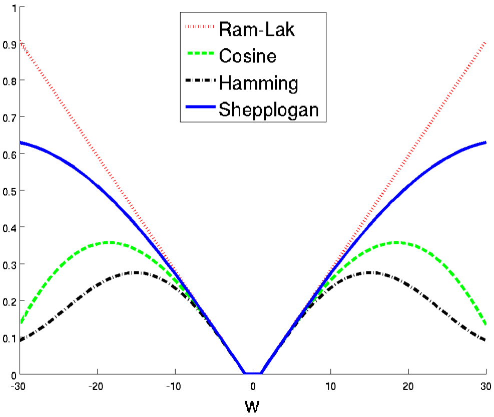

Figure 7.6: *Four different filters that can be used in filtered back projections. The standard filter is a linear Ram-Lak filter, but the others can be used if the higher frequencies need to be suppressed.*

7.7 Aligning tomographic projections in 3D

It is assumed that 2D images used for a tomographic reconstruction depict the same object from different angles. However, a common problem is that the object is not completely stationary. An example is CT scanning in medical settings where the patient is moving when breathing or not being able lie still during the scan. In laboratory experiments it is usually not possible to move the X-ray source, and therefore the position of the sample has to be adjustable. This process might affect the sample. This is especially true for ptychography where the sample for each projection has to be translated more than 700 times on a piezo stage with accelerations above 20 g.

If the sample has drifted or otherwise been affected by the translations this must be corrected before performing the tomographic reconstruction. This is a standard procedure in all commercial CT scanners, but all the commonly used algorithms are optimized towards quick correction of small errors. We have used a new approach for the correction of a drifting sample. In contrast to the majority of available methods we needed to correct larger drifting of the sample, thus sacrificing both speed and memory efficiency.

7.7.1 2D image registration

In the field of computer vision, image registration is the process of aligning two images from different coordinate systems into one common coordinate system. In terms of two photographs of the same object taken from different positions, image registration calculates how to align the same objects in the two images. This method is used by cameras for stiching together a series of photographs into a large panorama photograph.

The basic algorithm of image registration follows a well defined 4-step pattern. However, each of the steps must be adapted to the specific context. The basic flow of image registration is:

1. Identify a set of keypoint features
2. Create an invariant descriptor for each feature
3. Match keypoints across the two images based on keypoint descriptions
4. Calculate the transfer function between the two images

7.7.1.1 Locating keypoints

To align two images on top of each other a set of unique features, called *keypoints*, has to be identified. These keypoints are used to calculate the distance of the two images. The keypoints must be identifiable in both images and be resistant against small misalignments. A good set of keypoints can be achieved by calculating the auto-correlation surface of the images. From the auto-correlation surface a number of points with the largest gradient are chosen.

$$E_{AC}(\Delta u) = \sum_i [I_0(x_i + \Delta u) - I_0(x_i)]^2 \tag{7.21}$$

where Δu is the small variation in position.

The keypoints only measure how much the image changes within a specific region and therefore they tend to concentrate in certain areas. To get the keypoints evenly distributed in the image one or more constraints can be added. We found that a simple constraint of not selecting two keypoints within a distance of 15 pixels of each other worked well.

7.7.1.2 Feature Description

There are a many well known descriptors, and the majority of these describe features independent of scale and illumination but with limited support for rotation. Since we expected our images to be similar with regard to both scale and illumination we defined a simple descriptor that focused on rotation.

To match features from one image to another an appropriate feature descriptor has to be chosen. The descriptor we used was a simplified version of a published descriptor, the *Local Binary Pattern Histogram Fourier features* (LBP-HF)[1]. A histogram of a 5×5 window centered around the keypoint is used as description. To make the histograms comparable they were transformed into Fourier space by the Discrete Fourier Transform (DFT) and the Fourier components were stored in a vector.

7.7.1.3 Feature matching & Transfer function estimation

Feature matching was done using the naïve approach of matching all possible keypoints. The transfer function could be estimated in a number of ways. The simplest approach would be solving the linear equation for the median displacement of a keypoint. This method has shown to work well but we used the built in MATLAB function `tfestimate` which uses a more complicated model.

7.7.2 Aligning 3D images

If a sample has drifted significantly between two projections during a tomographic measurement it becomes necessary to compensate for the drift. If a reference image was available the drift could be compensated by using image registration as previously described. As no reference image exists it is tempting to use the projection from the adjacent angle due to their similarity. However, this approach can not be used since the small error from aligning projection $P_n + 1$ against projection P_n will accumulate when later aligning projection P_{n+2} against projection P_{n+1} and so forth.

We found that a better, but slower, approach was to use the original measured projections to make a crude reconstruction of the 3D sample. The 3D reconstruction was then projected back to a 2D image for each of the measured angles, and the projection of the crude reconstruction was used as a reference image. The aligned projections were iteratively used for creating a better 3D reconstruction which is projected back to 2D and used for more accurate registration of the original projections. The flow is illustrated on figure 7.7

7.7.3 Practical considerations and limitations

Since the sample may have drifted in relation to the sample holder it was necessary to define the sample as the Region Of Interest (ROI) when performing the 3D registration. Otherwise the sample holder would dominate in

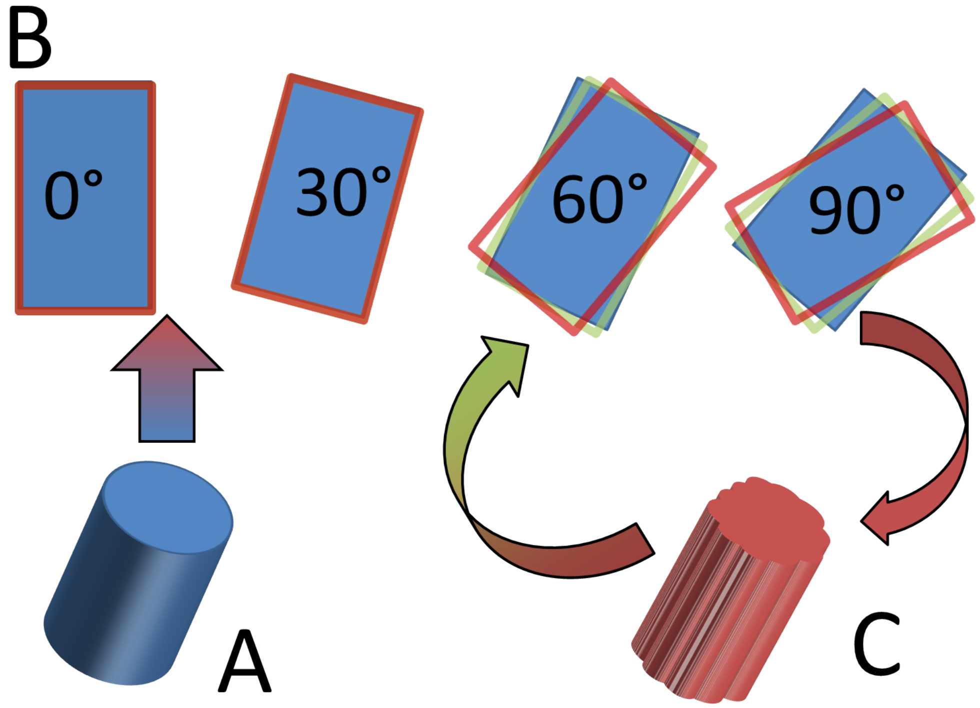

Figure 7.7: *Illustration of the 3D aligning. (A) The original object being measured. (B) The projection of the object from four different angles. The blue projections are the projections one would measure if there were no drift. The red projections represent the measured data where the sample drifts between 60° and 90° . (C) The measured (red) projections are reconstructed into a poor reconstruction. However, the poor reconstruction can be used to align the drifted projections (green). The process of reconstruction and using the reconstruction to align the drifted projections are continued until the algorithm converges.*

the transformation estimation and leave the sample almost unaligned. The current implementation can not align more than one object at the time. If the sample has multiple parts drifting independently of each other only one can be aligned.

7.7.4 Performance and parameters

The current implementation has been developed and tested using only a single tomographic measurement. Using 180 projections and a ROI of 200 × 300 pixels it was able to converge in 30 minutes on a laptop with an Intel i5 processor after 5 iterations. The most computationally expensive part of the operation was reconstructing and back projecting the tomogram, not the registration of 2D projections.

References

[1] Timo Ahonen, Matas, Chu He, and Matti Pietikainen. Rotation invariant image description with local binary pattern histogram fourier features. pages 61–70, 2009.

[2] Ana Diaz, Pavel Trtik, Manuel Guizar-Sicairos, Andreas Menzel, Pierre Thibault, and Oliver Bunk. Quantitative x-ray phase nanotomography. *Phys. Rev. B*, 85:020104, Jan 2012.

[3] Martin Dierolf, Andreas Menzel, Pierre Thibault, Philipp Schneider, Cameron M. Kewish, Roger Wepf, Oliver Bunk, and Franz Pfeiffer. Ptychographic X-ray computed tomography at the nanoscale. *NATURE*, 467(7314):436–U82, SEP 23 2010.

[4] James R Fienup et al. Phase retrieval algorithms: a comparison. *Applied optics*, 21(15):2758–2769, 1982.

[5] R. W. Gerchberg and W. O. Saxton. A practical algorithm for the determination of the phase from image and diffraction plane pictures. *Optik*, 35, 1972.

[6] W. Hoppe. Beugung im inhomogenen Primärstrahlwellenfeld. I. Prinzip einer Phasenmessung von Elektronenbeungungsinterferenzen. *Acta Crystallographica Section A*, 25(4):495–501, Jul 1969.

[7] W. Hoppe. Beugung im inhomogenen Primärstrahlwellenfeld. I. Prinzip einer Phasenmessung von Elektronenbeungungsinterferenzen. *Acta Crystallographica Section A*, 25(4):495–501, Jul 1969.

[8] W. Hoppe and G. Strube. Beugung in inhomogenen Primärstrahlenwellenfeld. II. Lichtoptische Analogieversuche zur Phasenmessung von Gitterinterferenzen. *Acta Crystallographica Seon A*, 25(4):502–507, Jul 1969.

[9] A. C. Kak and Malcolm Slaney. *Principles of Computerized Tomographic Imaging*. Society of Industrial and Applied Mathematics, 2001.

[10] Avinash C Kak and Malcolm Slaney. *Principles of computerized tomographic imaging*, volume 33. Siam, 1988.

[11] PD NELLIST, BC MCCALLUM, and JM RODENBURG. RESOLUTION BEYOND THE INFORMATION LIMIT IN TRANSMISSION ELECTRON-MICROSCOPY. *NATURE*, 374(6523):630–632, APR 13 1995.

[12] J. M. Rodenburg, A. C. Hurst, A. G. Cullis, B. R. Dobson, F. Pfeiffer, O. Bunk, C. David, K. Jefimovs, and I. Johnson. Hard-x-ray lensless imaging of extended objects. *Phys. Rev. Lett.*, 98:034801, Jan 2007.

[13] J.M. Rodenburg, B.C. McCallum, and P.D. Nellist. Experimental tests on double-resolution coherent imaging via {STEM}. *Ultramicroscopy*, 48(3):304 – 314, 1993.

[14] John M Rodenburg and Helen ML Faulkner. A phase retrieval algorithm for shifting illumination. *Applied physics letters*, 85(20):4795–4797, 2004.

[15] D. Sayre. Some implications of a theorem due to Shannon. *Acta Crystallographica*, 5(6):843, Nov 1952.

Chapter 8

Ptychographic experiments

Ptychography is a new method and therefore untested in most fields. It is a promising method due to its potential high resolution and ability to do tomography. Tomography can be used in combination with both TEM and STXM, but there are restrictions with regard to rotating the sample. Beam damage of the samples can also be problematic. We have used ptychographic measurements of inks in the active layer of a solar cell to test this technique, its possibilities and how it compares to TEM and STXM.

8.1 Experimental setup

The samples were measured in two stages. In both cases the ptychography experiments were performed at the Swiss Light Source (SLS) on the X12SA (cSAXS) beam line. The samples were mounted on a 3D piezo-stage on top of a rotation stage. The energy was set to 6.2 keV and in front of the sample a 2.5 µm pinhole defined the illumination to a confined area of the sample. Behind the sample, a 7 m helium filled flight tube followed by a PILATUS 2M detector[5], was placed. The setup is illustrated on figure 8.1

The first sample, the active layer from a R2R coated device, was scanned with 812 exposures of 0.1 s each. The exposures were 0.8 µm apart, following a concentric pattern from the center of the sample and outwards, rather than a raster scan, as illustrated on figure 8.2. The samples were measured at 296 different angles, but performed over 8 series. Each series rotated the sample from 0° to 180° in 37 steps with a specific offset. Including the overhead time the scan lasted for 36 hours in total.

The other samples were measured at 181 different angles. Including the overhead time, each of these 181 angle measurement lasted 8 hours per sample.

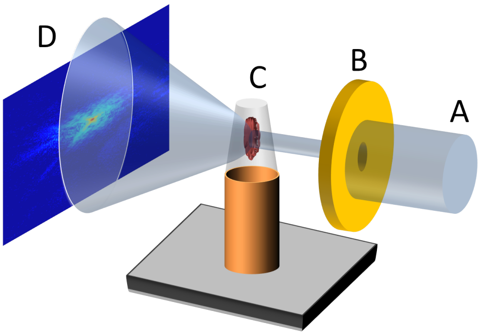

Figure 8.1: *Illustration of the experimental setup. (A) The beam. (B) A small part of the beam is selected by an apature. (C) The beam scatters from the samples which is mounted in a microcapillary on a pieze stage. (D) The scattered X-rays are recorded using a PILATUS 2M detector.*

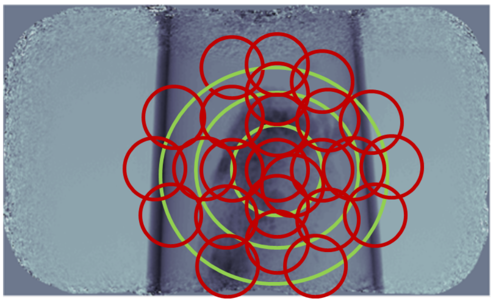

Figure 8.2: *schematic illustration of the exposure pattern. The red circles are the beam. The green circles are spaced* 0.8 µm *apart and are just added for clarity in order to show how the red circles are aligned*

8.2 Active layer from device

The first sample was a piece of active layer from a R2R coated device. It was measured in September 2011.

8.2.1 2D reconstruction

The ptychographic reconstruction, creating 2D images, was performed using the method described by P. Thibault[9]. In addition to the ptychographic reconstruction both phase unwrapping and phase ramp removal were applied[1] as well as subpixel alignment[4]. Figure 8.3 and 8.4 show the reconstructed amplitude and phase. The full field of view is 24 × 10 µm and the pixel size is 43 nm. The phase contrast reconstruction was better than the amplitude reconstruction. The peak signal to noise ratio (PSNR)[2] between the two images was 12.07 dB.

8.2.2 Beam damage and 3D reconstruction

The polymers should, according to prior research, be highly resistant to radiation. It has been shown that polymers are able to withstand a radiation dose of at least 2×10^7 MGy.[10] cSAXS delivers at best a coherent flux of 5×10^9 photons/s at 11.2 keV. Even at 100% absorption and full illumination this is approximately 30 MGy/s which should be well below the limit in a 10 hour scan.

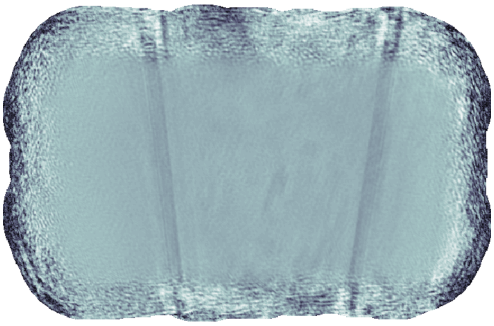

Figure 8.3: *Amplitude image of the ptychographic reconstruction*

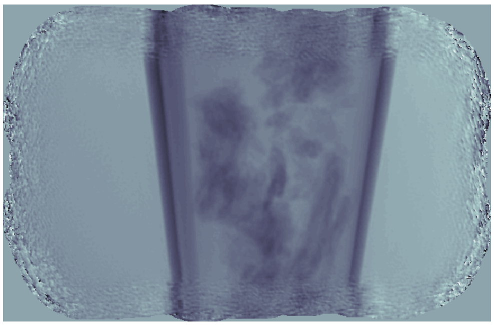

Figure 8.4: *Phase image of the ptychographic reconstruction*

However, during the first experiment there was significant beam damage over the timespan of a scan. Because the full scan was carried out in 8 series, we were able to compare the 2D sample from almost same angle every 5 hours. Figure 8.6, on page 89, shows the sample from the same angle at different times during the scan, and it is clear that the sample becomes severely damaged.

The changes between two neighbouring series were not pronounced but in addition to the degradation of the sample it could also be observed that the sample was moving inside the microcapillary over time.

While each series only contained 37 projections it was sufficient for a very rough tomographic reconstruction with strong artifacts. By reconstructing each series separately and comparing the tomograms we could calculate that about 30% of the sample disappeared due to beam damage during the entire scan, as shown on figure 8.5.

The drift of the sample could be dealt with using the 3D registration method introduced in section 7.6.2, on page 77. The quality of the reconstruction was found mainly to be limited by the beam damage. Using just two series of scanning gave the most detailed 3D reconstruction.

The 74 projections from series 2 and 3 were reconstructed into a 3D volume with filtered backprojection using a Ram-Lak filter. The resolution was determined by the transition from microcapillary to air. This transition is sharp and the resolution of the tomogram was estimated to 200 nm by fitting a Gaussian distribution to the density profile from capillary to air. The FWHM of this gaussian is used as a measure for the reconstructed 3D resolution.

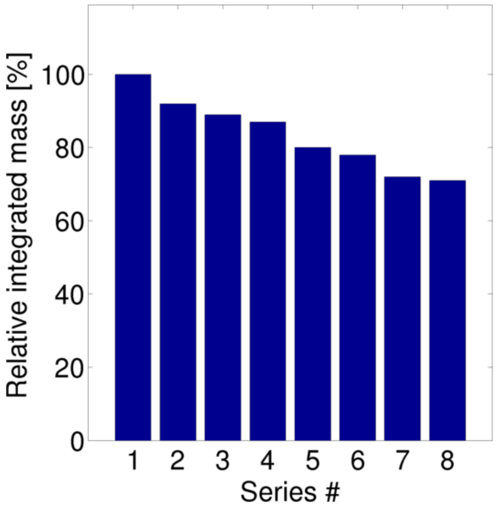

Figure 8.5: *The integrated mass of the 8 reconstructed tomograms relative to the first series.*

8.2.3 Results

Figure 8.7 displays a 2D slice of the reconstructed tomogram showing a piece of active layer inside a microcapillary. In spite of noise caused by the low number of angles, it is possible to see the sample inside the microcapillary. The sample contains a few dense particles, close to the limit of the resolution, and a large dense area in the lower part of the picture. The electron density of the particles was calculated to be $0.93\,\mathrm{e}/\text{Å}^3$ which is close to PCBM's electron density of $0.90\,\mathrm{e}/\text{Å}^3$. The bulk has a lower electron density of $0.63\,\mathrm{e}/\text{Å}^3$ which is slightly lower than the expected electron density of $0.66\,\mathrm{e}/\text{Å}^3$ for P3HT. The sample contains some very distinct particles and a denser region towards the bottom of the image. The majority, lighter, part of the sample has a density matching the electron density of P3HT. The denser part in the bottom is PCBM.

Figure 8.8 shows a 1D density profile along a line through figure 8.7. The arrow on figure 8.7 shows where the line intersects the sample but without covering the particle in the lower half of the image.

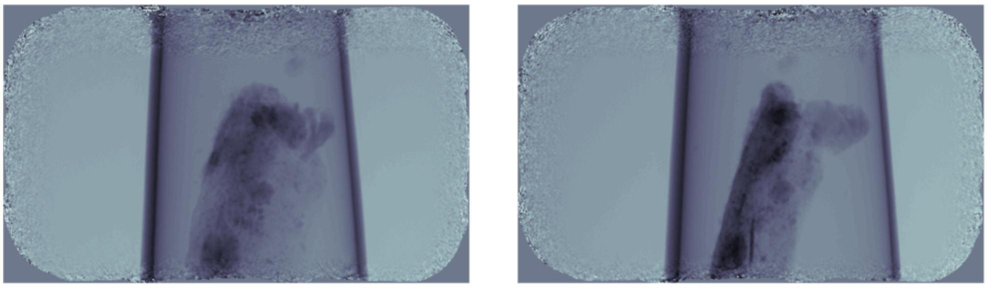

(a) *1. serie* ≈ 4.5 *hours.* ***(b)*** *2. serie* ≈ 9 *hours.*

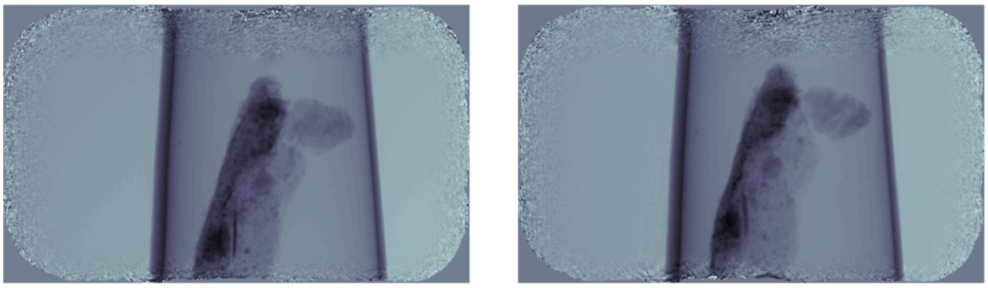

(c) *3. serie* ≈ 13.5 *hours.* ***(d)*** *4. serie* ≈ 17.5 *hours.*

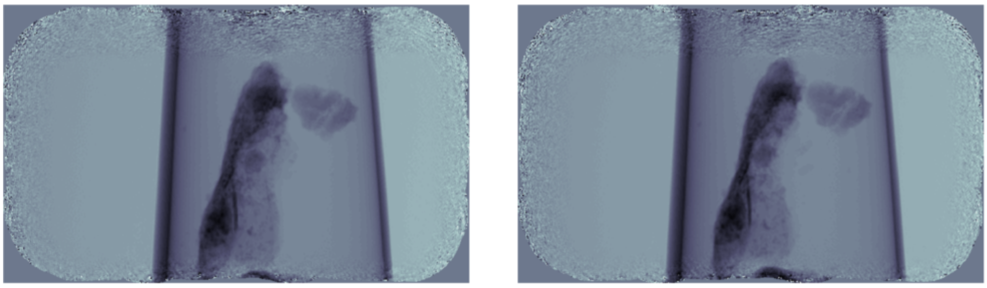

(e) *5. serie* ≈ 22 *hours.* ***(f)*** *6. serie* ≈ 26 *hours.*

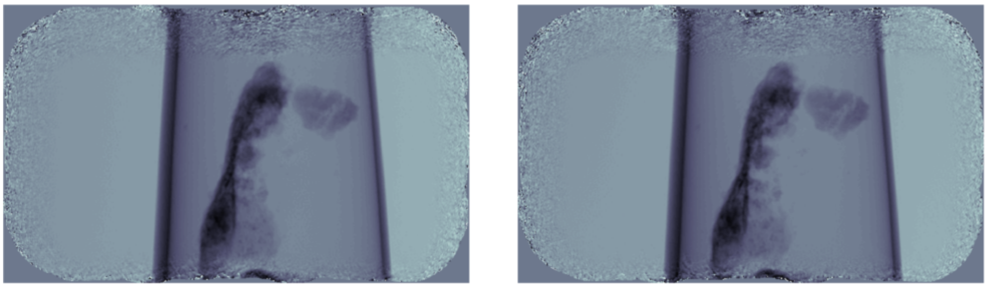

(g) *7. serie* ≈ 30 *hours.* ***(h)*** *8. serie* ≈ 34 *hours.*

Figure 8.6: *Illustration of the beam damage of the sample in different phases of the measurement. Each projection is taken from the same angle at the start of a new series of measurements. Series 2, 3 and 4 are the most similar projections.*

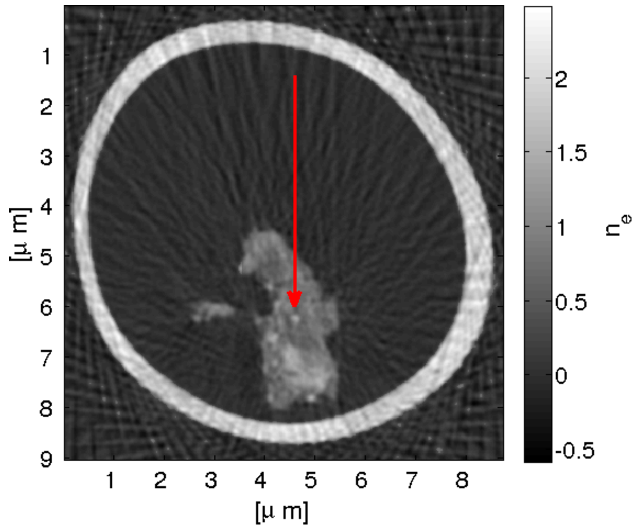

Figure 8.7: *Slice of the reconstructed R2R coated active layer. The sample contains some distinct particles (one is marked by the arrow) and a denser region towards the bottom of the image. The majority, lighter, part of the sample has a density matching the electron density of P3HT. The denser part in the bottom is PCBM.*

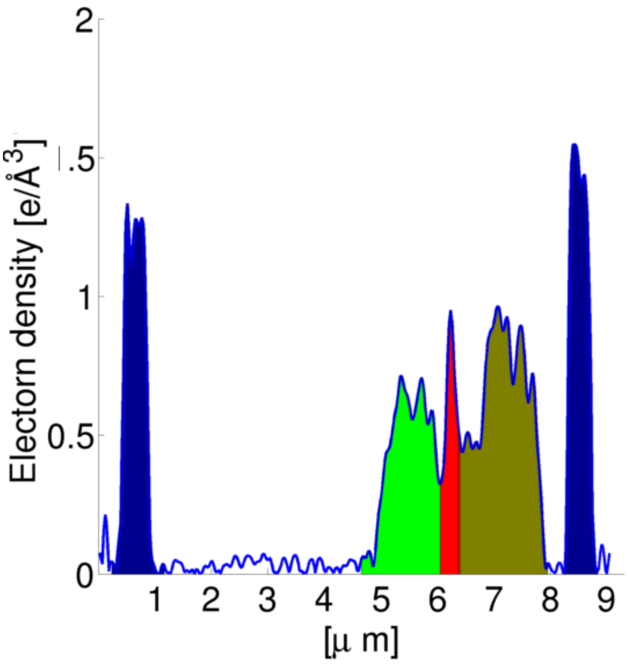

Figure 8.8

Figure 8.9: *A 1D density profile along a the direction of the arrow on figure 8.7. The light green is P3HT. The red is a particle of PCBM. The darker green is a PCBM cluster.*

8.3 Comparison of inks and material

In March 2012 three additional samples were measured.

P3HT particles An ink of nanoparticles only containing P3HT.

Heterogeneous particles An ink of nanoparticles containing P3HT:PCBM. The same ink used for R2R coating the device measured previously.

Homogeneous particles A mix of P3HT nanoparticles and PCBM nanoparticles.

The three samples were measured to study the effects of FSO added to the inks, as well as the diference compared to the R2R coated sample. All samples were prepared in microcapillaries and measured at cSAXS.

8.3.1 Additional setup

To protect the samples from beam damage, which is accelerated by the presence of oxygen, they were placed under a small plastic cap. The cap had two silicon nitride windows through which the beam could penetrate. The cap was connected to a nitrogen source and filled with nitrogen to minimize the presence of oxygen.

8.3.2 Reconstruction

The samples were reconstructed in the same way as the previous sample. The resolution was estimated by the same method used for the sample with the active layer, and was found to be 140 nm.

8.3.3 Density analysis

8.3.3.1 Inks

We used the variance from the N_2 peak as a measure for the instrument broadening. All the peaks could be fitted by a Gaussian distribution function, see figure 8.10, thus simplifying the deconvolution of the instrument broadening from the sample density distribution. Subtracting the instrument broadening from the pure P3HT particle peak gave a variance in the P3HT particle density of $8.0 \times 10^{-3}\,\mathrm{e}/\mathrm{\AA}^3$. Doing the same for the two samples with P3HT:PCBM resulted in a variance of $13.7 \times 10^{-3}\,\mathrm{e}/\mathrm{\AA}^3$ for the heterogeneous particles and $14.1 \times 10^{-3}\,\mathrm{e}/\mathrm{\AA}^3$ for the homogeneous.

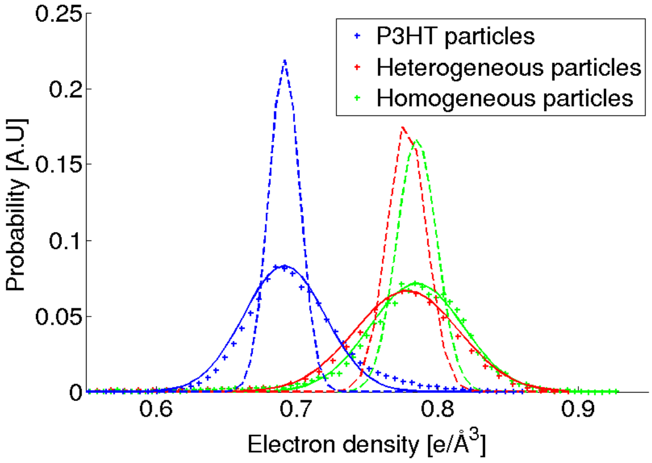

Figure 8.10: Dotted: *The electron density distribution of the P3HT- (blue), Hetero- (red) and Homo- (green) particle samples.* Solid: *A Gaussian fit corresponding to the measured histograms.* Dashed: *The density distribution based on the Gaussian fit and corrected for the instrument broadening.*

Comparing the FWHM of the corrected density distributions to the mean value gives us a resolution in electron densities of 3.4% for the P3HT particles. The two inks have a resolution of 4.6% and the active layer 7.1%. The electron density of PCBM is roughly 50% higher than P3HT thus providing more than enough contrast to separate the two materials. The variance of the density distribution for the inks and the variance in the density distribution of the N_2 were almost identical suggesting we did not have the spatial resolution to separate the different phases in the ink.

Sample name	Electron density [N_e/ Å^3]	Corrected variance [N_e/ Å^3]	Bulk density [g/ml]
P3HT particles	0.69	$8.0 \cdot 10^{-3}$	1.1
Heterogeneous particles	0.75	$13.7 \cdot 10^{-3}$	1.2
Homogeneous particles	0.77	$14.1 \cdot 10^{-3}$	1.3
R2R coated sample	0.80	$19.7 \cdot 10^{-3}$	1.3

We could compare the pure P3HT to the inks. Other studies have reported the densities of P3HT and PCBM to be 1.1 g/ cm^3 and 1.5 g/ cm^3, respectively[6,3]. Converting our measured electron densities to bulk densities we got a density of 1.1 g/ ml for the P3HT particles and 1.2 g/ ml and 1.3 g/ ml for the heterogeneous and homogeneous particles, respectively. The ratios between P3HT and PCBM were 1:1 which means our PCBM had a density between 1.4 g/ ml and 1.5 g/ ml.

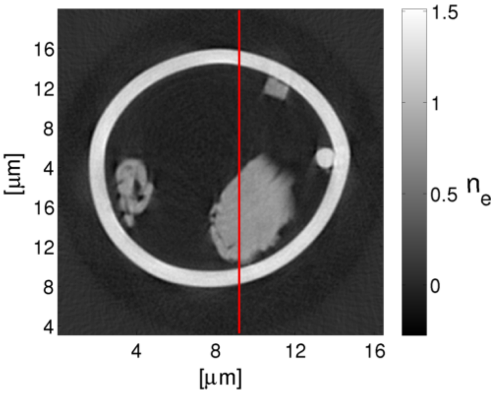

Figure 8.11: *The heterogeneous particles.*

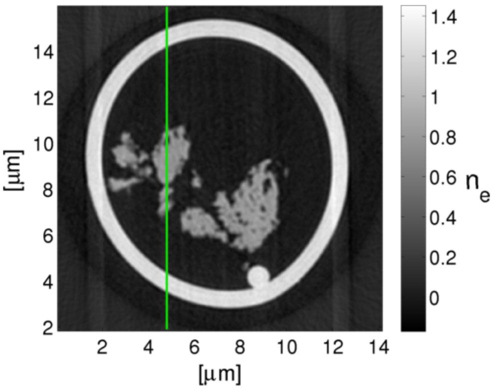

Figure 8.12: *The mixed homogeneous particles.*

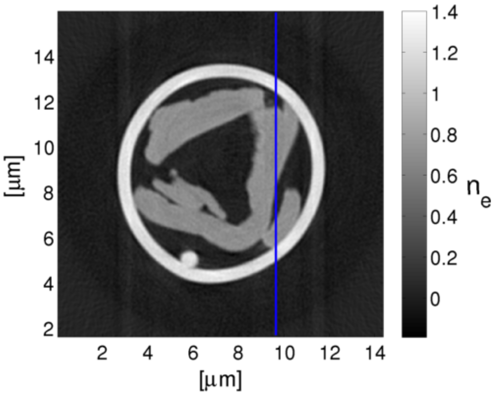

Figure 8.13: *The P3HT particles.*

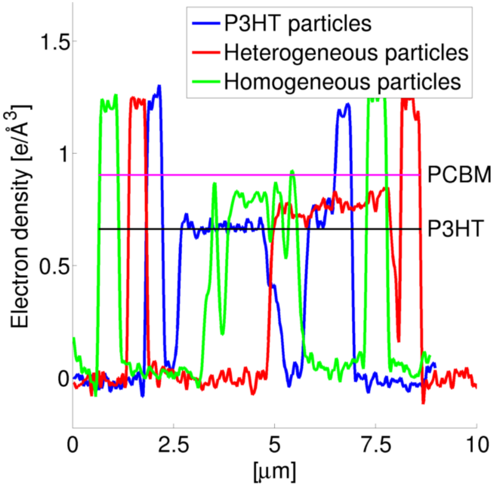

Figure 8.14: *A density profile along the annotated line on figure 8.11 (red), 8.12 (green) and 8.13 (blue). The electron densities for P3HT (black) and PCBM (magenta) are shown as well. The density of the pure sample corresponds to the value of P3HT while the two other samples corresponds to a 1:1 mix of P3HT and PCBM as expected.*

8.3.4 Spatial analysis of inks

The error due to uncorrelated noise of a tomographic reconstruction, computed with filtered backprojection, has been shown by S. J. Riederer *et al* to be proportional to $1/M^{3/2}$ for a circular averaging region of radius M[8,7].

The precision of a reconstruction is estimated by binning the voxels of a circular region of N_2 and calculating the variance. Figure 8.17 shows the result for the four tomograms. The figure shows the relative error compared to the N_2 electron density. i.e. $\sigma_r = \sigma/\delta$. The fitted line for the inks decreases as $r^{0.51}$ for the two mixed inks and $r^{0.56}$ for the pure. The pure inks decreases more slowly due to a slight misalignment. The best fit to the R2R coated sample decreased at $r^{0.36}$. Importantly it converged to a relative error of about 6%, three times larger than the inks. The reason that none of the errors decays as $r^{3/2}$, as predicted, was due to correlated noise from the filtered backprojection[8].

Figure 8.11, 8.12 and 8.13 show selected slices of the heterogeneous, homogeneous and pure particle ink, respectively. From the density distribution of the particles, shown on figure 8.10, the sample looks like a one phase system. Figure 8.14 displays a 1D density profile of the samples along the annotated line. The density profile shows how the density matches the expected average density for all three samples. However, in the two samples which contains PCBM it is not possible to resolve any domains with predominantly P3HT or PCBM.

One way of separating the phases was to only analyse a fraction of the

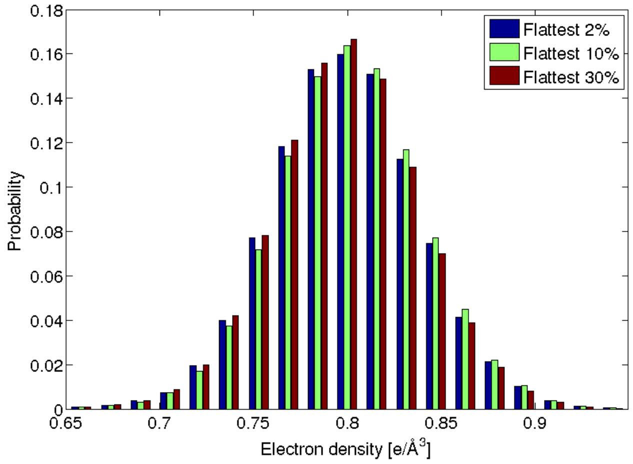

Figure 8.15: *The 2% (blue), 10% (green) and 30% (red) flattest voxels in a tomogram. The distributions are identical suggesting the variation in density is entirely dominated by noise.*

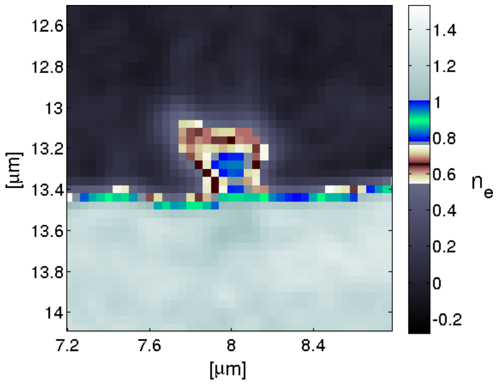

Figure 8.16: *Single particle from the heterogeneous P3HT:PCBM sample. The particle does contains PCBM in the center but it is not clear whether the shell is P3HT or due to the resolution.*

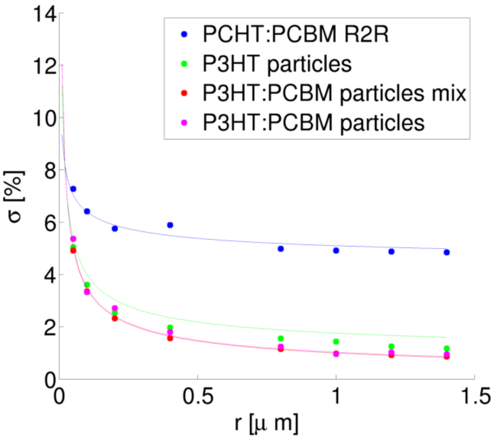

Figure 8.17: *The uncorrelated noise level in the four tomograms. The tomogram of the active layer has significant higher noise level due to the few projections.*

flattest areas. If the tomograms does contain structures of P3HT and/or PCBM those areas would have a flatter density profile than areas dominated by noise. Figure 8.15 displays the density distribution of the 2%, 10% and 30% flattest voxels regions in the tomograms without showing any changes in the density distribution. We therefore concluded that while the contrast resolution was able to distinguish P3HT from PCBM the spatial resolution was not good enough to resolve the particles in the inks.

However, the sample from the R2R coated device did contain visible areas and particles of PCBM. The uncorrelated noise levels were also significantly higher due to the few projections which should make the particles more difficult to observe. Our conclusion was that the particles mixed more thoroughly in the inks, and later aggregated during the R2R coating process. It was not possible to tell whether the observed particles were individual particles or small clusters, but the morphology were consistent with the images obtained from STXM.

8.4 Single particle analysis

The resolution was too coarse to resolve the individual particles in the inks. However, in multiple instances individual particles could be seen on the inside of the microcapillary as shown in figure 8.16. Two additional colourbars have been added to this figure. They are centered at the density of PCBM (green/blue) and P3HT (brown/beige). The colours show that the core of the

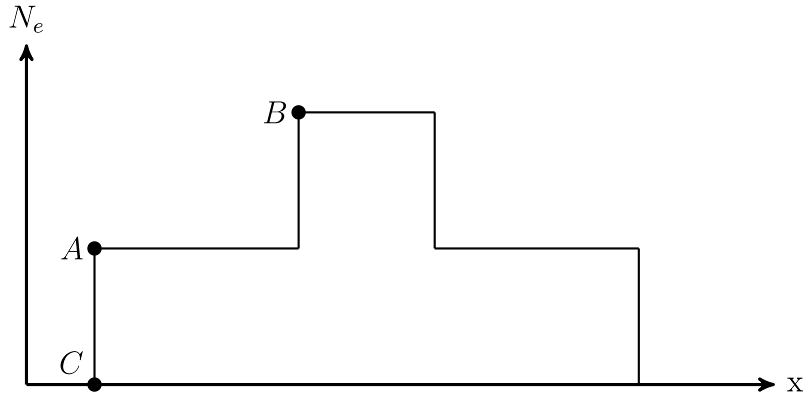

Figure 8.18: *A 1D model of a core-shell particle. It is assumed the core has a higher density than the shell because we see a PCBM core in our tomograms.*

particle is PCBM. It is difficult to conclude whether the surrounding shell is P3HT or due too insufficient spatial resolution.

To get an idea of the resolution of PCBM in P3HT we made a simple model. The model describes the resolution as a function of instrument broadening and the contrast between P3HT, PCBM and N_2. Figure 8.16 shows a 1D model of a material with high density encapsulating another material with lower density in a core-shell fashion.

The 1D particle can be described as:

$$N_e(x) = \begin{cases} B_{N_e} & \text{if } |x| \leq a \\ A_{N_e} & \text{if } |x| \leq b \text{ and } |x| > a \\ 0 & \text{otherwise} \end{cases} \tag{8.1}$$

The density profile is however smeared out by the instrument broadening.

$$P = N_e(x) \otimes V(x, \sigma)_{\text{Instrument}} \tag{8.2}$$

V is a Voigth but due to the almost zero contribution from the Lorentzian it can be substituted for a Gaussian distribution. P cannot be calculated in a simple manner and was done using Mathematica. By applying some physical contrainst such as $C_{N_e} < A_{N_e} < B_{N_e}$ the final expression can be written as:

$$
\begin{aligned}
P(x,\sigma,\mu,a,b,c,d) = \sqrt{\frac{\pi}{2}}\sigma\big(a\,\mathrm{erf}\,[\frac{x-\mu}{\sqrt{2}}] \\
+ (a-b)\big(\,\mathrm{erf}\,[\frac{c-x+\mu}{\sqrt{2}\sigma}] - \mathrm{erf}\,[\frac{c+d-x+\mu}{\sqrt{2}\sigma}]\big) \\
+ a\,\mathrm{erf}\,[\frac{2c+d-x+\mu}{\sqrt{2}\sigma}]\big)
\end{aligned}
\tag{8.3}
$$

Where x is the spatial coordinate, σ is the instrument broadening, μ is the position of the P, a is the width of the dense central part of the function, b is the width of the entire non-zero part of the function, c is the height of the low electron density and d is the height of the denser electron density.

With equation (8.3) we can compare the measured density profile of a core-shell particle with a homogeneous one. i.e. $c = d$.

$$
\begin{aligned}
& & P(x,\sigma,\mu,a,b,c,d) = P(x,\sigma,\mu,a,b,c,c) \\
&\Rightarrow & a\,\mathrm{erf}\,[\frac{x-\mu}{\sqrt{2}}] + a\,\mathrm{erf}\,[\frac{2c+d-x+\mu}{\sqrt{2}\sigma}] \\
&= & (a-b)\big(\,\mathrm{erf}\,[\frac{c-x+\mu}{\sqrt{2}\sigma}] - \mathrm{erf}\,[\frac{c+d-x+\mu}{\sqrt{2}\sigma}]\big) \\
&\Rightarrow & \mathrm{erf}\,[\frac{c-x+\mu}{\sqrt{2}\sigma}] = \mathrm{erf}\,[\frac{c+d-x+\mu}{\sqrt{2}\sigma}] \\
&\Rightarrow & c = c+d\,\mathrm{or}\,a = b
\end{aligned}
\tag{8.4}
$$

From the result above it is clear that a core-shell particle with a low instrument broadening never can have the same density distribution as a solid particle with a wider instrument broadening. By fixing all the variables in (8.3) to our experiment we simulated the density profile of the two types of particles. Figure 8.19 shows the calculated density for a core-shell and a homogeneous particle as well as the measured density for an observed particle.

The density profile of the measured particles was calculated by integrating, and normalising, the densities as a function of radius. The solid angle close to the capillary was ignored. The results were compared to the calculated profiles in figure 8.19. The errorbars display the standard deviation based on the variance of the densities at a given radius. Due to the lack of spatial resolution it was not possible to characterize the inner structure of the particle.

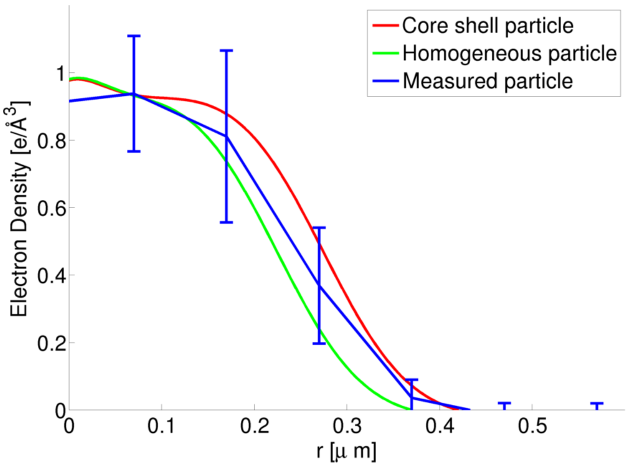

Figure 8.19: *The calculated density profile of a homogeneous PCBM (green) particle and a core-shell particle (red) using the our instrument broadening. The blue line shows our measured density.*

8.5 Conclusion

We have shown that it was possible to use ptychography to create tomographic images of the active layer of polymer solar cells. Despite the damaged sample we were able to resolve a few individual particles in the active layer from a device. The quantitative properties of ptychography allowed us to confirm the effect we had previously observed with STXM, showing that particles had separated into PCBM particles in a P3HT matrix.

Regarding the spin coated inks we were not able to resolve individual particles in them, despite being the same ink used in the R2R coated device.

As we could only see the heterogenous particles after R2R coating, and not in the original solution, we concluded that R2R coating separated P3HT from PCBM and the remaining PCBM particles aggregated into clusters. We also observed that the PCBM clusters were of the same size as seen in the STXM image of the active layer.

References

[1] Martin Dierolf, Andreas Menzel, Pierre Thibault, Philipp Schneider, Cameron M. Kewish, Roger Wepf, Oliver Bunk, and Franz Pfeiffer. Ptychographic X-ray computed tomography at the nanoscale. *NATURE*, 467(7314):436–U82, SEP 23 2010.

[2] Richard Dosselmann and Xue Dong Yang. Existing and emerging image

quality metrics. In *Electrical and Computer Engineering, 2005. Canadian Conference on*, pages 1906–1913. IEEE, 2005.

[3] Wim Geens, Tom Martens, Jef Poortmans, Tom Aernouts, Jean Manca, Laurence Lutsen, Paul Heremans, Staf Borghs, Robert Mertens, and Dirk Vanderzande. Modelling the short-circuit current of polymer bulk heterojunction solar cells. *Thin Solid Films*, 451:498–502, 2004.

[4] Manuel Guizar-Sicairos, Ana Diaz, Mirko Holler, Miriam S. Lucas, Andreas Menzel, Roger A. Wepf, and Oliver Bunk. Phase tomography from x-ray coherent diffractive imaging projections. *Opt. Express*, 19(22):21345–21357, Oct 2011.

[5] B. Henrich, A. Bergamaschi, C. Broennimann, R. Dinapoli, E.F. Eikenberry, I. Johnson, M. Kobas, P. Kraft, A. Mozzanica, and B. Schmitt. Pilatus: A single photon counting pixel detector for x-ray applications. *Nuclear Instruments and Methods in Physics Research Section A: Accelerators, Spectrometers, Detectors and Associated Equipment*, 607(1):247 – 249, 2009.

[6] Jonathan W Kiel, Brian J Kirby, Charles F Majkrzak, Brian B Maranville, and Michael E Mackay. Nanoparticle concentration profile in polymer-based solar cells. *Soft Matter*, 6(3):641–646, 2010.

[7] S J Riederer, N J Pelc, and D A Chesler. *Comput. Ass. Tomog.*, 64(1), 1977.

[8] S J Riederer, N J Pelc, and D A Chesler. The noise power spectrum in computed x-ray tomography. *Physics in Medicine and Biology*, 23(3):446, 1978.

[9] Pierre Thibault, Martin Dierolf, Andreas Menzel, Oliver Bunk, Christian David, and Franz Pfeiffer. High-resolution scanning x-ray diffraction microscopy. *Science*, 321(5887):379–382, 2008.

[10] J Wang, C Morin, L Li, AP Hitchcock, A Scholl, and A Doran. Radiation damage in soft x-ray microscopy. *Journal of Electron Spectroscopy and Related Phenomena*, 170(1):25–36, 2009.

Chapter 9

Upscaling X-ray characterization

While X-ray scattering techniques are a valuable tool in the characterizing of OPVs one of the great strengths of R2R printing is the great speed with which a large number of cells can be printed with varying parameters which is necessary to find the optimal processing parameters. However, many characterizing techniques are not up to date for R2R coating. The few existing techniques like LBIC and I-V work on a macroscopic level only[4,1].

Characterization of the micro- or nanoscale structure of printed cells has uptil now required the individual samples to be cut into small pieces manually. This procedure limits the number of samples that can be studied, and thus also the possibility to study the morphology in the micro- or nano-scale regime. These studieds are necessary to achieve optimal performance of the cells.

To solve this problem we started to look for methods to transfer X-ray scattering techniques to polymers coated on PET using R2R technology. By constructing a small and mobile unwinder-registration-winder unit, based on the principals of a cassette tape, with two spools of which one is connected to a motor. The unit, hereafter referred to as the *unwinder*, is shown in figure 9.1.

While transferring the flexible substrate from one spool to the other by gradually rotating them, just like playing a cassette tape, it was possible to measure the coated film with a very high spatial resolution, but without the overhead of manually changing sample. This approach was combined with the high flux from synchrotron based radiation to measure the nanostructure of coated films with continually changing coating parameters with an unprecedented resolution.

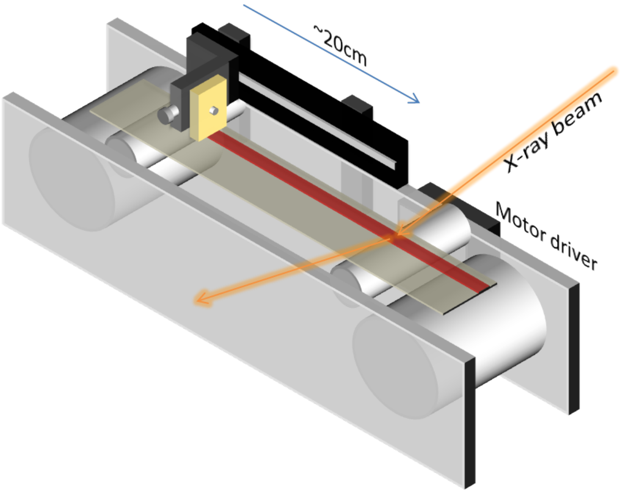

Figure 9.1: *A rendation of the mobile unwinder-registration-winder unit.*

9.1 GISAXS on R2R coated gradients

The two spools on the cassette unwinder both had a small indentation of 4 mm to support the flexible substrate and keep it at a fixed position while it was transferred from one spool to the other. With a spool diameter of 10 cm and a substrate thickness of 130 µm the unwinder was able to handle up to 15 m of foil. The unwinder could only transfer the foil in one direction, and the two spools were thus called the *source spool* and the *sink spool* respectively. To keep the tension of the film between the two spools during transfer the source spool had a break attached that could be adjusted when needed. In order to keep the film flat a third fixed cylinder was placed between the two spools and operate as supporting base for the foil. This is the position where the x-rays scatters from.

The unwinder measures roughly 1 m × 30 cm × 30 cm and weigths around 10 kg.

9.2 Experimental setup at cSAXS at PSI, Switzerland

The experiment was performed at the Swiss Light Source at the cSAXS (X12SA) beamline and the setup is illustrated on figure 9.2. The film was exposed 4 times for 0.1s at each position with an energy of 11.1 keV with a readout time of 3 ms. Including the overhead for detector readout and moving the film, each film was measured at slightly more than 2000 positions during

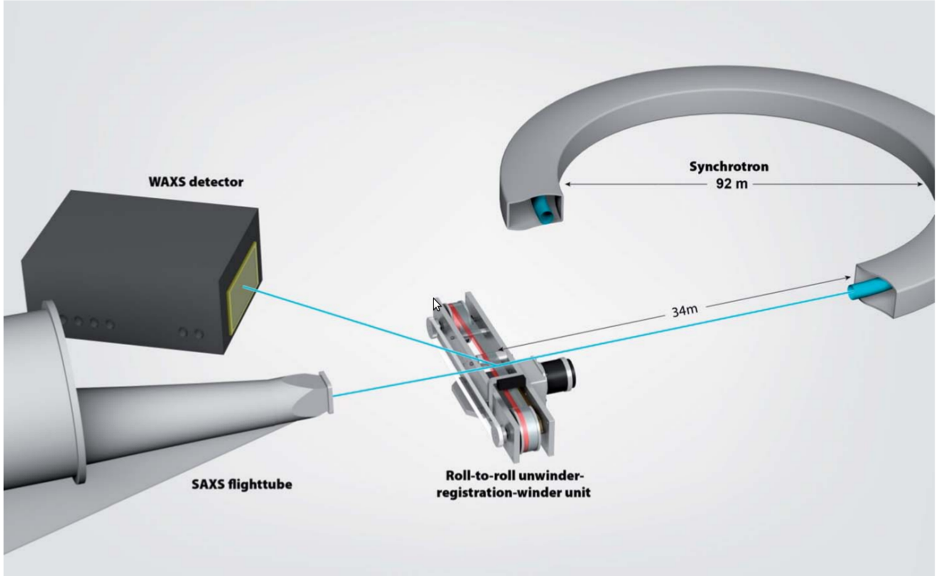

Figure 9.2: *A schematic rendation of the setup as used on the experiment at cSAXS. The synchrotron generates the X-ray beam which scatters from the foil on the unwinder unit. A SAXS and WAXS detector is then placed in order to detected the small and wide angle signal. The unwinder unit will roll the foil from the source-spool to the sink-spool in small steps of* 0.25 cm *resulting in approximately 2000 datapoints for a* 5 m *long foil*

8 hours, resulting in a datapoint every 0.25 cm. While our experiment was designed to capture four exposures at each position, it occasionally happened that the detector ran out of buffer and dropped a frame, thus only recording three of the frames.

The unwinder unit was mounted on a hexapod that could move the unwinder in all three dimensions, including tilting it, in relation to the incoming beam. A barcode scanner was mounted above the unwinder unit to track the position of the foil by recording barcodes as they passed by. The barcode numbers were recorded and written into the data file.

A 2.1 m evacuated flight tube was placed immediately downstream from the unwinder unit. The flight tube allowed for two detectors to be used in the experiment. At the end of the flight tube a 2 megapixel Pilatus detector[3] was placed for the GISAXS. Another Pilatus 100K detector[3] was placed in the plane of the substrate covering the GIWAXS signal in the angles from 13° to 26° with regards to the direct beam.

PET is known to contribute with a substantial amount of scattering, significantly reducing the signal to noise ratio of the P3HT signal.It is therefore preferrable to have an incident angle of the beam lower than the critical angle of the PET which is 0.2° thus only scattering from the P3HT film. However, in order to obtain a signal from the P3HT crystals oriented with the lamellar stacks parallel to the substrate we found that the sample had to be oriented relativly close to the angle fulfilling the Bragg condition for the P3HT 100 reflection at 1.92° . We were able to have the beam scatter from a slightly lower angle but not lower than 1.5° which we used for the measurements.

9.3 Data processing

The Pilatus 2M detector has a 24 bit dynamic range. With four exposures at each point and with over 2000 datapoints, each dataset comprises over 45 GB. Even simple tasks thus takes from days to weeks to process.

To compensate for the large amount of raw data the first step of the analysis was to divide the SAXS images into a regions of interest. These were then integrated into smaller data structures for further analysis as shown on figure 9.3.

9.3.1 GISAXS signal

First the average of the three to four exposures was calculated for each position.

The 100 reflection from the P3HT crystals aligned with the substrate, this is referred to as *textured P3HT*, corresponding to the bright peak in the center of the upper half of the scattering pattern in figure 9.3. We found the FWHM of the peak to be around 25° defined everything within the central region, spanning an azimuth angle of 50° , to be textured P3HT. From the SAXS image the 100 reflection was detected, and the position was recorded, in addition a Gaussian was fitted to the peak and the height, width and area was calculated as well.

The scattering from the randomly oriented P3HT crystals, contributing to the scattering outside the central region, was defined as the untextured P3HT. As for the textured P3HT the position, width, height and area of the scattering were calculated and saved.

The scattering along the Yoneda line, marked on figure 9.3, corresponds to the lateral film structure. The scattering signal was extracted and integrated into a 1D scattering profile for a fixed $\mathbf{q}_z$.

9.3.2 GIWAXS signal

The WAXS detector was intended to be used for measuring the PCBM 010 reflection. However, due to the high angle of incidence the penetration of

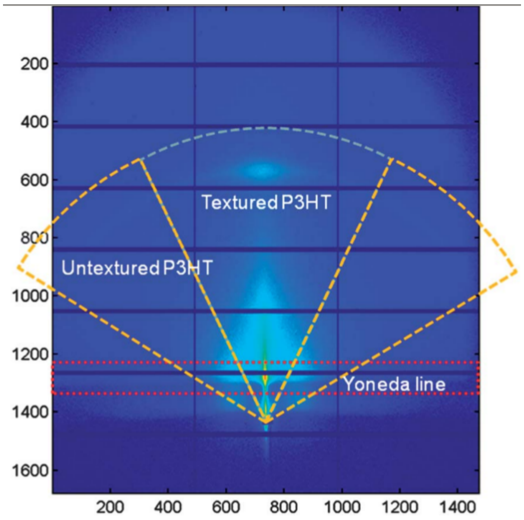

Figure 9.3: *A typical SAXS exposure with the regions of interest. Each of the outlined regions are integrated into a seperate 1D datastructure. The two dashed yellow areas labeled* untextured P3HT *as well as the area in between labeled* textured P3HT *is radial integrated. Textured P3HT refers to the lamellar stack aligned with the substrate. The width of the textured P3HT region was chosen to be 50° based on the FWHM of the textured P3HT peak. The red regoins labeled* Yoneda Line *and marks the region used for extracting SAXS data*[5]*.*

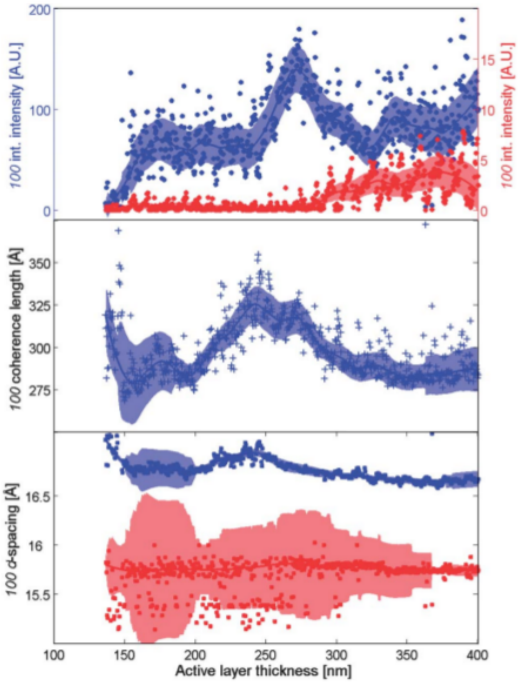

Figure 9.4: *The 100 P3HT reflection as a function of the P3HT film thickness. The blue datapoints are textured crystallites while the red datapoints are untextured crystallites. The colored band indicates the standard deviation.*

X-rays into the PET caused too much scattering in the high $\mathbf{q}$ regime. This, combined with air scattering, made the signal to noise ratio in the WAXS detector too low to be useful. The WAXS signal was therefore not analyzed.

9.4 P3HT thickness experiment

The first film was coated with P3HT with a gradually increasing dry thickness of the film. The intensity of the textured 100 reflection, shown in figure 9.4, showed a quick formation of crystallites that remained constant 170 nm to 250 nm. No untextured crystallites were observed suggesting. After 275 nm the thicker film with longer drying time allows the crystals to align themselves. This could be seen by the increasing untextured 100 reflection.

9.5 P3HT:PCBM ratio experiment

One of the samples consisted of a foil with both P3HT and PCBM. The ratio of the contents of the two components ranged from 0-100%. The parameters for the P3HT 100 reflection is shown in figure 9.5. One thing worth noticing was the lack of any P3HT crystalline structure when the weight percent was below 30%. Other have shown that the maximum PCE occurs at a P3HT:PCBM ratio of 1:1[1]. We showed that the maximum PCE correlates with the global minimum of the textured P3HT crystaline reflection intensity. The reflection from the untextured P3HT follows the same pattern but with a greatly reduced intensity.

9.6 Chloronaphthalene concentration experiment

A solution of P3HT:PCBM mixed in a 1:1 ratio, and with the addition of 0% - 5% of the additive 1-chloronaphtalene (Cl-naph) was also tested. Others have shown that the addition of Cl-naph increases the drying time of the polymer film[2]. The polymers use this longer drying time to self-organise leading to an improved device performance[2].

Chen *et al* reported a roughly 33% and 60% increase in the polymer crystalinity with 1% and 3% Cl-naph respectivly, compared to DCB only by measuring the P3HT reflection intensity with GISAXS[2].

We were unable to measure the entire film our experiment was limited to the 0%-3.5% range, however several rapid changes in the P3HT structure occurred. The 100 P3HT reflection had several local maximums and minimums. The most significant maxima were located at 1%, 2% and 3.2% Cl-naph and

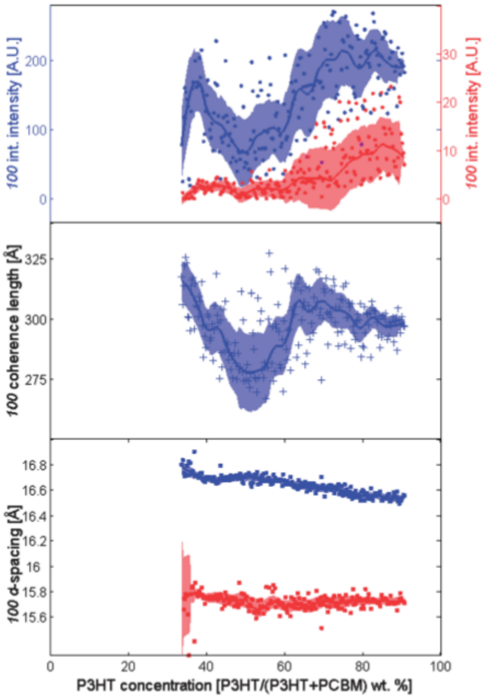

Figure 9.5: *The 100 P3HT reflection as a function of the P3HT:PCBM ratio. The blue datapoints are textured crystallites while the red datapoints are untextured crystallites. The colored band indicates the standard deviation. There is no crystal structure when the P3HT concentration is below* 1/3.

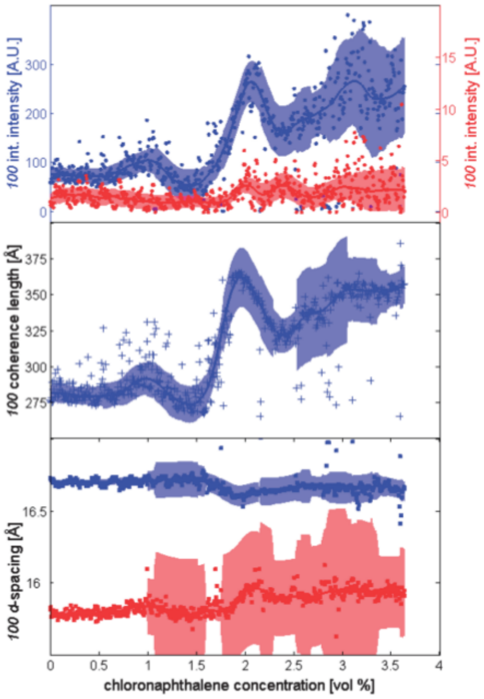

Figure 9.6: *The 100 P3HT reflection as a function of amount of Cl-naph. The blue datapoints are textured crystallites while the red datapoints are untextured crystallites. The colored band indicates the standard deviation. At 2% Cl-naph there is a large peak in the reflected intensity.*

the corresponding relative increase in scattering P3HT crystallites compared to 0% Cl-naph is 20%, 300% and 250%. While our results for the increase at 1% Cl-naph matches the results of Chen *et al* reasonably well, the mismatch at 3% Cl-naph could be explained by the uncertainty due to the rapidly changing scattering intensity.

9.7 SAXS at SSRF, China

The roller unit was also used at the SAXS beamline at the Shanghai Synchrotron Radiation Facility (SSRF). The roller was mounted in a similar way as the experiment at cSAXS, but due to a low flux, each position was measured for 500-600 seconds with an energy of 10 keV. Unfortunatly, the flux was too low to acquire any meaningful data from the unwinder.

9.8 Summary

The experiments in this chapter show that it was possible to characterize the crystalline structure of R2R coated polymers with high spatial resolution. It was possible to resolve changes in the texture which would otherwise be impossible with a fewer number of spin coated samples.

We observed that P3HT only creates textured crystallites as long as the wetting thickness is less than 270 nm. Above 270 nm the textured crystallites rapidly drop off while untextured crystallites begin to form.

Blends of P3HT:PCBM were shown to form crystal structures only in the presence of at least 30% P3HT.

Cl-naph seemed to enhance the crystallization of P3HT which reached its maximum when 2% Cl-naph was added.

Future experiments could be characterizing new samples, but also to implement the unwinder in a laboratory setting. A coating head could also be mounted on the unwinder to study the dynamics of polymer crystallization, drying and/or annealing in real time.

References

[1] Jan Alstrup, Mikkel Jørgensen, Andrew J. Medford, and Frederik C. Krebs. Ultra fast and parsimonious materials screening for polymer solar cells using differentially pumped slot-die coating. *ACS Applied Materials & Interfaces*, 2(10):2819–2827, 2010.

[2] Fang-Chung Chen, Hsin-Chen Tseng, and Chu-Jung Ko. Solvent mixtures for improving device efficiency of polymer photovoltaic devices. *Applied Physics Letters*, 92(10):103316, 2008.

[3] B. Henrich, A. Bergamaschi, C. Broennimann, R. Dinapoli, E.F. Eikenberry, I. Johnson, M. Kobas, P. Kraft, A. Mozzanica, and B. Schmitt. Pilatus: A single photon counting pixel detector for x-ray applications. *Nuclear Instruments and Methods in Physics Research Section A: Accelerators, Spectrometers, Detectors and Associated Equipment*, 607(1):247 – 249, 2009.

[4] Frederik C Krebs, Roar Søndergaard, and Mikkel Jørgensen. Printed metal back electrodes for r2r fabricated polymer solar cells studied using the lbic technique. *Solar Energy Materials and Solar Cells*, 95(5):1348–1353, 2011.

[5] Y. Yoneda. Anomalous Surface Reflection of X Rays. *Physical Review*, 131:2010–2013, September 1963.

Chapter 10

Conclusion & Outlook

10.1 Discussion

The P3HT:PCBM morphology of the nanoparticles, used in the waterbased inks, have proven to be unstable and the particles have shown to decompose into a PCBM particles in a P3HT matrix. It is not obvious whether this has a significant negative impact on the performance of the cell compared to the intended particles. However, since the domain size in some areas becomes significantly larger than the currently estimated maximum exciton diffusion length it is definitley a large problem for the efficiency of the cells, and may be the primary reason for the lacking performance of the water based ink compared to cells coated with organic solvents. Even if the particles do not collapse directly when being spin coated recent studies have shown that annealing will make them collapse[4]. The most obvious solution would be to continue to work on reducing the size of the nanoparticles or get better morphology control of the mixing of P3HT and PCBM, but also alternative morphologies like mixing particles of pure P3HT and pure PCBM could be considered.

Ptychography is still in a very early stage and despite its attractive properties, the far majority of published articles only demonstrates ptychography as a proof of concept, instead of utilizing it as a tool for material science. This is primarily due to the fact that both TEM and STXM still have superior resolution and STXM also offers chemical contrast of the samples.

For ptychography to offer something not available elsewhere today the sample needs to have structures in the $50\,\mathrm{nm} - 1\,\mu\mathrm{m}$ range where the contrast mechanism is too poor for TEM and STXM respectively. The requirements for 3D spatial resolution and/or samples too thick for soft X-rays and electrons is met by hard X-ray ptychography. While working on the border of the resolution we believed our sample with OPVs coated from a water based ink is a good candidate.

Organic samples, due to their low density contrast, are obvious candidates for ptychography and we believe our experience with beam damage, sample preparation and image registration can be transferred to other samples and experiments.

The core registration algorithm is very general purpose and can be utilized in a wide range of applications. It does however have a lot of currently fixed parameters which needs to be adjusted to the specific experiment in order to function properly. With some more work the registration algorithm could hopefully become yet another trivial step in the preprocessing of the data. The MATLAB implementation, in its current state, has been released on github[1] for everyone to use.

The registration algorithm should be tested on more samples to fine tune the various parameters, making it easier to use as a black box. Due to the very frequent and very high accelerations applied to the sample by the piezo stage we expect displacments of the sample to be a more common problem during ptychographic measurements compared to regular transmission tomography.

Furthermore the algorithm could be extended to include correction for physical beam damage. In the case of a beam damaged sample one would be able to detect the damaged areas by creating a tomographic reconstruction and projecting the reconstruction back to the measured angles. By comparing the measured projections with the reconstructed and backprojected ones it is possible to estimate which parts of the sample have been damaged and exclude those from further iterations.

The results from the unwinder unit showed changes in the crystallization of the polymer as a function of concentration and additives which would not have been possible to detect otherwise.

We have observed how P3HT when R2R coated only produces textured crystallites up to a film thickness of 272 nm. After this critical point, increased drying time allows the formation of untextured crystallites. From the ratio experiment we have observed how the formation of P3HT crystallites only occurs at ratios above 1:2 with PCBM and how the common 1:1 P3HT:PCBM ratio produces the shortest coherence length. Previous experiments by[2] showed what looked like a linear relation between added chloronaphthalene and the crystallinity of P3HT while our data shows a much more complicated pattern.

However, more importantly than the actual results it was demonstrated that it was possible to perform the experiment and achieve results in agreement with previous experiments but with much more detail, and that it would be technically possible to transfer the setup from a synchrotron context and into a lab scale setting where the flux is orders of magnitude lower, but also with much less constraint on time, equipment and availability.

10.2 Conclusion

One of the objectives of this thesis was to study the influence of R2R coating on the morphology of polymer solar cells.

Lab scale X-ray scattering has been applied to the basic characterization of polymer solar cells coated by spin coating and R2R coating. The size distribution of nanoparticles in dispersions, the crystal structure of coated polymers, the densities of the layers and the degree of crystallization were measured. The results have been used in a broad variety of our larger studies.

The active layer of the spin coated and the R2R coated cells were studied with scattering techniques, TEM, STXM and ptychography to understand the influence of the two different coating processes. We have studied the chemical composition of the active layers as well as the morphology in terms of size distributions and organization of the particles in the active layer. We believe that the particles must be prepared in an acidic environment thus hydrolysing the SDS into dodecanol to prevent degradation. The original motivation for creating the nanoparticles was to create water based ink. Therefore it is not necessarily bad that the particles degrade into bulk after coating. However, it is a problem that the P3HT and PCBM demix because the interface area between the two materials is significantly reduced.

Furthermore, we observed aggregation of the PCBM into clusters of almost 1 μm. This lead to further decrease of the interface area, leaving large areas of P3HT without an electron acceptor in reach for the exciton. Whether the aggregation of particles can be diminished with lower coating temperature or lower concentrations remains to be tested.

The degradation of the particles as well as the aggregation are probably responsible for the lower PCE that was obtained from cells coated with water-based inks by R2R coating. This is an important argument for the necessity of more focus on characterizing devices coated by R2R technology.

Today lab scale roll coaters exist and are commercially available. The unwinder unit has made it possible to measure foils coated with film by R2R coaters and generate data of the nanostructure with approximately two orders of magnitude higher spatial resolution than demonstrated previously. The high resolution revealed details of the formation of crystal structures in P3HT which would not be possible to detect with a smaller collection of 10 or 20 spin coated samples.

10.3 Outlook

In order to upscale the R2R production, water based inks needs to become a viable alternative to organic solvents. The low PCE in cells from water based inks, produced by R2R coating compared to spin coating, may be a consequence of the aggregation of the PCBM particles. Changing the film coating parameters such as lower temperature and different web speed need to be investigated in order to understand the aggregation process and how to prevent it.

Since the proof of concept the unwinder unit has been enhanced and is currently being implemented in a lab scale X-ray setup in order to scale down the requirements and make the technique more accessible. In addition to the unwinder unit a slot die coating head was added, making real time measurements of the coating process prossible. This will allow the study of the formation of crystalites in the film during the drying and annealing process. This will be a valuable tool for further investigations of the impact of coating parameters on the morphology of the active layer in polymer solar cells.

Ptychography is currently being rapidly improved and ptychographic images with sub 10 nm 2D and sub 50 nm 3D resolution have already been demonstrated at cSAXS[3]. The resolution is expected to improve even further. In contrast to STXM, Ptychography uses hard X-rays which can penetrate larger and denser samples. With the ability to perform quantitative tomography it is possible to image not only the active layer, but also the other layers in a polymer solar cell.

With sub 10 nm resolution and the ability to combine the images with quantitative tomography it will be possible to resolve not only the internal structure of nanoparticles but also bulk heterojunctions.

References

[1] Arvid Böttiger. 3D Image registration. `https://github.com/bottiger/3dregistration`, 2013.

[2] Fang-Chung Chen, Hsin-Chen Tseng, and Chu-Jung Ko. Solvent mixtures for improving device efficiency of polymer photovoltaic devices. *Applied Physics Letters*, 92(10):103316, 2008.

[3] Andreas Menzel, Ana Diaz, and Manuel Guizar-Sicairos. Ptychographic imaging at the swiss light source. *Synchrotron Radiation News*, 26(2):26–31, 2013.

[4] Syahrul Ulum, Natalie Holmes, Darmawati Darwis, Kerry Burke, AL David Kilcoyne, Xiaojing Zhou, Warwick Belcher, and Paul Dastoor. Determining the structural motif of p3ht: Pcbm nanoparticulate organic photovoltaic devices. *Solar Energy Materials and Solar Cells*, 110:43–48, 2013.

Appendices

View Article Online / Journal Homepage / Table of Contents for this issue
Dynamic Article Links

Journal of
Materials Chemistry

Cite this: *J. Mater. Chem.*, 2012, **22**, 22501

www.rsc.org/materials

PAPER

High-throughput roll-to-roll X-ray characterization of polymer solar cell active layers†

Arvid P. L. Böttiger,[a] Mikkel Jørgensen,[a] Andreas Menzel,[b] Frederik C. Krebs[a] and Jens W. Andreasen*[a]

Received 13th July 2012, Accepted 7th September 2012
DOI: 10.1039/c2jm34596j

Synchrotron-based X-rays were used to probe active materials for polymer solar cells on flexible polyester foil. The active material was coated onto a flexible 130 micron thick polyester foil using roll-to-roll differentially pumped slot-die coating and presented variation in composition, thickness, and additives. The coated foil was passed through a synchrotron X-ray beam on a small unit comprising unwinder and winder for the foil, an X-ray probe station, and a barcode reader for sample registration. Foil lengths of 10 meters were probed and yielded X-ray scattering data for approximately every 1 cm, probing linear variations in processing and coating parameters along the foil. The demonstration shows that real-time structural characterization of roll-to-roll coating at realistic web-speeds is feasible using synchrotron radiation. Off-line characterization with lower spatial resolution would be possible with dedicated laboratory instruments. We found that poly(3-hexyl)thiophene (P3HT) only crystallizes at a ratio above 1 : 2 with phenyl-C61-butyric acid methyl ester (PCBM) and that an optimum addition of 2 vol% chloronaphthalene (CN) as a processing additive significantly improves polymer crystallinity and crystallite size. In coated films thinner than 275 nm, textured poly(3-hexyl)thiophene crystallites with the lamellar stack aligned with the substrate dominate, similar to what is observed for spin-coated films.

Introduction

Some of the defining properties of polymer solar cells are characterized by the tremendous ease and speed with which they can be processed. The typical polymer solar cell is comprised of a multilayer stack of organic and inorganic materials that are processed one after the other using solution-based roll-to-roll coating and printing. For each layer the morphology and interface behavior present an intricate and complex dependency on the processing conditions and parameters. When polymer solar cell films are prepared by spin coating in a batch process, subsequent characterization is comparable in terms of the time required for the preparation, but when each layer is applied in a continuous process, roll-to-roll (R2R), new challenges must be met: the amount of data that needs to be efficiently collected and analyzed to characterize a given process or materials combination scales with the coated area. For the typical R2R coated polymer solar cell the web speeds employed are in the range of 1–10 m min^{-1} using web widths of 305 mm. This implies that an enormous amount of area is coated in a given amount of time compared to the speed at which that same area can be characterized using conventional methods such as optical methods, scanning probe techniques, discrete electrical measurements, and X-ray scattering. Unless the analysis method has the same throughput as the processing methods it is unlikely to be useful as a technique to optimize a given process or materials system. The characterization methods that have been demonstrated in an R2R setting are I–V characterization (current–voltage), optical microscopy, UV-visible spectroscopy, light beam induced current (LBIC), and incident photon to electron conversion efficiency (IPCE).[1,2] In addition to those techniques, ellipsometry, dark lock-in thermography, electroluminescence imaging, and optical coherence tomography have the potential to become R2R compatible.[3–6] Common to all these methods is that they yield macroscopic measures of the polymer solar cell such as structural and functional variations of the solar cells with a resolution of around 100 micron and particle detection down to around 10 micron. If one wishes to explore the microscopic nature of the organic solar cell stack on the micro- or nanoscale, new and rapid characterization tools are needed. One of the most powerful methods to probe the morphology and molecular organization of active materials in polymer solar cells is X-ray scattering methods. Intense synchrotron X-ray light sources allow X-ray characterization to be carried out at speeds compatible with roll-to-roll processing. There are a number of

---

[a] *Department of Energy Conversion and Storage, Technical University of Denmark, Frederiksborgvej 399, DK-4000 Roskilde, Denmark. E-mail: jewa@dtu.dk*
[b] *Paul Scherrer Institut, 5232 Villigen PSI, Switzerland*

† Electronic supplementary information (ESI) available: Quantification of the P3HT:PCBM ratio in the ratio gradient experiment by UV-vis characterization of the R2R printed modules, an example of a *100* reflection peak profile with Gaussian and Lorentzian fits, distribution of extracted parameters from film with unvaried composition, variation of *100* reflection azimuthal spread with gradient, an example of GIWAXS data as recorded, and animations showing the raw SAXS data acquired are available online. See DOI: 10.1039/c2jm34596j

challenges that must be overcome, among which are an efficient sample geometry on flexible plastic substrates and an automated sampling method coupled to an automated data analysis protocol. Until now very little work has been dedicated to study R2R processing using X-rays. Of relevance, though, are the recent intensive studies by Schmidt-Hansberg *et al.* of the drying process of polymer solar cell active layer solutions, in a knife-coating setup ("doctor-blading").[7–9] In these studies, X-ray diffraction of the drying film is measured in grazing incidence, while simultaneously monitoring the film thickness with a visible-light reflectometer. It was found for bulk heterojunctions of poly(3-hexyl)thiophene and [6,6]-phenyl-C61-butyric acid methyl ester (P3HT/PCBM) that the nanomorphology, phase separation, and crystallinity could be controlled by drying temperature through reduced molecular kinetics.[7] The effect of the P3HT:PCBM blend ratio on structural evolution of a drying doctor-bladed film indicated a strong molecular interaction between the two compounds, inhibiting P3HT π–π packing at a large excess of PCBM.[8] At an excess of P3HT it was found that crystallization of PCBM is inhibited long past the solubility limit. The addition of a "poor solvent" for P3HT (cyclohexane) caused aggregation of P3HT in solution and consequently a broader orientation distribution of crystallites as compared to the substrate/surface-induced crystallization from pure chlorobenzene.[9] While clearly relevant for the understanding of coating of polymer solar cell active layers these studies are essentially batch experiments and, therefore, still limited with respect to R2R coating. For efficient exploration of the materials and processing parameter space, a truly R2R compatible implementation is required. In this work we demonstrate roll-to-roll characterization of active layers for polymer solar cells using synchrotron X-ray scattering by employing a simple unwinder-registration-winder unit and flexible plastic foil as the substrate for the measurements, as shown in Fig. 1. Three different gradient experiments show the possibilities for exploring the structural phase diagram of the multicomponent parameter space of polymer solar cell processing: donor/acceptor ratio, active layer thickness, and concentration of a solvent additive.

Results and discussion

With thousands of measurements per experiment and diffraction data from area detectors, efficient analysis methods are required to evaluate the results. From inspection of the raw data we identified and extracted the following parameters from the data recorded on the Megapixel SAXS detector: integrated intensity, width, and position of the *100* reflection of P3HT, both from the peak centered on the surface normal corresponding to textured P3HT aligned with the substrate and for a segment of the diffraction ring corresponding to randomly oriented P3HT crystallites (Fig. 2). To observe the *100* reflection corresponding to textured P3HT, a relatively high X-ray incidence angle of 1.5° was required (see also the Experimental section) with the beam thus penetrating into the PET substrate causing strong background scattering in the WAXS detector. Combined with air scattering, this prevented the observation of diffraction signals from either P3HT or PCBM in the GIWAXS data recorded on the WAXS detector, and consequently, these data were not analyzed further. Thus, in the following, only data from the SAXS detector are discussed. For less crystalline polymers, it would likely be advantageous to choose a more shallow incidence angle to optimize the signal to noise ratio for GISAXS.

The parameters related to the P3HT *100* reflections were extracted by fitting a Gaussian function to the integrated peaks after subtracting a linear background function, yielding information about the amount of crystalline P3HT from the area of the fitted Gaussian, the crystalline coherence length from the fitted peak width through the Scherrer equation, and the lamellar packing density of the crystalline structure from the peak position. Although it is generally agreed that size–strain analysis on a single reflection cannot be used in a quantitative manner, we examined the possibility of separating peak broadening effects of size and strain by fitting a pseudoVoigt peak function where the Gauss–Lorentz mixing parameter might reveal useful information on trends in size/strain. We found, however, that the broad peaks are equally well fitted by "Gaussian" and "Lorentzian" pseudoVoigt functions therefore yielding very poorly determined mixing factors when fitted freely (see ESI Fig. S3†), and thus resorted to purely Gaussian fits to extract the parameters described above. The term coherence length is used to emphasize that these figures merely describe the limits to coherently diffracting regions without implying definite information on defects, strain or crystallite size.

In all the experiments, crystallites with the lamellar stack aligned with the substrate clearly dominate, similar to the texture observed for spin coated P3HT.[10] Because of difficulties in obtaining an automated, stable fit to the generally weak signal from untextured crystallites, the coherence lengths for these were found to be too unreliable and were not analyzed further, and only intensities and *d*-spacings were extracted. In some cases, clear outliers can be identified, caused by tilting of the substrate foil when moving to the next sampling positions. These are obvious, however, as lying many standard deviations from the mean, and represent less than 5% of the data points. The effect of sample position instability is most severe with respect to the scattering intensity, and much less so with respect to reflection peak widths and position. The maximal theoretical bias of the *100* peak position corresponds to scattering from either side of the film width of 10 mm equaling 0.08 Å in *d*-spacing. In general, standard deviations half of this or less are observed, except for very weak peaks. For constant composition, we observe relative standard deviations of 0.1% for the *100* *d*-spacing of textured P3HT, 20.7% for the integrated intensity and 3.2% for the coherence length (see ESI Fig. S4–S6†).

The data analysis was performed post-acquisition, but we consider it feasible to apply these analysis methods online, to allow monitoring of meaningful physical parameters during R2R coating. Thanks to the large amount of sampling points, we get information about correlations between these properties and their correlation with the controlled parameter with very high statistical significance.

A small-angle scattering pattern along the substrate surface (*i.e.* along q_{xy}) was extracted by integrating the scattered intensity in a region around a fixed q_z corresponding to the position of the Yoneda peak (Fig. 2). For each point we integrated data from four 100 ms exposures, but sufficient intensity is acquired in a single exposure. This allows for measurements with continuous foil movement at speeds of up to 6 m min^{-1} with the same spatial resolution as in the present experiments, thus enabling real-time

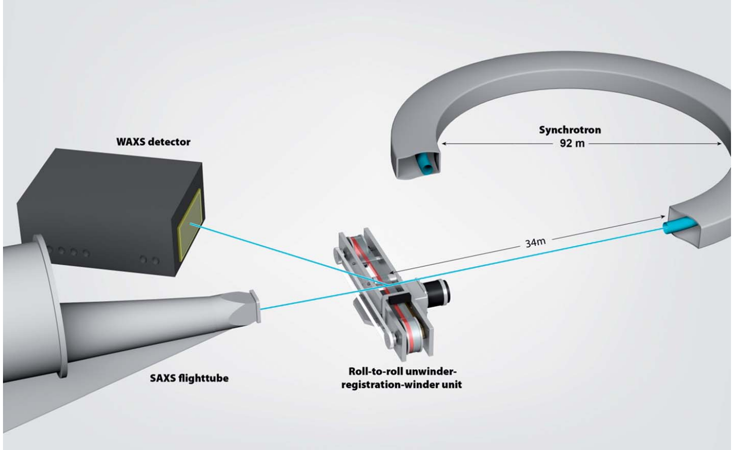

Fig. 1 Artist's rendition of the experiment showing the X-ray source (the synchrotron), the roller unit, and the detectors (WAXS detector and SAXS flight tube entry). Note that the WAXS data were found not to provide usable data in the reported experiments (see explanation below).

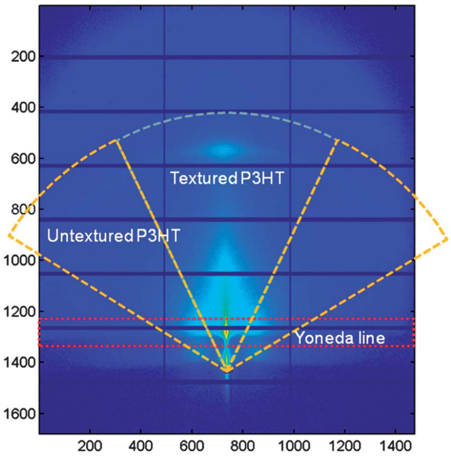

Fig. 2 A SAXS pattern from an R2R experiment showing the integration regions used to extract structural parameters of the film. The central region, covering an azimuthal angle of 50°, was chosen to represent the scattering of P3HT crystallites with the lamellar stack aligned with the substrate ("textured P3HT"). The two regions to the side, outlined in yellow, were used to integrate scattering from P3HT crystallites with random orientation ("untextured P3HT"). The rectangular region, outlined in red, corresponds to the region integrated to extract the GISAXS pattern along the "Yoneda line".[12] The numbering indicates the pixels. For an example of an integrated peak profile of the textured P3HT reflection, please refer to the ESI.†

analysis of coating processes. An optimized laboratory instrument[11] can deliver 10^7–10^8 photons on the sample *i.e.* 4–5 magnitudes lower flux as compared to an insertion device synchrotron beam line. The higher divergence of the laboratory instrument means that more crystallites are in diffraction condition for polycrystalline films at a given incidence angle. Accepting a lower spatial resolution (*e.g.* an exposure every 5 cm), gradient experiments as the ones reported here could be completed in a few days with an exposure time of 1000 s.

The GISAXS patterns integrated along the Yoneda line[12] are very susceptible to variations in the sample position, and contain a substantial scattering contribution from the substrate because of the high incidence angle. We have consequently only evaluated large changes in scattering intensity, as was observed in the ratio gradient experiment (discussed below).

Thickness gradient

The parameters for the textured and untextured P3HT *100* peaks are shown as a function of nominal dry film thickness in Fig. 3. A smoothed line to guide the eye is added to each dataset by calculating a weighted linear least squares local regression using a 2nd degree polynomial model across a data span of 15% of the total number of data points. Outliers outside six mean absolute deviations are assigned zero weight. The lighter colored band shows the standard deviation of the data points in the smoothing span centered on the corresponding data point, with respect to the smoothed mean. Some outliers representing very poor fits to the data are outside the plot region, but increase the standard deviation significantly (*e.g.* *d*-spacings of untextured crystallites in thin films, lower panel of Fig. 3).

The scatter in the data, caused by sample movement and film inhomogeneity, does not hide the clear trends, showing that the amount of crystalline textured P3HT increases with film thickness, but with a distinct maximum at 272 nm (top panel). With a larger thickness, untextured crystallites appear. The textured crystallite coherence length shows a broad maximum for a slightly thinner film, at 246 nm (Fig. 3, middle panel). For both textured and untextured crystallites, the lamellar spacing decreases slightly for the thickest films but with a maximum at 240 nm for the textured crystallites (lower panel).

In the scatterplots (Fig. 4) we observe a positive correlation between the lamellar *d*-spacing and the coherence length (top

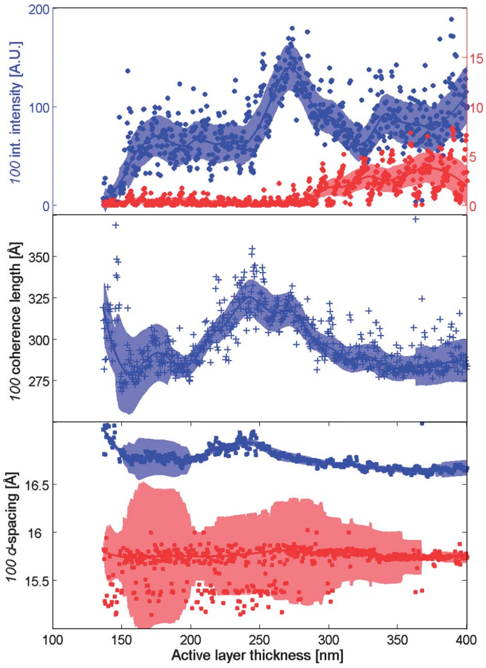

Fig. 3 Parameters of the crystalline P3HT *100* reflections shown as a function of the controlled gradient parameter, thickness. Data for the textured crystallites are shown in blue, for the untextured crystallites in red. Coherence lengths for untextured crystallites are not shown. A smoothed line is shown to guide the eye, with the associated band of one standard deviation of the data points with respect to the smoothed mean (see also main text for further explanation).

panel), but no correlation with the scattering intensity (middle panel). There is a positive correlation between integrated intensity and coherence length (lower panel). This is to be expected for a reflection from a population of a textured, semi-crystalline polymer, as in this case, both coherence length and integrated intensity will be related to the crystallinity of the polymer. The points corresponding to the smallest integrated intensity (below ~15, mostly dark blue) represent measurements where the *100* peak was ill defined, because the sample foil tilted during movement to a new measuring position. The recorded values in these points are thus viewed to be less accurate.

To summarize, we observe that, (1) up to 272 nm, the crystalline P3HT component of the active layer film is completely dominated by the textured population of crystallites presumably formed from nuclei in contact with the substrate, with the amount increasing with film thickness. (2) The largest of these crystallites occurs in films of 225–275 nm thickness. (3) The thickest films with longer drying times allow better organization of the polymer chains, and thus a shorter lamellar stacking, although the largest crystallites have the largest lamellar spacing, presumably due to steric hindrance during crystallization. (4) In films thicker than 275 nm, kinetics favor the formation of new crystalline nuclei in the drying film, with random orientation, and (5) these untextured crystallites adopt a different structure polymorph than the textured crystallites, presumably with partly interdigitated side chains as evidenced by very short lamellar spacings (form II identified by Prosa *et al.*[13]), or, the monoclinic structure identified by Brinkmann *et al.*[14] also characterized by a short lamellar packing distance.

Ratio gradient

The *100* peaks, corresponding to both textured and untextured crystallites, first appear at a ratio of 1 : 2 between P3HT and PCBM (Fig. 5). At first, the scattering intensity passes through a local maximum at about 40% P3HT and again increases for the highest P3HT:PCBM ratios above 1 : 1. The *100* coherence length of the textured crystallites shows a broad minimum at 1 : 1 ratio, whereas the lamellar *d*-spacing decreases with P3HT concentration, through a local minimum at ~42 wt% P3HT. The lamellar *d*-spacing of the untextured crystallites is constant at the very short distance of 15.7 Å in corroboration of the results obtained in the thickness gradient experiment.

Scatterplots show that the coherence length and lamellar *d*-spacing are uncorrelated (but the largest coherence lengths seen in the thickness gradient experiment are not observed here), whereas there is a negative correlation between integrated intensity and *d*-spacing (Fig. 6, top and middle panels). There is a

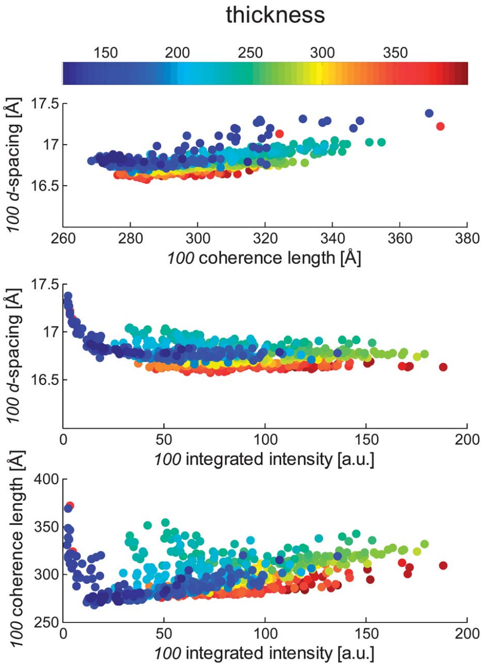

Fig. 4 Scatterplots showing relations between the parameters extracted from P3HT *100* reflections of textured crystallites for the thickness gradient experiment. Top panel: crystallite coherence length *vs.* *d*-spacing. Middle panel: integrated intensity *vs.* *d*-spacing. Lower panel: integrated intensity *vs.* crystallite coherence length. The color grading corresponds to the nominal film thickness, indexed as shown on the color bar at the top of the figure.

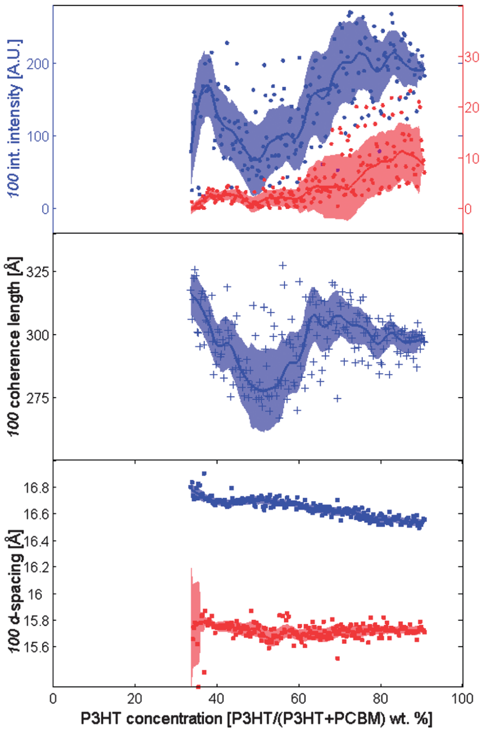

Fig. 5 Parameters of the crystalline P3HT *100* reflections shown as a function of the controlled gradient parameter, P3HT concentration [P3HT/(P3HT + PCBM) by weight]. The data for the textured crystallites are shown in blue, for the untextured crystallites in red. Coherence lengths for untextured crystallites are not shown. No data are available below 37% P3HT where there is no P3HT diffraction signal.

clear positive correlation between integrated intensity and the *100* coherence length (Fig. 6, lower panel).

The GISAXS patterns show a very dramatic change at exactly the point where P3HT crystallites appear, at the ratio of 1 : 2 P3HT:PCBM (Fig. 7).

The GISAXS intensity increases strongly and abruptly, indicating the sudden appearance of nanostructured inhomogeneities in electron density. These observations confirm the earlier findings by Schmidt-Hansberg *et al.* who found that strong intermolecular interaction between P3HT and PCBM may inhibit the crystallization of the minority component (in their case, PCBM).[9] Up to a ratio of 1 : 2, P3HT and PCBM are mixed on the molecular scale, but at a higher P3HT content, crystallites of P3HT form, creating nanoscale inhomogeneities which give a strong SAXS signal. The abrupt change is currently subject to further study and while corroborated by independent research groups[9] a possible explanation in this case is that it is also a result of the short drying time (~2 seconds) in the coating experiment. With fast drying the crystallization threshold is likely to be defined within a very narrow range in composition space.

The most important observations we note for the ratio experiment are as follows: (1) the P3HT crystallites show the smallest coherence length at a 1 : 1 P3HT:PCBM ratio. (2) P3HT crystallizes only above a 1 : 2 ratio with PCBM, and crystallinity increases just slightly at higher ratios. (3) The lamellar spacing is consistently larger for textured P3HT as compared to randomly oriented P3HT, which indicates that PCBM only interferes with the polymer chain packing in the textured crystallites. The short lamellar spacing of untextured crystallites indicates interdigitation of side chains as observed also in the thickness gradient experiment. (4) The lamellar spacing decreases with larger ratios of P3HT to PCBM showing a lessened effect of molecular interaction.

Additive gradient

The effect of solvent additives is variously described as improving phase separation, controlling donor–acceptor coherence lengths, or improving crystallinity. An example of the use of solvent additives is that of 1-chloronaphthalene (CN) for P3HT/PCBM active layer coating from *o*-dichlorobenzene (DCB).[15] CN is a high boiling point solvent (259 °C) as compared to chlorobenzene (CB, 131 °C) and DCB (181 °C), and fullerenes have a much better solubility in CN. Chen *et al.* concluded that these properties accounted for an improved solar cell performance because of improved phase separation and higher crystallinity of the polymer as deduced from grazing-incidence X-ray diffraction data taken along the surface normal of spin coated films.[15]

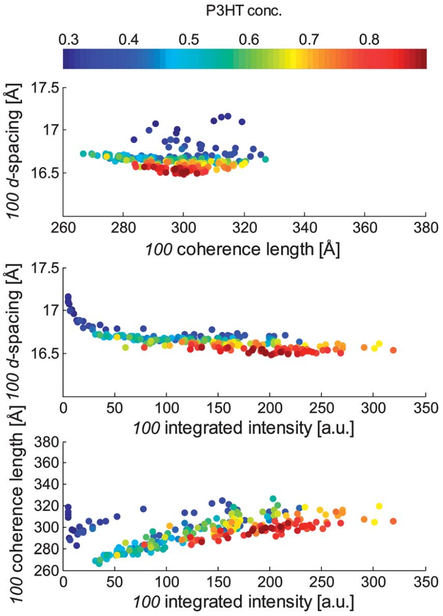

Fig. 6 Scatterplots showing relations between the parameters extracted from P3HT *100* reflections of textured crystallites for the P3HT/PCBM ratio experiment. Top panel: crystallite coherence length *vs.* *d*-spacing. Middle panel: integrated intensity *vs.* *d*-spacing. Lower panel: integrated intensity *vs.* crystallite coherence length. The color grading corresponds to the P3HT concentration P3HT/(P3HT + PCBM), indexed as shown on the color bar at the top of the figure.

View Article Online

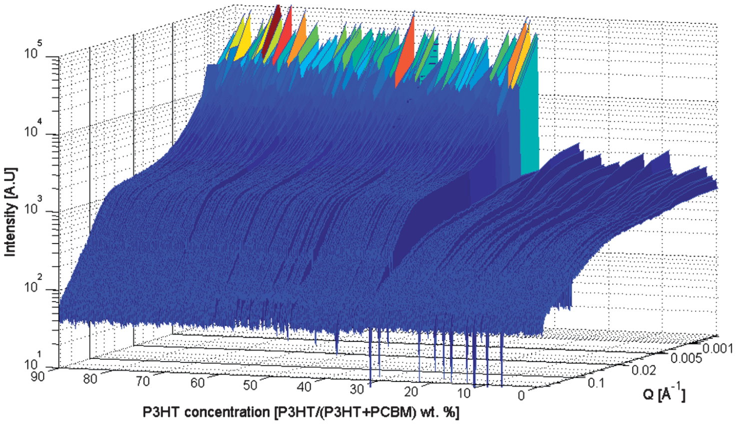

Fig. 7 GISAXS patterns from the ratio gradient experiment. The point where the scattering intensity increases dramatically corresponds to the P3HT concentration where P3HT crystallizes (~37 wt%).

In the present study, with the concentration of CN increasing from 0 to 3.5%, we observe several distinct and rapid changes, corresponding to changes in polymer texture and crystallinity.

The integrated intensity of the *100* peak from the textured P3HT crystallites increases with addition of chloronaphthalene (CN), with local maxima at 1.0, 2.0 and 3.2 vol% (Fig. 8). The intensity of the *100* peak of untextured crystallites also shows a weak increase with CN concentration, albeit with a large scatter of values. The coherence length of textured crystallites is positively correlated with the scattering intensity up to about 2 vol% CN (Fig. 8, top and middle panels). The effect of CN on the lamellar spacing is rather striking, with a clearly significant decrease of the *100* lattice spacing of the textured crystallites and an *increase* of the *100* lattice spacing of untextured crystallites at 1.5 to 2.0 vol% CN. The large standard deviations for the lamellar spacings of untextured crystallites are due to a relatively high number of outliers (outside the plot range) due to poor fits of these mostly weak peaks. Nevertheless, a positive shift of about 0.1 Å at 2 vol% CN addition appears to be significant. The average *d*-spacing of untextured crystallites below 1.5 vol% CN addition is 15.80(4) Å and 15.92(8) Å above 2.5 vol% CN addition (standard deviations in parentheses, excluding outliers).

From the scatterplot of P3HT *100* coherence length *vs.* lattice spacing we observe a weak negative correlation of the lamellar spacing with the coherence length, and further that the large coherence lengths appear for a CN concentration of 2 vol% and above (Fig. 9, top panel). Likewise, we observe a weak negative correlation between scattering intensity and lattice spacing with the highest intensities above 2 vol% CN (Fig. 9, middle panel). In the lower panel of Fig. 9, we observe the relationship between the scattering intensity and coherence length, with a clear positive correlation up to about 2 vol% CN, above which we see a constant coherence length.

Thus, we find that the addition of a solvent with high boiling point (1) clearly improves crystallinity and (2) facilitates crystal growth, while (3) allowing time for the polymer to adopt a good molecular packing as evidenced by the short lamellar *d*-spacing in corroboration of the results obtained by Prosa *et al.*[13] (4) The

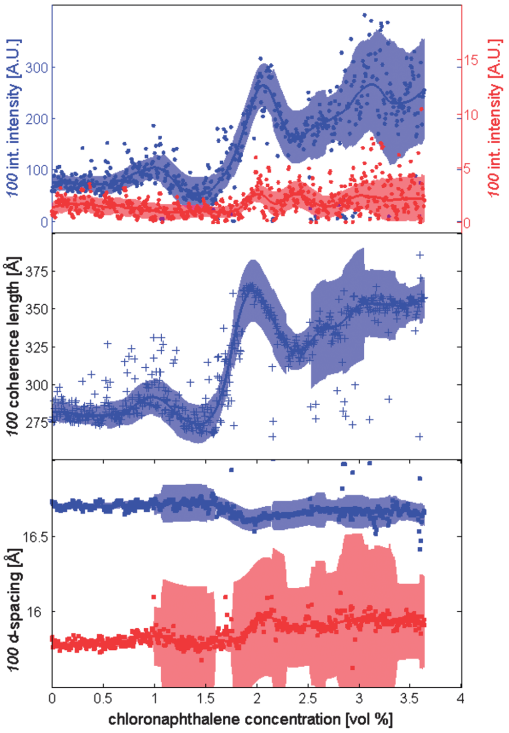

Fig. 8 Parameters of the crystalline P3HT *100* reflections shown as a function of the controlled gradient parameter, chloronaphthalene concentration. The data for the textured crystallites are shown in blue, for the untextured crystallites in red. Coherence lengths for untextured crystallites are not shown.

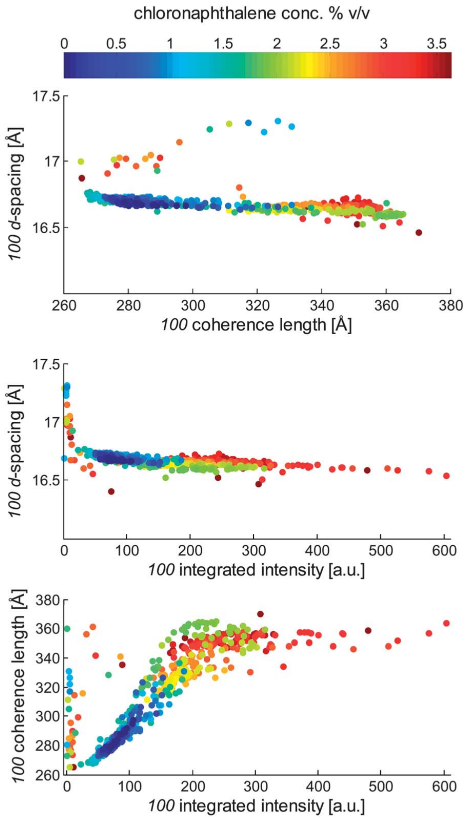

Fig. 9 Scatterplots showing relations between the parameters extracted from crystalline P3HT *100* reflections for the additive experiment. Top panel: crystallite coherence length *vs.* *d*-spacing. Middle panel: integrated intensity *vs.* *d*-spacing. Lower panel: integrated intensity *vs.* crystallite coherence length. The color grading corresponds to the CN concentration, indexed as shown on the color bar at the top of the figure.

strongest effect is realized at 2 vol% CN, and not much is gained by a higher percentage of additive. (5) Also at 2 vol% CN and higher concentrations, the lamellar spacing of untextured crystallites increases, which may indicate that CN facilitates molecular interaction between PCBM and P3HT, partly interfering with side-chain ordering of the polymer.

Conclusions

We have demonstrated an efficient means of characterizing polymer crystallinity and texture of R2R coated polymer solar cell active layers as a function of a variety of controlled processing parameters. This was done by recording a high spatial density of SAXS data from the gradient coated films, varying thickness, P3HT:PCBM ratio, and CN additive concentration over 10 meters substrate length, using a dedicated unwinder-registration-winder unit. In this manner we were able to identify significant changes to the polymer crystalline texture as a function of active layer thickness, P3HT:PCBM ratio and processing additive concentration. We find that highly textured P3HT dominates in films of up to about 270 nm thickness. In thicker films, we find increasing amounts of untextured P3HT crystallites, adopting a different structural form with a shorter lamellar spacing. An addition of 2 vol% chloronaphthalene to the processing solvent enhances the crystallization of P3HT.

This type of information can be correlated with other R2R characterization methods, including IPCE measurements, *e.g.* we find it significant that the minimal coherence length of P3HT coincides with the optimal 1 : 1 ratio with PCBM, found in many other studies. Such correlations may facilitate fast optimization of new material combinations. We envisage that the method may be extended to online coating characterization by supplementing the roller unit with the appropriate microsyringe pumping arrangements. More detailed structural information will be available from the WAXS detector and from the GISAXS signal in the SAXS detector by performing scans at several (more shallow) X-ray incidence angles, significantly attenuating scattering from the substrate. An obvious extension of the method is for partially completed multilayer solar cell stacks which will allow a direct correlation with cell performance. Microcrystalline, inorganic materials such as the transparent conducting oxide electrode and oxide blocking layers will not have substantial scattering in the small angle regime. Finally, a subject for further study using GISAXS is crystallization phenomena as a function of drying kinetics and additives.

Experimental

Materials

Poly-3-hexylthiophene with a molecular weight of 40 kDa and regioregularity of 96% was obtained from BASF (Sepiolid P200), PCBM was obtained from Solenne BV (99%), chlorobenzene was of analytical grade (Aldrich, purity 99%), and chloronaphthalene was of reagent grade (Aldrich, 97%). The substrate was polyethylene terephthalate (PET) with a thickness of 130 micron and a web width of 305 mm (Dupont-Teijin, Melinex ST506). *Roll-to-roll coating*: the method followed that described in the literature.[2] The foil was labeled using an ink jet barcode printer with a unique label for each of the 6 stripes on the foil. Both a machine-readable barcode and a human-readable alphanumeric text string were written every 10 cm along the foil. The foil was labeled with 6 sets of 5-digit barcodes with the first digit describing the experiment number and the last 4 digits being incremented for every 10 cm. After coating of the experiments the foil was sliced using a roll-to-roll cutting machine into rolls that were 30 mm wide containing only the barcode and the 13 mm wide coated stripe for X-ray testing.

Three different types of coating experiments were carried out in duplicate: ratio, thickness and additive experiments. For coating the web speed was 2 m min^{-1} with an oven temperature of 60 °C (2 m oven length). After experiment 1 had been carried out the foil was rewound and the same foil was passed through the machine while carrying out the next experiment. After the last coating experiment the foil was passed through an oven at 140 °C (2 m oven length) to anneal all stripes identically and to simulate conditions typically employed during roll-to-roll manufacture.[16–21] The coating setup employs a mini slot-die coating head and two piston pumps with a flow resolution of 10 μL. The output from each pump is combined in a mixing tee and fed to the mini slot-die coating head. The coated width was 13 mm and the flow was fixed at 250 μL min^{-1}. In the ratio experiments, pump A contained a chlorobenzene solution of P3HT (20 mg mL^{-1}) and pump B PCBM (20 mg mL^{-1}) in chlorobenzene. In the thickness experiment, pump A contained P3HT (20 mg mL^{-1}) and PCBM (20 mg mL^{-1}) in chlorobenzene while pump B contained pure chlorobenzene. The wet film thickness is 10 μm corresponding to a starting dry thickness of 400 nm assuming a dry film density of 1.1 g cm^{-3} (*cf.* similar experiments).[2] In the additive experiment, pump A contained P3HT (20 mg mL^{-1}) and PCBM (20 mg mL^{-1}) in chlorobenzene while pump B contained P3HT (20 mg mL^{-1}) and PCBM (20 mg mL^{-1}) in chlorobenzene with 1-chloronaphthalene (5% v/v). All solutions were stirred at 70 °C and immediately filtered (0.45 micro Teflon filter) before the coating experiment. In the experiment the coating was started while constantly pumping with either pump A or pump B and once the coating had been established as stable, the gradient mixing of pump A and pump B was commenced and continued over a length of 10 m (100 barcodes) upon completion of the gradient the coating was continued with constantly pumping pump B or pump A. After the X-ray experiments had been carried out a 4 cm piece of foil was cut every 1 meter and the material dissolved in a constant volume of chloroform (4 mL) that was subsequently analyzed using ultraviolet-visible spectroscopy (UV-vis). In this manner the start and end points of the gradient experiments were accurately confirmed (see also ESI† available online).

Roll-to-roll unwinder-registration-winder unit

The device shown in Fig. 10 consists of an unwinder and winder roll, handling up to 15 m of coated PET substrate foil, 130 μm thick. The foil is held tight to the central aluminum cylinder that serves as the X-ray measuring position. A barcode reader scans the foil continuously, registering the module number printed on the substrate, thus keeping track of the position along the gradient experiment. The recorded module numbers are stored in the header of the X-ray data files. A stepper motor advances the foil as controlled by the beam line control software.

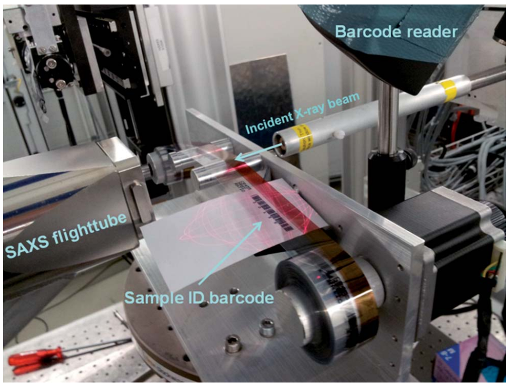

Fig. 10 The R2R unit in action at the cSAXS beam line, mounted on the sample stage hexapod. The beam flight tube exit is seen on the right and the SAXS flight tube entry on the left. On the substrate foil, the red active layer film can be seen as well as the bar code. The scanning pattern of the bar code reader laser can just be made out over the bar code.

The entire unit was mounted on a hexapod allowing full control of the positions and tilt with respect to the X-ray beam (Fig. 10). Two modes of operation were used: first a move until a barcode was read, followed by a series of X-ray measurements at shorter spacings on the foil. This method proved somewhat unreliable, as the reading of barcodes would fail at times. We consequently changed to a mode where the foil was advanced at a constant fixed amount, followed by X-ray measurements, repeatedly, while continuously reading out barcodes for registration of the position.

X-ray methods

The experiment was carried out at the cSAXS beam line (X12SA) at the Swiss Light Source. The scattering signal was recorded on two detectors (Fig. 1). A 2 Megapixel Pilatus detector[22] at 2.1 m from the sample behind an evacuated flight tube for measuring the small-angle X-ray scattering signal at grazing incidence (GISAXS) and a 100k Pilatus detector[22] positioned in the foil substrate plane covering angles from 13° to 26° to the direct beam for measuring the wide-angle X-ray scattering signal (GIWAXS). At each sampling position, four exposures of 0.1 s were acquired allowing 3 ms for readout after each. The X-ray energy was 11.1 keV. No corrections were applied to the data. In principle, both Lorentz and polarization corrections apply, but as we are only considering variations relating to the 100 reflection in a narrow region of reciprocal space, this was deemed to be unnecessary. As the incidence angle was far above the critical angle for total reflection, the scattering intensities can be treated in the kinematical approximation,[23] *i.e.* not requiring a correction for effects of refraction.[24] From the experiment geometry we estimate an instrumental broadening amounting to about 10% of the 100 peak width in reciprocal Å, corresponding to a negligible 1 Å in real space assuming a Gaussian instrumental broadening.[25]

To obtain a signal from P3HT crystals oriented with lamellar stacks parallel to the substrate, we found that it was necessary to use an X-ray incidence angle relatively close to the angle fulfilling the Bragg condition for the *100* reflection ($\theta = 1.92°$). The lowest incidence angle giving a satisfactory scattering intensity from the *100* reflection was found at 1.5°. This does however compromise the GISAXS and GIWAXS signals, because the beam penetrates into the PET substrate, giving substantial background scattering (an example of GIWAXS data is shown in the ESI†). Animations showing the raw SAXS data acquired are available online.

Acknowledgements

This work was supported by the Danish National Research Foundation and the work carried out within the Danish–Chinese Center for Organic-based photovoltaic cells with morphology control. Travel support for the synchrotron experiments was provided by the Danish Center for the use of Synchrotron, X-ray and Neutron facilities 2012, DANSCATT, FNU-11109227. The authors acknowledge financial support from the European Commission under the Seventh Framework Program by means of the grant agreement for the Integrated Infrastructure Initiative no. 262348 European Soft Matter Infrastructure (ESMI). We gratefully acknowledge X. Donath for technical assistance with implementation of the roller setup at the cSAXS beam line and T. Kjær for manufacturing the first roller device.

References

1 F. C. Krebs, R. Søndergaard and M. Jørgensen, Printed metal back electrodes for R2R fabricated polymer solar cells studied using the LBIC technique, *Sol. Energy Mater. Sol. Cells*, 2011, **95**, 1348–1353.

2 J. Alstrup, M. Jørgensen, A. J. Medford and F. C. Krebs, Ultra fast and parsimonious materials screening for polymer solar cells using differentially pumped slot-die coating, *ACS Appl. Mater. Interfaces*, 2010, **2**, 2819–2827.

3 R. Roesch, F. C. Krebs, D. M. Tanenbaum and H. Hoppe, Quality control of roll-to-roll processed polymer solar modules by complementary imaging methods, *Sol. Energy Mater. Sol. Cells*, 2012, **97**, 176–180.

4 R. Roesch, D. M. Tanenbaum, M. Jørgensen, M. Seeland, M. Barenklau, M. Hermenau, E. Voroshazi, M. T. Lloyd, Y. Galagan, B. Zimmermann, U. Wurfel, M. Hosel, H. F. Dam, S. A. Gevorgyan, S. Kudret, W. Maes, L. Lutsen, D. Vanderzande, R. Andriessen, G. Teran-Escobar, M. Lira-Cantu, A. Rivaton, G. Y. Uzunoglu, D. Germack, B. Andreasen, M. V. Madsen, K. Norrman, H. Hoppe and F. C. Krebs, Investigation of the degradation mechanisms of a variety of organic photovoltaic devices by combination of imaging techniques-the ISOS-3 inter-laboratory collaboration, *Energy Environ. Sci.*, 2012, **5**, 6521–6540.

5 L. Thrane, T. M. Jørgensen, M. Jørgensen and F. C. Krebs, Application of optical coherence tomography (OCT) as a 3-dimensional imaging technique for roll-to-roll coated polymer solar cells, *Sol. Energy Mater. Sol. Cells*, 2012, **97**, 181–185.

6 M. V. Madsen, K. O. Sylvester-Hvid, B. Dastmalchi, K. Hingerl, K. Norrman, T. Tromholt, M. Manceau, D. Angmo and F. C. Krebs, Ellipsometry as a nondestructive depth profiling tool for roll-to-roll manufactured flexible solar cells, *J. Phys. Chem. C*, 2011, **115**, 10817–10822.

7 M. Sanyal, B. Schmidt-Hansberg, M. F. G. Klein, A. Colsmann, C. Munuera, A. Vorobiev, U. Lemmer, W. Schabel, H. Dosch and E. Barrena, *In situ* X-ray study of drying-temperature influence on the structural evolution of bulk-heterojunction polymer-fullerene solar cells processed by doctor-blading, *Adv. Energy Mater.*, 2011, **1**, 363–367.

8 M. Sanyal, B. Schmidt-Hansberg, M. F. G. Klein, C. Munuera, A. Vorobiev, A. Colsmann, P. Scharfer, U. Lemmer, W. Schabel, H. Dosch and E. Barrena, Effect of photovoltaic polymer/fullerene blend composition ratio on microstructure evolution during film solidification investigated in real time by X-ray diffraction, *Macromolecules*, 2011, **44**, 3795–3800.

9 B. Schmidt-Hansberg, M. Sanyal, M. F. G. Klein, M. Pfaff, N. Schnabel, S. Jaiser, A. Vorobiev, E. Muller, A. Colsmann, P. Scharfer, D. Gerthsen, U. Lemmer, E. Barrena and W. Schabel, Moving through the phase diagram: morphology formation in solution cast polymer-fullerene blend films for organic solar cells, *ACS Nano*, 2011, **5**, 8579–8590.

10 H. Sirringhaus, P. J. Brown, R. H. Friend, M. M. Nielsen, K. Bechgaard, B. M. W. Langeveld-Voss, A. J. H. Spiering, R. A. J. Janssen, E. W. Meijer, P. Herwig and D. M. de Leeuw, Two-dimensional charge transport in self-organized, high-mobility conjugated polymers, *Nature*, 1999, **401**, 685–688.

11 J. Kehres, J. W. Andreasen, F. C. Krebs, A. M. Molenbroek, I. Chorkendorff and T. Vegge, Combined *in situ* small- and wide-angle X-ray scattering studies of TiO_2 nanoparticle annealing to 1023 K, *J. Appl. Crystallogr.*, 2010, **43**, 1400–1408.

12 Y. Yoneda, Anomalous surface reflection of X rays, *Phys. Rev.*, 1963, **131**, 2010–2013.

13 T. J. Prosa, M. J. Winokur and R. D. Mccullough, Evidence of a novel side chain structure in regioregular poly(3-alkylthiophenes), *Macromolecules*, 1996, **29**, 3654–3656.

14 N. Kayunkid, S. Uttiya and M. Brinkmann, Structural model of regioregular poly(3-hexylthiophene) obtained by electron diffraction analysis, *Macromolecules*, 2010, **43**, 4961–4967.

15 F. C. Chen, H. C. Tseng and C. J. Ko, Solvent mixtures for improving device efficiency of polymer photovoltaic devices, *Appl. Phys. Lett.*, 2008, **92**, 103316.

16 F. C. Krebs, S. A. Gevorgyan, B. Gholamkhass, S. Holdcroft, C. Schlenker, M. E. Thompson, B. C. Thompson, D. Olson, D. S. Ginley, S. E. Shaheen, H. N. Alshareef, J. W. Murphy, W. J. Youngblood, N. C. Heston, J. R. Reynolds, S. J. Jia, D. Laird, S. M. Tuladhar, J. G. A. Dane, P. Atienzar, J. Nelson, J. M. Kroon, M. M. Wienk, R. A. J. Janssen, K. Tvingstedt, F. L. Zhang, M. Andersson, O. Inganas, M. Lira-Cantu, R. de Bettignies, S. Guillerez, T. Aernouts, D. Cheyns, L. Lutsen, B. Zimmermann, U. Wurfel, M. Niggemann, H. F. Schleiermacher, P. Liska, M. Gratzel, P. Lianos, E. A. Katz, W. Lohwasser and B. Jannon, A round robin study of flexible large-area roll-to-roll processed polymer solar cell modules, *Sol. Energy Mater. Sol. Cells*, 2009, **93**, 1968–1977.

17 F. C. Krebs, Roll-to-roll fabrication of monolithic large-area polymer solar cells free from indium-tin-oxide, *Sol. Energy Mater. Sol. Cells*, 2009, **93**, 1636–1641.

18 F. C. Krebs, All solution roll-to-roll processed polymer solar cells free from indium-tin-oxide and vacuum coating steps, *Org. Electron.*, 2009, **10**, 761–768.

19 F. C. Krebs, Polymer solar cell modules prepared using roll-to-roll methods: knife-over-edge coating, slot-die coating and screen printing, *Sol. Energy Mater. Sol. Cells*, 2009, **93**, 465–475.

20 F. C. Krebs, S. A. Gevorgyan and J. Alstrup, A roll-to-roll process to flexible polymer solar cells: model studies, manufacture and operational stability studies, *J. Mater. Chem.*, 2009, **19**, 5442–5451.

21 F. C. Krebs, T. Tromholt and M. Jørgensen, Upscaling of polymer solar cell fabrication using full roll-to-roll processing, *Nanoscale*, 2010, **2**, 873–886.

22 B. Henrich, A. Bergamaschi, C. Broennimann, R. Dinapoli, E. F. Eikenberry, I. Johnson, M. Kobas, P. Kraft, A. Mozzanica and B. Schmitt, PILATUS: a single photon counting pixel detector for X-ray applications, *Nucl. Instrum. Methods Phys. Res., Sect. A*, 2009, **607**, 247–249.

23 P. Busch, M. Rauscher, D. M. Smilgies and D. Posselt, Papadakis grazing-incidence small-angle X-ray scattering from thin polymer films with lamellar structures – the scattering cross section in the distorted-wave born approximation, *J. Appl. Crystallogr.*, 2006, **39**, 433–442.

24 S. Lilliu, T. Agostinelli, E. Pires, M. Hampton, J. Nelson and J. E. Macdonald, Dynamics of crystallization and disorder during annealing of P3HT/PCBM bulk heterojunctions, *Macromolecules*, 2011, **44**, 2725–2734.

25 D. M. Smilgies, Geometry-independent intensity correction factors for grazing-incidence diffraction, *Rev. Sci. Instrum.*, 2002, **73**, 1706–1710.

Influence of Roll to Roll coating on the morphology of polymer solar cells coated from aqueous inks

Arvid P. L. Böttiger[1], Thue T. Larsen-Olsen[1], Thomas R. Andersen[1], Ana Diaz[2], Jostein B. Fløystad[3], Morteza Esmaeili[3], Karl Thyden[1], Dag Breiby[3], Xiaoniu Yang[4], Frederik C. Krebs[1], Jens W. Andreasen*[1]

1 Department of Energy Conversion and Storage, Technical University of Denmark, Frederiksborgvej 399, DK-4000 Roskilde, Denmark
2 Swiss Light Source, Paul Scherrer Institute, Villigen, Switzerland
3 The Norwegian University of Science and Technology, NO-7491 Trondheim, Norway
4 Changchun Institute of Applied Chemistry, No.5625, Ren Min St., Changchun, P.R.China

e-mail: jewa@dtu.dk

Keywords: polymer solar cells, 3D X-ray imaging, STXM, phase contrast, TEM

Abstract

In organic photovoltaics, water based inks of the active materials are emerging as a new environmentally friendly alternative to organic solvents. Using various X-ray and TEM techniques, for 2D and 3D imaging we report changes in the nanostructures of films made from nanoparticles of poly-(3-hexylthiophene) (P3HT) and phenyl-C61-butyric acid methyl ester (PCBM) and produced by roll-to-roll (R2R) coating. We observe a phase separation of the particles into pure PCBM particles in a bulk of P3HT because of hydrolysis of the SDS. During the spin coating the otherwise closely packed PCBM particles are distributed and the P3HT film is further homogenized, while R2R coating also creates clusters of PCBM particles.

Introduction

Polymer solar cells have been developed to impressive power conversion efficiencies, approaching and in some cases surpassing established technologies such as amorphous silicon[1][2]. Record results are limited however to small scale devices, whereas reports of large area devices processed in a scalable fashion are still scarce[2]. The experience gained through years of optimizing processing parameters for small scale devices appears to have limited applicability to scalable processing techniques for large area devices such as R2R coating. There can be many reasons for this, from the macroscopic level to the nanostructure of the final device. There is a general consensus in the field that the power conversion efficiency is closely related to the nanostructure of the polymer solar cell active layer, usually referred to as the bulk heterojunction[3], [4], but controlling and characterizing this morphology has proven difficult.

Aqueous processing of polymer solar cells are a viable solution to the environmental challenges associated with the organic solvents commonly employed (i.e. chlorobenzene). Aqueous processing have been demonstrated producing working cells using the industrial roll to roll (R2R) printing technology for high volume production[5]. However, the power conversion efficiency achieved on average for R2R processed large area OPV is somewhat smaller then record reports and very little is known about the effects of R2R on the morphology. This is especially true for solar cells prepared by R2R coating from aqueous solutions which to our knowledge never have been studied in depth.

Utilizing both new and proven imaging techniques combined with x-ray scattering we investigate the nanoparticles, physically and chemically, used as the active layer. We investigate the particles as ink and as coated films from working devices. In addition we investigate the influence of other factors such as wetting agents and annealing might have.

The size and materials of the particles in this study were chosen for optimal device performance. Even if materials with higher contrast or larger particles could simplify some of the experiments our focus was targeted towards the morphology of state-of-the-art-devices. Small angle X-ray scattering (SAXS), Transmission Electron Microscopy (TEM), Scanning Transmission X-ray microscopy (STXM) and a new state of the art x-ray imaging technique called Ptychography was used for the physical characterization. For the chemical characterization we used Wide Angle X-ray Scattering (WAXS), STXM and Selected area (electron) diffraction (SAED).

While films from working cells may contain contamination from the surrounding layers and adds additional constraints on the experiments compared to clean lab study we believe our work adds valuable knowledge about the effects of R2R processing.

Methods

Materials

Nanoparticles prepared for these studies were fabricated from P3HT (SepiolidP200, BASF) and [60]PCBM (99%,Solenne B.V.) be the usage of different solvents, concentration, and as homo-nanoparticles by the method previously descript[5].

Nanoparticle preparation

The nanoparticles were created in two batches, B1 and B2. Both batches were made from P3HT and/or PCBM, dissolved in chloroform or chlorobenzene, and mixed with an aqueous sodium dodecyl sulfate (SDS) solution in a tall beaker. The mixture was stirred vigorously for 1 hour and then subjected to ultrasound (0.65 kW) using an UIP 1000 hd transducer from Hielscher ultrasound technology fitted with a booster head. The mixture was stirred on a hot plate, at a 70 °C and 110 °C for chloroform and chlorobenzene, respectively, until the solvent had evaporated. Excess of SDS were removed from the aqueous dispersions by dialysis against pure water using two different methods. B1 were prepared using dialysis tubes (Milipore), B2 were prepared using a labscale tff system. In the final step the dispersions were concentrated to approximately 60 mg/mL.

Sample	P3HT (g)	PCBM (g)	Chloroform (mL)	Chlorobenzene (mL)	SDS (g/L)	SDS (mL)	Ultrasound (min.)	FSO (mg/mL)
heterogeneous particles	0.3	0.3	0	15	30	50	4	0
homogeneous P3HT particles	0.3	0	10	0	30	25	6	0
Homogeneous PCBM particles	0	0.2	5	0	40	20	6	0
Ink for R2R, heterogeneous particles	4	4	181	0	30	480	6.5	5

Ink comprising a mixture of P3HT-material and PBCM-material was added 5 mg/mL FSO. The ink was spin coated on a piece of glass.

Small Angle X-ray Scattering (SAXS)

The (Grazing incidence) small angle x-ray scattering was performed at laboratory setup at DTU. The source was a rotating Cu anode operating at 46 kV and 46 mA delivering a beam from the corresponding K_α emission at 1.5418 Å. The detector for the small angle scattering was a 2D “Gabriel”-type gas-proportional delay line detector[6]. The SAXS data was reduced into a 1D cross section by azimuthal averaging and GISAXS was similarly reduced to 1D by taking a projection along the Yoneda line[6]. The 1D scattering intensities was analyzed using the Bayesian Inverse Fourier Transform[7].

Wide angle X-ray Scattering (WAXS)

The GIWAXS data was acquired on a similar setup operating at 50 kV and 200mA. The major difference was the detector, in this case being an offline image plate detector located 121 mm from the sample.

Roll to Roll coating

The R2R coating was performed as previously reported[5] with minor variations.

Phase contrast tomography (ptychograhy)

The Ptychography was performed at the Swiss Light Source (SLS) on the cSAXS (X12SA) beam line. The sample was mounted on a 3D piezo-stage on top of a rotation stage. The energy was set to 6.2 keV and in front of the sample a 2.5 micron pinhole defining the illumination to a confined area of the sample. After the sample there was a 7 m helium filled flight tube followed by a PILATUS 2M detector. A sample in this experiment was scanned using 702 exposures of 0.1 seconds. Each exposure was 0.8 microns apart, following a concentric pattern from the center of the sample and out, rather than a square scan. The samples were measured at 181 angles. Including overhead one 181 angle measurement took roughly 8 hours.

The microcapillaries used as sample holder were pulled on a Sutter P-97 Flaming/Brown Micropipette Puller (Sutter Co, Novato, CA, U.S.A.) to a few microns in diameter at the tip. They were all produced by pulling them at 590 °C and 0.1 atm pressure. A nitrogen flow was used to blow the material into the tip of the micro-capillaries. The borosilicate has a mass density of 2.23 g/cm^3 which translate into an electron density of 1.3 e/Å^3.

Scanning Transmission X-ray Microscopy (STXM)

The soft x-ray imaging was performed at the MAXYMUS beamline at BESSY II in Berlin using a 25 nm zone plate. The atmosphere was below 10E-8 mbar and the detector was a light sensitive diode connected to a photomultiplier. The beemline could be tuned to an energy from 240 eV up to 1.8 keV but during our scans around the carbon edge the energy range was from 280 eV to 320 eV. The data was analyzed using Axis2000 and Matlab.

Transmission Electron Microscopy (TEM)

Some of the TEM images was acquired at DTU Center for Electron Nanoscopy (CEN) using their FEI Tecnai T20 G2 microscope and measured at 300 keV. The TEM images for the annealing experiment at the Changchun Institute of Applied Chemistry were performed on a *JEOL*-2100F microscope operated at 200 kV.

Experimental

Ptychography

Due to the limited dissemination of the Ptychography the following section will explain the basics.

Ptychography is a hard X-ray imaging technique which is currently being commissioned on various beamlines around the world. It is suitable for tomography (3D imaging) and has been shown to produce tomograms with a resolution below 100 nm, currently only limited by various technical stabilities in the setups [8]–[11].

It works by illuminating the sample by a series over partially overlapping exposures. The redundant information from the overlapping is used to overcome the phase problem and makes it possible to reconstruct the sample as well as the wave front. Ptychography gives the opportunity to measure both the amplitude and phase change caused to the beam by the sample.

David Sayre[12] was one of the first pioneers in coherent diffractive imaging (CDI), proposing methods to solve the phase problem by oversampling. Ptychography is one of several coherent imaging techniques and was developed by Walter Hoppe who was the first to theorize a solution for crystalline samples[13]. J. M. Rodenburg was the first to demonstrate it using electron microscopy and broke the traditional scanning transmission electron microscopy resolution (STEM) for his sample. Ptychography differentiates itself from other coherent scattering techniques in solving the phase problem by measuring the interference pattern created from the scattering of the sample for a large number of overlapping measurments, providing a lot of redundant information. The measured signal is then converted into a real space image by deconvoluting the interference pattern with an iterative algorithm called the ptychographic engine. One of the big advantages of Ptychography compared to other CDI techniques is the simplicity of the setup since there is no need for a reference beam, known sample or other additional information. Hoppes solution only aimed to solve the phase problem for small crystals, but J. M. Rodenburg later expanded the theory to include continuous samples using the Wigner-Distribution Deconvolution[14]. Rodenburg was also the first to transfer ptychography from electron microscopy to x-ray imaging[9].

The phase retrieval process uses an iterative algorithm where the object constantly is transformed back and forth between real space and frequency space applying the few known constraints available. The basic algorithm uses a series of measurements and an initial arbitrary distribution of the electron in the sample. Using the initial (and completely wrong) electron distribution the interference pattern cause by the sample to the beam is calculated and the resulting wave front is propagated downstream until it reaches the detector. The wave front is then converted into intensity, but applied diffraction constrains set by the aperture. In order to use the redundant information obtained from making overlapping measurements, the diffraction constraints applied to one pattern is carried on to the next overlapping pattern. Thus providing extra information about the sample and narrowing the amount of possible solutions.

In practical setups more advanced algorithms are used which applies more sophisticated constrains, but the basic iterative constraining loop remains the same. A modern approach to the reconstruction was demonstrated by Martin Dierolf [15] who created the first practical 3D ptychographic measurement using a reconstruction algorithm proposed by P. Thibault.

If there is enough redundancy the reconstruction algorithm will converge at some point. However, although the numbers of required iterations are relatively low (below 300) it still presents a very significantcomputational intensity and it is also the likely reason that ptychography has not been adopted until recently,even if it was being pioneered in the 1970's. The coherence requirement of the beam also limits the techniques to third generation synchrotrons for x-rays.

Because ptychography aims to reconstruct the wave front after the illuminated object, both the change in amplitude and phase is measured. This results in two images where the phase image usually is the better one, with the highest peak signal to noise ratio, for soft materials. Since the phase change in the wavefield is directly related to the electron density without any major uncertainties it easy to quantify the contrast. The resolution of the densities is reported to be within 1% [16].

For X-rays the refractive index of materials, n, is slightly smaller than unity, by an amount $(\delta + i\beta)$. δ is directly related to the refraction, or phase shift, caused by the sample whereas the imaginary part *iβ* is related to X-ray absorption in the material. Absorption, and thus β, is relatively easy to measure and has been the conventional contrast mechanism exploited in X-ray imaging. The real part of the refraction index, δ is however usually about 2 orders of magnitude larger than β and offers a much better contrast mechanism, especially for samples with a low mean atomic number and for X-rays with high energy.

The relation between the material density ρ and δ is straight forward and can be derived by combining the relation between δ and the electron density, $n_e = 2\pi\delta/\lambda^2$[17], with the relation between bulk material density and electron density, $\rho = n_e A/N_A Z$. [17]

$$\rho = \frac{2\pi\delta(\vec{r})A}{\lambda^2 r_0 N_A Z} \tag{1}$$

For organic materials, A/Z ~ ½.

Ptychography is a very well suited technique for imaging soft materials. It provides high contrast which can be quantified and converted into electron densities. Furthermore the sensitivity for density variations is also very high making it well suited for organic materials which are otherwise very difficult to distinguish with other imaging techniques, and the high penetration depth of hard X-rays makes it possible to penetrate samples which would otherwise be opaque to electrons and soft x-rays. The complicated reconstruction process has been automated and can be processed on an average computer. This leaves spatial resolution as the primary focus for improvements, and while very good today it is expected to improve significantly in the near future due to technical improvements in the setups.

Results

The aqueous nanoparticle dispersions were characterized by SAXS. Figure 1 shows the scattering cross sections of the different nanoparticle dispersions together with a line representing Q^{-4} intensity dependence. It has been suggested that the nanoparticles forms core-shell structures, and the PCBM:P3HT 1:1 nanoparticles do indeed exhibit Q^{-3} intensity dependence, as expected for core-shell particles [18].

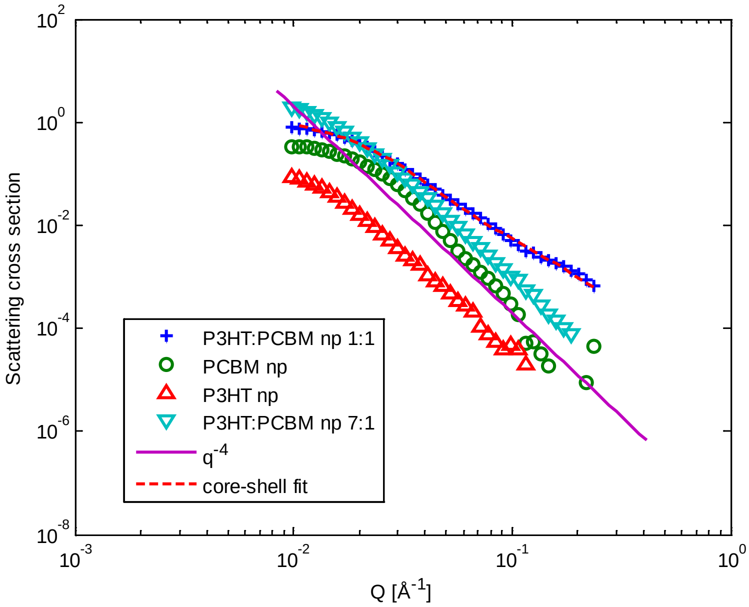

Figur 1: SAXS measurements of the nanoparticle dispersion. Dark blue plus signs: 1:1 P3HT:PCBM, cyan triangles: 7:1 P3HT:PCBM, green circles: PCBM nanoparticles, red triangles: P3HT nanoparticles. The purple line shows a Q^{-4} intensity dependence. The broken red line represents the fit of a polydisperse size distribution of core-shell particles.

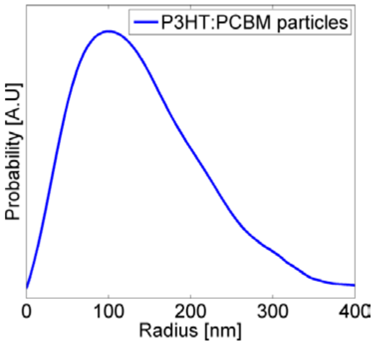

Figur 2: The size distribution of the P3HT:PCBM 1:1 particles measured in dispersion using SAXS. The Size distribution was calculated using BIFT and assuming the particles are spherical. The median particle size is 102 nm.

The size distribution is displayed on figure 2 and was calculated by assuming the particles in solution were spherical. The distribution includes particles from almost 0 nm up to 400 nm in radius with a median radius of 102 nm.

Repeating the experiment with particles made of pure P3HT and pure PCBM only the PCBM particles scattered enough to be distinguished from the water. It is therefore worth noting that the size distribution calculated for the heterogeneous nanoparticles are based on the PCBM domains only.

WAXS and the ordering of P3HT

The particles were also measured with WAXS. It is a well-known phenomenon that when spin coated P3HT will form a semi crystalline structure with their side chains normal to the substrate as well as the chain backbone and the p-faces in the plane of the substrate (edge-on).The WAXS scattering is displayed on Figure 3.

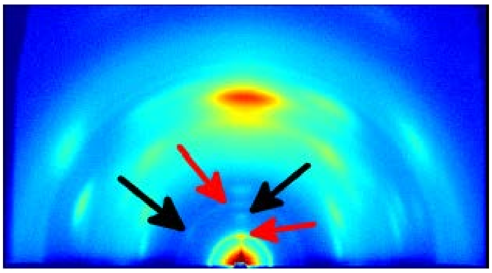

Figur 3 WAXS image of the R2R coated film with the ink. The red arrows mark the 100 and the 200 peaks for P3HT. The black arrows mark 100 and the 010 peaks for PCBM.

One interesting observation was the ordered structure of the P3HT crystals remains in the film from nanoparticles with R2R coating. One would still expect P3HT to form similar semicrystals inside a nanoparticle but since each nanoparticle would be randomly oriented when coated the WAXS scattering from P3HT should be independent of the orientation. However, WAXS measurements from coated nanoparticles shows the same orientation of the P3HT crystals suggesting that the particles are either all aligning themselves in the same direction or that the P3HT somehow interacting.

TEM experiments

Initially one sample with dropcasted nanoparticles and one sample with the same nanoparticles from the active layer in a R2R coated device. Figure 4 shows the dropcasted nanoparticles shortly after being treated by ultrasound and upconcentration. The dropcasted particles are very round and the size distribution corresponds to the previous SAXS measurements. The largest particles are almost 600 nm while the smallest we can resolve are around 30 nm. The R2R coated sample shows a very different structure (figure 5). There are visible particles but the structure does not resemble the dropcasted, but they present a more course surface than the spherical particals from the drop casting. Furthermore they are connected by a gray homogeneous mass of unknown substance, hereby referred to as bulk.

Several steps in the coating process could affect the nanoparticles and it is unknown what causes the morphological change. This could be caused by the addition of FSO while making the ink from, it could be mixing between the ink and the other layers in the cell, it could be the annealing of the cells, the delamination or a combination of them all.

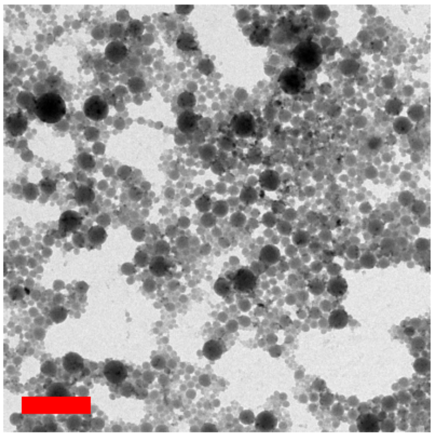

Figure 4: TEM image of the dropcasted particle (scale bar = 1 micron).

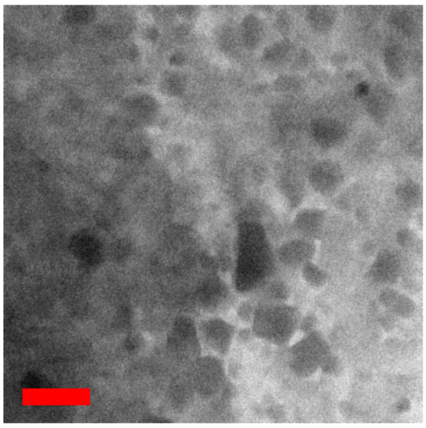

Figure 5: TEM image of the particles from R2R coated device (scale bar = 1 micron).

Annealing

We performed annealing experiments with the nanoparticles in order to see the affect annealing had on the morphology. Using the P3HT:PCBM nanoparticle ink we spin coated 6 samples and annealed them at 140°C in 1, 3, 5, 10 and 15 minutes. The results are shown in Figure 6 and while the morphology looks similar for all of the samples the contrast between the particles and the bulk increases with longer annealing time. Since PCBM, in contrast to P3HT, is known to crystalize into larger and denser structures when annealed we believe the bulk is PCBM free[19]. We therefore believe the bulk is homogenous and not a collection of smaller unresolved particles.

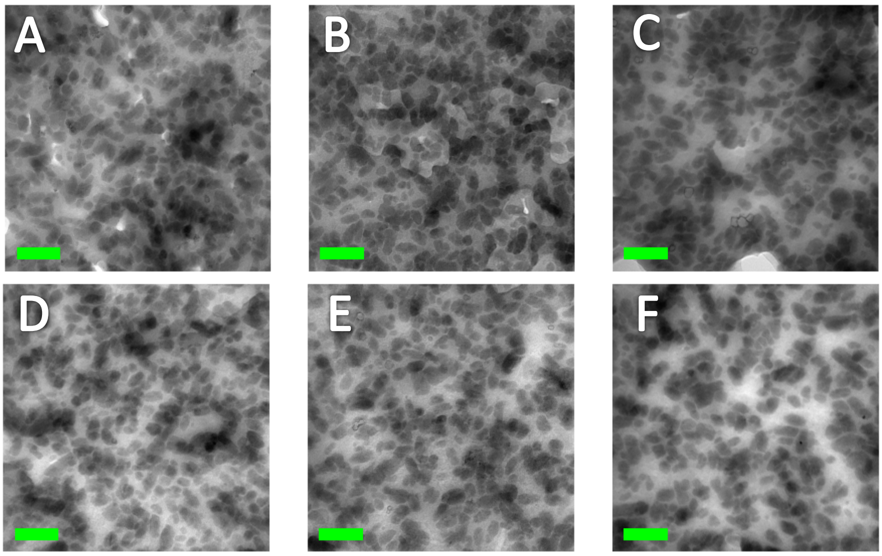

Figure 6: TEM images of P3HT:PCBM particles annealed for different times at 140 C. a) 1 min b) 2 min c) 3 min d) 5 min e) 10 min f) 15 min. There are no obvious physical changes in the morphology (scale bar = 0.3 micron).

Selected Area Electron diffraction (SAED) confirmed that the particles contained a large number of PCBM crystals. The particle packing density on the coated films however was too high in order to get a diffraction image of solely the bulk.

The bulk was initially suspected to be FSO. We measured a new sample using TWEEN80 as a new wetting agent and an additional sample completely without wetting agent. The sample without wetting agent was dropcasted instead of spin coated.

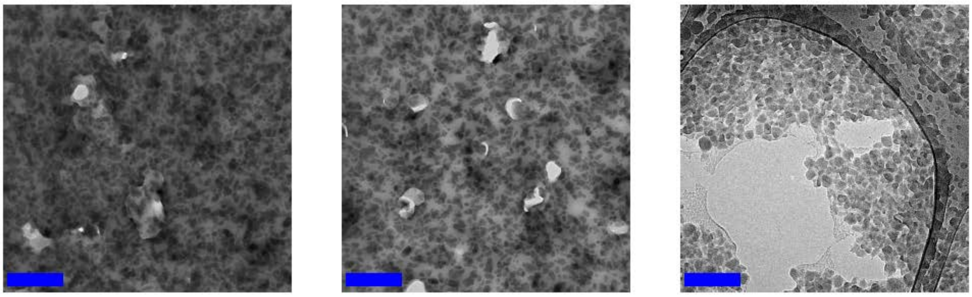

Figure 7: (left) TEM image of P3HT:PCBM nanoparticles, spin coated with FSO-100 as wetting agent. (middle) TEM image of P3HT:PCBM nanoparticles spin coated with TWEEN80 as wetting agent. (right) TEM image P3HT:PCBM nanoparticles dropcasted without any wetting agent (scale bars = 2 micron).

Figure 7 shows films spin coated with either TWEEN80 or FSO as wetting agent (left and middle) compared with a film drop cast without wetting agent. The particles are more densely packed in the drop cast film. Otherwise, the structure of the films appear similar.

STXM images

A 6 * 4 micron STXM overview image of the active layer from a R2R coated device was recorded and is shown in figure 8. We observe the same patterns as with the TEM images were the particles are not spherical but course and in a connecting matrix of the unknown substance. We observe the particles are not as homogeneously distributed as in the spin coated film and here are two large areas without particles while the rest of the active layer is more densely packed compared to the spin coated samples. The particles also seem to aggregate in clusters.

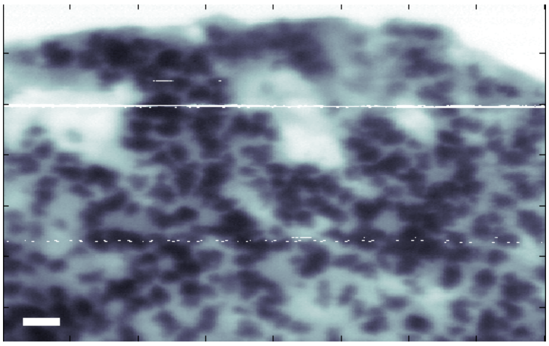

Figure 8: STXM overview of a 6 * 4 micron area of the active layer from a R2R coated device. Scale bar 0.5 µm

NEXAFS

Different chemical compositions are resolved by NEXAFS scans around the carbon edge. The contrast arises because the π* K-edge of P3HT and PCBM are slightly shifted. The carbon absorption edges for both P3HT and PCBM are well defined and located at 285.2 and 284.5 eV respectively[20]. A NEXAFS did show that the particles as expected contained large amounts of PCBM, but the energy resolution is too coarse to determine whether the broad absorption top, peaking at 285 eV is due to the existence of P3HT or just a second π* K-edge of PCBM at 285.7 eV. The surrounding material however is more conclusive and only shows the presence of a narrower absorption peak at 285.4 eV suggesting it must be P3HT and eliminating the possibility of containing significant amounts of PCBM. In addition we

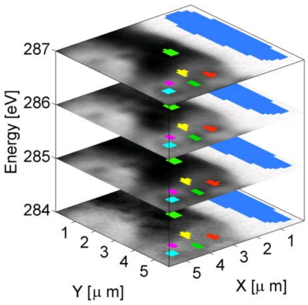

Figure 9: A STXM image of a 5*5 µm^2 region from 282 eV to 287eV. The red, light green and cyan areas are painted on particles. Yellow and Magenta on the bulk. The Dark green is a large dark area. The blue is outside the sample for reference.

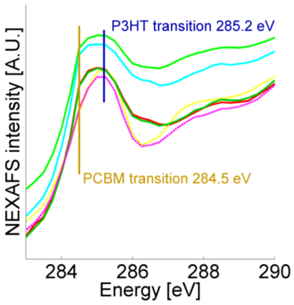

Figure 10: The energy profiles of the areas on figure 9. The yellow and magenta have maximum absorption at the P3HT transition. The others are shifted towards PCBM.

scanned the film at the Na edge at 1072 eV in order to test for the presence of SDS but without any success.

Ptychography

The tomogram was segmented into three parts. The sample made of nanoparticles, the micro capillary containing the sample, and the N_2 filling the void. We selected a volume from each region in order to analyze the densities. While using filtered back projection for reconstruction, the absolute values may be shifted a bit due to the finite amount of angles. By calculating the expected value of N_2 by eq. 1 and for each measurement comparing it to the reconstructed value we applied the difference as a correction to the other densities.

We used the variance from the N_2 as a measure for the experimental broadening. All the peaks can be fitted by a Gaussian distribution function, thus simplifying the deconvolution of the instrument broadening from the sample density distribution. Subtracting the instrument broadening from the sample gives a variance in the density of $3.0*10^{-3}$ e/Å. Comparing the variance to the mean value gives us a resolution in electron densities of around 15%. This number is however artificially high due to the low number of angles and a typical reconstruction will have an energy resolution around 5%.

The electron density of PCBM is roughly 50% higher than P3HT thus providing more than enough contrast to separate the two materials. The variance of the density distribution for the ink and the variance in the density distribution of the N_2 are almost identical suggesting we do not have the spatial resolution to separate the different phases in the ink.

Even with the lack of projections for reconstruction there are clearly visible high density particles inside the tomogram. Calculating the density of the particles gives an electron density of 8.3 e/Å^3 which is close to the density of PCBM and the surroundings have a lower density of 6.3 e/Å^3 which is a bit higher than for P3HT. Figure 11 displays a slice of the tomogram with a piece of active layer inside a microcapillary. The sample contains some very distinct particles and a denser region towards the bottom of the image. The majority, lighter, part of the sample has a density matching the electron density of P3HT. The denser part in the bottom is

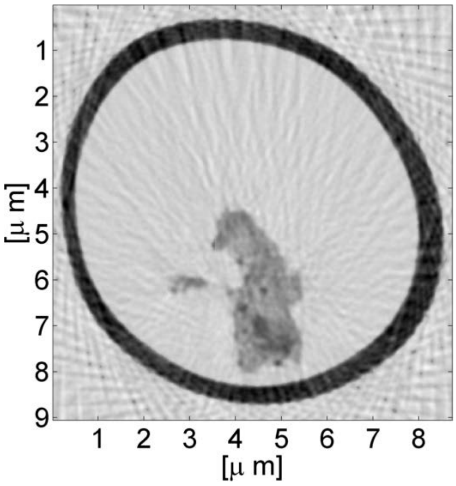

Figure 11: A slice of the tomogram showing the active layer in a microcapillary. The sample contains a few very distinct particles. The bottom half of the sample contains a much denser region

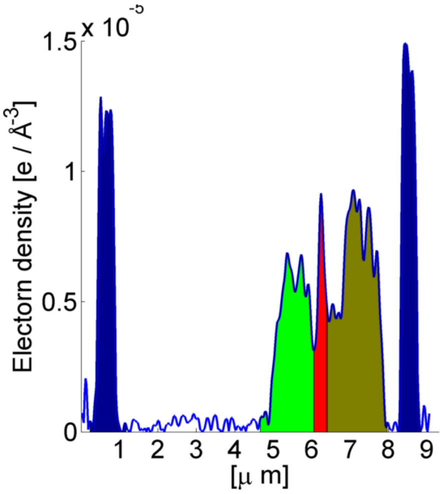

Figure 12: A 1D line through the sample on figure 11. The Dark blue areas are the capillary. The light green area is the lesser dense part of the sample, matching the density of P3HT. The red area is a particle. The brown area is den denser part of the sample.

almost entirely PCBM. Comparing with the STXM images we believe that the dense part in the bottom is an area with a lot of dense packed PCBM particles. The particles we observe are not the only ones but a few particularly large ones which we are able to resolve. The presence of smaller particles which we do not have the spatial resolution to resolve is given by the increase density we measure in the P3HT.

Discussion

Because the method of dialyzing the SDS is the only parameter varying in the preparation method between the batches of nanoparticles we believe this explains the observed difference in morphology. As illustrated on figure 13 we speculate that the slow dialysis of the first batch, B1, caused the hydrolysis to create a more rigid structure, keeping the nanoparticles spherical. In the second batch, B2, the dialysis was carried out using a labscale tff system for SDS-removal. The hydrolysis of the sulfuric groups is dramatically accelerated in acidic environments. Since the dialysis machine used for B2 is much faster and can dialyse the solution in 6-8 hours in contrast to 6-8 days the degree of hydrolysis of the sulfate groups at the surface of the particles higher for the particles that have been dialyzed for longer periods of time. It has been suggested that micelles in solution require chain flexibility for their stability[21].Without the hydrolysis the nano particles will therefore degrade. We believe this is because of the repulsion from the negatively charged sulfate groups which creates a more rigid surface structure, unable to contain the P3HT. The crystalline PCBM part of the particle remains a particle while the P3HT part turns into a bulk film.

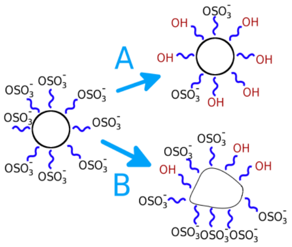

Figure 13: A nanoparticle in a solution being dialyzed. A) A slow dialysis will hydrolyze most of the SDS chains. B) A faster process will leave most SDS chains.

Conclusion & Outlook

The morphology of nanoparticles formed by a miniemulsion is strongly affected by how much of the SDS is hydrolyzed. Unless enough of the SDS hydrolyzes the particles will become irregular grain shaped PCBM particles in a bulk of P3HT. This has been observed using different samples using different techniques each with their own contrast mechanism.

Using both STXM and ptychography we have been able to image the active layer from R2R coated devices. Both techniques showed the same pattern where the particles in R2R coated devices, as opposed to spin coated devices may aggregate into larger clusters and leave some regions with no or very few particles.

Ptychography is also demonstrated as a viable characterization technique for OPV. It has a high contrast mechanism which also allows for quantitative calculations of densities. While the resolution is still inferior to other nanoimaging techniques it is rapidly improving and is expected to be comparable in a few years.

References

[1] M. A. Green, K. Emery, Y. Hishikawa, W. Warta, and E. D. Dunlop, “Solar cell efficiency tables (version 42),” *Prog. Photovoltaics Res. Appl.*, vol. 21, no. 5, pp. 827–837, Aug. 2013.

[2] A. Victor Shah, F. Christian Krebs, A. N. Tiwari, J. Poortmans, A. McEvoy, M. Jørgensen, J. E. Carlé, R. R. Søndergaard, M. Lauritzen, N. A. Dagnæs-Hansen, S. L. Byskov, T. R. Andersen, T. T. Larsen-Olsen, A. P. L. Böttiger, B. Andreasen, L. Fu, L. Zuo, Y. Liu, E. Bundgaard, X. Zhan, H. Chen, and F. C. Krebs, “The state of organic solar cells—A meta analysis,” *Sol. Energy Mater. Sol. Cells*, vol. 119, pp. 84–93, 2013.

[3] J. J. M. Halls, C. A. Walsh, N. C. Greenham, E. A. Marseglia, R. H. Friend, S. C. Moratti, and A. B. Holmes, “Efficient Photodiodes from Interpenetrating Polymer Networks,” *Nature*, vol. 376, no. 6540, pp. 498–500, 1995.

[4] G. Yu and A. J. Heeger, “Charge Separation and Photovoltaic Conversion in Polymer Composites with Internal Donor-Acceptor Heterojunctions,” *J. Appl. Phys.*, vol. 78, no. 7, pp. 4510–4515, Oct. 1995.

[5] T. R. Andersen, T. T. Larsen-Olsen, B. Andreasen, A. P. L. Böttiger, J. E. Carlé, M. Helgesen, E. Bundgaard, K. Norrman, J. W. Andreasen, M. Jørgensen, and F. C. Krebs, “Aqueous processing of low-band-gap polymer solar cells using roll-to-roll methods.,” *ACS Nano*, vol. 5, no. 5, pp. 4188–96, May 2011.

[6] Y. Yoneda, “Anomalous Surface Reflection of X Rays,” *Phys. Rev.*, vol. 131, no. 5, pp. 2010–2013, Sep. 1963.

[7] S. Hansen and J. S. Pedersen, “A comparison of three different methods for analysing small-angle scattering data,” *J. Appl. Crystallogr.*, vol. 24, no. 5, pp. 541–548, Oct. 1991.

[8] K. Giewekemeyer, M. Beckers, T. Gorniak, M. Grunze, T. Salditt, and A. Rosenhahn, “Ptychographic coherent x-ray diffractive imaging in the water window,” *Opt. Express*, vol. 19, no. 2, p. 1037, Jan. 2011.

[9] J. Rodenburg, A. Hurst, A. Cullis, B. Dobson, F. Pfeiffer, O. Bunk, C. David, K. Jefimovs, and I. Johnson, “Hard-X-Ray Lensless Imaging of Extended Objects,” *Phys. Rev. Lett.*, vol. 98, no. 3, Jan. 2007.

[10] P. Kraft, A. Bergamaschi, C. Bronnimann, R. Dinapoli, E. F. Eikenberry, H. Graafsma, B. Henrich, I. Johnson, M. Kobas, A. Mozzanica, C. M. Schleputz, and B. Schmitt, “Characterization and Calibration of PILATUS Detectors,” *IEEE Trans. Nucl. Sci.*, vol. 56, no. 3, pp. 758–764, Jun. 2009.

[11] P. Thibault, M. Dierolf, A. Menzel, O. Bunk, C. David, and F. Pfeiffer, “High-resolution scanning x-ray diffraction microscopy.,” *Science*, vol. 321, no. 5887, pp. 379–82, Jul. 2008.

[12] D. Sayre, *Imaging Processes and Coherence in Physics*. 1980, pp. 229–235.

[13] W. Hoppe, “Beugung im inhomogenen Primärstrahlwellenfeld. I. Prinzip einer Phasenmessung von Elektronenbeungungsinterferenzen,” *Acta Crystallogr. Sect. A*, vol. 25, no. 4, pp. 495–501, Jul. 1969.

[14] J. M. Rodenburg and R. H. T. Bates, “The Theory of Super-Resolution Electron Microscopy Via Wigner-Distribution Deconvolution,” *Philos. Trans. R. Soc. A Math. Phys. Eng. Sci.*, vol. 339, no. 1655, pp. 521–553, Jun. 1992.

[15] M. Dierolf, A. Menzel, P. Thibault, P. Schneider, C. M. Kewish, R. Wepf, O. Bunk, and F. Pfeiffer, “Ptychographic X-ray computed tomography at the nanoscale,” *Nature*, vol. 467, no. 7314, pp. 436–439, Sep. 2010.

[16] A. Diaz, P. Trtik, M. Guizar-Sicairos, A. Menzel, P. Thibault, and O. Bunk, “Quantitative x-ray phase nanotomography,” *Phys. Rev. B*, vol. 85, no. 2, Jan. 2012.

[17] *Elements of Modern X-ray Physics*. .

[18] K. B. Burke, A. J. Stapleton, B. Vaughan, X. Zhou, A. L. D. Kilcoyne, W. J. Belcher, and P. C. Dastoor, “Scanning transmission x-ray microscopy of polymer nanoparticles: probing morphology on sub-10 nm length scales.,” *Nanotechnology*, vol. 22, no. 26, p. 265710, Jul. 2011.

[19] S. Lilliu, T. Agostinelli, E. Pires, M. Hampton, J. Nelson, and J. E. Macdonald, “Dynamics of Crystallization and Disorder during Annealing of P3HT/PCBM Bulk Heterojunctions,” *Macromolecules*, vol. 44, no. 8, pp. 2725–2734, Apr. 2011.

[20] D. S. Germack, C. K. Chan, B. H. Hamadani, L. J. Richter, D. a. Fischer, D. J. Gundlach, and D. M. DeLongchamp, “Substrate-dependent interface composition and charge transport in films for organic photovoltaics,” *Appl. Phys. Lett.*, vol. 94, no. 23, p. 233303, 2009.

[21] C. D. Casson, Brian D and Braun, Rüdiger and Bain, “Phase transitions in monolayers of medium-chain alcohols on water studied by sum-frequency spectroscopy and ellipsometry,” *Faraday Discuss.*, vol. 104, pp. 209–229, 1996.

Polymer Degradation and Stability 97 (2012) 2412–2417

Contents lists available at SciVerse ScienceDirect

Polymer Degradation and Stability

journal homepage: www.elsevier.com/locate/polydegstab

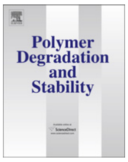

Influence of processing and intrinsic polymer parameters on photochemical stability of polythiophene thin films

Morten V. Madsen, Thomas Tromholt, Arvid Böttiger, Jens W. Andreasen, Kion Norrman, Frederik C. Krebs*

Department of Energy Conversion and Storage, Technical University of Denmark, Frederiksborgvej 399, DK-4000 Roskilde, Denmark

ARTICLE INFO

Article history:
Received 16 May 2012
Received in revised form
15 June 2012
Accepted 10 July 2012
Available online 16 July 2012

Keywords:
P3HT
Photooxidation
Organic photovoltaics
Photo-chemical stability
Degradation

ABSTRACT

Intrinsic polymer parameters such as regio-regularity, molecular weight, and crystallinity play an important role when studying polymer stability. 18 different batches of poly-3-hexyl-thiophene (P3HT) were degraded in a solar simulator (AM1.5G, 1000 W/m^2) and the degradation kinetics were monitored. The results suggest that the radical reaction responsible for the photodegradation takes place at terminal thiophene rings exposed at points were the conjugation is broken. This proposed mechanism is supported by the fact that stability scales with regio-regularity following the ratio of head-to-tail connected thiophene units. Annealing was found to relax the P3HT films and increase conjugation length and, in turn, increase stability observed as a delayed spectral blueshift caused by photochemical degradation. Crystallinity was found to play a minor role in terms of stability. Oxygen diffusion and light shielding effects were shown to have a negligible effect on the photochemical degradation rate. The results obtained in this work advance the understanding of polymer stability and will help improve the design of materials used for polymer solar cells resulting in longer lifetimes, which will push the technology closer to large-scale applications.

1. Introduction

The field of polymer solar cells (PSC) is growing fast, manifested in an exponential increase in publications [1]. The technology has reached a point where focus has shifted to application, demonstration and commercialization. The technology combines low cost, flexibility, and fast processability well-suited for large scale production that, in turn, will constitute a strong alternative to energy production. State-of-the-art in terms of efficiency has been reported to have increased to above 10% for small area laboratory devices [2,3]. Large scale production based on roll-to-roll techniques is now possible and production of 10,000 units has been demonstrated [4]. However, limited lifetime of the devices is still an issue and it is thus crucial to be able to both characterize and understand the different degradation mechanisms responsible for the performance deterioration of PSCs. It is well-known that several aspects affect the final lifetime of the device including stability of the morphology, oxygen, and water diffusion, and polymer photodegradation [5,6]. The exact nature of the degradation mechanisms depends on the specific materials used in the multilayer stack of the solar cell. Consequently, when studying the overall PSC device stability, the actual stability of each layer cannot be deduced. Specifically, the stability of the photo-active layer is highly important since this layer accommodates the free charge carrier generation. Evaluation of the stability of this layer is therefore paramount to overcome the issue of lifetime for PSC. The evaluation of polymer photo-chemical stability using primarily UV–vis spectroscopy is an emerging field as documented by a number of recent reports on comparative studies. Manceau et al. reported a study involving 20 different polymers from which relative stabilities of an extensive range of functional groups were established [7]. In an extensive material screening by Tromholt et al. material stabilities were also resolved in terms of the optical density of the samples [8]. An exponential increase of stability was observed for all materials and it was concluded that identical optical densities are needed when comparing stabilities between different materials.

This paper focuses solely on the intrinsic photo-chemical stability of the well-known conjugated polymer poly-3-hexyl-thiophene (P3HT). Degradation of P3HT is well-documented and can be facilitated by exposure to light and molecular oxygen that destroys the π-conjugation and consequently induces loss of

---

* Corresponding author.
E-mail address: frkr@dtu.dk (F.C. Krebs).

0141-3910/$ – see front matter © 2012 Elsevier Ltd. All rights reserved.
http://dx.doi.org/10.1016/j.polymdegradstab.2012.07.021

absorption. P3HT is degraded under these conditions in solution as well in a solid form (e.g. a film). The consequence of degradation is well-established but the mechanism responsible for it has been subject to discussion. Whereas singlet oxygen is known to be the cause of degradation in solution [9], the degradation mechanism in the solid state is believed to be different. Manceau et al. have proposed a degradation mechanism based on a radical process beginning from an abstraction of an allylic hydrogen, leading to side-chain and sulfur oxidation [10,11]. This process is responsible for breaking the macromolecular backbone resulting in loss of conjugation and consequent bleaching of the sample. This mechanism occurs under both photo- and thermal oxidation enforcing the notion that singlet oxygen is not the main intermediate in the degradation process. Hintz et al. have conjectured that the polymer is mainly attacked at the terminal thiophene rings under photo-oxidation [12]. The authors concluded this from observing the kinetics of the blueshift in the optical absorption. They observed that the blueshift, indicating loss of conjugation (observed for oligomers with less than 20 thiophene units), is not observed until the end of the degradation of the polymer. Hintz et al. have also demonstrated that a strong increase in photon effectiveness is observed for photo-degradation of P3HT films for decreasing irradiation wavelengths [13]. Changing the illumination wavelength from 554 to 335 nm leads to an increase by a factor of 50 in effectiveness of the P3HT photo-oxidation. This observation supports the radical chain mechanism driven by photo-generation of radicals by the photolysis of precursors absorbing in the UV-region.

The absolute stability of polymers is known to be affected by degradation parameters such as light spectrum, room temperature, ozone level, and humidity. Thus, direct comparisons of absolute stabilities assessed with different degradation setups in different laboratories are not straightforward. To reduce influence of different degradation parameters in photo-chemical stability reports, material stabilities are normally expressed in units of stability of a reference material of well-known stability, typically P3HT. However, this assumes that P3HT presents an intrinsic, constant stability that is independent of synthesis routes, regioregularity (RR), molecular weight, molecular weight distribution, crystallinity etc. The overall effect is that the material stabilities expressed in units of P3HT stability as reported in the literature may be associated with significant uncertainty. Furthermore, until now, development of stable conjugated polymers for PSCs has been focused on the stability of the different functional groups used for the synthesis. However, understanding the influence of the above described intrinsic polymer properties on the photo-chemical stability is highly appealing, since this will provide a new set of tools when designing novel materials for PSCs.

In this report we describe the influence of the intrinsic polymer properties on the photo-chemical stability of P3HT. This involves 18 different batches of P3HT from different manufacturers and batches made in house. P3HT polymers with significantly different M_w and RR are studied. The effect of inducing crystallinity by thermal annealing is reported by studying stabilities for different annealing temperatures. Furthermore, the degradation kinetics is studied for films of different thicknesses, which allows for studying the influence of light shielding and oxygen availability in the film.

2. Experimental

2.1. Degradation setup and data evaluation

A fully automated, high-throughput photo-chemical degradation setup was used for the degradation of all materials in this study as described elsewhere [8]. The setup utilized a Steuernagel solar simulator with an Osram 1200 W metal halide arc lamp providing an approximate AM1.5G spectrum with an intensity of 1000 W/m^2. The sample exchanger had a capacity of 22 samples and a UV–vis spectroscopic probe based on an optical fiber-based CCD spectrometer (Avantes AvaSpec 1024) and a halogen/deuterium light source (Avantes AvaLight-DHc) were used to measure the evolution in the absorbance of the samples. For this study, the setup was programmed to monitor 28 degradation points per sample. A fully loaded sample exchanger with 22 samples consequently monitors 616 degradation points in parallel. A C# based automated software infrastructure was established to handle the high number of data files. To avoid spectral shielding from the substrate, illumination was always performed from the polymer side.

Degradation rates were extracted from the rate of decrease of the calculated total number of absorbed photons per second as absorbed by the polymer when the recorded absorption spectrum is folded with a theoretical AM1.5G solar spectrum as described in reference [14]. We observed that plotting the rate of decrease of number of absorbed photons as a function of initial absorption maximum yields a constant value for a broad interval from 0.4 to 1 in absorbance, see Fig. 1. The ordinate axis in this plot is dependent on the choice of integration range and therefore the same integration range (400–600 nm) has been used for all materials. It was thus possible to run a large number of degradation experiments for different polymers and compare their stablities while the effect of thickness was canceled. This behavior has been observed for P3HT, poly[5-methoxy-2-(2-ethyl-hexyloxy)phenylenevinylene] (MEH-PPV), and polythiophene (PT). Normalized degradation rates in all comparisons are given in units of the stability of the polymer designated R1, see Table 1. Consequently, values below 1 describe polymers more stable than R1 and values above 1 describe polymers less stable.

Using degradation rates based on loss of absorbance directly allows for correlating the degradation state to the number of intact monomer units. The number of monomers scales directly with the absorbance, and thus the degradation state can be written as

$$D_{\text{state}} = \frac{N_{\text{Monomer}}}{N_{\text{initial}}} = \frac{A}{A_{\text{initial}}},$$

where N_{initial} is the initial number of monomers, A_{initial} and A are the initial and current absorbance respectively. The number of monomers at a given time during degradation can be expressed by

$$N_{\text{Monomer}} = \frac{N_A \rho}{M} t \cdot D_{\text{state}},$$

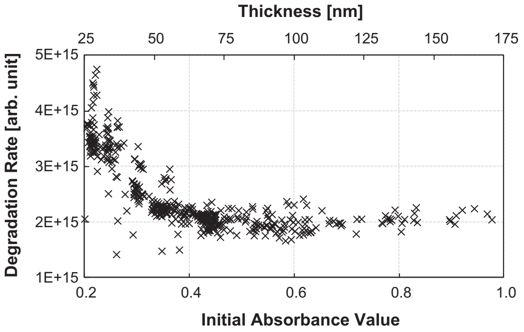

Fig. 1. Rate of change in number of absorbed photons as a function of initial absorbance value and thickness.

Table 1
The 18 different samples of P3HT studied. The manufacturers and their batch numbers have been stated as well as the abbreviations used. The regio-regularity has been determined using ^{1}H NMR. R2 was not measured by NMR as the polymer had been depleted.

Code	Manufacturer	Batch	RR	M_n [kDa]
M1	Merck	EE-97802	94.8%	19.6
M2	Merck	EE-99202	94.0%	23.7
M3	Merck	EE-101702	95.8%	29.6
M4	Merck	EE-99120	93.0%	15.7
R1	Rieke metals	PTL 10-87	91.7%	28.8
R2	Rieke metals	BS19-60A	–	21.6
R3	Rieke metals	BS16-24	92.1%	23.3
B1	BASF	GK-2126-108	96.8%	–
B2	BASF	GK-2566/77	93.7%	–
B3	BASF	2010_A6-7	94.6%	–
P1	Plextronics	11-11822	96.0%	–
P2	Plextronics	P04205	96.0%	34.7
P3	Plextronics	PO2122	91.6%	–
P4	Plextronics	PO4054	95.1%	–
D1	DTU (in house)	McCullough route, chloroform fraction [15]	96.1%	17.3
D2	DTU (in house)	McCullough route, hexane fraction [15]	96.0%	2.8
D3	DTU (in house)	Method B, Soxhlet purified [15]	76.2%	40
D4	DTU (in house)	Method A, Soxhlet purified [15]	76.1%	–

where N_A is Avogadro's number, ρ is the polymer density, M is the molar mass, and t is the film thickness. According to the Lambert–Beer law, the thickness of the film scales with the absorbance. Using the absorption to thickness conversion presented in reference [8] for regio-regular P3HT, the film thickness can be expressed by $t = (A_{\max} - 0.622)\ 188.68$ nm, where $A_{\max}$ is the peak absorbance. The density was determined to be $\rho = 1.07$ g/cm^2 by X-ray reflectometry for polymer R2. The molar mass of the P3HT monomer is $M = 166.3$ g/mol. The reciprocal rate of monomer loss yields the degradation event interval,

$$\tau = \left(\frac{\mathrm{d}N_{\mathrm{Monomer}}}{\mathrm{d}t}\right)^{-1}.$$

2.2. NMR

^{1}H NMR was used to determine the regio-regularity of P3HT in deuterated chloroform solution. For P3HT the regio-regularity is determined as the ratio between the signal at 2.8 ppm, originating from the preferred head-to-tail connected monomers, and the signal at 2.6 ppm being associated with the head-to-head coupled monomers.

2.3. X-ray diffraction

X-ray diffraction was used to quantify the crystallinity of annealed films. The position of the P3HT *100* reflection was determined by a specular scan using a dedicated reflectometry setup, with a rotating Cu anode as source, operating at 50 kV, 200 mA. The X-ray beam is monochromatized ($\lambda = 1.5418$ Å) and collimated by a 1D multilayer optic and the beam is further collimated by incident and diffracted beam slits.

With a point detector positioned at the diffracted beam angle (2θ) for the *100* reflection, rocking scans were recorded by rotating the sample from incidence angle zero to 2θ. The integrated intensity, less background, was used as a measure of the polymer crystallinity.

2.4. Materials

P3HT films were spin-coated on microscopy slides obtained from Menzel from 12 mg/mL chlorobenzene solutions. 18 different batches of P3HT from different manufactures as well as in-house manufactured batches were studied. For each batch the manufacturer, the batch number and an abbreviation have been indicated in Table 1. The regio-regularity was measured by ^{1}H NMR.

3. Results and discussion

Fig. 2 shows the relative stabilities expressed as normalized rate of degradation of the 18 different polymers in units of R1, evaluated as described in the experimental section. The polymers are grouped according to manufacturer; D is DTU in-house synthesized batches of P3HT, M are commercial P3HT polymers from Merck, R from Rieke Metals, B from BASF, and P from Plextronics. The complete list of polymers is shown in Table 1. The polymers D3 and D4 are regio-random P3HT polymers, while the rest are regio-regular to different degrees. While all regio-regular P3HT polymers exhibit relative degradation rates close to 1, the regio-random polymers are significantly less stable exceeding relative degradation rates of 2. This is consistent with the work by Hintz et al. where an increase in degradation rate by a factor of five was observed, in fair agreement with the factor of three observed on average in this work [13].

While the regio-regularity clearly affects the stability of the polymer, the molecular weight seems to have no significant effect in agreement with Dupuis et al. [16] When comparing the polymer D2 that has a particularly low molecular weight ($M_n = 2.8$ kDa), with the polymer D1 that has a significantly higher molecular weight ($M_n = 17.3$ kDa) it is clearly evident that both polymers have similar regio-regularities close to 96% and clearly have identical degradation rates (Fig. 2) if the error bars are considered. This suggests that molecular weight has either no or a negligible influence on the degradation rate. Indeed plotting the normalized degradation rate against the number average molecular weight (not shown) reveals that no correlation is present. It can thus be concluded that the length of the polymer chain is much less important than the conjugation length. However, for very low molecular weights this is probably not true, but is at least valid for polymers with M_n above 2.8 kDa as shown in this work. It therefore seems that the regio-regularity is the major dominating factor on the stability of the polymer. Dupuis et al. have reported that regio-regularity is the crucial parameter that controls the photo stability and reported a linearity between degradation rate and regio-regularity in the range from 93% regio-regularity to 98% [16].

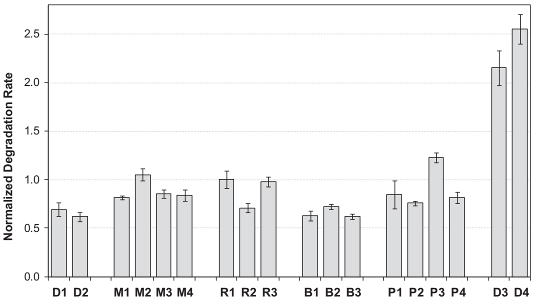

Fig. 2. Degradation rates normalized to the value of R1. For each polymer a minimum of three samples with 28 sample points each, were monitored for the full degradation. The error bars indicate the standard deviation.

Reaction kinetics are indicative of the underlying reaction mechanism determining the rate constants. Fig. 3 shows the degradation event interval for selected polymers ranging from a regio-random (D4) to three different degrees of increasing regio-regularity. It is evident that all four polymers follow strict 0th order kinetics for the first 70% of the degradation as the interval is constant. Furthermore, the degradation event interval is observed to increase with regio-regularity. The timescales of photolysis in the absence of oxygen are many orders of magnitude slower than photo-oxidative degradation [17]. Likewise, thermolysis at moderate temperatures (<400 K) is negligible [11]. Both contributions can therefore be neglected in the analysis of the degradation kinetics. The degradation kinetics of the initial part of the degradation is expected to be 0th order assuming that only terminal thiophene rings are attacked during the photo-oxidation. Preferential surface degradation could possibly explain the 0th order kinetics. However, this possibility can be excluded based on the blue-shift dynamics of the polymers, see Fig. 3. Observing the regio-regular B1 it is evident that no significant blueshift occurs in the initial parts of the degradation process. This would not be the case if the top layer was preferentially degraded. The hypothesis is that if only terminal thiophene rings are attacked, there should not be a significant blueshift of the spectrum in the initial part of the degradation process. Fig. 3 confirms that B1 (RR = 96.8%) only exhibits a limited blueshift for the initial 80% of the degradation process. For the regio-random D4 (RR = 76.1%) a strong blueshift is observed during the entire degradation process. R1 (RR = 91.7%) and P3 (RR = 91.6) show stronger blueshift compared to B1. The strong blueshift observed for regio-random P3HT is ascribed to the shorter initial conjugation length of the chain like morphology in the regio-random polymer. Fig. 3 shows that the initial peak position for the regio-random D4 at ~490 nm is close to the value at which the regio-regular polymers initiate their quick peak shift, indicating that the conjugation length of D4 is sufficiently short at the initial stage that every monomer contributes strongly to the size of the bandgab and each monomer loss is thus associated with a peak shift. The observation suggests that breaking the regularity induces attack points for the radical reaction, implying that a regio-random polymer is more susceptible to photo-degradation. If true, the stability of the polymer must scale with regio-regularity.

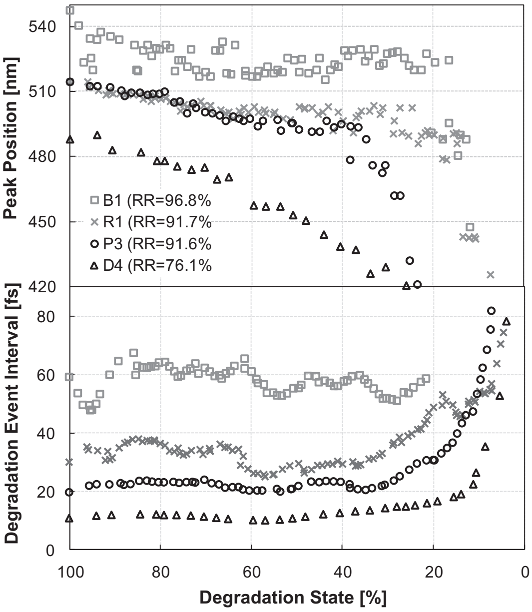

Fig. 3. (Top) Absorption peak position as a function of degradation state. (Bottom) Degradation event interval plotted against degradation state. All data is based on polymer films of 140 nm thickness.

Assuming that each breach of regularity introduces two new attack points, it is possible to model the degradation rate as a function of regio-regularity. The relative number of attack points can then be written as

$$N_{\mathrm{ap}} = \frac{2(1-\mathrm{RR}_x)}{2(1-\mathrm{RR}_{\mathrm{R1}})},$$

where N_{ap} is the number of attack points relative to R1, RR_x is the regio-regularity of the specific polymer, and $\mathrm{RR}_{\mathrm{R1}}$ is the regio-regularity of R1. Fig. 4 shows a plot of the normalized degradation rate as a function of regio-regularity and relative number of attack points. The degradation rate appears to scale with regio-regularity by a linear relationship between regio-regularity and polymer stability. The dotted line in the graph is the theoretical value of degradation rate, calculated from the degradation rate of R1. It is evident that the simple model is capable of explaining the behavior in a convincing manner, suggesting that each breach of regularity induces new attack points that weaken the system. The conjugation length is proportional to the regio-regularity since the conjugation breaks when the polymer is not planar and the π electrons are not in the same plane.

Besides the difference in ratio of head-to-tail connected thiophene units, regio-random and regio-regular P3HT films differ in a more distinct manner. Regio-regular P3HT has been reported to exhibit vanishing intersystem crossing and thereby low triplet yield in contrast to regio-random P3HT [18]. Triplet states are more photochemically active due to their longer lifetime and therefore have been proposed as the cause for the increased degradation rate [13]. It was further implied that the fragmentation of the conjugated π-system in regio-random P3HT takes place on a random basis, while for regio-regular P3HT, terminal thiophene rings are attacked. The results presented in this work, however, demonstrate a strict 0th order degradation rate for both regio-random batches,

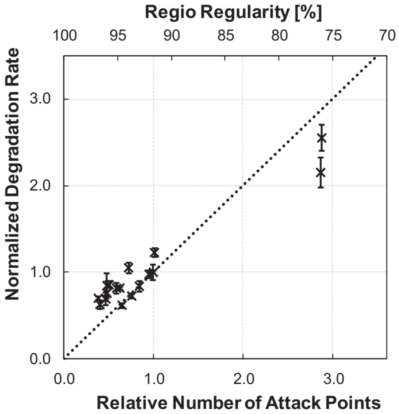

Fig. 4. Normalized degradation rate plotted against the calculated relative conjugation length/regio-regularity. The dotted line represents the predicted degradation rate.

enforcing the notion that only terminal thiophene rings at points of broken conjugation are attacked. The increase in degradation rate can be explained by an increase in attack points resulting from the lower regularity and the blueshift dynamics is explained by the change in initial conjugation length.

Dupuis et al. offered an alternative explanation suggesting that difference in degradation rate is related to the fact that oxygen can diffuse more readily through the amorphous zones and is not soluble in the crystal domains amorphous phase of semicrystalline polymers, or at the interface amorphous/crystalline phase [16]. Regio-regular P3HT films crystallizes more readily, whereas a regio-random film maintains a more chain like morphology. Fig. 5 shows a plot of the degradation rate superimposed on the reciprocal crystallinity as measured by X-ray diffraction for the regio-regular polymer R2. As is evident from Fig. 5 annealing at 120 °C and 140 °C for one hour was found to induce relative degradation rates of 0.75 and 0.68, respectively, relative to the pristine sample. This indicates that the crystallinity of the sample has affected the stability. While an increase in crystallinity is obtained for regio-regular P3HT, annealing is not expected to increase the crystallinity of regio-random P3HT significantly. Indeed, when the regio-random D4 was annealed, no diffraction peaks were observed in the X-ray diffractogram (not shown). This is also consistent with a glass transition temperature of −3 °C reported for regio-random P3HT, indicating that the polymer is indeed amorphous [19]. However, comparable relative stabilizations were observed relative to the regio-regular R2, see Fig. 5. Considering that the degradation rate has been shown to scale with the number of kinks in the polymer, it is hypothesized that the main contribution of the annealing step is the relaxation of the polymer leading to an increased conjugation length. Consequently, thermal annealing of P3HT is favorable to the photo-chemical stability. During spin coating the polymers are frozen in a morphology that is not necessarily the lowest energy state. Annealing the films generally relaxes the films, i.e. the chains are stretched and high-energy kinks are avoided. If the annealing effect can be ascribed to an increased conjugation length, a difference in the degradation kinetics as observed in Fig. 3 for regio-regularity is expected. This was indeed observed when the regio-regular R1 batch was studied by comparing the pristine polymer to films annealed for two hours at 80 °C and 120 °C. The samples were allowed to cool at a slow rate for 48 h prior to the degradation experiment. Based on 200 degradation points for each sample type, the degradation state for which the absorption peak reaches 480 nm was 20.85, 18.85, and 17.5% for the pristine, 80 °C and 120 °C annealed samples, respectively. Consequently, annealing the polymer introduces the same delay of the blueshift as observed for higher regio-regular samples. This is in accordance with the hypothesis that the relaxation of the film to a lower energy state increases the conjugation length, which in turn increases film stability.

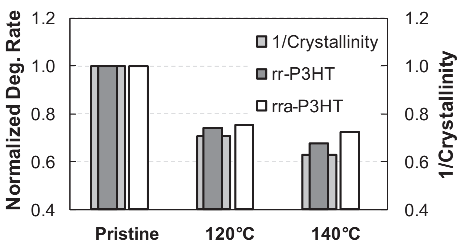

Fig. 5. (Left scale) Degradation rate of (dark grey) regio-regular and (white) regio-random P3HT normalized to their respective pristine degradation rates. (Right scale) Reciprocal crystallinity as deduced from X-ray diffraction studies.

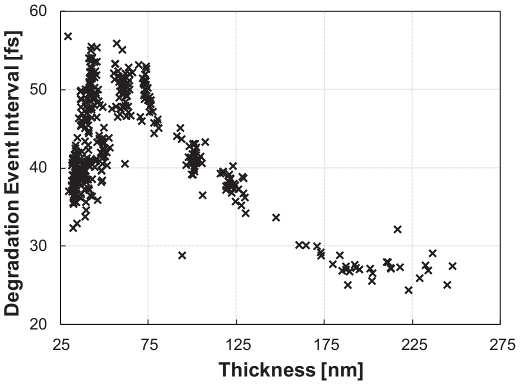

Fig. 6. Degradation event interval plotted against the thickness of a film of R1 polymer.

As a final validation of the hypothesis, the stabilization of the amorphous polymer poly (2-methoxy-5-(2′-ethyl)hexoxy-phenylenevinylene) (MEH-PPV) was assessed as a function of annealing temperature (not shown). For this polymer, stabilization by a factor of 3.5 was observed. The strong stabilization of the MEH-PPV film supports the hypothesis that the relaxation of the polymer is the main contributing factor in the stabilization.

3.1. Effect of thickness on degradation kinetics

Studying films of different thicknesses gives insight into oxygen availability in the film and effects of light shielding. Assuming that oxygen diffusion is not limited and that light shielding from the top layer of the film is insignificant, the concentration of oxidized thiophene rings is independent of film thickness. No significant spatial reaction gradient is observed in the top 10 nm of a degraded P3HT film, as deduced from angle dependent X-ray photoelectron spectroscopy measurements [12]. This suggests that there is no shielding effect in at least the top layer of the film. Fig. 6 shows a plot of degradation event interval against film thickness. It is clear from Fig. 6 that a peak is observed around 60 nm. Thin films (below 60 nm) are less stable and very sensitive to changes in film thickness (i.e. steep slope in Fig. 6). Thicker films are also less stable manifested in decreasing intervals between degradation events for increasing film thickness, which is close to being a linear

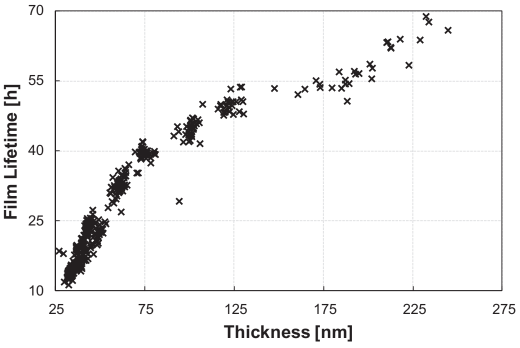

Fig. 7. The film lifetime as calculated from the time between degradation events and the initial number of monomers. Thereby the film lifetime is extrapolated from the initial 50% of the degradation.

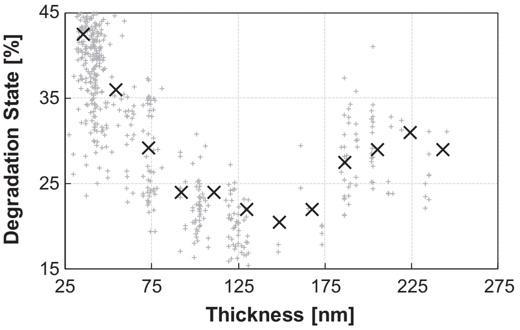

Fig. 8. Wavelength shift observed for different thicknesses of P3HT films. The black crosses represent data bins of a width of 40 nm.

correlation between 75 and 175 nm. The decrease in the time between degradation events for thicker films is expected since the thicker film contains a higher number of monomers, and thus more reaction sites. Fig. 7 shows the film lifetime plotted against thickness, and it is evident that in the range 125–175 nm the film lifetime is constant. The plot is constructed by multiplying the event interval by the initial number of monomers. The existence of a constant lifetime region implies that the degradation takes place in parallel for the entire depth of the film. This means that for this region light shielding is negligible and oxygen is equally available for all depths in accordance with the findings of Hintz et al. [13] For films thicker than 175 nm, either light shielding or lack of oxygen sets the bottom part of the film apart from rest of the film with a lower degradation rate. The event interval is therefore observed to stabilize in this region.

In Fig. 8 the degradation state at which the blueshift reaches 480 nm is plotted. For films in the stable region of 125–175 nm, the blueshift occurs late near the last 20% of the degradation. For films thicker than 175 nm the blueshift appears earlier. This is consistent with the fact that parts of the film degrade later than the top part of the film, thereby extending the degradation. A key point of Fig. 8 is the fact that thin films ($<$75 nm) blueshift rather quickly. This indicates that another mechanism is involved. Ozone has been shown to cause 1st order degradation kinetics and to attack the polymer at random sites [12]. It is conceivable that the relatively high ozone content of the laboratory environment affects the degradation for thin films. This would explain the decrease in degradation interval seen in Fig. 6 and also the strong blueshift in Fig. 8. However, the kinetics of the degradation remained 0th order. Another likely candidate for the increase in reaction rate is the higher surface to volume ratio. If the reactions are more likely on the surface the rate may easily be different. The polymers in the top layer can be expected to have a higher density of kinks, introducing more attack points for the reaction. This would also explain the fast blueshift observed for thin films.

4. Conclusion

18 different batches of P3HT were degraded under simulated sunlight (AM1.5G, 1000 W/m^2) and the respective stabilities were evaluated from the decrease in optical absorption. A highly automated setup allowed for monitoring hundreds of degradation points in parallel to allow for statistically sound investigations of degradation kinetics. It was shown to be evident that the polymer degradation follows strict 0th order degradation kinetics for the initial part of degradation. The typical blueshift of the absorption peak observed during degradation was found to appear later for the more regio-regular films. This indicates that the radical reaction responsible for the photo-degradation attacks terminal thiophene rings exposed at points where the conjugation is broken. Stability was found to increase with regio-regularity following the ratio of head-to-tail connected thiophene units, demonstrating that the polymer is indeed attacked at points of broken conjugation. Annealing relaxes the films and increases conjugation length. This, in turn, increases stability and delays spectral blueshift. For films of different thicknesses, the interval between degradation events is observed to scale linearly with the initial number of thiophene rings for medium thick films (75–175 nm) indicating that oxygen diffusion and light shielding effects have negligible or no effect for medium thickness films.

Acknowledgments

This work was supported by the Danish Strategic Research Council (2104-07-0022), EUDP (j. no. 64009-0050) and PVERA-NET (project acronym POLYSTAR).

References

[1] Jørgensen M, Norrman K, Gevorgyan SA, Tromholt T, Andreasen B, Krebs FC. Stability of polymer solar cells. Adv Mater 2012;24:580–612.

[2] UCLA. UCLA engineers create tandem polymer solar cells that set record for energy-conversion, http://newsroom.ucla.edu/portal/ucla/ucla-engineers-create-tandem-polymer-228468.aspx [accessed 05.05.12].

[3] Heliatek. Heliatek sets new record efficiency of 10.7% for its organic tandem cell, http://www.heliatek.com/?p=1923&lang=en [accessed 05.05.12].

[4] Krebs FC, Fyenbo J, Tanenbaum DM, Gevorgyan SA, Andriessen R, van Remoortere B, et al. The OE-A OPV demonstrator anno domini 2011. Energy Environ Sci 2011;4:4116–23.

[5] Jørgensen M, Norrman K, Krebs FC. Stability/degradation of polymer solar cells. Sol Energy Mater Sol Cells 2008;92:686–714.

[6] Norrman K, Madsen MV, Gevorgyan SA, Krebs FC. Degradation patterns in water and oxygen of an inverted polymer solar cell. J Am Chem Soc 2010;132:16883–92.

[7] Manceau M, Bundgaard E, Carlé JE, Hagemann O, Helgesen M, Roar S, et al. Photochemical stability of π-conjugated polymers for polymer solar cells a rule of thumb. J Mater Chem 2011;21:4132–41.

[8] Tromholt T, Madsen MV, Carlé JE, Helgesen M, Krebs FC. Photochemical stability of conjugated polymers, electron acceptors and blends for polymer solar cells resolved in terms of film thickness and absorbance. J Mater Chem 2012;22:7592–601.

[9] Koch M, Nicolaescu R, Kamat PV. Photodegradation of polythiophene-based polymers?: excited state properties and radical. J Phys Chem C 2009;113:11507–13.

[10] Manceau M, Rivaton A, Gardette J-L. Involvement of singlet oxygen in the solid-state photochemistry of P3HT. Macromol Rapid Commun 2008;29:1823–7.

[11] Manceau M, Rivaton A, Gardette J-L, Guillerez S, Lemaître N. The mechanism of photo- and thermooxidation of poly(3-hexylthiophene) (P3HT) reconsidered. Polym Degrad Stab 2009;94:898–907.

[12] Hintz H, Egelhaaf HJ, Peisert H, Chassé T. Photo-oxidation and ozonization of poly(3-hexylthiophene) thin films as studied by UV/VIS and photoelectron spectroscopy. Polym Degrad Stab 2010;95:818–25.

[13] Hintz H, Egelhaaf HJ, Lüer L, Hauch J, Peisert H, Chassé T. Photodegradation of P3HT–a systematic study of environmental factors. Chem Mater 2010;23:145–54.

[14] Tromholt T, Manceau M, Helgesen M, Carlé JE, Krebs FC. Degradation of semiconducting polymers by concentrated sunlight. Sol Energy Mater Sol Cells 2010;95:1308–14.

[15] Krebs FC. Polymer photovoltaics a practical approach. SPIE; 2008.

[16] Dupuis A, Wong-Wah-Chung P, Rivaton A, Gardette J-L. Influence of the microstructure on the photooxidative degradation of poly(3-heaxylthiophene). Polym Degrad Stab 2012;97:366–74.

[17] Manceau M, Chambon S, Rivaton A, Gardette J-L, Guillerez S, Lemaître N. Effects of long-term UV–visible light irradiation in the absence of oxygen on P3HT and P3HT: PCBM blend. Sol Energy Mater Sol Cells 2010;94:1572–7.

[18] Korovyanko O, Österbacka R, Jiang X, Vardeny Z, Janssen R. Photoexcitation dynamics in regioregular and regiorandom polythiophene films. Phys Rev B Condens Matter 2001;64:235122 (1–6).

[19] Hugger S, Thomann R, Heinzel T, T.-A. T. Semicrystalline morphology in thin films of poly(3-hexylthiophene). Colloid Polym Sci 2004;282:932–8.

Solar Energy Materials & Solar Cells 97 (2012) 22–27

Contents lists available at SciVerse ScienceDirect

Solar Energy Materials & Solar Cells

journal homepage: www.elsevier.com/locate/solmat

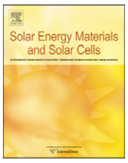

Simultaneous multilayer formation of the polymer solar cell stack using roll-to-roll double slot-die coating from water

Thue T. Larsen-Olsen, Birgitta Andreasen, Thomas R. Andersen, Arvid P.L. Böttiger, Eva Bundgaard, Kion Norrman, Jens W. Andreasen, Mikkel Jørgensen, Frederik C. Krebs*

Risø National Laboratory for Sustainable Energy, Technical University of Denmark, Frederiksborgvej 399, DK-4000 Roskilde, Denmark

ARTICLE INFO

Available online 23 September 2011

Keywords:
Double slot-die coating
Organic solar cells
Roll-to-roll coating polymer solar cells
Simultaneous multilayer formation
Slot-die coating

ABSTRACT

Double slot-die coating using aqueous inks was employed for the simultaneous coating of the active layer and the hole transport layer (HTL) in fully roll-to-roll (R2R) processed polymer solar cells. The double layer film was coated directly onto an electron transport layer (ETL) comprising doped zinc oxide that was processed by single slot-die coating from water. The active layer comprised poly-3-hexylthiophene:Phenyl-C_{61}-butyric acid methyl ester (P3HT:PCBM) as a dispersion of nanoparticles with a radius of 46 nm in water characterized using small-angle X-ray scattering (SAXS), transmission electron microscopy (TEM), and atomic force microscopy (AFM). The HTL was a dispersion of poly(3,4-ethylenedioxythiophene) poly(styrenesulfonate) (PEDOT:PSS) in water. The films were analyzed using time-of-flight secondary ion mass spectrometry (TOF-SIMS) as chemical probe and X-ray reflectometry as physical probe, confirming the identity of the layered structure. The devices were completed with a back electrode of either Cu tape or evaporated Ag. Under standard solar spectrum irradiation (AM1.5G), current–voltage characterization (J–V) yielded an open-circuit voltage (V_{oc}), short-circuit current (J_{sc}), fill factor (*FF*), and power conversion efficiency (*PCE*) of 0.24 V, 0.5 mA cm^{-2}, 25%, and 0.03%, respectively, for the best double slot-die coated cell. A single slot-die coated cell using the same aqueous inks and device architecture yielded a V_{oc}, J_{sc}, *FF*, and *PCE* of 0.45 V, 1.95 mA cm^{-2}, 33.1%, and 0.29%, respectively.

1. Introduction

Flexible polymer solar cells can be manufactured by roll-to-roll (R2R) processes, which are inherently faster than batch processing of solar cells [1]. The manufacture of polymer solar cells using R2R processing has been reported demonstrating high speed of manufacture even on a small scale [2–4]. Thus, polymer solar cell modules with the size of an A4 sheet of paper have total processing times in the range of one minute (45–90 s) [3]. This period of time is from the moment the fresh carrier substrate enters the process until the completed, encapsulated, and tested polymer solar cell module exits the process as a finished product. It is impossible to envisage such throughput speeds with any process that handles the solar cell as a discrete unit. The above example employed relatively simple R2R processing equipment and low web speeds in the range of 0.3–2 m min^{-1} processing one layer at a time by subsequent single passes through the machinery. In order to improve throughput speed there are a few routes, which can be followed. One obvious route is to increase the processing speed, which puts significant requirements on the drying equipment. The faster the web speed, the larger and more complex the ovens and driers become. Another option is to make an inline printing and coating machine where the same web passes through several printing stations with each station representing each layer in the solar cell stack. This method has the advantage of minimizing handling damage of the web. The method does put some constraints on the chosen printing and coating methods as they all have to operate in the same window of web speed and the final web speed will be determined by the slowest process. A final route is the simultaneous formation of several layers of the solar cells stack. This method is in many ways ideal as it lowers the number of passages through the processing equipment thus lowering the handling damage, increases the processing speed significantly without increasing the web speed and thus does not necessarily require more complex drying technology. In addition, there are advantages in the context of life cycle analysis and the method provides a path to a reduction of the energy payback time (EPBT) by significantly reducing the direct process energy involved in the manufacture [5]. The approach also introduces a massive challenge in

---

* Corresponding author. Tel.: +45 46 77 47 99.
E-mail address: frkr@risoe.dtu.dk (F.C. Krebs).

0927-0248/$ - see front matter © 2011 Elsevier B.V. All rights reserved.
doi:10.1016/j.solmat.2011.08.026

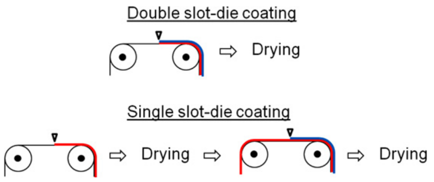

Fig. 1. Illustration of the double slot-die coating of the active layer (red) and the HTL (blue) in a R2R process, compared to the equivalent process using single slot-die coating. (For interpretation of the references to color in this figure legend, the reader is referred to the web version of this article).

the ink formulation for the layers that are coated simultaneously as the formation and drying of a wet multilayer film is highly complex. The successful application of the technique is however rewarding in terms of processing speed and simplicity, see Fig. 1.

In this work we demonstrate the simultaneous formation of two of the layers in the polymer solar cell stack by double slot-die coating of the active layer and the hole transporting layer (HTL) from aqueous dispersions. We describe the ink formulation and the required steps to efficiently design inks that give stable bilayer structures in the wet film and during drying.

2. Experimental

2.1. Materials

P3HT (Sepiolid P-200 from BASF) was employed as the donor polymer and technical grade PCBM was employed as the acceptor material (Solenne BV). An aqueous precursor solution for the ZnO was prepared as described earlier [6] and comprised $Zn(OAc)_2.2H_2O$ (100 mg mL^{-1}), $Al(OH)(OAc)_2$ (2 mg mL^{-1}), and the non- ionic fluorosurfactant (FSO-100) (2 mg mL^{-1}) in water. PEDOT:PSS was based on an aqueous dispersion (2:1 w/w) of Orgacon EL-P 5010 from Agfa that was used directly as received. The electrode material was either Cu tape or evaporated silver. The substrate was a 130 μm poly(ethylene terephthalate) (PET) substrate with a patterned ITO layer (nominally 60 Ω square^{-1}) (acquired from IST).

2.2. Nanoparticle preparation and ink

P3HT (4 g, Sepiolid P200, BASF) and PCBM (4 g, 99%, Solenne B.V.) were dissolved in chloroform (268 g, Spectrophotometric grade, Sigma-Aldrich) and mixed with an aqueous 100 mM sodium dodecyl sulfate (SDS) solution (480 mL) (99%, Sigma-Aldrich) in a large beaker. The mixture was stirred vigorously for one hour and then subjected to ultrasound (0.9 kW) for 6.5 min using an UIP 1000 hd transducer from Hielscher ultrasound technology fitted with a booster head. The mixture was then stirred on a hot plate at 65 °C for three hours until all the chloroform had evaporated. The aqueous dispersion was dialyzed to remove SDS using a Millipore system with a capacity of 500 mL. The mixture was concentrated by dialysis from a volume of 500 mL to a volume of 100 mL with a forward pressure of 1.4 bar and a pressure gradient across the filter of 0.7 bar. Pure water (400 mL) was then added and the procedure was repeated 4 times corresponding to a dilution of the solution by a factor of 625. In the final step the suspension were concentrated to have a solid content of 60 mg mL^{-1}. FSO-100 was added to the dialyzed aqueous suspension of the P3HT:PCBM nanoparticles. The concentration of fluorosurfactant was 5 mg mL^{-1} and the P3HT:PCBM concentration was 60 mg mL^{-1}. This solution was employed directly for slot-die coating.

2.3. TOF-SIMS

Depth profiling analysis was performed using a TOF-SIMS IV (ION-TOF GmbH, Münster, Germany). 25-ns pulses of 25-keV Bi^+ (primary ions) were bunched to form ion packets with a nominal temporal extent of <0.9 ns at a repetition rate of 10 kHz yielding a target current of 1 pA. Depth profiling was performed using an analysis area of $100 \times 100\ \mu m^2$ and a sputter area of $300 \times 300\ \mu m^2$. 30 nA of 3-keV Xe^+ was used as sputter ions. Electron bombardment (20 eV) was used to minimize charge build-up at the surface. Desorbed secondary ions were accelerated to 2 keV, mass analyzed in the flight tube, and post-accelerated to 10 keV before detection.

2.4. SAXS

The X-ray source for the SAXS measurements was a Cu rotating anode (Rigaku H3R), collimated and monochromatized by 2D multilayer optics (K_α radiation, $\lambda = 1.5418$ Å). The anode was operated in fine focus mode at 46 kV/46 mA and the beam diameter was collimated by 3 pinholes to 1.0 mm diameter at the sample position. An 18×18 cm^2 2D position sensitive gas detector was used for collecting the scattering data, and a 4 mm beamstop was placed in front of the gas detector, situated 4579 mm from the sample.

2.5. Reflectrometry

The reflectrometry measurement was made on setup with a rotating Cu-anode (Rigaku RU-200) operated at 50 kV/200 mA as X-ray source, focused and monochromatized by a 1D multilayer optic (K_α radiation, $\lambda = 1.5418$ Å).

2.6. AFM

The P3HT:PCBM nanoparticle dispersion was spin-coated on a glass substrate. The AFM imaging was performed on an N8 Neos (Bruker Nano GmbH, Herzogenrath, Germany) operating in an intermittent contact mode using PPP-NCLR cantilevers (NANOSENSORS, Neuchatel, Switzerland). The images were recorded at a scan speed of 0.8 lines s^{-1}.

2.7. Substrate preparation

A PET substrate with an ITO pattern was prepared and cleaned as described earlier [2]. The ZnO solution was microfiltered immediately prior to use (filter pore size of 0.45 μm) and then slot-die coated at a speed of 2 m min^{-1} with a wet thickness of 4.9 μm. After the initial drying of the precursor film it was converted into an insoluble film by passage through an oven at a temperature of 140 °C with a speed of 0.2 m min^{-1} (oven length=4 m). This gave an insoluble doped zinc oxide film with a thickness of 25 ± 5 nm.

2.8. Double slot-die coating

The web was forwarded at a speed of 1 m min^{-1} when the aqueous P3HT:PCBM nanoparticle dispersion was pumped into the first chamber of a double slot-die coating head. The aqueous PEDOT:PSS dispersion was pumped into the second chamber of the double slot-die coating head. The double film was then slot-die coated at a nominal wet thickness of 23 μm for both the P3HT:PCBM film and the PEDOT:PSS dispersion. The slot-die coating head and the coating roller had temperatures of 60 °C and 80 °C, respectively. The temperature of the foil was kept at

80 °C until it reached the oven at 140 °C. The distance from the point of coating to the oven entry was 18 cm.

2.9. Device characterization

The devices were placed under simulated sunlight in a solar simulator with the following specifications: 1000 W m^{-2}, AM1.5G, 85 ± 2 °C, and 45 ± 5% relative humidity. The J–V curves were measured here were carried out at 85 °C by scanning both forwards and backwards in steps of 20 mV ensuring that no hysteresis was present. The scanning speed was 0.1 V s^{-1}.

3. Results and discussion

The simultaneous multilayer formation by roll coating methods has been achieved with only a few techniques such as curtain coating, slide coating, and slot-die coating [1]. The two former are only operational in the very high speed regime (typically >4 m s^{-1}) and require relatively viscous solutions. In return, they offer the simultaneous formation of many layers. Slot-die coating has been explored for multilayer film formation with up to three layers (in triple slot-die coating) or in combination with the slide coating technique in slot-slide coating. In the context of polymer solar cells the simultaneous multilayer formation has not been reported so far.

There are many good reasons for double slot-die coating not having been employed for polymer solar cells. Firstly, the multilayer formation requires that the same solvent is used for the coated layers and that the layer coated first has the highest surface tension. Secondly, the drying has to be sufficiently fast to minimize diffusion of solutes between the layers. For a bilayer film with a total wet thickness of 100 μm, diffusion of solutes such as small molecules and ions are exceptionally fast unless the viscosity is high. In our case we employ water and the viscosity of the solutions are low (<25 mPa s) implying that it would be difficult to prevent interlayer diffusion. The mean displacement for a molecule such as phenyl-C$_{61}$-butyric acid methyl ester (PCBM) is on the order of 30 μm s^{-1} and with wet thicknesses on the order of $\ll$ 100 μm this would imply that drying should be completed on timescales much faster than a second to avoid complete interlayer mixing by diffusion. We estimated the diffusion lengths using the Einstein equation [7] where we have the diffusion constant and mean displacement, as follows:

$$D = \frac{k_B T}{6\pi\eta r},\quad \lambda_{1d} = \sqrt{2Dt}.$$

here k_B is boltzman's constant, T is absolute temperature, η is the viscosity (of the ink), r is the particle radius, and t is time. Eliminating D, we get the following mean displacement, during 1 s diffusion, for a C$_{60}$ molecule (taken to be similar to PCBM) at 80 °C:

$$\lambda_{C_{60}} = \sqrt{\frac{k_B}{3\pi} \times \frac{1\,\mathrm{s} \times 353\,\mathrm{K}}{1\,\mathrm{mPa\,s} \times 0.5\,\mathrm{nm}}} = 3.22 \times 10^{-5}\,\mathrm{m}.$$

For $r = 50$ nm particle

$$\lambda_{np} = \sqrt{\frac{k_B}{3\pi} \times \frac{1\,\mathrm{s} \times 353\,\mathrm{K}}{1\,\mathrm{mPa\,s} \times 50\,\mathrm{nm}}} = 3.22 \times 10^{-6}\,\mathrm{m}.$$

here we have assumed a constant viscosity of 1 mPa s, which should be considered a conservative estimate, as it is likely to be higher and will increase as the drying proceeds. In our case, the inks P3HT:PCBM, and poly(3,4-ethylenedioxythiophene):poly(styrenesulfonate) (P3HT:PCBM and PEDOT:PSS) are both aqueous dispersions of large aggregates with average sizes 50–100 times larger than the PCBM molecule, hence interlayer mixing due to diffusion of the particles between the two layers would be 1–2 orders of magnitude slower, thus enabling drying without detrimental interlayer mixing. At the same time a limited amount of interdiffusion should be advantageous as it gives a diffusive interface between the coated layers with much higher adhesion, possibly lowering device degradation due to layer delamination. Experience gained from the actual coating experiments suggests that the process is very parameter sensitive. However, a stable operation regime was found and a very illustrative example of the simultaneous bilayer formation from the coating experiment is shown in Fig. 2, where it was possible to turn on and off the flow of one of the inks, thus revealing a sharp transition from single- to bilayer.

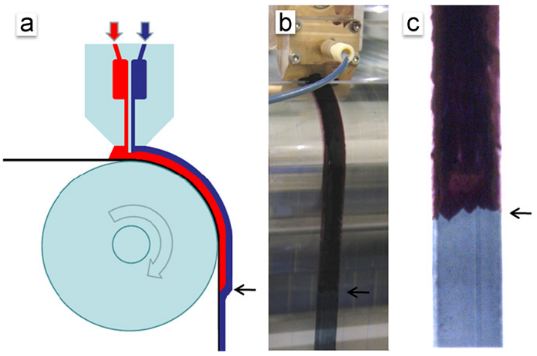

Fig. 2. Double slot-die coating experiment at an instance where the film changes appearance going from a single layer of PEDOT:PSS (blue) to a simultaneous coating of P3HT:PCBM (red) and PEDOT:PSS. The transition is marked by the arrows going from **(a)** a schematic of the experimental situation, to **(b)** a photograph of the experiment, and to **(c)** a close-up photograph of the same foil piece, taken after the coating experiment. (For interpretation of the references to color in this figure legend, the reader is referred to the web version of this article.)

3.1. Nanoparticle characterization

3.1.1. X-ray scattering

The aqueous ink was studied by small angle X-ray scattering (SAXS) in order to determine the size of the particles. The ink was placed in 1 mm capillaries and sealed with epoxy glue, and the data were analyzed using the Bayesian Indirect Fourier Transform [8]. The average particle radius was found to be 46 nm, see Fig. 3.

3.1.2. Microscopy

The drop-cast and spin-coated samples of the nanoparticles were imaged using transmission electron microscopy (TEM) (Fig. 3b) and atomic force microscopy (AFM) (Fig. 3c), respectively. The image documented that spherical nanoparticles had formed.

3.2. Bilayer characterization

3.2.1. Time-of-flight secondary ion mass spectrometry (TOF-SIMS) depth profiling analysis

The obvious concern when performing double slot-die coating is whether the expected bilayer is formed, or whether complete mixing of the layers had occurred. An experiment was designed to resolve this issue. A piece of double slot-die coated sample was submerged in a sodium hydroxide solution in order to facilitate delamination (Fig. 4b). After a while a discrete PEDOT:PSS film simply floated off the top of the surface leaving a P3HT:PCBM film

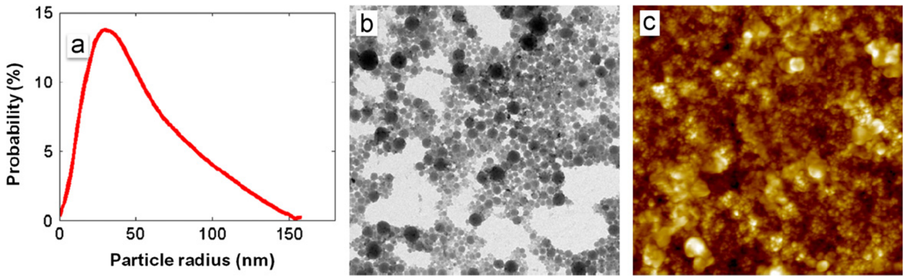

Fig. 3. (**a**) Volume weighted size distribution of the nanoparticles calculated from the SAXS measurement. (**b**) TEM image ($5 \times 5\ \mu m^2$) of a drop-cast sample. (**c**) AFM image ($5 \times 5\ \mu m^2$) of a spin-coated sample.

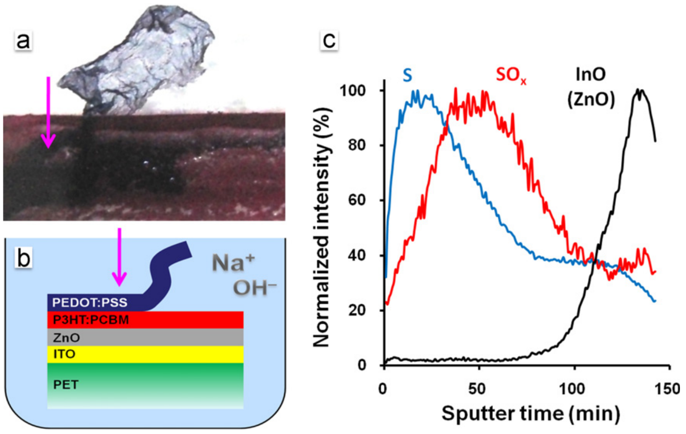

Fig. 4. (**a**) Photography showing a $18 \times 7\ mm^2$ film section delaminated from the double slot-die coated film in NaOH (aq). (**b**) Schematic of the submerged sample showing the surface location (purple arrow) for the TOF-SIMS depth profiling analysis. (**c**) TOF-SIMS depth profiles in negative ion mode confirming that the double slot-die coated film has formed a bilayer. The ZnO layer was so thin that the resulting profile was too noisy, so it was left out for clarity. The noisy ZnO profile is superimposed (due to the thin nature of the film) on the InO^- profile.

on the substrate surface (Fig. 4a). This is clear visual evidence that the double slot-die coating experiment yields a discrete bilayer film. The observations were confirmed by chemical analysis using TOF-SIMS.

TOF-SIMS depth profiling was in addition employed to support the observation and to further document that a bilayer had indeed formed during the double slot-die coating process. Fig. 4a–b shows the surface location where the depth profiling analysis was carried out. Several factors complicate the depth profiling analysis: (i) the sputter depth resolution (under the conditions in question) in soft materials is very poor (compared to hard materials, e.g. metals), and (ii) depth profiles are typically based on unique mass spectral markers that consist of molecular fragment ions or atomic ions, but no unique mass spectral markers are formed under the given experimental conditions. However, due to the fact that equivalent mass spectral markers originating from different molecular environments will produce a different signal response, the different materials may still be uniquely resolved. It turns out that the signal intensities for the S^- and SO_x^- fragment ions (formed in both layers) are extremely dependent on their origin. S^- is intense in PEDOT:PSS and relatively weak in P3HT:PCBM whereas SO_x^- exhibits the opposite behavior. Fig. 4c shows the depth profiles using S^- and SO_x^- as mass spectral markers. In spite of the complicated experimental conditions it was still possible to confirm that a bilayer was formed during the double slot-die coating process. In addition, a depth profile was acquired at a surface location where delamination had occurred that showed the presence of the expected one layer (see Fig. S1 in supporting information). Due to the aforementioned factors affecting the analysis it is not possible to conclude anything about the extent of interlayer mixing that was a consequence of the coating process. From the delamination experiment shown in Fig. 4 we however assume that the interface is discrete when viewed on the scale of the film thickness and probably resembles the roughness that an individual film of the P3HT:PCBM nanoparticles would.

3.2.2. *Reflectrometry*

The coated films were studied with reflectrometry in order to determine whether the two double slot-die coated liquids had mixed. Two samples were measured, a double slot-die coated PEDOT:PSS/P3HT:PCBM bilayer and a single slot-die coated PEDOT:PSS layer, both on a ZnO/ITO/PET substrate. The top layer of the two samples showed the critical angle for total reflection at the same position corresponding to the same electron density for the top layer in both preparations, see Fig. 5.

3.3. *Device performance*

The *J*–*V* characteristics of the freshly prepared solar cells are shown in Fig. 6 together with a reference device, also processed using the aqueous P3HT:PCBM nanoparticle ink as active layer

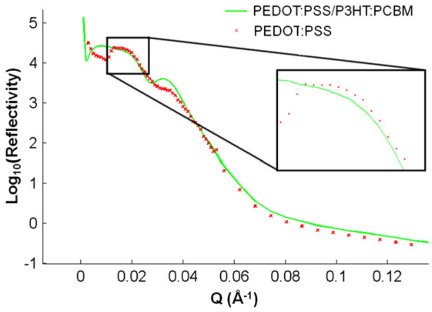

Fig. 5. Reflected intensity for two coated samples. One with PEDOT:PSS and one double slot-die coated PEDOT:PSS/P3HT:PCBM bilayer. The critical angle (θ_c) for total reflection is at 0.176° for both films corresponding to a scattering vector Q_c of 0.025 Å^{-1} ($Q=4\pi\sin\theta/\lambda$, $\lambda=1.5418$ Å).

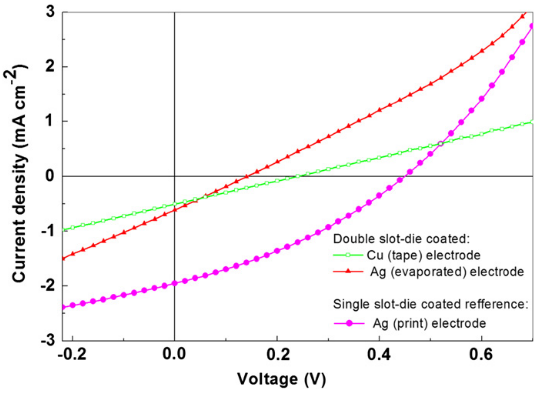

Fig. 6. *J–V* curves of the double slot-die coated devices shown in comparison with a device of similar layer structure processed by standard single slot-die coating.

Table 1
Summary of the *J-V* characterization.

Cell ID	*PCE* (%)	J_{sc} (mA cm^{-2})	V_{oc} (V)	FF (%)
Double slot-die (Cu tape)	0.03	0.5	0.24	25.0
(Ag evaporated)	0.02	0.61	0.14	25.6
Single slot-die	0.29	1.95	0.45	33.1

and PEDOT:PSS as HTL, but prepared by two sequential single slot-die coating steps (i.e. one layer at the time). The use of this nanoparticle ink constitutes a unique route for aqueous processing of large area low band gap polymer solar cells recently demonstrated by our group [9]. The extracted photovoltaic parameters are summarized in Table 1. As is evident the photovoltaic response is significantly lower for the double slot-die coated devices compared to the reference device with respect to all photovoltaic parameters. One notable feature is the linearity of the *J–V* curves within the active quadrant (FF of 25%), which suggests that the operation of the cells is dominated by the internal resistances in the devices, i.e. a low shunt resistance and a high series resistance. A low shunt resistance can be ascribed to two possible effects: (1) from the complex dynamic nature of the simultaneous bilayer formation, as it is likely that PEDOT:PSS forms percolation paths through the active layer during formation, which, in turn, will short the device. (2) It could also be linked to the known photoinduced defects in ZnO as reported recently [10].

Furthermore, the devices having the evaporated Ag electrode display the lowest shunt resistances and consequently lowest V_{oc}, probably due to shunts being formed during evaporation, while the Cu-tape avoids shunts by preferentially contacting the topmost part of the bilayer film, suggesting a somewhat inhomogeneous film. However, the higher series resistance for the devices utilizing a Cu-tape electrode hints to a large contact resistance at the PEDOT:PSS/Cu interface.

We also constructed the reference (blank) devices comprising ITO/ZnO/P3HT:PCBM/Cu-tape, and ITO/ZnO/PEDOT:PSS/Cu-tape, where ITO is indium tin oxide. The corresponding *J–V* curves under standard illumination conditions revealed no photovoltaic response thus documenting the photovoltaic properties of double slot-die coated films. The relatively poor performance of the double slot-die coated devices possibly also has its roots in the large areas we explore (several cm^2) compared to relative film inhomogeneity for the double slot-die coated films. Also the shunts might be located at the edges as is evident from the photograph in Fig. 4a where the PEDOT:PSS has the possibility to overspill the undercoat of P3HT:PCBM and thus short circuit the device. By further tuning the coating conditions, surface tensions for the inks and substrate surface energies it should be possible to minimize these effects.

4. Conclusions

We have successfully demonstrated double slot-die coated polymer solar cells processed roll-to-roll, using two aqueous inks for the simultaneous formation of both the active layer (P3HT:PCBM) and hole transporting layer (PEDOT:PSS). The devices performed relatively poor compared to similar devices processed by single slot-die coating. This is ascribed to far from perfect layer separation due to the complex nature of the bilayer formation process; resulting in shunts and low current extraction efficiencies. This convincingly demonstrates a possible route for lowering the energy payback time of polymer solar cells, which is an important factor in a possible future scenario of large scale energy production.

Acknowledgements

This work was supported by the Danish National Research Foundation. We also thank Dr. T. Kasama at DTU Center for Electron Nanoscopy for TEM measurements.

Appendix A. Supporting information

Supplementary data associated with this article can be found in the online version at doi:10.1016/j.solmat.2011.08.026.

References

[1] F.C. Krebs, Fabrication and processing of polymer solar cells. A review of printing and coating techniques, Solar Energy Materials and Solar Cells 93 (2009) 394–412.
[2] F.C. Krebs, T. Tromholt, M. Jørgensen, Upscaling of polymer solar cell fabrication using full roll-to-roll processing, Nanoscale 2 (2010) 873–886.
[3] F.C. Krebs, T.D. Nielsen, J. Fyenbo, M. Wadstrøm, M.S. Pedersen, Manufacture, integration and demonstration of polymer solar cells in a lamp for the Lighting Africa initiative, Energy & Environmental Science 3 (2010) 512–525.
[4] F.C. Krebs, J. Fyenbo, M. Jørgensen, Product integration of compact roll-to-roll processed polymer solar cell modules: methods and manufacture using flexographic printing, slot-die coating and rotary screen printing, Journal of Materials Chemistry 20 (2010) 8994–9001.

[5] N. Espinosa, R. García-Valverde, A. Urbina, F.C. Krebs, A life cycle analysis of polymer solar cell modules prepared using roll-to-roll methods under ambient conditions, Solar Energy Materials and Solar Cells 95 (2010) 1293–1302.

[6] R. Søndergaard, M. Helgesen, M. Jørgensen, F.C. Krebs, Fabrication of polymer solar cells using aqueous processing for all layers including the metal back electrode, Advanced Energy Materials 1 (2011) 68–71.

[7] A. Einstein, On the motion of small particles suspended in liquids at rest required by the molecular-kinetic theory of heat, Annalen Der Physik 17 (1905) 549–560.

[8] S. Hansen, Bayesian estimation of hyperparameters for indirect Fourier transformation in small-angle scattering, Journal of Applied Crystallography 33 (2000) 1415–1421.

[9] T.R. Andersen, T.T. Larsen-Olsen, B. Andreasen, A.P.L. Böttiger, J.E. Carle´, M. Helgesen, E. Bundgaard, K. Norrman, J.W. Andreasen, M. Jørgensen, F.C. Krebs, Aqueous processing of low-band-gap polymer solar cells using roll-to-roll methods, ACS Nano 5 (2011) 4188–4196.

[10] A. Manor, E.A. Katz, T. Tromholt, F.C. Krebs, Electrical and photo-induced degradation of ZnO layers in organic photovoltaics, Advanced Energy Materials (2011) 836–843.

Solar Energy Materials & Solar Cells 97 (2012) 43–49

Contents lists available at SciVerse ScienceDirect

Solar Energy Materials & Solar Cells

journal homepage: www.elsevier.com/locate/solmat

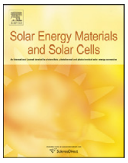

Roll-to-roll processed polymer tandem solar cells partially processed from water

Thue T. Larsen-Olsen, Thomas R. Andersen, Birgitta Andreasen, Arvid P.L. Böttiger, Eva Bundgaard, Kion Norrman, Jens W. Andreasen, Mikkel Jørgensen, Frederik C. Krebs*

Risø National Laboratory for Sustainable Energy, Technical University of Denmark, Frederiksborgvej 399, DK-4000 Roskilde, Denmark

ARTICLE INFO

Available online 21 September 2011

Keywords:
Roll-to-roll processing
Tandem solar cells
Polymer solar cells
Printing and coating
Aqueous processing

ABSTRACT

Large area polymer tandem solar cells completely processed using roll-to-roll (R2R) coating and printing techniques are demonstrated. A stable tandem structure was achieved by the use of orthogonal ink solvents for the coating of all layers, including both active layers. Processing solvents included water, alcohols and chlorobenzene. Open-circuit voltages close to the expected sum of sub cell voltages were achieved, while the overall efficiency of the tandem cells was found to be limited by the low yielding back cell, which was processed from water based ink. Many of the challenges associated with upscaling the multilayer tandem cells were identified giving valuable information for future experiments and development.

1. Introduction

The ultimate efficiency of polymer solar cells is inherently limited by the narrow absorption bands of the chromophores that constitute the photoactive layer of the solar cells. One obvious route to circumvent this is to stack several junctions having complementary absorption bands, thus increasing the spectral overlap of the solar cell and the terrestrial solar spectrum. The benefits of the tandem architecture over single junction cells have been thoroughly studied and reviewed [1–4], and within reasonable assumptions it has been found that a tandem architecture can increase the ultimate efficiency of polymer solar cells with 20–50%, where the highest increase is seen in the case where the single junction cells perform under their ultimate potential [1,2].

The most advantageous approach to polymer solar cell fabrication, with respect to application as an energy technology, is to allow for fast processing of all layers relying on as few coating/printing methods as possible using roll-to-roll (R2R) processing. With regards to tandem polymer solar cells the most obvious device is an all solution processed monolithic tandem cell where the sub cells are connected in series rather than parallel. This naturally presents some challenges in multilayer coating where the typical number of layers required in a tandem cell is around 6–8. All these layers (some of them very thin) have to be coated on top of each other without having subsequent coating steps adversely affecting already coated layers. The traditional laboratory approach to building up the stack is thus not expected to be easily scalable since it often employs vacuum deposition of many of the layers and a rational choice in the order of application. With the boundary condition that all layers have to be processed in air without vacuum, using only solution based printing and coating techniques, it becomes very challenging to realize functional tandem structures. So far only one report has documented vacuum free solution processing of all layers, including the printed metal back electrode [5], while large stacks by solution processing (and vacuum deposited back electrodes) have been reported [6]. Most tandem solar cell reports today employ one or more vacuum coating steps.

In this report we demonstrate R2R processing of tandem polymer solar cells on flexible substrates and show that there are many challenges associated not only with solution processing of entire tandem solar cell stacks, but also with the transfer from laboratory scale batch processing on rigid substrates to a full R2R only process on flexible films.

2. Experimental section

2.1. Materials

Poly-3-hexylthiophene (P3HT) was commercially available and had an M_n of ~20000 Da and an M_w ~40000 Da. Phenyl-C_{61}-butyric acid methyl ester (PC[60]BM) had a purity of 99%. Poly-[thiophene-2,5-diyl-*alt*-(2,3-bis(3-octyloxyphenyl)quinoxaline-5,8-diyl] (TQ-1) was synthesized according to the method described in the literature [7] and had an M_n of ~29000 Da and an M_w ~89000 Da.

The ink used for the front bulk heterojunction (BHJ) active layer comprised PC[60]BM as the acceptor material (18 mg mL^{-1}) and

---

* Corresponding author. Tel.: +45 46 77 47 99.
E-mail address: frkr@risoe.dtu.dk (F.C. Krebs).

0927-0248/$ - see front matter © 2011 Elsevier B.V. All rights reserved.
doi:10.1016/j.solmat.2011.08.025

P3HT as the donor polymer (22 mg mL^{-1}) dissolved in chlorobenzene. For the back BHJ active layer an aqueous ink [8] comprising an aqueous dispersion of nanoparticles consisting of the low band gap polymer TQ-1 (Fig. 1) and PC[60]BM prepared as described earlier [8]. An aqueous precursor solution for the zinc oxide (ZnO) used as electron transporting layer (ETL) was prepared as described earlier [9] and comprised $Zn(OAc)_2$ $2H_2O$ (100 mg mL^{-1}), $Al(OH)(OAc)_2$ (2 mg mL^{-1}) and FSO-100 (2 mg mL^{-1}) in water. Vanadium(V)oxide (V_2O_5) employed as hole transporting layer (HTL) was prepared by diluting a base solution of vanadium(V)-oxiisopropoxide with isopropanol to a concentration of 25 mg mL^{-1}, following recommendations of earlier studies [10,11]. Poly(3,4-ethylenedioxythiophene) poly(styrenesulfonate) (PEDOT:PSS) was based on Orgacon EL-P 5010 from Agfa diluted 2:1 (w:w) with isopropanol. The printable silver back electrode was PV410 from Dupont. The substrate was a 130 micron PET substrate with a patterned ITO layer (nominally 60 Ω square^{-1}).

2.2. Slot-die coating

The bottom electron contact was prepared directly on the PET/ITO substrate, prepared and cleaned as described earlier [12]. The zinc oxide precursor solution was microfiltered immediately prior to use (filter pore size of 0.45 μm) and then slot-die coated at a speed of 2 m min^{-1} with a wet thickness of 4.9 μm. After the initial drying of the precursor film it was converted into an insoluble film by passage through an oven at a temperature of 140 °C with a speed of 0.2 m min^{-1} (oven length = 4 m). This gave an insoluble doped zinc oxide film with a thickness of 25 ± 5 nm. The P3HT:PC[60]BM ink described above was microfiltered and slot die-coated with at a web speed of 1.6 m min^{-1} and a wet thickness of 11.2 μm. The film was dried by passage through an oven (2 m) at 140 °C. The recombination layer comprised a V_2O_5/ZnO stack that was slot-die coated in two steps. The V_2O_5 layer was slot-die coated directly on top of the dried P3HT:PC[60]BM layer, with a web speed of 2 ml min^{-1} and a wet thickness of 8 μm. The film was dried by passage through an oven (2 m) at 140 °C. The second zinc oxide layer was prepared exactly as the first (anode) layer, directly on the V_2O_5 layer. The back cell was prepared by slot-die coating an aqueous TQ-1:PC[60]BM nanoparticle dispersion (Fig. 2) at a web speed of 0.2 m min^{-1} and a wet thickness of 30 μm. The wet film was dried at 140 °C (oven length = 2 m) as described earlier [8]. The back electrode was prepared by applying PEDOT:PSS by slot-die coating at a speed of 0.2 m min^{-1} with drying at 140 °C (oven length = 2 m). It was found unnecessary to wet the film surface prior to coating the PEDOT:PSS and this might be due to the beneficial interaction between the fluorosurfactants in the aqueous nanoparticle dispersion and in the PEDOT:PSS. Finally, the device was completed by R2R screen printing a silver grid electrode and drying at 140 °C. The devices were encapsulated using R2R lamination of a simple food packaging barrier with a pressure sensitive adhesive onto both sides of the foil [12b].

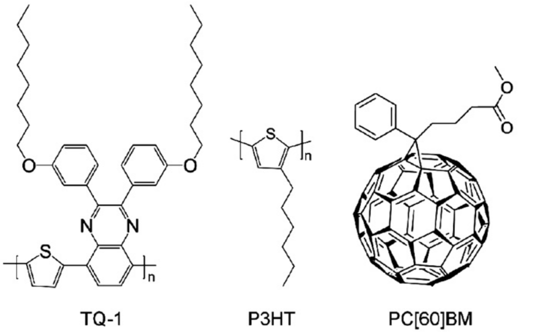

Fig. 1. Structure of poly-[thiophene-2,5-diyl-*alt*-(2,3-bis(3-octyloxyphenyl)quinoxaline-5,8-diyl] (TQ-1), poly-3-hexylthiophene (P3HT), and phenyl-C_{61}-butyric acid methyl ester (PC[60]BM).

2.3. TOF-SIMS depth profiling analysis

Time-of-flight secondary ion mass spectrometry (TOF-SIMS) was employed to perform a depth profiling analysis. The experiments were conducted using a TOF-SIMS IV (ION-TOF GmbH, Münster, Germany). 25-ns pulses of 25-keV Bi^+ (primary ions) were bunched to form ion packets with a nominal temporal extent of <0.9 ns at a repetition rate of 10 kHz yielding a target current of 1 pA. These primary ion conditions were used to obtain depth profiles in both negative and positive ion mode. Depth profiling was performed using an analysis area of 100 × 100 μm^2

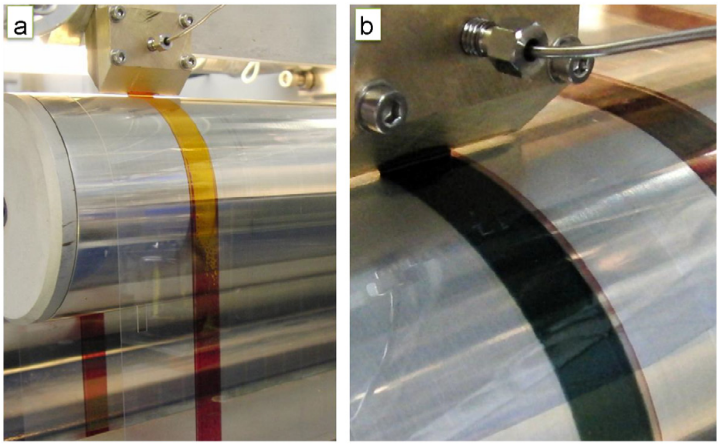

Fig. 2. Photographs of the actual R2R coating experiment in progress. (a) Coating of the front BHJ material (the drying process of the film is visible). (b) Coating of the back BHJ material.

and a sputter area of 300 × 300 μm^2. 30 nA of 3-keV Xe$^+$ were used as sputter ions. Electron bombardment (20 eV) was used to minimize charge build-up at the surface. Desorbed secondary ions were accelerated to 2 keV, mass analyzed in the flight tube, and post-accelerated to 10 keV before detection.

2.4. *J–V characterization*

The final devices were put under simulated sunlight at 1000 W m^{-2}, 85 ± 5 °C, 40 ± 10% relative humidity (rh) (AM1.5G). *J–V* curves were recorded by sweeping from −1 V to +1 V in steps of 20 mV and a rate of 0.1 V s^{-1} to ensure that no dynamic effects resulted in over/under estimation of J_{sc} and V_{oc}. The time evolution of the photovoltaic performance was recorded by continuously illuminating the device under the above conditions while recording complete IV data every one minute according to ISOS-L-1 [13].

3. Results and discussion

3.1. *The tandem cell*

This study describes the transfer of a laboratory scale tandem solar cell process on rigid glass substrates to a R2R process on flexible plastic substrates. The laboratory process was described previously [11] and was developed with an aim of being compatible with R2R processing. The tandem solar cell structure comprised a multilayer stack with the composition PET/ITO/ZnO/front-BHJ/V_2O_5/ZnO/back-BHJ/PEDOT:PSS/Ag, where PET is poly(ethylene terephthalate) (substrate), ITO is indium tin oxide (transparent front electrode), ZnO is the electron transport layer, front-BHJ is the front bulk heterojunction consisting of P3HT:PC[60]BM (active layer 1), V_2O_5/ZnO is the recombination layer, back-BHJ consists of TQ-1:PC[60]BM (active layer 2), PEDOT:PSS is the hole transport layer, and Ag is the back electrode. Illustrative photographs of the coating process are shown in Fig. 2.

The first attempts resulted in very poorly performing devices typically showing open-circuit voltages around what is expected for single junction devices. Optical inspection of the completed devices revealed the possible origin of this malfunction to be cracks in the V_2O_5 part of the recombination layer (Fig. 3). It was found that these cracks form at some point during the processing of the V_2O_5 layer, possibly due to the heat treatment and/or bending of the substrate as it passes through the R2R equipment. As is also hinted in Fig. 3 these cracks persist after processing of the ZnO layer thus rendering the recombination layer penetrable to the solute of the back BHJ as this is coated. This would most likely solubilize the front BHJ and thus seriously compromise the integrity of the serial connection of the two sub cells. This situation is schematically described in Fig. 4a. Such a short-circuiting of the recombination layer would make the two active layers effectively function as one poorly performing active layer, in turn, explaining the single junction-like low open-circuit voltage observed for these devices.

However, it was possible to work around this issue by utilizing an aqueous ink for the processing of the back BHJ using a method recently described by Andersen et al. [8]. This presented a unique opportunity for orthogonal processing since water cannot solubilize the front BHJ. From the photomicrographs shown in Fig. 4 it is evident that the back cell looks less affected by the cracks in the recombination layer when water based processing is employed (Fig. 4b compared to Fig. 4a).

3.2. *TOF-SIMS depth profiling analysis*

TOF-SIMS depth profiling analysis was employed in both negative and positive ion mode in order to document the layer stack order. The encapsulation film is too thick for a depth profiling analysis, so it was necessary to delaminate the tandem solar cell. TOF-SIMS mass spectra of the exposed surfaces revealed that delamination took place at the PEDOT:PSS/back BHJ interface.

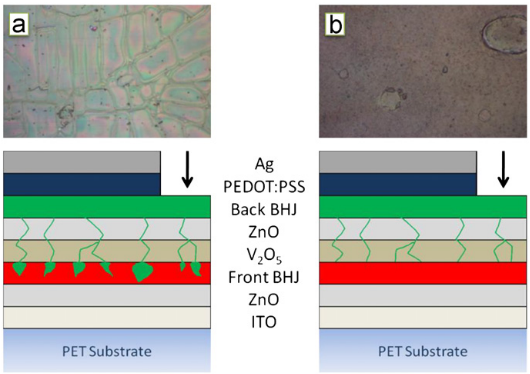

Fig. 4. Schematics of the tandem solar cell under study and photomicrographs (230 × 150 μm^2) obtained at the indicated positions (black arrows), which illustrates the proposed consequence of the observed cracks in the recombination layer when using (a) a non-orthogonal solvent (chloroform) and (b) an orthogonal solvent (water), for the processing of the back BHJ.

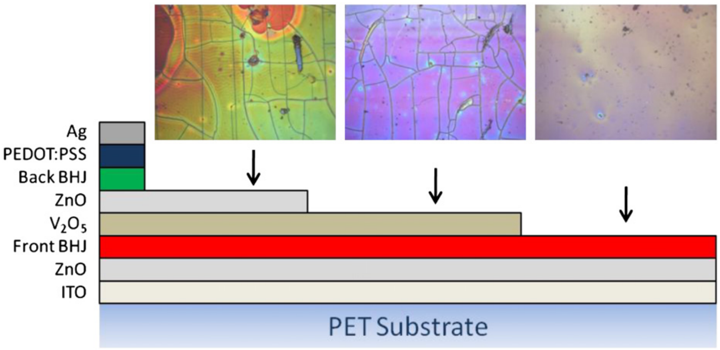

Fig. 3. Schematic of the tandem solar cell under study and photomicrographs (260 × 195 μm^2) revealing cracks in the V_2O_5 layer, which persist through the ZnO layer.

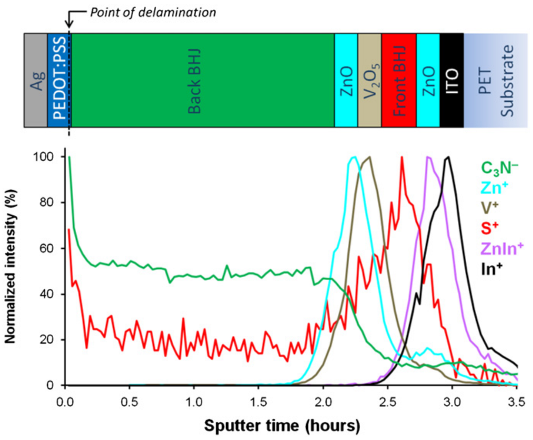

Fig. 5. TOF-SIMS depth profiles through the delaminated tandem solar cell. C_3N^- is a marker for the back BHJ obtained from a depth profile run in negative mode, Zn^+ is a marker for the ZnO, V^+ is a marker V_2O_5, S^+ is a marker for both front and back BHJ, and $ZnIn^+$ (formed during the ionization step of the analysis) is a marker for the front ZnO and In^+ is a marker for ITO.

Fig. 5 shows the results of the depth profile analysis. Various factors complicated the analysis, such as interface roughness, which is well known phenomenon in R2R processing (e.g. compared to spin coating). Furthermore, depth profiling in soft materials is associated with an inferior depth resolution (under the given sputter conditions), compared to hard materials (e.g. metals). These conditions constitute a challenge especially when it comes to performing depth profiling on very thin layers such as the ZnO (~25 nm) and V_2O_5 (~15 nm) layers present in this device. However, as is evident from Fig. 5 it was quite possible, in spite of the conditions, to document the multilayer stack composition in the tandem solar cell device. Residual PEDOT:PSS was present in the PEDOT:PSS/back BHJ interface after the delamination process presumably due to a small degree of interlayer mixing that resulted in presumably a matrix effect, which is observed as initially elevated signals from the back BHJ material (i.e. at the beginning of the sputter time window). During the ionization process the Zn^+ signal is discriminated due to the formation of the $ZnIn^+$ cluster ion caused by the close vicinity of the ITO (i.e. an ionization phenomenon). Finally, a significantly long sputter time window is observed for the back BHJ compared to the front BHJ, which suggests that the back BHJ is significantly thicker (assuming similar sputter rates) than the front BHJ consistent with an expected layer thickness of ~600 nm [8] for the back BHJ as compared to the thickness of the front BHJ ~200 nm.

3.3. Electrical characterization

J–V characteristics for the best performing tandem device are shown in Fig. 6, (blue triangles) together with representative *J–V* curves for both tandem and back cell reference devices with and without photo-annealing (800 min). The key photovoltaic parameters are summarized in Table 1, while the dynamic evolutions of the short circuit current (I_{sc}) and open-circuit voltage (V_{oc}) are shown in Fig. 7. By summing the V_{oc} values from the sub cell reference devices (Table 1) it is possible to estimate that the perfect tandem device would have an open-circuit voltage close to 1 V. As is clear from the presented data in Table 1, the actual tandem devices gave, at best, a V_{oc} around 0.9 V while V_{oc} values around 0.75 V were readily measured, hence between 0.1 and 0.25 V less than the expected ideal value.

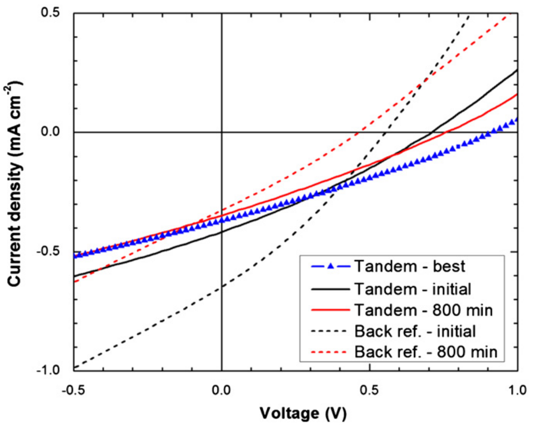

Fig. 6. *J–V* characteristics (AM1.5G 1000 W m^{-2}) for the best performing tandem cells. Also shown is a more average cell, before (initial) and after (800 min) photo-annealing.

Table 1
Summary of the *J–V* characterization.

Cell	PCE (%)	J_{sc} (mA cm^{-2})	V_{oc} (V)	FF (%)
Tandem ([a])				
(Initial)	0.09	−0.42	0.71	28.8
(800 min)	0.07	−0.35	0.76	27.5
(Best)	0.10	−0.37	0.91	28.2
Back cell ([a])				
(Initial)	0.11	−0.65	0.55	30.2
(800 min)	0.04	−0.33	0.46	27.7
Front cell (Ref. [11])	1.32	−7.17	0.50	36.9

[a] Cell active area of 4 cm^2.

Various loss mechanisms can influence the tandem voltage, of which most are related to the nature of the sub cell interconnection, i.e. the recombination layer. In this case it is highly probable that the before mentioned observed defects (Fig. 3) are likely to have a negative influence on V_{oc} if the mechanism schematically shown in Fig. 4b is considered, i.e. shunts across the recombination layer would lower the tandem V_{oc}. Furthermore, the results show that the front and back reference cells both exhibit a decreasing V_{oc} during the dynamic evolution *J–V* experiment as observed in Fig. 7 and S7 (see e-component). For the tandem devices the trend is opposite, i.e. increasing V_{oc} over time. Both reference cells display saturation at around 0.45 V, which fits well with the peak value of the best tandem cell.

It appears that the sub cell interconnection improves over time, possibly due to burning of shunts across the recombination layer, originally formed as a consequence of the defects. With respect to the I_{sc} it is noticeable that the tandem device and the back cell reference device have rather similar I_{sc} values. This should be compared to the front cell I_{sc}, which is a factor of 10 to 20 times larger. Thus the tandem device is severely current limited by the poor performing back cell.

This significant current mismatch is likely to influence the current–voltage characteristics of the tandem cell. Hadipour et al. [14] found that the excess current will cause the surplus of free holes to pile up at the middle electrode (recombination layer), which will result in a lowering of the effective internal field in the

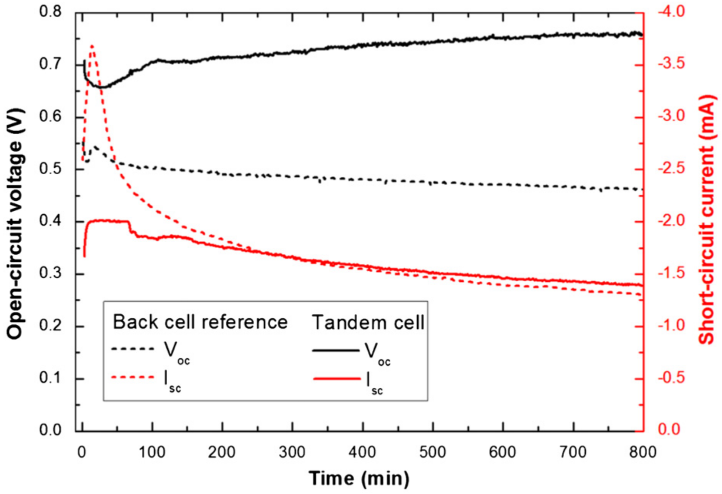

Fig. 7. Time evolution of the open-circuit voltage and short-circuit current during the 800 min of photo-annealing (AM1.5G 1000 W m^{-2}) of the tandem cell, and a corresponding single junction reference cell mimicking the current-limiting back cell.

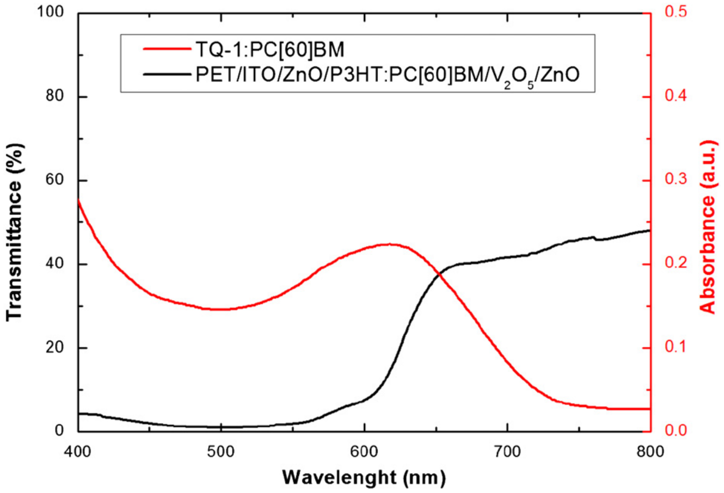

Fig. 8. Transmittance of the front cell and the recombination layer relative to the absorbance of the back cell active layer.

front sub cell, while for the back sub cell the opposite will be the case and the internal field will increase.

Hence the sub cell currents will equilibrate at some intermediate value, resulting in a higher I_{sc} value for the tandem device compared to the expected current of the limiting sub cell reference device. How the tandem current equilibrates is very much dependent on the slope of the *J*–*V* curves of the sub cells around short-circuit as well as the degree of current mismatch, as recently pointed out by Braun et al. [15] for the case of an inorganic tandem cell. This can be easily understood, e.g. in the case of the current limiting sub cell; as the reverse biasing caused by the current mismatch will only result in a significant increase in current if the *J*–*V* curve of the sub cell has a non zero slope in reverse bias, which is the case for the cells under study here. Furthermore, according to Fig. 8 the tandem back cell will suffer from an obvious poor spectral matching with the front cell transmission spectrum, and thus receive a significantly lower photon flux than the reference cell. From this, a significant lowering of the back cell current would be expected. However, as the *J*–*V* data shows that the I_{sc} of the tandem is not lower but rather comparable to that of the current limiting back cell reference device this would in fact imply a combination of the spectral mismatch and the increased quantum efficiency of the tandem back cell due to current mismatch (the effect described in Refs. [14 and 15]). To support this, we construct the ideal tandem curve from the two reference sub cells by summing voltages at equal currents, as described in Ref. [14]. We take into account the spectral mismatch by a mismatch factor *S*, which is simply multiplied with the current of the back cell reference. These can be seen in Fig. 9, for the case of $S=1$ and $S=0.5$, together with the

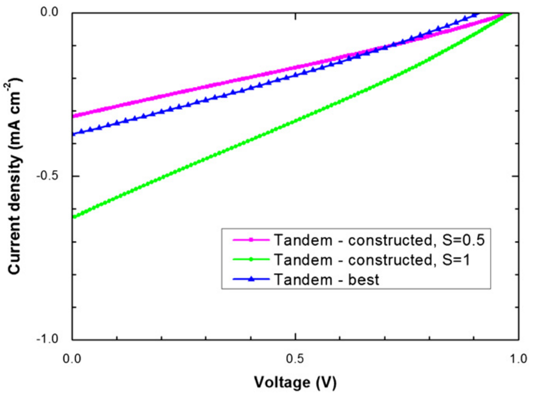

Fig. 9. Constructed tandem J–V characteristics with spectral mismatching ($S=0.5$) and without ($S=1$), compared with the best measured tandem device.

best tandem curve. As can be seen, it is likely that severe spectral mismatching is the cause of the low short-circuit current of the tandem cell, while the discrepancy between the model and the measurement can be explained by the somewhat crude model, such as negligence of V_{oc} dependence on light intensity [16], and the assumption of a perfect ohmic connection between the sub cells, e.g. a perfect recombination layer.

3.4. *Future developments*

The tandem approach within polymer photovoltaics has so far been utilized in an attempt to maximize efficiency, i.e. without constraints on materials and fabrication methods. The present work, however, demonstrates the fragility of the tandem device approach from a solution processing point of view, and in doing so, stresses the importance of having certain constraints in mind when assessing a given set of materials and processing methods. In this regard especially the recombination layer presents an all-determining weak-point of the tandem cell; a perfect recombination layer would be insoluble and solvent impenetrable, being either a pn-junction preferably a highly doped tunnel junction or alternatively having metal like characteristics. This has so far been achieved only for small area devices using rigid substrates [6,11,17–21]. Lee et al. [22] successfully demonstrated a small area tandem device on a flexible substrate but using vacuum deposition. However, as for upscaling of the fabrication, it is the view of the authors that a stable and highly reliable solution process for polymer tandem solar cells can only be ensured by a completely orthogonalized process in which none of the processing steps can seriously harm any of the previously processed layers. This has to do with the inherently rough nature of a high throughput R2R process, during which cracks and small coating imperfections would act as solvent paths leading to partial dissolution of underlying layers. The aqueous emulsion approach utilized in this work is one possible solution presenting both a stable and possibly environmentally friendly fabrication process. At the same time it allows for the use of the large amount of existing polymers. However, the success of this technique of course depends on whether significantly better device performance can be achieved. Another foreseeable solution would be a process where the layers by some in-line post process are rendered insoluble, for instance using thermal- or light-induced thermocleavage of the solubilizing groups as demonstrated earlier [5,23,24]. This would be very desirable as it ensures free choice of solvent for the subsequent layers, and also removes constraints on the recombination layer in terms of materials and layer thicknesses, thus opening for a wider range of tweakable parameters.

4. Conclusions

We have successfully demonstrated large area flexible polymer tandem solar cells with all layers processed entirely from solution, and partially from water. The multilayer stack on flexible PET substrate comprised a cathode of ITO/ZnO, a recombination layer of V_2O_5/ZnO, and a PEDOT:PSS/Ag (printed) anode. The two serially connected BHJs was comprised of a P3HT:PC[60]BM front cell processed from chlorobenzene and a back cell processed from an aqueous dispersion of poly[2,3-bis-(3-octyl oxyphenyl)-quinoxaline-5,8-diyl-alt-thiophene-2,5-diyl]:PC[60]BM nanoparticles. The composition and integrity of the multilayer stack was confirmed by TOF-SIMS depth profiling. The V_{oc} of the best tandem device was 0.9 V, while both the corresponding single junction reference devices had a V_{oc} around 0.5 V. This confirms a serial connection of the sub cells while the observed voltage losses are ascribed to visible defects in the recombination layer and a non-ohmic connection of the two sub cells.

Acknowledgment

This work was supported by the Danish National Research Foundation. We gratefully acknowledge Lasse Gorm Jensen for creating graphical illustrations and Jon E. Carlé and Martin Helgesen for preparing polymer materials.

Appendix A. Supplementary materials

Supplementary data associated with this article can be found in the online version at doi:10.1016/j.solmat.2011.08.025.

Details of GIWAXS measurements and time evolution for the back reference cell.

References

[1] T. Ameri, G. Dennler, C. Lungenschmied, C.J. Brabec, Organic tandem solar cells: a review, Energy & Environmental Science 2 (2009) 347–363.

[2] G. Dennler, M.C. Scharber, T. Ameri, P. Denk, K. Forberich, C. Waldauf, C.J. Brabec, Design rules for donors in bulk-heterojunction tandem solar cells. Towards 15% energy-conversion efficiency, Advanced Materials 20 (2008) 579–583.

[3] J.D. Kotlarski, P.W.M. Blom, Ultimate performance of polymer: fullerene bulk heterojunction tandem solar cells, Applied Physics Letters 98 (2011) 053301.

[4] Y.M. Nam, J. Huh, W.H. Jo, A computational study on optimal design for organic tandem solar cells, Solar Energy Materials and Solar Cells 95 (2011) 1095–1101.

[5] O. Hagemann, M. Bjerring, N.C. Nielsen, F.C. Krebs, All solution processed tandem polymer solar cells based on thermocleavable materials, Solar Energy Materials and Solar Cells 92 (2008) 1327–1335.

[6] J. Gilot, M.M. Wienk, R.A.J. Janssen, Double and triple junction polymer solar cells processed from solution, Applied Physics Letters 90 (2007) 143512.

[7] E. Wang, L. Hou, Z. Wang, S. Hellström, F. Zhang, O. Inganäs, M.R. Andersson, An easily synthesized blue polymer for high-performance polymer solar cells, Advanced Materials 22 (2010) 5240–5244.

[8] T.R. Andersen, T.T. Larsen-Olsen, B. Andreasen, A.P.L. Böttiger, J.E. Carle´, M. Helgesen, E. Bundgaard, K. Norrman, J.W. Andreasen, M. Jørgensen, F.C. Krebs, Aqueous processing of low-band-gap polymer solar cells using roll-to-roll methods, ACS Nano 5 (2011) 4188–4196.

[9] R. Søndergaard, M. Helgesen, M. Jørgensen, F.C. Krebs, Fabrication of polymer solar cells using aqueous processing for all layers including the metal back electrode, Advanced Energy Materials 1 (2011) 68–71.

[10] N. Espinosa, H.F. Dam, D.M. Tanenbaum, J.W. Andreasen, M. Jørgensen, F.C. Krebs, Roll-to-roll processing of inverted polymer solar cells using hydrated vanadium(V)oxide as a PEDOT:PSS replacement, Materials 4 (2011) 169–182.

[11] T.T. Larsen-Olsen, E. Bundgaard, K.O. Sylvester-Hvid, F.C. Krebs, A solution process for inverted tandem solar cells, Organic Electronics 12 (2011) 364–371.

[12] a) F.C. Krebs, T. Tromholt, M. Jørgensen, Upscaling of polymer solar cell fabrication using full roll-to-roll processing, Nanoscale 2 (2010) 873–886; b) J. Alstrup, M. Jørgensen, A.J. Medford, F.C. Krebs, Ultra fast and parsimonious materials screening for polymer solar cells using differentially pumped slot-die coating, ACS Applied Materials & Interfaces 2 (2010) 2819–2827.

[13] M.O. Reese, S.A. Gevorgyan, M. Jørgensen, E. Bundgaard, S.R. Kurtz, D.S. Ginley, D.C. Olson, M.T. Lloyd, P. Morvillo, E.A. Katz, A. Elschner, O. Haillant, T.R. Currier, V. Shrotriya, M. Hermenau, M. Riede, K.R. Kirov, G. Trimmel, T. Rath, O. Inganäs, F. Zhang, M. Andersson, K. Tvingstedt, M. Lira-Cantu, D. Laird, C. McGuiness, S. Gowrisanker, M. Pannone, M. Xiao, J. Hauch, R. Steim, D.M. DeLongchamp, R. Rösch, H. Hoppe, N. Espinosa, A. Urbina, G. Yaman-Uzunoglu, J.-B. Bonekamp, A.J.J.M. van Breemen, C. Girotto, E. Voroshazi, F.C. Krebs, Consensus stability testing protocols for organic photovoltaic materials and devices, Solar Energy Materials and Solar Cells 95 (2011) 1253–1267.

[14] A. Hadipour, B. de Boer, P.W.M. Blom, Device operation of organic tandem solar cells, Organic Electronics 9 (2008) 617–624.

[15] A. Braun, N. Szabo´, K. Schwarzburg, T. Hannappel, E. Katz, J.M. Gordon, Current-limiting behavior in multijunction solar cells, Applied Physics Letters 98 (2011) 223506.

[16] T. Tromholt, E. Katz, B. Hirsch, A. Vossier, F.C. Krebs, Effects of concentrated sunlight on organic photovoltaics, Applied Physics Letters 96 (2010) 073501.

[17] A. Hadipour, B. de Boer, J. Wildeman, F.B. Kooistra, J.C. Hummelen, M.G.R. Turbiez, M.M. Wienk, R.A.J. Janssen, P.W.M. Blom, Solution-processed organic tandem solar cells, Advanced Functional Materials 16 (2006) 1897–1903.

[18] J.Y. Kim, K. Lee, N.E. Coates, D. Moses, T.–Q. Nguyen, M. Dante, A.J. Heeger, Efficient tandem polymer solar cells fabricated by all-solution processing, Science 317 (2007) 222–225.

[19] S. Sista, M.–H. Park, Z. Hong, Y. Wu, J. Hou, W.L. Kwan, G. Li, Y. Yang, Highly efficient tandem polymer photovoltaic cells, Advanced materials 22 (2010) 380–383.

[20] D.J.D. Moet, P. de Bruyn, P.W.M. Blom, High work function transparent middle electrode for organic tandem solar cells, Applied Physics Letters 96 (2010) 153504.

[21] C.–H. Chou, W.L. Kwan, Z. Hong, L.–M. Chen, Y. Yang, A. Metal-Oxide, Interconnection layer for polymer tandem solar cells with an inverted architecture, Advanced Materials 23 (2011) 1282–1286.

[22] B.J. Lee, H.J. Kim, W. -ik Jeong, J.–J. Kim, A transparent conducting oxide as an efficient middle electrode for flexible organic tandem solar cells, Solar Energy Materials and Solar Cells 94 (2010) 542–546.

[23] T. Tromholt, S.A. Gevorgyan, M. Jørgensen, F.C. Krebs, K.O. Sylvester-Hvid, Thermocleavable materials for polymer solar cells with high open circuit voltages – a comparative study, ACS applied materials & interfaces 1 (2009) 2768–2777.

[24] F.C. Krebs, K. Norrman, Using light induced thermocleavage in a roll-to-roll process for polymer solar cells, ACS applied materials & interfaces 2 (2010) 877–887.

Supporting Information for:

Roll-to-roll processed polymer tandem solar cells partially processed from water

Thue T. Larsen-Olsen, Thomas R. Andersen, Birgitta Andreasen, Arvid P. L. Böttiger, Jon E. Carlé, Martin Helgesen, Eva Bundgaard, Kion Norrman, Jens W. Andreasen, Mikkel Jørgensen and Frederik C. Krebs*

Risø National Laboratory for Sustainable Energy, Technical University of Denmark,

Frederiksborgvej 399, DK-4000 Roskilde, Denmark

e-mail: frkr@risoe.dtu.dk

GIWAXS

By orienting the substrate surface at or just below the critical angle for total reflection with respect to the incoming X-ray beam (≈0.2°), scattering from the deposited film is maximized with respect to scattering from the substrate. In the wide-scattering-angle range (>5°), X-ray scattering is sensitive to crystalline structure. The GIWAXS data were acquired using a camera comprising an evacuated sample chamber with an X-ray photosensitive image plate. A rotating Cu-anode (Rigaku 18 kW) operating at 50 kV/200mA was used as X-ray source, focused, and monochromatized (Cu K_α, λ=1.5418Å) by a 1D multilayer.

A standard PET film with PCBM yields the following characteristic diffraction pattern where most of the diffraction is due to the PET while a few features are caused by the crystalline PCBM.

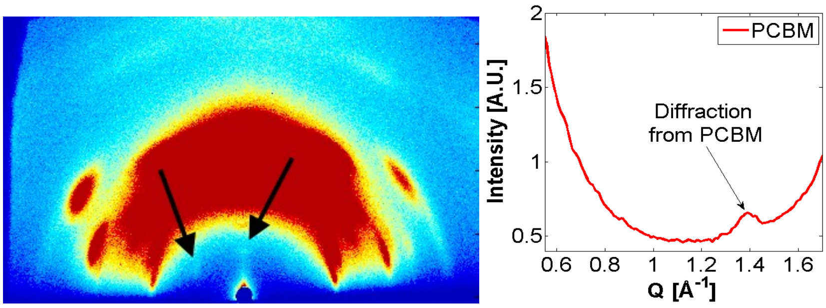

Figure 1, Left: The diffraction pattern from PCBM on PET. The two arrows mark diffraction peaks from PCBM. **Figure 1, Right:** A cross section of the diffraction pattern along the Q-direction with the same diffraction pattern marked.

Both of the active layers where studied by GIWAXS at RISØ DTU. Both individually coated on PET and both of them together as the complete cell.

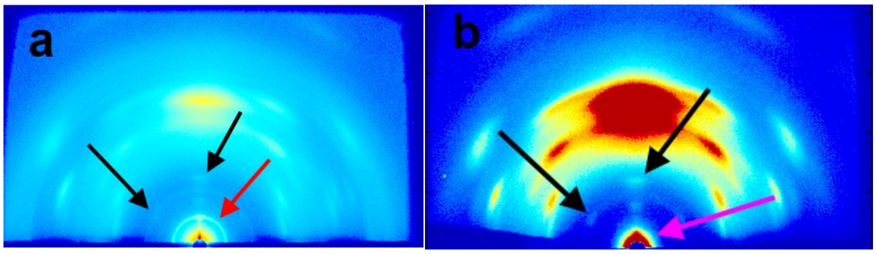

Figure 2a: The front active layer. The diffraction peaks from P3HT is marked by the red arrow, and the features from PCBM is marked with black arrows. **Figure 2b:** The diffraction from the back active layer is marked by the purple arrow, but is not directly visible from the GIWAXS image.

The diffraction peak for P3HT at 0.38 Å^{-1} is marked on Figure 2a. There is no directly observable diffraction peak from the back active layer on Figure 2b. However, by integrating the intensity along the Q-direction the back active layer shows weak diffraction at 0.27 Å^{-1}.

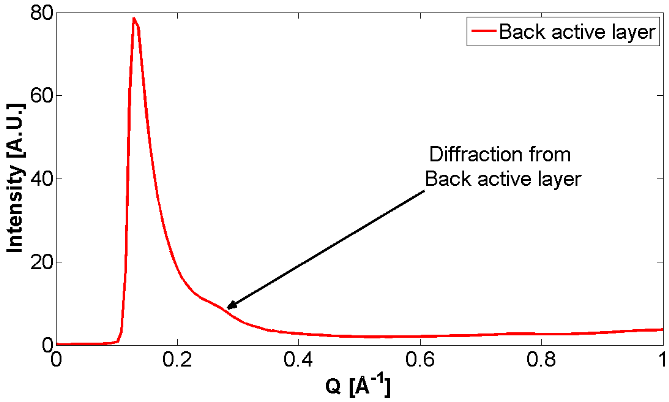

Figure 3: The integrated intensity for the back active layer along the Q-direction. It shows a small diffraction peak at Q = 0.27 Å^{-1}

Plotting the intensity along the Q-direction for the front active layer shows the position for the first and second order diffraction peak.

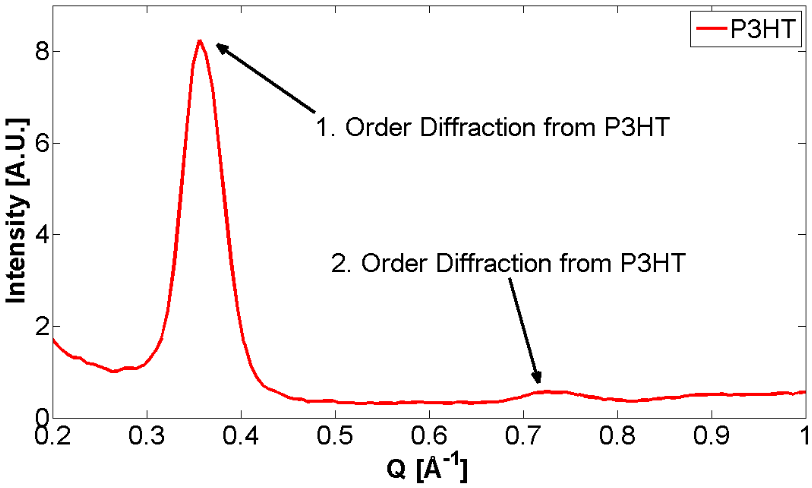

Figure 4: The integrated intensity for P3HT. It shows both the main diffraction peak at 0.38 Å^{-1} and second order peak can be observed at 0.74 Å^{-1}

The full tandem cell look very much like pure P3HT:PCBM, but looking at the integrated 1D intensity the presence of the back active layer can be observed.

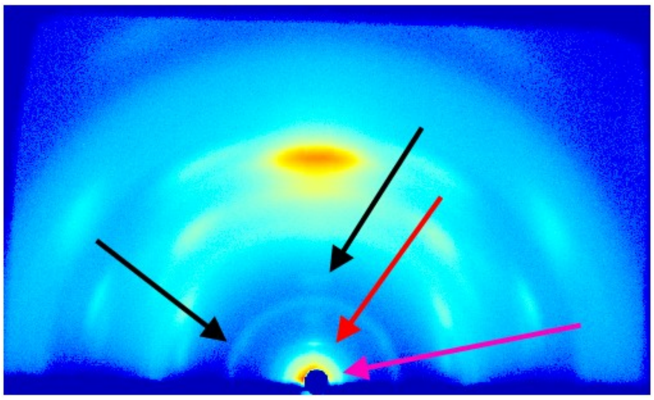

Figure 5: The diffraction pattern for the tandem cell. Black: PCBM Red: Front active layer, Purple: Back active layer

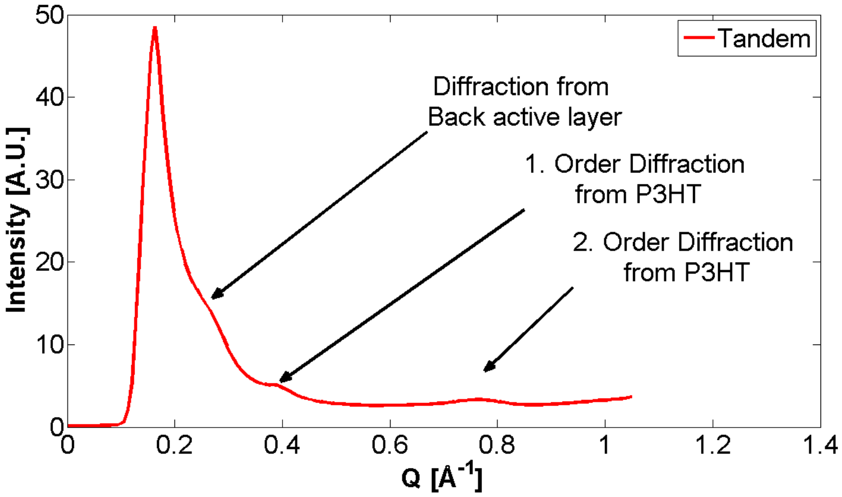

Figure 6: The integrated intensity for the tandem cell. It shows diffraction peak from both the front and back active layer.

J-V Characteristics

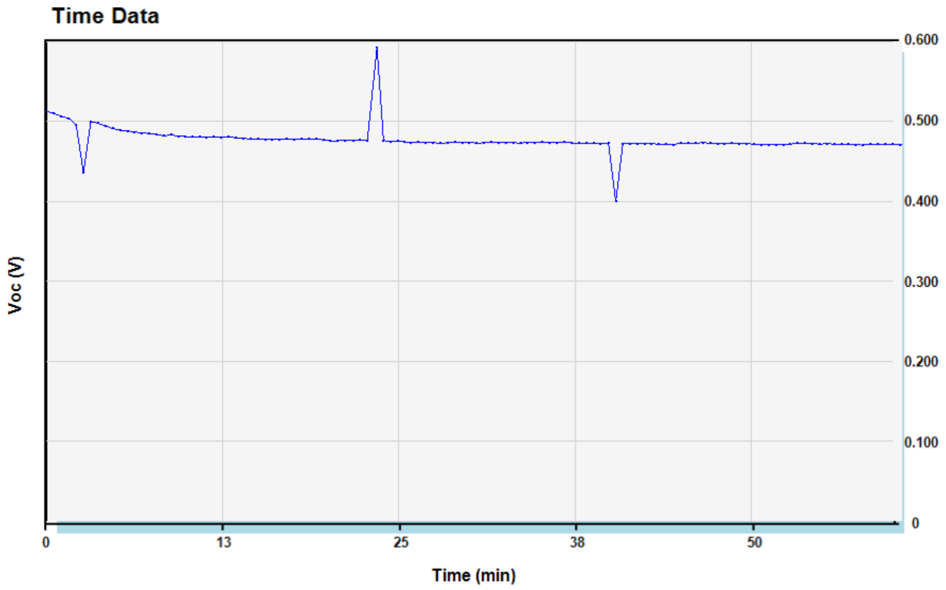

Figure 7: Time evolution of the reference front cell V_{oc}.

Aqueous Processing of Low-Band-Gap Polymer Solar Cells Using Roll-to-Roll Methods

Thomas R. Andersen, Thue T. Larsen-Olsen, Birgitta Andreasen, Arvid P. L. Böttiger, Jon E. Carlé, Martin Helgesen, Eva Bundgaard, Kion Norrman, Jens W. Andreasen, Mikkel Jørgensen, and Frederik C. Krebs*

Solar Energy Programme, Risø National Laboratory for Sustainable Energy, Technical University of Denmark, Frederiksborgvej 399, DK-4000 Roskilde, Denmark

ABSTRACT Aqueous nanoparticle dispersions of a series of three low-band-gap polymers poly[4,8-bis(2-ethylhexyloxy)benzo(1,2-b:4,5-b′)dithiophene-alt-5,6-bis(octyloxy)-4,7-di(thiophen-2-yl)(2,1,3-benzothiadiazole)-5,5′-diyl] (P1), poly[(4,4′-bis(2-ethylhexyl)dithieno[3,2-b:2′,3′-d]silole)-2,6-diyl-alt-(2,1,3-benzothiadiazole)-4,7-diyl] (P2), and poly[2,3-bis-(3-octyloxyphenyl)quinoxaline-5,8-diyl-alt-thiophene-2,5-diyl] (P3) were prepared using ultrasonic treatment of a chloroform solution of the polymer and [6,6]-phenyl-C_{61}-butyric acid methyl ester ([60]PCBM) mixed with an aqueous solution of sodium dodecylsulphate (SDS). The size of the nanoparticles was established using small-angle X-ray scattering (SAXS) of the aqueous dispersions and by both atomic force microscopy (AFM) and using both grazing incidence SAXS (GISAXS) and grazing incidence wide-angle X-ray scattering (GIWAXS) in the solid state as coated films. The aqueous dispersions were dialyzed to remove excess detergent and concentrated to a solid content of approximately 60 mg mL^{-1}. The formation of films for solar cells using the aqueous dispersion required the addition of the nonionic detergent FSO-100 at a concentration of 5 mg mL^{-1}. This enabled slot-die coating of high quality films with a dry thickness of 126 ± 19, 500 ± 25, and 612 ± 22 nm P1, P2, and P3, respectively for polymer solar cells. Large area inverted polymer solar cells were thus prepared based on the aqueous inks. The power conversion efficiency (PCE) reached for each of the materials was 0.07, 0.55, and 0.15% for P1, P2, and P3, respectively. The devices were prepared using coating and printing of all layers including the metal back electrodes. All steps were carried out using roll-to-roll (R2R) slot-die and screen printing methods on flexible substrates. All five layers were processed using environmentally friendly methods and solvents. Two of the layers were processed entirely from water (the electron transport layer and the active layer).

KEYWORDS: roll-to-roll coating polymer solar cells · organic solar cells · slot-die coating · aqueous inks · nanoparticle dispersions

Aqueous processing of polymer solar cells presents the ultimate challenge in terms of environmental friendliness and has only been reported in a few instances. The approaches to solubilization of the conjugated and active material in water fall in three categories: solubilization through (1) ionic side chains such as sulfonic acid, carboxylic acid, or ammonium, (2) nanoparticle dispersions of hydrophobic polymers in water, or (3) nonionic alcohol and glycol side chains. The latter approach is the most recent and most successful in terms of performance where PCEs of up to 0.7% have been reached on indium tin oxide (ITO) substrates with aqueous processing of the four subsequent layers in the solar cell stack (including the printed metal back electrode).[1] The approach employing ionic side chains is perhaps conceptually the most appealing as it opens up for layer-by-layer assembly of the films or interface layers[2] but has so far not been employed successfully for the active layer itself. The nanoparticle dispersion approach developed by Landfester *et al.*[3−7] is particularly appealing as it allows for control of the nanoparticle size and for processing using pure water as solvent for common hydrophobic conjugated polymers. In terms of development of the polymer and organic photovoltaic (OPV) technology, the latter point is of some significance since the large body of polymers available today has been developed for processing in organic solvents such as chlorobenzene, 1,2-dichlorobenzene, *etc.* One could envisage a complete redesign of the chemistry as described above[1] (method 3) but it will require a complete rediscovery of the solvent−material interaction and morphology relationships. While this may be necessary, in the end it is of interest to simply adapt the large body of materials at hand to an aqueous process. It is also of critical importance to replace the organic solvents if one has the ambition to manufacture polymer solar cells on a gigawatt scale.

There are several concerns associated with the use of chlorinated and aromatic solvents on a very large scale. Concern for the people working at the manufacturing machine is crucial both in terms of toxicity and, in the case of aromatic solvents,

* Address correspondence to frkr@risoe.dtu.dk.

Received for review March 11, 2011 and accepted April 14, 2011.

10.1021/nn200933r

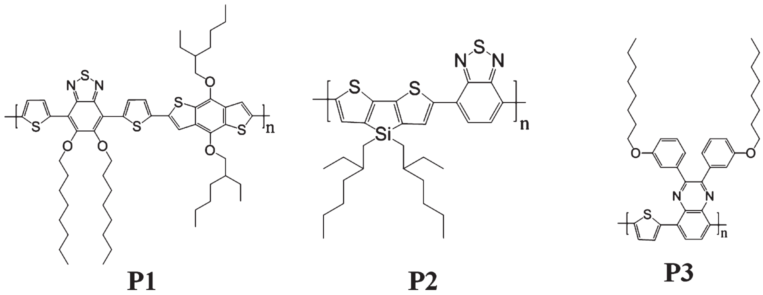

Figure 1. The structure for the three polymers used, P1, P2, and P3 (see text for the systematic names).

flammability. In the case of the chlorinated solvents the environmental concern is large, and it is unlikely that large scale manufacturing using such solvents is possible in a European setting. As an example, the current state of the art based on ProcessOne[8] would involve approximately 16 million liters of chlorobenzene for the production of 1 GW_p of polymer solar cell. An additional concern is the cumulative energy needed for raw materials production, where a poor choice of processing method and processing materials can severely affect the energy payback time (EPBT) of the solar cell. Life cycle analysis has confirmed that water is the solvent that is most beneficial to use, requiring only a small electrical energy input for production.[9] The cumulative thermal energy in materials production of chlorobenzene alone, as given in the example above, would be 880 TJ, adding 10 days to the EPBT. In contrast the use of water as the solvent would require only 17 TJ, adding only 4 h to the EPBT.

In terms of active materials the most successful approach so far has been the use of low-band-gap materials based on the donor–acceptor approach as shown in Figure 1. The UV–vis spectra of the three polymers **P1**, **P2**, and **P3** were recorded, and the optical band gaps were determined to be 1.8, 1.5, and 1.8 eV, respectively (Figure 2).

In this work we prepared aqueous nanoparticle dispersions of the known low-band-gap polymers poly[4,8-bis(2-ethylhexyloxy)benzo(1,2-b:4,5-b′)dithiophene-alt-5,6-bis(octyloxy)-4,7-di(thiophen-2-yl)(2,1,3-benzothiadiazole)-5,5′-diyl] (**P1**),[10] poly[(4,4′-bis(2-ethylhexyl)-dithieno[3,2-b:2′,3′-d]silole)-2,6-diyl-alt-(2,1,3-benzothiadiazole)-4,7-diyl] (**P2**),[11] and poly[2,3-bis-(3-octyloxyphenyl)-quinoxaline-5,8-diyl-alt-thiophene-2,5-diyl] (**P3**)[12] (Figure 1) in mixtures with [60]PCBM. We developed an aqueous R2R manufacturing process for flexible polymer solar cells through careful ink formulation and processing.

RESULTS AND DISCUSSION

Overview. The polymer solar cell has grown from a laboratory experiment to an emerging technology with great potential to significantly contribute to future energy production. Currently, polymer solar cells can be prepared using industrial roll-to-roll methods[8] and are sufficiently stable for demonstration products. They have for instance been employed as a low cost lighting solution for developing countries.[13] While upscaling has been described successfully their current potential should be viewed critically[14,15] and compared to existing thin film solar cell technologies such as CdTe and amorphous silicon. The polymer solar cell is currently the poorest performing PV technology (in existence) in terms of power conversion efficiency, while it has distinct advantages of high speed production, adaptability, and an abundance of raw materials. Recent work on the life cycle analysis from several groups[9] have highlighted the potential of the technology and in one case, where the source of data was fully public, revealed EPBTs in the range of 1.35–2.02 years.[9] As outlined in the introduction there is an urgent need for processes and processing materials that lower the embedded energy and the process energy, as this is a necessary method for lowering the EPBT. This should of course go in hand with an increase in efficiency. In this work where we aim at replacing the organic solvent for processing of the active area with water there is a direct gain at the site of manufacture but it should be emphasized that solvents and large amounts of

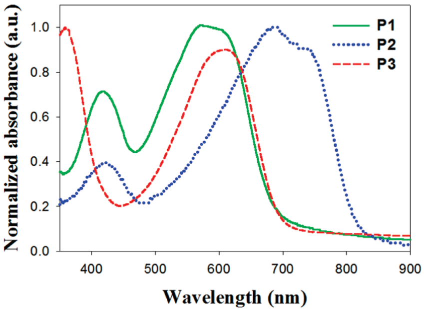

Figure 2. The UV–vis spectra of P1, P2, and P3. The optical band gap was determined to be 1.8, 1.5, and 1.8 eV for P1, P2, and P3, respectively.

detergent are required for the manufacture of the nanoparticle dispersions. It is assumed that those can be recycled to fully benefit from the aqueous processing of hydrophobic materials that has already been developed. If this is not the case then there might not be any gain in the cumulative energy for raw materials production but there will still be a large gain in terms of human safety and lower emission of chlorinated or aromatic solvent into the environment because the preparation of the nanoparticle dispersions inherently allows for containment and reuse of solvents. A detailed life cycle analysis of the inks is thus warranted and until this has been carried out a complete comparison is not possible. At this point however the benefits of an aqueous ink are large enough to justify research in this direction.

Formation of Nanoparticle Dispersions. The generic method developed by Landfester *et al.* in a series of original research papers during the period from 1999 to 2004 was followed and found to be directly applicable with minor modifications.[3−7] A significantly larger amount of SDS was found to be needed than reported previously for a given nanoparticle size. The correlation between the size of the nanoparticles and the amounts of solvent, water, and SDS seem to be depending on the properties of the individual polymers. We found that a 100 mM SDS solution and a solid content in the organic phase of ∼40 mg mL^{-1} reproducibly gave nanoparticles with a size below 150 nm as established with SAXS measurements. We also found that the nanoparticles were conserved in the coated films (*vide supra*). The observed discrepancy in particle size as a function of SDS content could also be linked to the method of particle size determination where light scattering was employed previously. The reported method for the removal of the excess detergent comprises dialysis and centrifugal dialysis. These methods however allow for the preparation of only small quantities of ink. In our case large volumes (>100 mL) of inks with a high solid content was needed, and we initially attempted using a large basket centrifuge allowing for the continuous addition of water but finally settled on a Millipore filter system with a processing volume of 500 mL. Using this method, ink volumes of 100 mL with a solid content of 60 mg mL^{-1} could be prepared in a few hours. The inks were diluted 625 times corresponding to a final SDS concentration in the ink of 0.16 mM.

TABLE 1. The Average Particle Diameter in P1, P2, and P3 As Determined by SAXS and AFM. The Standard Deviation Is Given in the Brackets

polymer	SAXS (dispersions)	AFM (films)	GISAXS (films)
P1	130(38) nm	*a*	*a*
P2	32(10) nm	69(47) nm	32(22) nm
P3	87(21) nm	120(82) nm	107(72) nm

[a] Not possible to establish due to aggregation in the sample.

Particle Size and Crystalline Order. SAXS was employed on both the aqueous dispersions and on the solid films to determine particle sizes. AFM images of the films were analyzed to determine particle size distributions and gave similar results.

GIWAXS data showed poorly developed crystalline order of polymers **P2** and **P3**, with only weak first order reflections corresponding to lamellar spacings of 18.2 and 24.0 Å, respectively, and a broad peak at ∼1.34 Å^{-1} that we ascribe to packing of disordered side chains. **P1** showed very weak scattering, with no features that may be attributed to crystalline order of the polymer (the wide peak at high q values is the background signal from the glass substrate). All three films show a weak peak at ∼0.69 Å^{-1} that we ascribe to nanocrystalline [60]PCBM (Table 1 and Figures 3 and 4).

Inks and Roll-to-Roll Coating. The spin coating of thin films was possible, whereas large area films with the thickness/coverage required for making functional OPV devices was not possible. It was further found impossible to successfully coat these inks even with very fast web speeds and fast drying on a heated roller and a short distance (18 cm) between the coating head and the oven. Web speeds as high as 8 m min^{-1} were employed with a roller temperature of 80 °C. By heating the foil just after coating, quick drying was possible (within seconds), but significant dewetting was still observed (see Supporting Information).

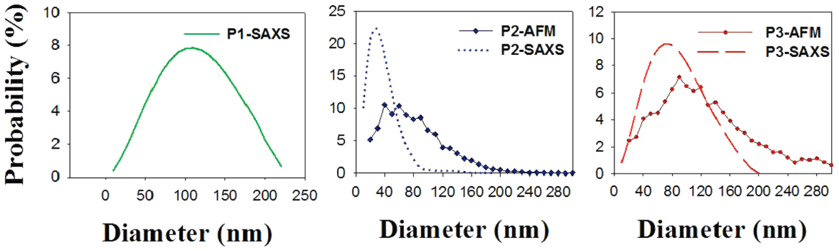

Figure 3. Size distributions of the particles P1 (left), P2 (middle), P3 (right) measured by AFM and SAXS. The SAXS measurements were performed with the particles in a water suspension, and the AFM was measured from spin-coated films. The distribution of P1 could not be determined by AFM due to aggregation of the particles.

Careful inspection of the wetting behavior revealed that the ink initially wets the surface and then dewets leaving a thin film (possibly comprising a single layer of nanoparticles). We ascribe this to the initial wetting and drying followed by lowering of the surface energy of the first layer and subsequent dewetting of the higher surface tension solution.

This phenomenon is quite well-known in the area of coating technology and is in essence a result of poisoning the otherwise wetable surface by the surface active properties of the ink itself. To solve this problem, the addition of a nonionic fluorosurfactant (FSO-100) was found to be necessary. The amount added was critical, and with too little material dewetting was still observed, whereas too much led to films with extremely poor adhesion. A concentration of 5 mg mL^{-1} was found to be the best compromise between coatability and adhesion. Films prepared in this manner passed the tape test.[16] The age of the meniscus was found to be of critical importance for efficient wetting and good adhesion of the dried film. This phenomenon is well-known in the area of coating technology, where shear induced in the ink as a result of the coating process itself leads to depletion of surfactant at the surface of the ink. In the case of water based inks this implies that the surface tension of the ink in the region of coating increases to a level where dewetting occurs. In such cases the speed of the coating process must be decreased to a level where the surfactant has time to diffuse to the surface and maintain the lower surface tension. Web speeds of 1 m min^{-1} were found to present the best conditions even though web speeds as high as 1.6 m min^{-1} could also be employed. A web speed of 0.6 m min^{-1} was used in all experiments to fabricate the devices presented in this work. Examples of dewetting during coating can be seen in the Supporting Information, and correct wettings are shown in Figure 5. The thickness of the dry active layers of **P1**, **P2**, and **P3** were measured by AFM profilometry and were found to be 126 ± 19, 500 ± 25, and 612 ± 22 nm, respectively.

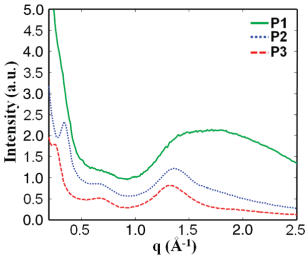

Figure 4. GIWAXS patterns of the three polymers, spin-coated on glass. No texture was observed, and the 2D patterns were thus azimuthally averaged as a function of *q*. The patterns are scaled for clarity.

The devices were completed by slot-die coating poly(3,4-ethylenedioxythiophene) poly(styrenesulfonate) (PEDOT:PSS) on top of the active layer and interestingly

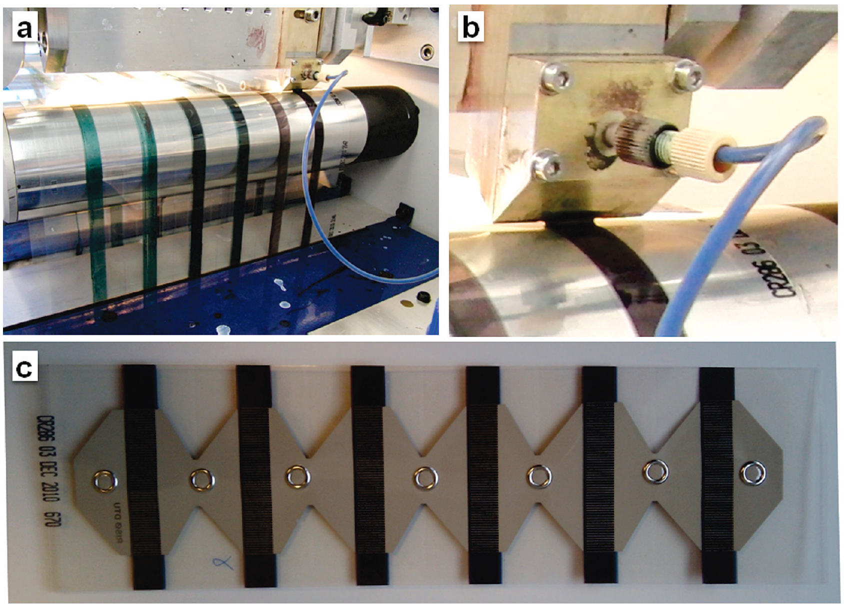

Figure 5. (a) Slot-die coating of the active layer using the aqueous nanoparticle dispersions and (b) an enlargement of the coating head, coating bead and wet film, and (c) showing a complete device with six individual solar cells.

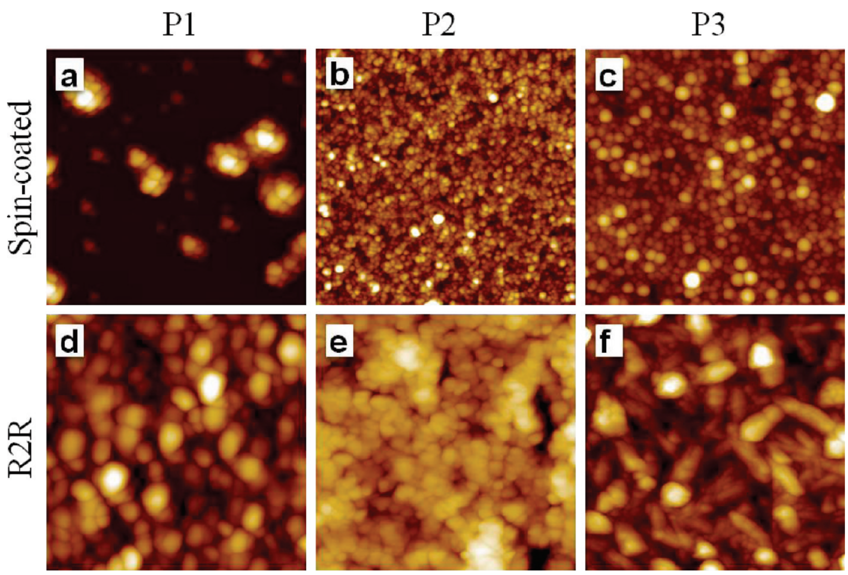

Figure 6. AFM topography images of spin-coated (a–c) and R2R (d–f) prepared samples of P1, P2, and P3. All the images were taken at 5 × 5 μm^2.

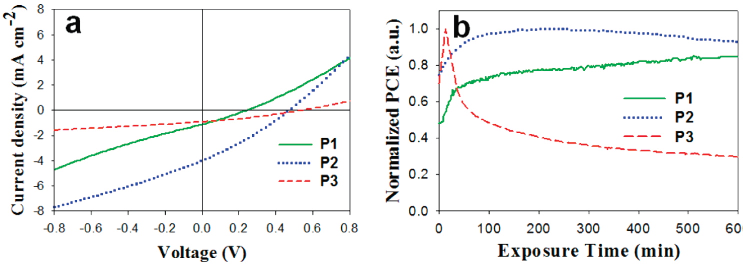

Figure 7. (a) *IV*-curves for the devices based on the three different polymers, at peak performance (AM1.5G, 1000 W m^{-2}, 85 ± 5 °C). (b) The development of the solar cell PCE during the initial 10 h of the exposure to 1 sun is shown for the three different polymers. Values are normalized to the corresponding peak value for each polymer (see Table 2).

no prewetting of the active layer with isopropyl alcohol was needed. We ascribe this to a fortuitous interaction between the fluorosurfactants in the PEDOT:PSS formulation and in the coated active layer. The devices were completed by screen printing a silver ink onto the PEDOT:PSS electrode. The devices were finally encapsulated using a simple barrier foil as described earlier and tested using an automated roll-to-roll IV-tester.[8,14,15]

Morphology. The morphology differences between spin-coated and R2R prepared samples and between the different sample materials can clearly be observed in the AFM images in Figure 6. On the spin-coated samples the individual nanoparticle shapes can be observed (with exception of **P1**, which looks like agglomerates made up of smaller particles). In the R2R samples the nanoparticles can no longer be clearly distinguished; instead it looks like the nanoparticles have merged in places. The different morphologies observed across the R2R samples could be caused by the "harsh" process conditions, where annealing at high temperatures is involved, and due to the different thermal properties of the polymers.

When the R2R coated samples in Figure 6 panels d, e, and f are compared, it looks like the particles are increasingly merged (d < f < e). This could be because these samples were prepared at slightly different conditions with the annealing time increasing (d < f < e). Each roll-to-roll experiment (a roll of foil) comprises six coated stripes as described earlier.[15] The first coated stripe will thus pass the oven a total of eight times, whereas that last coated stripe will pass the oven a total of three times (including the two passages when coating PEDOT:PSS and printing the silver back electrode).

Device Performance. The freshly prepared devices were put under a calibrated solar simulator (AM1.5G, 1000 W m^{-2}) and *IV*-scans were recorded every 1 min, for up to 36 h (according to the ISOS-L-1 procedure[26] using a temperature of 85 ± 5 °C). For all devices an initial steady increase in PCE during exposure to sunlight was generally observed.

However the optimum period of light exposure was significantly different for the three photoactive polymers, as can be seen in Figure 7. The PCE increase was caused by improvement of both the short circuit current and open circuit voltage, while the fill-factor was relatively constant. This behavior is not unique for these cells prepared from water-dispersed nanoparticles, but is readily observed for other polymer solar cells, having the same layer structure but an active layer processed from organic solvents such as chlorobenzene.[15] It is ascribed to a combination of effects such as photodoping of the zinc oxide layer by UV-light, accompanied by beneficial morphological changes in the active layer due to the relatively high temperature (85 ± 5 °C).[14]

The devices prepared from the aqueous dispersions show poorer performance compared to earlier reported efficiencies for devices based on **P1**, **P2**, and **P3**, prepared using chlorobenzene as solvent (Figure 7).[10−12] The source of this most likely shunts across the active layer. Because of the particle nature of the active layers (Figure 6), the film will be somewhat porous and thus susceptible to shunting by the subsequent processing of PEDOT:PSS. It is thus likely that the amount of shunts should be dependent on the layer thickness relative to the particle diameters. When the obtained PCEs for the different polymers are compared, it is observed that thicker layers and smaller particle size seem to give a higher performance. Apart from these suspected microscopic shunts, there are some larger shunts for some devices due to incomplete coverage evident from optical inspection of the film and even more so from the light beam induced current (LBIC) scan shown in Figure 8 where (blue) dots within the (red/green) active area reveal such shunts. Furthermore, effects from the significant amount of fluorosurfactant present in the ink along with the residual SDS bound to the surface of the nanoparticles have not been determined. This does however show that it is possible to prepare devices from water with a nonnegligible performance, and worth noting that a large part of the relatively low performance of these devices prepared from water could be due to coating technicalities that are bound to become less pronounced as further experience is gained.

TABLE 2. The Photovoltaic Properties Obtained for the Devices When Processed from Water[a]

polymer	V_{oc} (V)	J_{sc} (mA cm^{-2})	FF (%)	PCE (%)
P1	0.24	1.10	27.5	0.07
P2	0.47	3.99	29.3	0.55
P3	0.54	0.92	30.8	0.15

[a] The device geometry was PET/ITO/ZnO/polymer-[60]PCBM/PEDOT:PSS/Ag-(printed), and the active area of the devices was 4 cm^2. The testing conditions were AM1.5G, 1000 W m^{-2}, 85 ± 5 °C.

Directions for Future Work. The possibility of achieving aqueous processing and operator safety and avoiding the emission of environmentally harmful solvents to the environment was demonstrated, and while this is a great step forward it was achieved at the expense of using a fluorinated surfactant. There is a well-documented concern over release of fluorinated surfactants to the environment where extremely harmful effects have been documented.[17] In our case the surfactant is not released directly to the environment but will follow the solar cell until the end of its life cycle, where it should be properly disposed. The identification of existing environmentally friendly surface active materials or the development of new ones for coating should be researched actively to avoid the use of fluorinated detergents while maintaining the advantages of aqueous processing of OPV.

The relationship between the chemical disposition of the polymer materials and nanoparticle size in the final ink will have to be established along with the relationship between the size of the nanoparticles and the performance of the solar cell printed from them. Since this requires quite large quantities of conjugated polymer material, the type of materials that perform best should be identified followed by replacement of the fluorinated surfactant. Once the truly environmentally friendly ink with the best performance has been identified the ink can be finally optimized with respect to nanoparticle size, solid content, drying time, *etc.*

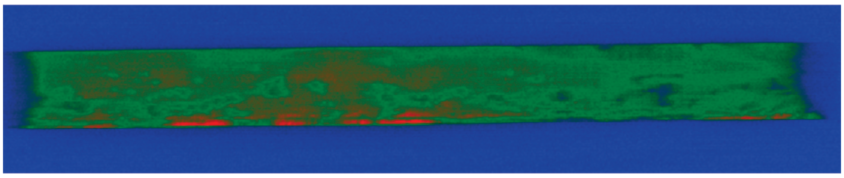

Figure 8. The LBIC image for a mapping of a P2 cell. The intensity scale is going from blue with no intensity over green to red with high intensity.

In our case **P2** proved to work best and further optimization using this class of materials should be pursued.

CONCLUSIONS

We have successfully prepared aqueous nanoparticle dispersions of three low-band-gap polymers and formulated inks for roll-to-roll processing into polymer solar cells on a flexible substrate which resulted in PCEs of 0.55, 0.15, and 0.07% for poly[(4,4′-bis(2-ethylhexyl)dithieno[3,2-b:2′,3′-d]silole)-2,6-diyl-alt-(2,1,3-benzothiadiazole)-4,7-diyl], poly[2,3-bis-(3-octyloxyphenyl)-quinoxaline-5,8-diyl-alt-thiophene-2,5-diyl], and poly[4,8-bis(2-ethylhexyloxy)benzo(1,2-b:4,5-b′)dithiophene-alt-5,6-bis(octyloxy)-4,7-di(thiophen-2-yl)(2,1,3-benzothiadiazole)-5,5′-diyl], respectively. We analyzed the nanoparticles in aqueous dispersion using SAXS and in solid film using GISAXS, GIWAXS, and AFM. The ink formulation and roll-to-roll processing was found to be challenging, however a reproducible method giving homogeneous films that adhered well to the surface of the zinc oxide based electron transport layer was obtained. The relatively poor device performance is ascribed to shunting and non-optimum morphology. Further work should be directed at improving coating condition and ink formulation as this has been successful in the case of organic solvent systems.

METHODS

Materials. The polymers were prepared as described in the literature.[10−12] They had values for M_n, M_w, and polydispersities of, respectively, 11.0 kDa, 28.7 kDa, and 2.6 for **P1**, 6.0 kDa, 10.9 kDa and 1.8 for **P2,** and 21.0 kDa, 89.0 kDa, and 4.2 for **P3**. [60]PCBM, SDS and chloroform were purchased in standard grade. An aqueous precursor solution for the zinc oxide was prepared as described in the literature.[1] PEDOT:PSS was based on EL-P 5010 from Agfa that was diluted with isopropyl alcohol to a viscosity of 200 mPa·s. The printable silver back electrode was PV410 from Dupont.

Nanoparticle Preparation. The typical recipe for small scale production, the polymer material (0.3 g) was together with [60]PCBM (0.3 g) dissolved in chloroform (15.5 mL) and mixed with an aqueous 100 mM SDS solution (50 mL) in a large beaker. The mixture was stirred vigorously for 1 h and then subjected to ultrasound (1 kW) for 5 min using an UIP 1000hd transducer from Hielscher ultrasound technology fitted with a booster head. The mixture was then stirred on a hot plate at 65 °C for 3 h until all the chloroform had evaporated. For small scale preparations, the aqueous dispersion was then dialyzed in dialysis tubing against 2 × 10 L pure water. In the final step the suspensions were concentrated to have a solid content of approximately 60 mg mL^{-1}.

For large scale preparations, the aqueous dispersion was dialyzed using a Millipore system with a capacity of 500 mL. The mixture was concentrated by dialysis from a volume of 500 mL to a volume of 100 mL with a forward pressure of 1.4 bar and a pressure gradient across the filter of 0.7 bar. Pure water (400 mL) was then added and the procedure was repeated 4 times corresponding to a dilution of the solution by a factor of 625. In the final step the suspensions were concentrated to have a solid content of 60 mg mL^{-1}.

X-ray Scattering. The SAXS and grazing incidence SAXS (GISAXS) experiments were performed at a laboratory setup using a rotating Cu-anode operating at 46 kV and 46 mA as X-ray source. The SAXS instrument was configured for a fully evacuated sample to detector distance of 4579 mm covering a q-range of $2.5 \times 10^{-3} < q < 0.12$ Å^{-1}, where the length of the scattering vector $q = 4\pi \sin(\theta)/\lambda$, with θ equal to half the scattering angle, and λ being the X-ray wavelength for Cu Kα (1.5418 Å). The X-rays are monochromated and collimated by two-dimensional multilayer optics and detected by a 2D "Gabriel"-type gas-proportional delay line detector.[18] The nanoparticle dispersions were measured in 1 mm borosilicate capillaries, sealed with epoxy glue for the SAXS experiments, and GISAXS of films spin-coated on glass were measured by orienting the substrate at an X-ray incidence angle of 0.5°. The 2D scattering images of the randomly oriented particles in dispersion were reduced to 1D cross sections by azimuthal averaging, whereas the GISAXS scattering were reduced to 1D curves by taking projections through the Yoneda peak[18] at constant q_z. The reduced 1D data were analyzed by using the Bayesian inverse Fourier transform (BIFT).[19]

GIWAXS of spin-coated films on glass were acquired by orienting the substrate surface just below the critical angle for total reflection with respect to the incoming X-ray beam (0.18°), maximizing scattering from the deposited film with respect to scattering from the substrate. In the wide scattering angle range (>5°), the X-ray scattering is sensitive to crystalline structure. For the experiment we used a camera comprising an evacuated sample chamber with an X-ray photosensitive image plate as detector and a rotating Cu-anode operating at 50 kV/200 mA as X-ray source, focused and monochromatized (Cu Kα, λ = 1.5418 Å) by a 1D multilayer.[19] The samples were mounted 120 mm from the detector. The GIWAXS data were analyzed by reducing the acquired 2D data by azimuthal averaging of intensity as a function of scattering vector length, q, to determine the characteristic d-spacings of the polymers, using the software SimDiffraction.[20]

Atomic Force Microscopy. AFM imaging was performed on an N8 NEOS (Bruker Nano GmbH, Herzogenrath, Germany) operating in an intermittent contact mode using PPP-NCLR cantilevers (NANOSENSORS, Neuchatel, Switzerland). Images were recorded at a scan speed of 0.8 lines min^{-1}. The images were analyzed using the image processing software package SPIP 5.1.5 (Image Metrology A/S, Hørsholm, Denmark).

The samples were first delaminated by ripping the plastic laminate off in a swift motion and thereafter placed on a glass slide using double sided tape.

It is well-known that AFM can at times overestimate particle sizes in the lateral plane and therefore the height z is often used as a measure for the diameter of spherical particles.[21−23] However, since the particles in the samples at hand are closely packed the height measurements of individual particles would be too time-consuming and inaccurate.[24] Therefore the best estimate to determine the particle size was to employ the Particle & Pore Analysis module included in the SPIP 5.1.5 software. The size was analyzed on at least two different positions of the sample analyzing a minimum of 2000 particles on each sample.

The thicknesses of the dry films were measured by AFM profilometry, see Figure 9. The thickness was measured at a minimum of three different positions on each film, with each position consisting of at least three individual measurements.

Light Beam Induced Current (LBIC) Mapping. The LBIC experiments were carried out using a custom-made setup with 410 nm laser diode (5 mW output power, 100 μm spot size (≈ 65 W/cm^{-2}), ThorLabs) mounted on a computer controlled XY-stage and focused to a spot size of <100 μm. The short circuit current from the device under study was measured using a computer

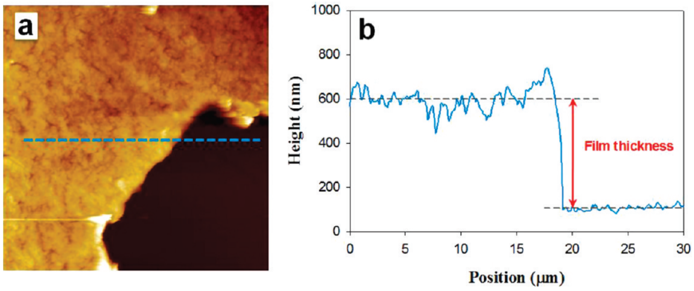

Figure 9. (a) 30 × 30 μm^2 AFM topography image indicating where the thickness was measured. (b) line profile extracted from the AFM image (dashed line).

controlled source measure unit (Keithley 2400), and mapped by raster scanning across the device. Further details are available elsewhere.[25]

Ink Formulation. The nonionic fluorosurfactant (FSO-100) was added to the dialyzed aqueous suspension of the polymer/[60]PCBM nanoparticles. The concentration of fluorosurfactant was 5 mg mL^{-1} and the polymer/[60]PCBM concentration was 60 mg mL^{-1}. This solution was employed directly for slot-die coating

Roll-to-Roll Coating. A PET substrate with an ITO pattern was prepared and cleaned as described earlier.[13−15] The zinc oxide precursor solution was prepared as described earlier[1] and comprised $Zn(OAc)_2 \cdot 2H_2O$ (100 mg mL^{-1}), $Al(OH)(OAc)_2$ (2 mg mL^{-1}), and FSO-100 (2 mg mL^{-1}) in water. This solution was microfiltered immediately prior to use (0.45 μm) and then slot-die coated at a speed of 2 m min^{-1} with a wet thickness of 4.9 μm. After the initial drying of the precursor film it was converted into an insoluble film by passage through an oven at a temperature of 140 °C with a speed of 0.2 m min^{-1} (oven length = 4 m). This gave an insoluble doped zinc oxide film with a thickness of 25 ± 5 nm. The aqueous polymer/[60]PCBM nanoparticle dispersion was then slot-die coated at a speed of 1 m min^{-1} with a wet thickness of 30.4, 17.6, and 20.8 μm for **P1**, **P2**, and **P3**, respectively. The coating speed and the time between application of the wet film and the drying were critical for successful formation of a homogeneous film without dewetting. The slot-die coating head had a temperature of 60 °C, the coating roller had a temperature of 80 °C, and the temperature of the foil was kept at 80 °C until it reached the oven at 140 °C. The distance from the point of coating to the oven entry was 18 cm. PEDOT:PSS was then applied by slot-die coating at a speed of 0.2 m min^{-1} and dried at 140 °C (oven length = 2 m). It was found unnecessary to wet the film surface prior to coating the PEDOT:PSS and this might be due to the beneficial interaction between the fluorosurfactants in the active layer film and in the PEDOT:PSS. Finally the device was completed by roll-to-roll screen printing a silver grid electrode and drying at 140 °C. The devices were encapsulated using roll-to-roll lamination of a simple food packaging barrier with a pressure sensitive adhesive onto both sides of the foil.[13−15]

***IV*-Characterization.** In each coated stripe that represents one set of experiments a total of 150 solar cells were prepared (900 cells for each roll). The devices were light soaked with continuous sweeping of the *IV*-curve until a constant performance was reached. Typically the performance dropped rapidly during the first 10 min of light soaking followed by a slow improvement in performance over 4−6 h where a stable level of performance was reached. The data reported is for the stable regime. The devices were initially tested using a roll-to-roll tester and the functional devices were the recovered for further testing using a calibrated solar simulator (AM1.5G, 1000 W m^{-2}, 85 ± 5 °C). The prolonged testing was made according to the ISOS-L-1 procedure.[26]

Acknowledgment. This work was supported by the Danish National Research Foundation. We gratefully acknowledge the assistance of Steen Hansen with modifying the BIFT algorithm for use with polydisperse systems and Lasse Gorm Jensen for creating graphical illustrations.

Supporting Information Available: Details of the GISAXS analysis of solid films, with data and the description of the data reduction procedure; details of dewetting during coating. This material is available free of charge *via* the Internet at http://pubs.acs.org.

REFERENCES AND NOTES

1. Søndergaard, R.; Helgesen, M.; Jørgensen, M.; Krebs, F. C. Fabrication of Polymer Solar Cells Using Aqueous Processing for All Layers Including the Metal Back Electrode. *Adv. Eng. Mater.* **2011**, *1*, 68–71.
2. Rider, D. A.; Worfolk, B. J.; Harris, K. D.; Lalany, A.; Shahbazi, K.; Fleischauer, M. D.; Brett, M. J.; Buriak, J. M. Stable Inverted Polymer/Fullerene Solar Cells Using a Cationic Polythiophene Modified PEDOT:PSS Cathodic Interface. *Adv. Funct. Mater.* **2010**, *20*, 2404–2415.
3. Landfester, K. The Generation of Nanoparticles in Miniemulsions. *Adv. Mater.* **2001**, *13*, 765–768.
4. Kietzke, T.; Neher, D.; Landfester, K.; Montenegro, R.; Güntner, R.; Scherf, U. Novel Approaches to Polymer Blends Based on Polymer Nanoparticles. *Nat. Mater.* **2003**, *2*, 408–412.
5. Piok, T.; Gamerith, S.; Gadermaier, C.; Plank, H.; Wenzl, F. P.; Patil, S.; Montenegro, R.; Kietzke, T.; Neher, D.; Scherf, U.; *et al.* Organic Light-Emitting Devices Prepared from Semiconducting Nanospheres. *Adv. Mater.* **2003**, *15*, 800–804.
6. Kietzke, T.; Neher, D.; Kumke, M.; Montenegro, R.; Landfester, K.; Scherf, U. A Nanoparticle Approach to Control the Phase Separation in Polyfluorene Photovoltaic Devices. *Macromolecules* **2004**, *37*, 4882–4890.
7. Antonietti, M.; Landfester, K. Polyreactions in Miniemulsions. *Prog. Polym. Sci.* **2002**, *27*, 689–757.
8. Krebs, F. C.; Gevorgyan, S. A.; Alstrup, J. A Roll-to-Roll Process to Flexible Polymer Solar Cells: Model Studies, Manufacture, and Operational Stability Studies. *J. Mater. Chem.* **2009**, *19*, 5442–5442.
9. Espinosa, N.; García-Valverde, R.; Urbina, A.; Krebs, F. C. A Life Cycle Analysis of Polymer Solar Cell Modules Prepared Using Roll-to-Roll Methods Under Ambient Conditions. *Sol. Energy Mater. Sol. Cells* **2011**, *95*, 1293–1302.
10. Bundgaard, E.; Hagemann, O.; Jørgensen, M.; Krebs, F. C. Low-Band-Gap Polymers for Roll-to-Roll Coated Organic Photovoltaics Design, Synthesis and Characterization. *Green* **2011**, *1*, 55–64.
11. Hou, J.; Chen, H. Y.; Zhang, S.; Li, G.; Yang, Y. Synthesis, Characterization, and Photovoltaic Properties of a Low Band Gap Polymer Based on Silole-Containing Polythiophenes and 2,1,3-Benzothiadiazole. *J. Am. Chem. Soc.* **2008**, *130*, 16144–16145.
12. Wang, E.; Hou, L.; Wang, Z.; Hellström, S.; Zhang, F.; Inganäs, O.; Andersson, M. R. An Easily Synthesized Blue

Polymer for High-Performance Polymer Solar Cells. *Adv. Mater.* **2010**, *22*, 5240–5244.
13. Krebs, F. C.; Nielsen, T. D.; Fyenbo, J.; Wadstrøm, M.; Pedersen, M. S. Manufacture, Integration and Demonstration of Polymer Solar Cells in a Lamp for the "Lighting Africa" Initiative. *Energy Environ. Sci.* **2010**, *3*, 512–512.
14. Krebs, F. C.; Tromholt, T.; Jørgensen, M. Upscaling of Polymer Solar Cell Fabrication Using Full Roll-to-Roll Processing. *Nanoscale* **2010**, *2*, 873–886.
15. Alstrup, J.; Medford, A. J.; Jørgensen, M.; Krebs, F. C. Ultrafast and Parsimonious Materials Screening for Polymer Solar Cells Using Differentially Pumped Slot-Die Coating. *ACS Appl. Mater. Interfaces* **2010**, *2*, 2819–2827.
16. ASTM INTERNATIONAL Standards Worldwide. Standard Test Methods for Measuring Adhesion by Tape Test. p. 8.
17. Renner, R. Growing Concern over Perfluorinated Materials. *Environ. Sci. Technol.* **2001**, *35*, 154A–160A.
18. Yoneda, Y. Anomalous Surface Reflection of X-Rays. *Phys. Rev.* **1963**, *131*, 2010–2013.
19. Apitz, D.; Bertram, R.; Benter, N.; Hieringer, W.; Andreasen, J.; Nielsen, M.; Johansen, P.; Buse, K. Investigation of Chromophore-Chromophore Interaction by Electro-optic Measurements, Linear Dichroism, X-ray Scattering, and Density-Functional Calculations. *Phys. Rev. E* **2005**, *72*, 036610-1–036610-10.
20. Breiby, D. W.; Bunk, O.; Andreasen, J. W.; Lemke, H. T.; Nielsen, M. M. Simulating X-ray Diffraction of Textured Films. *J. Appl. Crystallogr.* **2008**, *41*, 262–271.
21. Villarrubia, J. Algorithm for Scanned Probe Microscope Image Simulation, Surface Reconstruction, and Tip Estimation. *J. Res. Natl. Inst. Stand. Technol.* **1997**, *102*, 425–454.
22. Hoo, C. M.; Starostin, N.; West, P.; Mecartney, M. L. A Comparison of Atomic Force Microscopy (AFM) and Dynamic Light Scattering (DLS) Methods to Characterize Nanoparticle Size Distributions. *J. Nanopart. Res.* **2008**, *10*, 89–96.
23. Boyd, R. D.; Cuenat, A. New Analysis Procedure for Fast and Reliable Size Measurement of Nanoparticles from Atomic Force Microscopy Images. *J. Nanopart. Res.* **2011**, *13*, 105–113.
24. Dias, A.; Buono, V. T. L.; Vilela, J. M. C.; Andrade, M. S.; Lima, T. M. Particle Size and Morphology of Hydrothermally Processed MnZn Ferrites Observed by Atomic Force Microscopy. *J. Mater. Sci.: Mater. Med.* **1997**, *32*, 4715–4718.
25. Krebs, F. C.; Søndergaard, R.; Jørgensen, M. Printed Metal Back Electrodes for R2R Fabricated Polymer Solar Cells Studied Using the LBIC Technique. *Sol. Energy Mater. Sol. Cells* **2011**, *95*, 1348–1353.
26. Reese, M. O.; Gevorgyan, S. A.; Jørgensen, M.; Bundgaard, E.; Kurtz, S. R.; Ginley, D. S.; Olson, D. C.; Lloyd, M. T.; Morvillo, P.; Katz, E. A.; *et al.* Consensus Stability Testing Protocols for Organic Photovoltaic Materials and Devices. *Sol. Energy Mater. Sol. Cells* **2011**, *95*, 1253–1267.

Solar Energy Materials & Solar Cells ∎ (∎∎∎∎) ∎∎∎–∎∎∎

Contents lists available at SciVerse ScienceDirect

Solar Energy Materials & Solar Cells

journal homepage: www.elsevier.com/locate/solmat

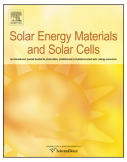

The state of organic solar cells—A meta analysis

Mikkel Jørgensen [a], Jon E. Carlé [a], Roar R. Søndergaard [a], Marie Lauritzen [a],
Nikolaj A. Dagnæs-Hansen [a], Sedi L. Byskov [a], Thomas R. Andersen [a],
Thue T. Larsen-Olsen [a], Arvid P.L. Böttiger [a], Birgitta Andreasen [a], Lei Fu [b], Lijian Zuo [b],
Yao Liu [c], Eva Bundgaard [a], Xiaowei Zhan [c], Hongzheng Chen [b], Frederik C. Krebs [a,*]

[a] *Department of Energy Conversion and Storage, Technical University of Denmark, Frederiksborgvej 399, DK-4000 Roskilde, Denmark*
[b] *State Key Laboratory of Silicon Materials, MOE Key Laboratory of Macromolecular Synthesis and Functionalization, Department of Polymer Science and Engineering, Zhejiang University, Hangzhou 310027, People's Republic of China*
[c] *Beijing National Laboratory for Molecular Sciences, CAS Key Laboratory of Organic Solids, Institute of Chemistry, Chinese Academy of Sciences, Beijing 100190, People's Republic of China*

ARTICLE INFO

Keywords:
Polymer solar cells
All data reported until 2012
Statistical analysis
Comparison with other PV
Tandem cells

ABSTRACT

Solar cells that convert sunlight into electrical power have demonstrated a large and consistent growth through several decades. The growth has spawned research on new technologies that potentially enable much faster, less costly and environmentally friendly manufacture from earth abundant materials. Here we review carbon based solar cells through a complete analysis of all the data that has been reported so far and we highlight what can be expected from carbon based technologies and draw scenarios of how it can be made of immediate use.

1. Introduction

Organic photovoltaic (OPV) research has been in an exponential growth phase since the early reports [1–6] as witnessed by the number of papers produced yearly and the number of new scientists joining the field. This is naturally due to the pressing problem of finding sustainable energy solutions for the future, but perhaps also because the OPV technology is actually not very mature and possess a rich complexity offering many opportunities for research. This also has consequences for commercial exploitation, seemingly representing an uphill battle for an inferior PV technology having to compete with superior and established PV technologies that when taken together have to compete with many high performing renewable technologies such as wind energy and hydropower [7,8]. The OPV technology is attracting because it promises to be very low cost, light weight, produced from abundant materials and easily manufactured at high speed in large scale on simple roll-to-roll printing machinery [9–11]. On the other hand there are some evident hurdles to overcome: the present power conversion efficiency (PCE) is very low (≤10%) while optimistic projections have been made [12,13] and the stability is also considered lacking [14,15]. Another problem that has not received much interest is the transition from square millimeter sized scientific devices arduously prepared in the laboratory to large scale technical production. In many ways it seems that the scientific pursuit of OPV has developed into a race for the best efficiency number through clever schemes of optimizing the chemistry and device fabrication rather than the more distant goal of producing practically useful solar cells. One of the reasons is perhaps that it is by no means settled which materials should be used and what the optimum construction of the OPV device is. It can thus be viewed as one of the attractions (and pitfalls) of OPV research that almost infinite variation is possible. The interesting question is whether research in OPV is indeed justified or whether it is simply an oversold scientific idea? If it is not what can we realistically expect from it? And finally, how would or could we make use of its distinctive features?

2. Seeing OPV “en large”

The progress of photovoltaic technologies is often summed up in a simple diagram of efficiency *versus* time and shows an impressive learning curve for OPV [13], but it is based on a few hero cells and does not reflect the overall status of the field. It would be far more interesting to have all the data to give a comprehensive overview and to be able to extract information on different types of OPV with respect to composition and fabrication. Unfortunately, PV device parameters are not directly accessible in a central database, but are distributed in the ca. 9000 individual

---

[*] Corresponding author. Tel.: +45 46 77 47 99.
E-mail address: frkr@dtu.dk (F.C. Krebs).

0927-0248/$ - see front matter © 2013 Elsevier B.V. All rights reserved.
http://dx.doi.org/10.1016/j.solmat.2013.05.034

Please cite this article as: M. Jørgensen, et al., The state of organic solar cells—A meta analysis, Solar Energy Materials and Solar Cells (2013), http://dx.doi.org/10.1016/j.solmat.2013.05.034

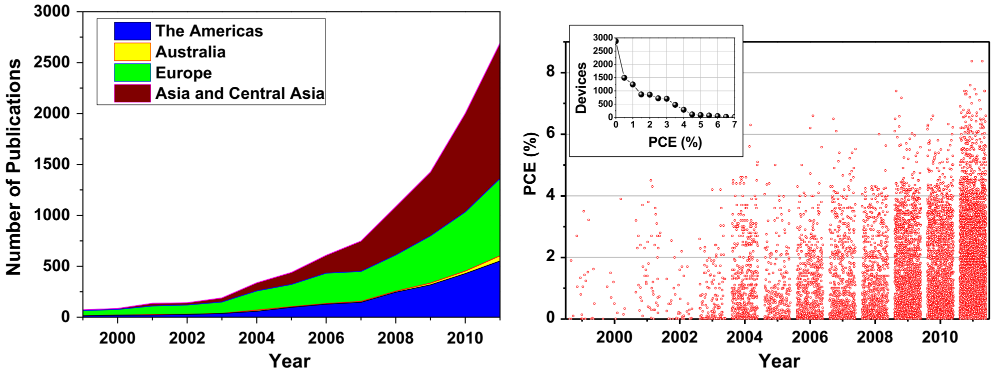

Fig. 1. Number of publications as a function of time with contributions from main countries (left). The PCE values obtained as a function of publication year (right). The inset show the distribution of PCE values.

scientific papers. We judged that this might be the last time that it would be feasible to collect these data by reading through each paper.[1] A search using the terms: "polymer solar cells" or "organic solar cells" were conducted in September 2011 using the Thomson Reuters Web of Knowledge database to compile a series of text files containing the bibliographic information including the digital object identifier (DOI) for each paper excluding review and conference proceeding papers; In total 8962 papers. An Excel database was constructed with a record for each solar cell device found in these papers. Each record has 26 fields comprising bibliographic information, materials used (polymers and acceptors), fabrication details and photovoltaic parameters of efficiency (PCE), open circuit voltage (V_{oc}), short circuit current density (J_{sc}), fill factor (FF), active area *etc.* The database was filled using a custom written program as a front to enter the data into the database read from each article. This resulted in a database of 10533 individual records of solar cells that are used as the basis for this paper. The process of reading papers and entering data took half a year with the help of a number of students and hired assistants. Recently, a smaller database study has been conducted on selected papers concerned with the P3HT:PCBM solar cell including 579 papers covering 2002–2010 [16]. Our aim was to construct a complete database covering all reports and we will in the following try to expose the actual state of OPV based on all publically available solar cell data rather than on single hero cells and also show that certain correlations appear some of which we believe are linked to PV based on carbon and others that may even reach beyond OPV to PV technologies at large.

3. The state of OPV

The search gave 8962 papers written by 15374 individual authors (by Jan 2012). Since year 2000 the growth has been exponential with over 2144 publications in 2011 from 6218 authors of which 5766 had not published in the previous years (in this field). In the beginning most of the contributions came from USA and European countries, but lately the Asia has taken lead. In this search the country of origin was taken from the address of the corresponding author. The exponential increase also means that about half of the authors have only contributed one paper and in the other end of the spectrum 169 (1%) authors have 25 or more papers and in total co-authored 4025 (45%) papers.

In Fig. 1 the PCE value of the individual 10533 solar cells are plotted against the year of submission for the paper. In most OPV papers the term "state of the art solar cells" are equated with the best or "hero" cells produced and these are normally used to indicate the status of the research field. It is clear that substantial progress is being made, but also that hero cells account for a very small part of the population and that they are not representative. Instead, the bulk of PCE values fall far below suggesting that these coveted results are actually rare exceptions. Remarkably, when the number of OPV devices is plotted as a function of PCE one does not get a normal distribution, but rather one that is skewed heavily toward zero PCE. This is in stark contrast to the study by Dang et al. [16] which only considered the maximum PCE for the limited and selected subset for P3HT:PCBM in 579 publications. One of the reasons is of course that the OPV field has become very complex with a huge number of possible variations in structure, chemical composition, fabrication history, interfacial layers *etc.* [17,18]. As a consequence many less performing devices are reported describing non-ideal choices. Some are also due to comparative studies varying different factors and others may simply reflect less competent procedures. It must also be a testament to how poorly defined and documented OPV production is. Even skilled workers may have a hard time duplicating hero cells because it involves factors that are simply unknown or not made public.

The PCE is a function of the product of the open circuit voltage (V_{OC}), short circuit density (J_{SC}) and fill factor (FF) divided by the incident power of the light source (P_i):

$$PCE = \frac{V_{OC} J_{SC} FF}{P_i} \tag{1}$$

When the PCE is plotted as a function of J_{SC} it appears that almost all OPV fall below a diagonal line corresponding to $PCE^{max} \sim 0.55 \times J_{SC}$ (Fig. 2, top left). Remarkably, the best inorganic solar cells also obey this rule except for gallium arsenide (GaAs) cells which have V_{OC} values above 1 V [19]. This limit to the PCE can be derived from the definition (Eq. (1)). For bulk heterojunction type OPV the upper limit for V_{OC} is believed to be determined by the energy difference between the LUMO energy level of the polymer/organic molecule donor and the HOMO energy level of the acceptor material [20–22]. It is further reduced by the exciton binding energy and other factors. The fill factor of OPV devices vary greatly, but rarely exceeds 60%. It immediately follows that the factor of 0.55 is simply the product of V_{OC}^{max} and FF^{max}. It is not a strict physical limit that cannot be overcome, but as the results show it seems very hard to do so. The V_{OC}^{max} is also a linear function of the band gap which means that there is a trade-

---

[1] A recent search (Aug 2012) resulted in 13151 papers.

Please cite this article as: M. Jørgensen, et al., The state of organic solar cells—A meta analysis, Solar Energy Materials and Solar Cells (2013), http://dx.doi.org/10.1016/j.solmat.2013.05.034

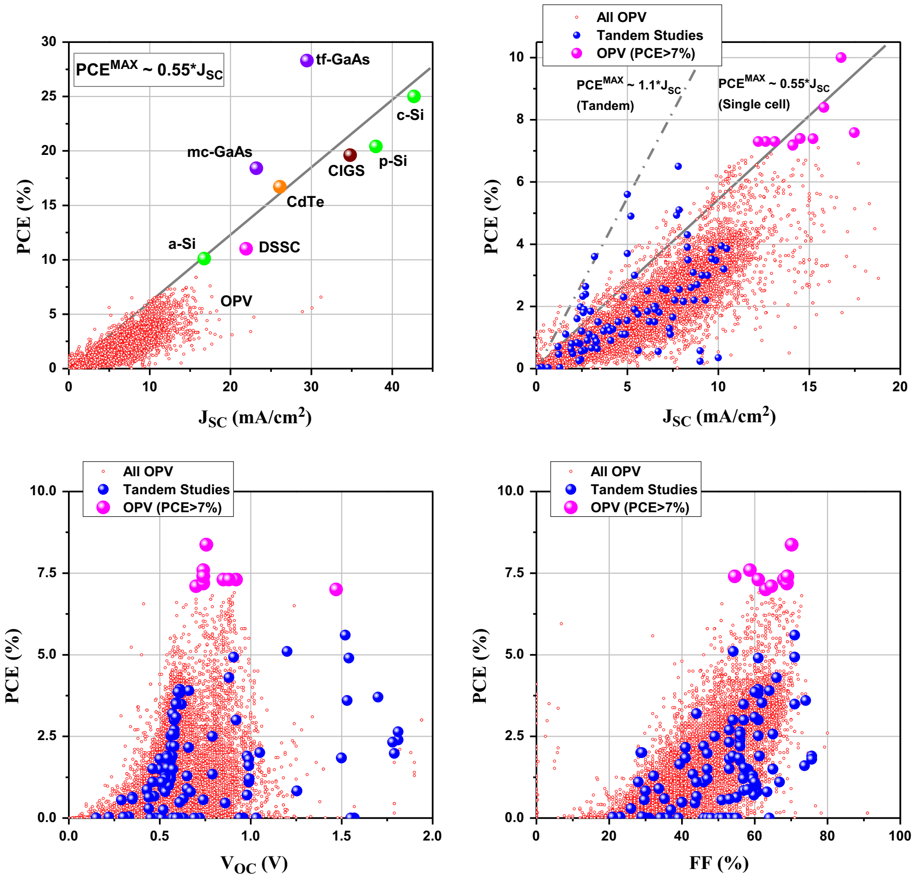

Fig. 2. Top left: A plot of PCE *versus* J_{SC} for all OPV data (small red circles) together with examples of the best inorganic PV devices (a-Si, p-Si, c-Si: amorphous, polycrystalline and crystalline silicon; DSSC: dye sensitized solar cell; mc-GaAs, tf-GaAs: multicrystalline and thin film Gallium Arsenide; CdTe: Cadmium Telluride; CIGS: Copper Indium Gallium Selenide). The line represents the correlation $PCE^{max}=0.55\times J_{SC}$. Top right: A close-up of the OPV region where values from tandem cell studies are marked as larger circles filled with blue color and hero cells with a $PCE>7\%$ is marked by circles filled with magenta color (this group also contains a few tandem cells). The solid gray line show the correlation $PCE^{max}=0.55\times J_{SC}$, while the dash-dot line represents the correlation $PCE^{max}=1.1\times J_{SC}$ expected for tandem cells. Bottom left: The plot of PCE *versus* V_{OC} show a narrow distribution of V_{OC} rarely exceeding 1 V. Bottom right: PCE *versus* fill factor (FF). (For interpretation of the references to color in this figure legend, the reader is referred to the web version of this article.)

off in using low band gap polymers that harvest more low energy photons in that it reduces the possible V_{OC}^{max} [23]. The fill factor is a complex function of the electrical resistance elements in the device which in part depend on the sheet resistance of the electrodes [20]. A common solution has been to decrease the cell size to less than 1 mm^2 to minimize these losses [24], which would of course also limit their use in any practical application. Previous authors have reviewed the theoretical limits for the PCE of single cell OPV and estimated upper bounds of 10–20% [12,25].

4. Outliers

An escape from the limitations of single cells is to construct tandem cell devices with two cells stacked on top of each other. The top and bottom cells should ideally harvest complementary regions of the spectrum and could at best double the V_{OC} [26–30]. The effect would be to increase the slope to obtain: $PCE^{max}=1.1\times J_{SC}$ doubling the possible efficiency. The number of papers describing tandem cells is still very small and the technical difficulties in the production of them seem to be very large [31–34]. Understandably, most of the cells reported are not optimal and it is yet impossible to judge if this correlation holds true. It is, however, intriguing that a few of the best small molecule OPVs actually follow this prediction very closely [35].

Due to the limited spectral absorption range of the active components of OPV it has proven very hard to increase J_{SC} beyond 15 mA/cm^2 [36]. These few (18) data points therefore deserve extra scrutiny. Chan et al. described two Copper Phthalocyanine/Rubrene based devices with staggering $J_{SC}=22.9$ mA/cm^2, PCE$=4.72\%$ and $J_{SC}=30.1$ mA/cm^2, $PCE=5.58\%$ [37]. Kim et al. used an optimized FTO electrode with the standard active layer mixture P3HT:PCBM to give four devices with J_{SC} 16.8–22.5 mA/cm^2 [38]. A few of these high J_{SC} data points are due to devices with low band gap materials. Chen et al. described a silole-benzothiadiazole based copolymer (DTS-BDT) ($J_{SC}=16.5$ mA/cm^2) [39]. Exchanging silicon for germanium Fei et al. obtained devices with $J_{SC}=18.4$ and 18.6 mA/cm^2 [40]. In such cases

Please cite this article as: M. Jørgensen, et al., The state of organic solar cells—A meta analysis, Solar Energy Materials and Solar Cells (2013), http://dx.doi.org/10.1016/j.solmat.2013.05.034

experimental detail concerning the light source and illumination condition would enable more in depth analysis.

5. Polymers and acceptors

Each record in our database also contained fields for a crude division of which polymers and acceptors were used. The polymers were subdivided into five categories: P3HT, MEH-PPV, MDMO-PPV, other polymers (mainly low band gap polymers) and none (usually molecular solar cells). Fig. 3 shows how the relative number of devices with these polymer categories are distributed for the J_{SC} and V_{OC} parameters.

The J_{SC} distribution for P3HT show a broad peak centered at 8 mA/cm^2 with a tail out to ca. 12.5 mA/cm^2 while the V_{OC} distribution show a very sharp peak at 0.6 V. If a fairly decent fill factor of 60% is chosen this would imply that P3HT containing devices should give PCE values in the range of 2.5–4.5%. In the case of the two other polymer categories the J_{SC} distribution has no prominent peaks, but are rather dominated by a large population of low performance devices. For the “Other Polymers” category there is, however, a small peak around 14 mA/cm^2 which is due to low band gap polymers that can harvest a greater portion of the spectrum relative to P3HT [40–42]. This category is of course diverse and thus contains many examples of polymers that do not work well in OPV. In the V_{OC} distribution both the PPV and the “Other Polymer” categories show sharp peaks with PPV centered at 0.82 V while “Other Polymers” have two maxima at 0.63 V and 0.83 V. A similar subdivision was performed for different types of acceptor materials as shown in Fig. 4.

In the case of acceptor materials a somewhat larger selection were used to subdivide the data. Solar cells incorporating C60, C70, [60] PCBM and Bis [60] PCBM are mainly located in the lower left hand corner of the PCE *versus* J_{SC} plot, whereas those with [70] PCBM and ICBA stretch further up giving more efficient devices. The effect of the acceptor type on the V_{OC} can be seen in the plot of the relative number

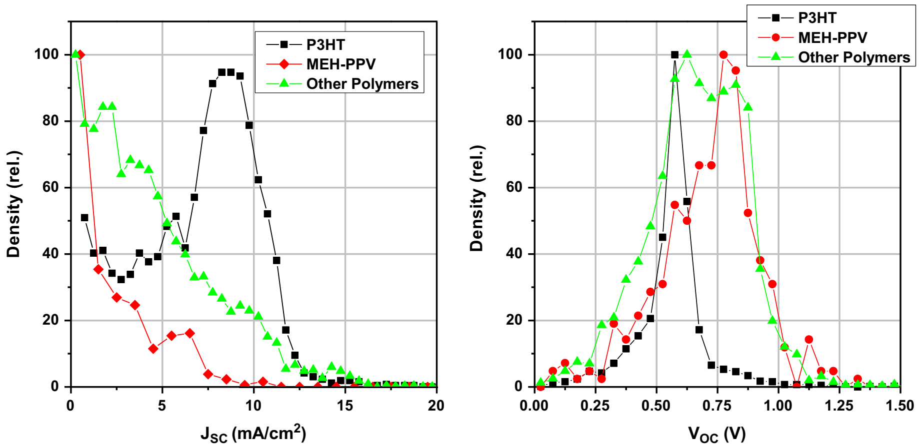

Fig. 3. Relative number of devices *versus* J_{SC} (left) and V_{OC} (right) for different polymer types.

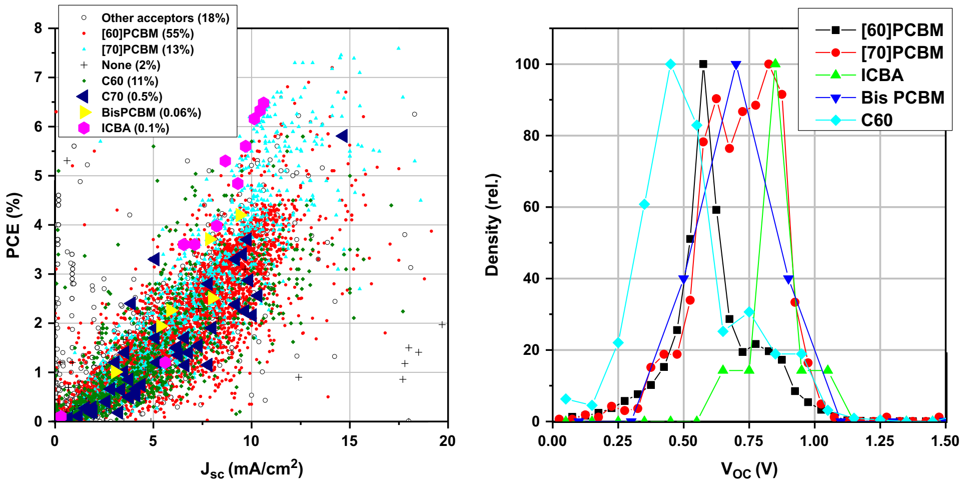

Fig. 4. PCE *versus* J_{SC} plot (left) and relative number of devices *versus* V_{OC} plot (right) for different types of acceptor materials used.

Please cite this article as: M. Jørgensen, et al., The state of organic solar cells—A meta analysis, Solar Energy Materials and Solar Cells (2013), http://dx.doi.org/10.1016/j.solmat.2013.05.034

of devices *versus* V_{OC} (Fig. 3, right) where it is clear that C60 and [60]. PCBM give lower values than [70]. PCBM, ICBA and Bis-PCBM.

The improvements in efficiency have been gained both in increased light harvesting resulting in a larger J_{SC}, but also by significantly increasing the V_{OC}. The main factors are obviously the shift from higher to lower band gap polymers and the choice of acceptors to match energy levels for maximizing the V_{OC} [43–46]. It is therefore interesting to look at the combined effects of the polymer and acceptor. We selected four categories: P3HT or other polymers with either [60] PCBM or [70]. PCBM. The result is shown in Fig. 5 as a plot of PCE *versus* J_{SC} for all four types of devices and a plot of V_{OC} *versus* J_{SC} of the mean values of the four categories. Exchanging [60] PCBM for [70] PCBM increases both the J_{SC} and V_{OC} though the effect is larger for the "Other Polymer" types ($\Delta J_{SC}\sim$1.4 mA/cm^2, $\Delta V_{OC}\sim$0.15 V). This can probably be explained by assuming that many new low band gap materials ("Other Polymers") have been engineered so that their energy levels have been optimized for [70] PCBM [47,48].

6. Annealing and additives

In most OPV devices the active layer responsible for photon absorption and carrier generation is of the bulk heterojunction type where the donor (polymer) and acceptor microphase separate into a bi-continuous network with a high internal surface where electron hole separation can take place and act as channels for transport of the two carrier types [49–52]. The optimum

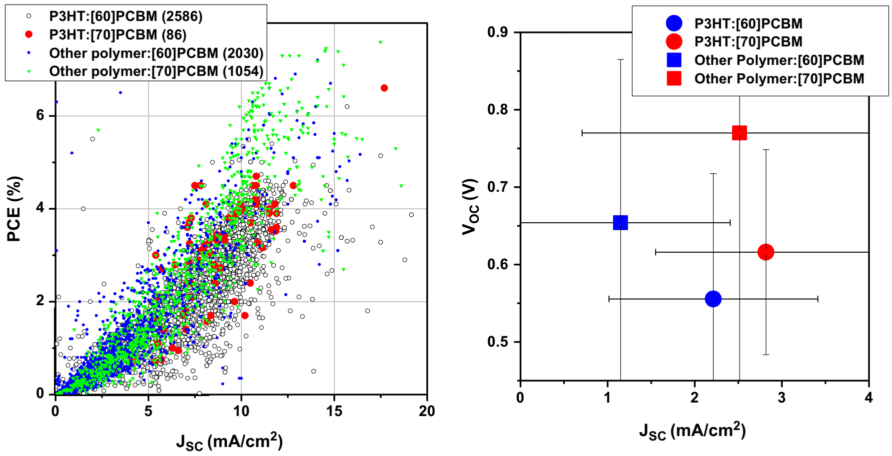

Fig. 5. Comparison of P3HT *versus* other polymers with either [60] PCBM or [70] PCBM.

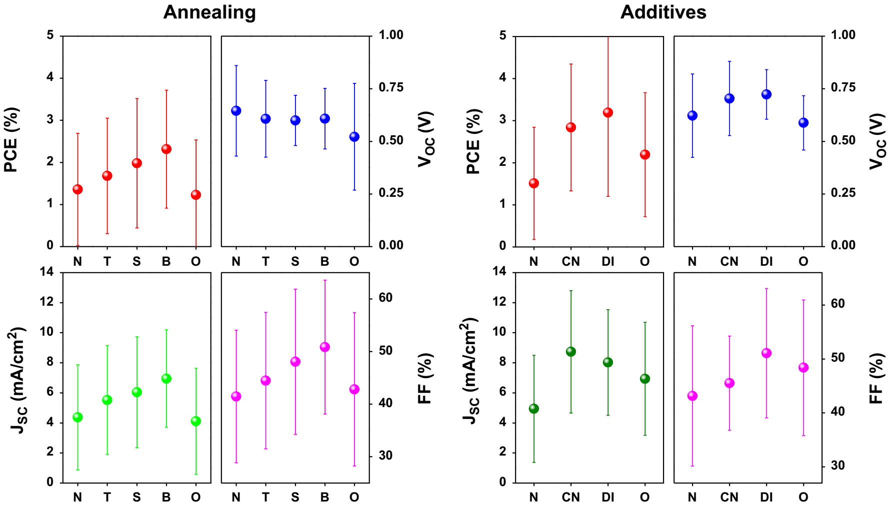

Fig. 6. Left: variation in mean values of solar cell parameters for devices annealed with different methods. (*N*: no annealing; *T*: temperature annealing; *S*: solvent annealing; *B*: both temperature and solvent annealing, *O*: Other annealing method). Right: variation of solar cell parameters with additives. (N: none; CN: 1-chloro-naphthalene; DI:1,8-diiodooctane; and O: other additive).

Please cite this article as: M. Jørgensen, et al., The state of organic solar cells—A meta analysis, Solar Energy Materials and Solar Cells (2013), http://dx.doi.org/10.1016/j.solmat.2013.05.034

morphology may require some post treatment procedures and the most common method is to anneal the devices by heating them for a short period of time [53–55]. An alternative option is to expose the devices to solvent vapors that have been proposed to dissolve selectively into one of the components of the active layer mobilizing it enough to help the morphology to change [56–58]. A statistical analysis was carried out with the result shown in the plots in Fig. 6 left which clearly show that both temperature and solvent annealing increases PCE, mainly through increases in J_{SC} and FF, while V_{OC} is negatively affected.

Another popular stratagem is to use additives such as 1,8-diiodooctane or 1-chloronaphthalene to the active layer solution which increase the efficiency [45,59–62] as shown in Fig. 6 right. This time the better PCE is due to increases in all the parameters: V_{OC}, J_{SC} and FF. Molecular OPV devices account for 14% of the database where the active layer may be composed of discrete molecules of compounds such as phthalocyanines (CuPc, ZnPc), pentacene, tetracene, oligothiophenes [63–66]. Typical devices are constructed using chemical vapor deposition of these compounds sometimes creating gradients or mixtures of several of these to obtain bulk heterojunction type structures [67].

7. Normal *versus* inverted geometry

One of the important developments in OPV has been the shift from “normal” geometry of the OPV stack, where electrons exit from the top electrode (usually aluminum) and holes from the bottom (usually ITO), to the “inverted” geometry where electrons exit at the bottom and holes at the top [68–70]. This change allows (or determine) the use of other metals such as silver to be used as the top electrode which are much more resistant to oxygen and water [14,71,72]. The result is usually far more stable OPV devices that with proper encapsulation may even last for years alleviating the operational stability challenge [73–75]. The normal geometry is still by far the most common accounting for 90% even in 2011. It also still has a slight edge over the inverted geometry in terms of PCE and J_{SC} as seen in Fig. 7.

8. Fabrication methods and environment

The standard method of fabricating OPV is still using spin coating to apply thin layers of solutions such as the polymer: acceptor and PEDOT:PSS. The reason for its widespread use is of course that it is a simple technology offering some control over the wet thickness of the film [76]. On the other hand it also constrains experiments to small individual rigid substrates which are far removed from any projected industrial production of OPV. Much of today's literature on OPV focuses on methods to optimize the efficiency and they may be hard to transfer from the laboratory to an industrial process [9]. So there is a real danger that much of this effort will have to be duplicated when a shift to roll-to-roll (R2R) fabrication methods occur. Most fabrication environments include a glovebox to minimize exposure to oxygen/water that are known to rapidly degrade devices [10,14,15]. Substrates are almost exclusively glass with a layer of ITO acting as one electrode. Finally nearly all fabrication methods involve a vacuum step such as evaporation of a metal electrode. R2R fabrication on flexible

Table 1
Fabrication methods and environment.

Fabrication method		Environment		Substrate		Vacuum	ITO
Spin Coating	86%	**Glovebox**	90%	**Glass**	99%	99%	95%
Roll-to-roll (R2R)	0.5%	**Ambient air**	10%	**Flexible**	0.5%		
Unknown or other	13%						

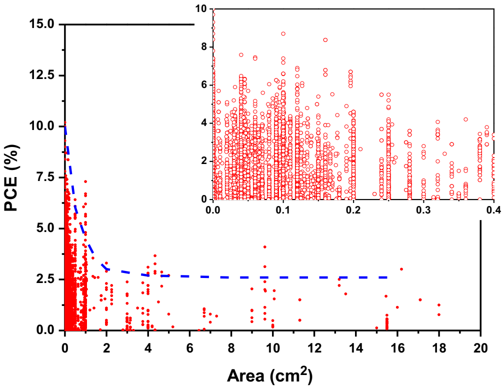

Fig. 8. A plot of the power conversion efficiency as a function of active area. The dotted blue curve is a guide to the eye. The insert is a zoom in on areas below 0.4 cm^2 that are very popular.

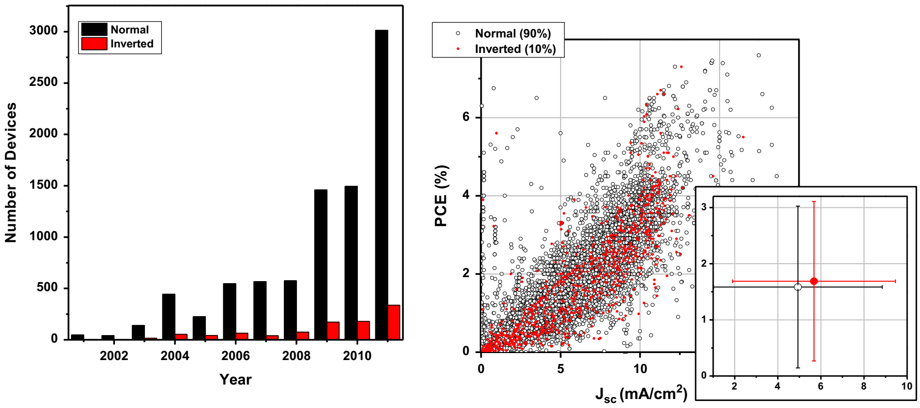

Fig. 7. Normal *versus* inverted geometry of the OPV stack. Number of devices per year (left). PCE *versus* J_{SC} (right).

Please cite this article as: M. Jørgensen, et al., The state of organic solar cells—A meta analysis, Solar Energy Materials and Solar Cells (2013), http://dx.doi.org/10.1016/j.solmat.2013.05.034

substrates only account for 0.5% of the solar cell devices listed in the literature (Table 1). It must be mentioned, however, that at least one study has been carried out with R2R production of 10,000 solar cell modules (160,000 solar cells) made over a few days which is similar to the total number of devices in the present study [77]. This demonstrates the huge difference in production speed between these two modes of fabrication.

9. The active area of OPV

Mature photovoltaic technologies usually measure the device area in many square centimeters and upwards. Most OPV devices on the other hand are less than 0.2 cm^2 as shown in Fig. 8. One reason is the larger sheet resistivity of ITO compared to metals such as silver limiting the charge collection and thus also the efficiency [24]. Although the data is limited for device areas above 1 cm^2 it seems the efficiency falls of exponentially with size at very small active areas and stabilize at higher active areas. How the sheet resistivity influences the maximum obtainable PCE depends on the geometry of the device and use of metal bus bars to help charge collection [78]. In a typical layout this would lead to a more linear dependence between PCE and the area which does not seem in accordance with the data. Another factor that must be considered is the uncertainty in measuring the area correctly [79]. For a rectangular device with an area of *e.g.* 0.04 cm^2 which seems very popular this means accurately determining side lengths of 2 mm. Reporting the correct efficiency is not trivial involving both the accurate determination of the active area, the lamp power (if using a solar simulator) and the accurate measurement of small currents in an IV curve. This has led to a number of recommendations on how to perform and report these measurements [80]. Many authors advocate that exceptionally high efficiencies be checked by certified institutions such as NREL or Fraunhofer ISE and others. This is, however, a costly and time consuming practice that has not been widely adopted. A common practice is to use a shadow mask in front of the solar cell to define the illuminated area. This of course serves to define the active area and eliminate errors in harvesting light outside the active area, but still involves the accurate measurement of the aperture of the mask [81]. Other subtle errors are also introduced by this procedure due to the distance between the mask and the active layer and the amount of diffuse light from the lamp in comparison to the real sun which is outside the scope of this review [82–84]. The data suggests that it might be appropriate to also set a minimum standard area for the measurement of OPV efficiency. It is also striking that while most authors adhere to the promise of OPV as a low cost alternative to mature PV technologies the combined active area of all the laboratory scale OPV devices only cover 0.98 m^2 and the 86% of the devices which have an area of less than or equal to 0.2 cm^2 amount to only 0.04 m^2 in total.

10. Seeing the field of OPV from above

It is clear that the field of OPV has drawn an enormous number of researchers to it and from the analysis above it is also evident that the furtherance of the field will require some mode of direction other than what is in operation today. Currently the research carried out in the field is self-justified with a few exponents defining research targets through achievement of extreme values for a single parameter which is most often the efficiency but also the operational stability has been used as a metric [1,2,4–6,54,69,70,85,86]. In achieving those values which serve as a firm ground for competition the field is in near contradiction with the original vision of OPV. To recite the advantages of OPV (and perhaps also its purposes) they are large area, flexible solar cells with a thin outline prepared under ambient conditions using fast modes of manufacture without the use of scarce elements such as indium, silver, gold or toxic solvents [87–89]. State-of-the-art OPV falls far from the vision in all these aspects [90]. The clearest conclusion to draw from the database study above (Fig. 8) is perhaps that the active area that one should as a minimum employ is 1 cm^2 and perhaps 4–5 cm^2 is a more conservative measure guaranteeing some level of scalability based on a report. It is, however, unreasonable to expect that scientists are willing to (or can) change the set of rules that are already in operation. It must also be borne in mind that this commonly practiced approach is linked to the questions of how good a value that can be achieved? but also to whom the result is addressed? The answer to the former question is still open while the data presented in Fig. 2 does show some clear boundaries. The answer to the latter question is that it is mostly for the scientists themselves in their isolated community. To change it, in the aim of widespread practical dissemination of OPV for energy production we would have to create a new and valiant purpose or indeed pursue the original purpose as per the vision of OPV. A second observation that might be partly linked to the active area is that OPV would seem to follow the empirical relationship plotted in Fig. 2 and thus imply that practical total area efficiencies for single junction carbon based PV will be around 5% (and perhaps 8% for tandem solar cells) when deployed over many square meters.

11. The new ground for competition

The most natural way to approach the vision of OPV would simply be to create meaningful energy with it and this would also resolve the challenge outlined above. The best measure of the usefulness of an energy technology is how fast it pays back the energy invested in it which is known as the energy payback time (EPBT) [91,92] and how many times it can do this in its service life known as the energy return factor (ERF) [91]. To be useful as a technology and do less harm to the environment requires that the ERF is significantly larger than one unless the technology in question (OPV) replaces something worse or more harmful [93]. The most obvious approach would be to measure the amount of electricity delivered to the electricity grid by reporting the reading from an electricity meter and relating it to the total area of the platform as exposed to the sun in a given geographical location. Clearly the area should be meaningful and on the order of square meters in an effort to allow for easy comparison to other PV technologies but also other renewable energy technologies. The calculation of the EPBT is achieved through life cycle analysis (LCA) and requires quite extensive knowledge of the process and also of the origin of all the ingredients entering the process leading to OPV [87,89,92–94]. Turning things upside down using such an approach may seem radical but is likely to be the necessary step up for OPV thus establishing whether it is indeed justifiably viewed as an energy technology or whether it is a phantom of scientific thinking.

12. What an OPV plant should look like and how it is different

Under the assumption given above that single junction carbon based solar cells will maximally yield 5% power conversion efficiency on the total area (for square meter sized panels) in a form that can be mass produced, it is possible to pose the question of how an OPV power plant should be constituted to be useful? Firstly, the general view is that solar parks based on crystalline silicon solar cells are barely profitable due to the performance which is viewed as low for the purpose (12–20%) unless the geographic location provides favorable conditions in the form of

Please cite this article as: M. Jørgensen, et al., The state of organic solar cells—A meta analysis, Solar Energy Materials and Solar Cells (2013), http://dx.doi.org/10.1016/j.solmat.2013.05.034

a high degree of insolation or the local policy enables investment through favorable subsidy. It is thus clear that for a solar park based on OPV with the premise that the maximally achievable total area power conversion efficiency is 5% (8% on tandem architectures) will be unsuccessful if it is simply a deployment following the same methods as those currently employed for crystalline silicon solar cells [7,91]. This somber (but factual) view of the future of OPV will come true unless one takes specific advantage of the competitive edges that OPV does present while circumventing the distinct weaknesses that OPV admittedly also possess. To summarize, the weaknesses are linked solely to the power conversion efficiency [95–97] and the operational stability [14,90] and in the following we assume a total (large) area efficiency of 5% for single junctions and an operational lifetime under outdoor conditions of 5 years. The list of competitive edges of OPV compared to other solar cell technologies is long and even when compared to other renewable energy technologies OPV does have significant vantage points. The OPV technology is the only renewable energy technology that enables energy payback times of less than a few months, it is also the only technology that in spite of the relatively short service life potentially offer energy return factors in excess of 100 [91]. Finally, it is also the only energy technology that enables ultra-fast manufacture of a given energy producing unit [91]. This all implies that the OPV technology is already competitive and one can ask why it is not in use yet. The answer to this question is linked to the low performance and the consequent requirement for a large landmass. Also to make use of the advantages listed above the mode of deployment and the scaffold used for mounting the OPV has to be significantly different from traditional PV and clearly the landmass has to be available at very low cost. Arid regions that have no agricultural value are an obvious choice for PV and would be mandatory in the case of large scale deployment of OPV. Since insolation in such regions is usually high this would also be beneficial. One advantage of OPV is that it can be printed on flexible foil in near endless form [9] and if this property was employed in the deployment such that for instance a roll of solar cells was installed by simply rolling it out along a long fixed scaffold the installation rates would exceed panel based PV by several orders of magnitude such that the installation rate ideally matches the manufacturing rate. This implies that the installation would have to be achieved in an automated fashion and would also have to enable simultaneous de-installation for potential re-use while reinstalling new OPV at the end of the service life. The scaffold would of course be a lasting and reusable structure. We can thus outline how OPV should be installed to be useful and also highlight that this can already be realized with the currently available version of OPV. In the ultimate vision OPV is deployed in conjunction with other large renewable energy harvesting parks such as solar farms on- or off-shore thus minimizing infrastructure requirements and thus exploiting the synergy inherent in the complementarity between the different renewable energy technologies such as wind and solar power.

13. Conclusions

We compiled a database with all reported data for organic and polymer solar cells and found more than 10,000 recorded observations. We presented all these data in the context of photovoltaics in general and viewed single junction and tandem OPV. We also analyzed the effect of post processing treatments such as thermal annealing and solvent additives and viewed all these data. We found an enormous spread in data and that the reported high performance of OPV is resting on a few reports whereas the vast majority fall much lower and we conclude that the technological performance of OPV is much lower than the reported state-of-the art. The possible reason for this is an observed exponential increase in reported efficiency with decreasing active area and we propose that and active area $> 1\ \mathrm{cm}^2$ should be employed to obtain meaningful data. To conclude, the polymer and organic solar cells have to rise to power in grid connected installations and focus should be turned to a gain in widespread use or alternatively we have to accept it as a stimulating scientific discipline serving the purpose of being a useful educational tool for the academic environment.

Acknowledgments

This work was supported the Danish National Research Foundation.

Reference

[1] C.W. Tang, 2-Layer organic photovoltaic cell, Applied Physics Letters 48 (1986) 183–185.
[2] S.E. Shaheen, C.J. Brabec, N.S. Sariciftci, F. Padinger, T. Fromherz J.C. Hummelen, 2.5% efficient organic plastic solar cells, Applied Physics Letters 78 (2001) 841–843.
[3] P. Peumans, S. Uchida, S.R. Forrest, Efficient bulk heterojunction photovoltaic cells using small-molecular-weight organic thin films, Nature 425 (2003) 158–162.
[4] N.S. Sariciftci, L. Smilowitz, A.J. Heeger, F. Wudl, Photoinduced electron-transfer from A conducting polymer to buckminsterfullerene, Science 258 (1992) 1474–1476.
[5] S. Morita, A.A. Zakhidov, K. Yoshino, Doping effect of buckminsterfullerene in conducting polymer: Change of absorption spectrum and quenching of luminescene, Solid State Communications 82 (1992) 249–252.
[6] J.J.M. Halls, C.A. Walsh, N.C. Greenham, E.A. Marseglia, R.H. Friend, S.C. Moratti, A.B. Holmes, Efficient photodiodes from interpenetrating polymer networks, Nature 376 (1995) 498–500.
[7] B. Azzopardi, C.J.M. Emmott, A. Urbina, F.C. Krebs, J. Mutale, J. Nelson, Economic assessment of solar electricity production from organic-based photovoltaic modules in a domestic environment, Energy and Environmental Science 4 (2011) 3741–3753.
[8] T.D. Nielsen, C. Cruickshank, S. Foged, J. Thorsen, F.C. Krebs, Business, market and intellectual property analysis of polymer solar cells, Solar Energy Materials and Solar Cells 94 (2010) 1553–1571.
[9] R. Søndergaard, M. Hösel, D. Angmo, T.T. Larsen-Olsen, F.C. Krebs, Roll-to-roll fabrication of polymer solar cells, Materials Today 15 (2012) 36–49.
[10] Y. Galagan, I.G. de Vries, A.P. Langen, R. Andriessen, W.J.H. Verhees S.C. Veenstra, J.M. Kroon, Technology development for roll-to-roll production of organic photovoltaics, Chemical Engineering and Processing 50 (2011) 454–461.
[11] F.C. Krebs, J. Fyenbo, M. Jørgensen, Product integration of compact roll-to-roll processed polymer solar cell modules: methods and manufacture using flexographic printing, slot-die coating and rotary screen printing, Journal of Materials Chemistry 20 (2010) 8994–9001.
[12] M.C. Scharber, D. Wuhlbacher, M. Koppe, P. Denk, C. Waldauf, A.J. Heeger C.L. Brabec, Design rules for donors in bulk-heterojunction solar cells—towards 10% energy-conversion efficiency, Advanced Materials 18 (2006) 789–794.
[13] C.J. Brabec, S. Gowrisanker, J.J. Halls, D. Laird, S. Jia, S.P. Williams, Polymer-fullerene bulk-heterojunction solar cells, Advanced Materials 22 (2010) 3839–3856.
[14] M. Jørgensen, K. Norrman, S.A. Gevorgyan, T. Tromholt, B. Andreasen F.C. Krebs, Stability of polymer solar cells, Advanced Materials 24 (2012) 580–612.
[15] N. Grossiord, J.M. Kroon, R. Andriessen, P.W.M. Blom, Degradation mechanisms in organic photovoltaic devices, Organic Electronics 13 (2012) 432–456.
[16] M.T. Dang, L. Hirsch, G. Wantz, P3HT:PCBM, best seller in polymer photovoltaic research, Advanced Materials 23 (2011) 3597–3602.
[17] G. Li, R. Zhu, Y. Yang, Polymer solar cells, Nature Photonics 6 (2012) 153–161.
[18] S.R. Forrest, The path to ubiquitous and low-cost organic electronic appliances on plastic, Nature 428 (2004) 911–918.
[19] H. Matsubara, T. Tanabe, A. Saegusa, S. Takagishi, T. Shirakawa, GaAs solar cell with GaInP window grown by all metalorganic source MOVPE, in: Proceedings of the IEEE Photovoltaic Specialists Conference vol. 2 (1994) pp. 1871–1873.
[20] C. Winder, N.S. Sariciftci, Low bandgap polymers for photon harvesting in bulk heterojunction solar cells, Journal of Materials Chemistry 14 (2004) 1077–1086.
[21] T.M. Clarke, J.R. Durrant, Charge photogeneration in organic solar cells, Chemical Reviews 110 (2010) 6736–6767.
[22] S. Yamamoto, A. Orimo, H. Ohkita, H. Benten, S. Ito, H. Ohkita, Molecular understanding of the open-circuit voltage of polymer:fullerene solar cells, Advanced Energy Materials 2 (2012) 229–237.
[23] R. Kroon, M. Lenes, J.C. Hummelen, P.W.M. Blom, B. de Boer, Small bandgap polymers for organic solar cells (polymer material development in the last 5 years), Polymer Reviews 48 (2008) 531–582.

Please cite this article as: M. Jørgensen, et al., The state of organic solar cells—A meta analysis, Solar Energy Materials and Solar Cells (2013), http://dx.doi.org/10.1016/j.solmat.2013.05.034

[24] J.D. Servaites, S. Yeganeh, T.J. Marks, M.A. Ratner, Efficiency enhancement in organic photovoltaic cells: consequences of optimizing series resistance, Advanced Functional Materials 20 (2010) 97–104.

[25] Z.M. Beiley, M.D. McGehee, Modeling low cost hybrid tandem photovoltaics with the potential for efficiencies exceeding 20%, Energy and Environmental Science 5 (2012) 9173–9179.

[26] L. Dou, J. You, J. Yang, C.C. Chen, Y. He, S. Murase, T. Moriarty, K. Emery, G. Li, Y. Yang, Tandem polymer solar cells featuring a spectrally matched low-bandgap polymer, Nature Photonics 6 (2012) 180.

[27] S. Sista, Z. Hong, L.M. Chen, Y. Yang, Tandem polymer photovoltaic cells-current status, challenges and future outlook, Energy and Environmental Science 4 (2011) 1606–1620.

[28] J.Y. Kim, K. Lee, N.E. Coates, D. Moses, T.Q. Nguyen, M. Dante, A.J. Heeger, Efficient tandem polymer solar cells fabricated by all-solution processing, Science 317 (2007) 222–225.

[29] J. Gilot, M.M. Wienk, R.A.J. Janssen, Optimizing polymer tandem solar cells, Advanced Materials 22 (2010) E67–E71.

[30] T. Ameri, G. Dennler, C. Lungenschmied, C.J. Brabec, Organic tandem solar cells: a review, Energy and Environmental Science 2 (2009) 347–363.

[31] T.T. Larsen-Olsen, T.R. Andersen, B. Andreasen, A.P. Böttiger, E. Bundgaard, K. Norrman, J.W. Andreasen, M. Jørgensen, F.C. Krebs, Roll-to-roll processed polymer tandem solar cells partially processed from water, Solar Energy Materials and Solar Cells 97 (2012) 43–49.

[32] A. Hadipour, B. de Boer, J. Wildeman, F.B. Kooistra, J.C. Hummelen, M.G. R. Turbiez, M.M. Wienk, R.A.J. Janssen, P.W.M. Blom, Solution-processed organic tandem solar cells, Advanced Functional Materials 16 (2006) 1897–1903.

[33] A. Hadipour, B. de Boer, P.W.M. Blom, Organic tandem and multi-junction solar cells, Advanced Functional Materials 18 (2008) 169–181.

[34] V. Shrotriya, G. Li, Y. Yao, C.W. Chu, Y. Yang, Transition metal oxides as the buffer layer for polymer photovoltaic cells, Applied Physics Letters 88 (2006) 073508-1–073508-3.

[35] M. Riede, C. Uhrich, J. Widmer, R. Timmreck, D. Wynands, G. Schwartz, W. Gnehr, D. Hildebrandt, A. Weiss, J. Hwang, S. Sundarraj, P. Erk, M. Pfeiffer, K. Leo, Efficient organic tandem solar cells based on small molecules, Advanced Functional Materials 21 (2011) 3019–3028.

[36] Y. Li, Molecular design of photovoltaic materials for polymer solar cells: toward suitable electronic energy levels and broad absorption, Accounts of Chemical Research 45 (2012) 723–733.

[37] M.Y. Chan, S.L. Lai, M.K. Fung, C.S. Lee, S.T. Lee, Doping-induced efficiency enhancement in organic photovoltaic devices, Applied Physics Letters 90 (2007) 089902-1–089902-2.

[38] H. Kim, G.P. Kushto, R.C.Y. Auyeung, A. Piqué, Optimization of F-doped SnO_2 electrodes for organic photovoltaic devices, Applied Physics A 93 (2008) 521–526.

[39] S. Chen, K.R. Choudhury, J. Subbiah, F. So, C.M. Amb, J.R. Reynolds, Photo-carrier recombination in polymer solar cells based on P3HT and silole-based copolymer, Advanced Energy Materials 1 (2011) 963–969.

[40] Z. Fei, J.S. Kim, J. Smith, E.B. Domingo, T.D. Anthopoulos, N. Stingelin, S. E. Watkins, J.S. Kim, M. Heeney, A low band gap co-polymer of dithienogermole and 2,1,3-benzothiadiazole by Suzuki polycondensation and its application in transistor and photovoltaic cells, Journal of Materials Chemistry 21 (2011) 16257–16263.

[41] B.C. Thompson, J.M.J. Frechet, Organic photovoltaics—polymer–fullerene composite solar cells, Angewandte Chemie-International Edition 47 (2008) 58–77.

[42] J. Hou, H.Y. Chen, S.Q. Zhang, G. Li, Y. Yang, Synthesis, characterization, and photovoltaic properties of a low band gap polymer based on silole-containing polythiophenes and 2,1,3-benzothiadiazole, Journal of the American Chemical Society 130 (2008) 16144–16145.

[43] E. Wang, L. Hou, Z. Wang, S. Hellström, F. Zhang, O. Inganäs, M.R. Andersson, An Easily Synthesized Blue Polymer for High-Performance Polymer Solar Cells, Advanced Materials 22 (2010) 5240–5244.

[44] E.G. Wang, L. Wang, L.F. Lan, C. Luo, W.L. Zhuang, J.B. Peng, Y. Cao, High-performance polymer heterojunction solar cells of a polysilafluorene derivative, Applied Physics Letters 92 (2008) 033307-1–033307-3.

[45] T.Y. Chu, J. Lu, S. Beaupre¦ü, Y. Zhang, J.R.ü. Pouliot, S. Wakim, J. Zhou, M. Leclerc, Z. Li, J. Ding, Y. Tao, Bulk heterojunction solar cells using thieno [3,4-c]pyrrole-4,6-dione and dithieno[3,2-b:2',3'-d]silole copolymer with a power conversion efficiency of 7.3%, Journal of the American Chemical Society 133 (2011) 4250–4253.

[46] J. Yuan, Z. Zhai, H. Dong, J. Li, Z. Jiang, Y. Li, W. Ma, Efficient polymer solar cells with a high open circuit voltage of 1 V, Advanced Functional Materials (2012) 885–892.

[47] M. Zhang, X. Guo, Y.F. Li, Synthesis and characterization of a copolymer based on thiazolothiazole and dithienosilole for polymer solar cells, Advanced Energy Materials 1 (2011) 557–560.

[48] J.C. Bijleveld, A.P. Zoombelt, S.G.J. Mathijssen, M.M. Wienk, M. Turbiez, D.M. de Leeuw, R.A.J. Janssen, Poly(diketopyrrolopyrrole-terthiophene) for ambipolar logic and photovoltaics, Journal of the American Chemical Society 131 (2009) 16616.

[49] S. Bertho, G. Janssen, T.J. Cleij, B. Conings, W. Moons, A. Gadisa, J. D'Haen, E. Goovaerts, L. Lutsen, J. Manca, D. Vanderzande, Effect of temperature on the morphological and photovoltaic stability of bulk heterojunction polymer: fullerene solar cells, Solar Energy Materials and Solar Cells 92 (2008) 753–760.

[50] M. Drees, H. Hoppe, C. Winder, H. Neugebauer, N.S. Sariciftci, W. Schwinger, F. Schäffler, C. Topf, M.C. Scharber, Z. Zhu, R. Gaudiana, Stabilization of the nanomorphology of polymer–fullerene "bulk heterojunction" blends using a novel polymerizable fullerene derivative, Journal of Materials Chemistry 15 (2005) 5158–5163.

[51] J.S. Moon, J.K. Lee, S. Cho, J. Byun, A.J. Heeger, "Columnlike" structure of the cross-sectional morphology of bulk heterojunction materials, Nano Letters 9 (2009) 230–234.

[52] H. Hoppe, N.S. Sariciftci, Morphology of polymer/fullerene bulk heterojunction solar cells, Journal of Materials Chemistry 16 (2006) 45–61.

[53] F. Padinger, R.S. Rittberger, N.S. Sariciftci, Effects of postproduction treatment on plastic solar cells, Advanced Functional Materials 13 (2003) 85–88.

[54] W. Ma, C. Yang, X. Gong, K. Lee, A.J. Heeger, Thermally stable, efficient polymer solar cells with nanoscale control of the interpenetrating network morphology, Advanced Functional Materials 15 (2005) 1617–1622.

[55] L.H. Nguyen, H. Hoppe, T. Erb, S. Günes, G. Gobsch, N.S. Sariciftci, Effects of Annealing on the Nanomorphology and Performance of Poly(alkylthiophene): Fullerene Bulk-Heterojunction Solar Cells, Advanced Functional Materials 17 (2007) 1071–1078.

[56] G. Li, V. Shrotriya, Y. Yao, Y. Yang, Investigation of annealing effects and film thickness dependence of polymer solar cells based on poly(3-hexylthiophene), Journal of Applied Physics 98 (2005) 043704-1–043704-5.

[57] M. Campoy-Quiles, T. Ferenczi, T. Agostinelli, P.G. Etchegoin, Y. Kim T.D. Anthopoulos, P.N. Stavrinou, D.D.C. Bradley, J. Nelson, Morphology evolution via self-organization and lateral and vertical diffusion in polymer: fullerene solar cell blends, Nature Materials 7 (2008) 158–164.

[58] Y. Zhao, Z. Xie, Y. Qu, Y.H. Geng, L.X. Wang, Solvent-vapor treatment induced performance enhancement of poly(3-hexylthiophene): methanofullerene bulk-heterojunction photovoltaic cells, Applied Physics Letters 90 (2007) 043504-1–043504-3.

[59] S.J. Lou, J.M. Szarko, T.J. Marks, L.X. Chen, S.J. Lou, J.M. Szarko, L. Yu, T.J. Marks, L.X. Chen, T. Xu, L. Yu, L.X. Chen, Effects of additives on the morphology of solution phase aggregates formed by active layer components of high-efficiency organic solar cells, Journal of the American Chemical Society 133 (2011) 20661–20663.

[60] Y.Y. Liang, Z. Xu, J.B. Xia, S.T. Tsai, Y. Wu, G. Li, C. Ray, L.P. Yu, For the bright future-bulk heterojunction polymer solar cells with power conversion efficiency of 7.4%, Advanced Materials 22 (2010) E135–E138.

[61] J. Peet, C. Soci, R.C. Coffin, T.Q. Nguyen, A. Mikhailovsky, D. Moses, G.C. Bazan, Method for increasing the photoconductive response in conjugated polymer/fullerene composites, Applied Physics Letters 89 (2006) 252105-1–252105-3.

[62] J. Peet, J.Y. Kim, N.E. Coates, W.L. Ma, D. Moses, A.J. Heeger, G.C. Bazan, Efficiency enhancement in low-bandgap polymer solar cells by processing with alkane dithiols, Nature Materials 6 (2007) 497–500.

[63] D.Y. Kim, F. So, Y. Gao, Aluminum phthalocyanine chloride/C60 organic photovoltaic cells with high open-circuit voltages, Solar Energy Materials and Solar Cells 93 (2009) 1688–1691.

[64] T.S. van der Poll, J.A. Love, T.Q. Nguyen, G.C. Bazan, Non-basic high-performance molecules for solution-processed organic solar cells, Advanced Materials 24 (2012) 3646–3649.

[65] S. Yoo, B. Domercq, B. Kippelen, Efficient thin-film organic solar cells based on pentacene/C-60 heterojunctions, Applied Physics Letters 85 (2004) 5427–5429.

[66] B. Walker, C. Kim, T.Q. Nguyen, Small molecule solution-processed bulk heterojunction solar cells, Chemistry of Materials 23 (2011) 470–482.

[67] Y.Z. Lin, Y.F. Li, X.W. Zhan, Small molecule semiconductors for high-efficiency organic photovoltaics, Chemical Society Reviews 41 (2012) 4245–4272.

[68] M. Niggemann, M. Glatthaar, P. Lewer, C. Müller, J. Wagner, A. Gombert, Functional microprism substrate for organic solar cells, Thin Solid Films 511–512 (2006) 628–633.

[69] C. Waldauf, M. Morana, P. Denk, P. Schilinsky, K. Coakley, S.A. Choulis, C. J. Brabec, Highly efficient inverted organic photovoltaics using solution based titanium oxide as electron selective contact, Applied Physics Letters 89 (2006) 233517-1–233517-3.

[70] M.S. White, D.C. Olson, S.E. Shaheen, N. Kopidakis, D.S. Ginley, Inverted bulk-heterojunction organic photovoltaic device using a solution-derived ZnO underlayer, Applied Physics Letters 89 (2006) 143517-1–143517-3.

[71] M. Hermenau, M. Riede, K. Leo, S.A. Gevorgyan, F.C. Krebs, K. Norrman, Water and oxygen induced degradation of small molecule organic solar cells, Solar Energy Materials and Solar Cells 95 (2011) 1268–1277.

[72] K. Norrman, M.V. Madsen, S.A. Gevorgyan, F.C. Krebs, Degradation patterns in water and oxygen of an inverted polymer solar cell, Journal of the American Chemical Society 132 (2010) 16883–16892.

[73] S. Cros, R. de Bettignies, S. Berson, S. Bailly, P. Maisse, N. Lemaitre, S. Guillerez, Definition of encapsulation barrier requirements: a method applied to organic solar cells, Solar Energy Materials and Solar Cells 95 (2011) 65–69.

[74] F.C. Krebs, S.A. Gevorgyan, B. Gholamkhass, S. Holdcroft, C. Schlenker, M. E. Thompson, B.C. Thompson, D. Olson, D.S. Ginley, S.E. Shaheen, H. N. Alshareef, J.W. Murphy, W.J. Youngblood, N.C. Heston, J.R. Reynolds, S. J. Jia, D. Laird, S.M. Tuladhar, J.G.A. Dane, P. Atienzar, J. Nelson, J.M. Kroon, M. M. Wienk, R.A.J. Janssen, K. Tvingstedt, F.L. Zhang, M. Andersson, O. Inganäs, M. Lira-Cantu, R. de Bettignies, S. Guillerez, T. Aernouts, D. Cheyns, L. Lutsen, B. Zimmermann, U. Würfel, M. Niggemann, H.F. Schleiermacher, P. Liska, M. Grätzel, P. Lianos, E.A. Katz, W. Lohwasser, B. Jannon, A round robin study of flexible large-area roll-to-roll processed polymer solar cell modules, Solar Energy Materials and Solar Cells 93 (2009) 1968–1977.

[75] C. Lungenschmied, G. Dennler, H. Neugebauer, S.N. Sariciftci, M. Glatthaar, T. Meyer, A. Meyer, Flexible, long-lived, large-area, organic solar cells, Solar Energy Materials and Solar Cells 91 (2007) 379–384.

Please cite this article as: M. Jørgensen, et al., The state of organic solar cells—A meta analysis, Solar Energy Materials and Solar Cells (2013), http://dx.doi.org/10.1016/j.solmat.2013.05.034

[76] K. Norrman, A. Ghanbari-Siahkali, N.B. Larsen, 6 Studies of spin-coated polymer films, Annual Reports on the Progress of Chemistry Section C: Physical. Chemistr 101 (2005) 174–201.
[77] F.C. Krebs, J. Fyenbo, D.M. Tanenbaum, S.A. Gevorgyan, R. Andriessen, B. van Remoortere, Y. Galagan, M. Jorgensen, The OE-A OPV demonstrator anno domini 2011, Energy & Environmental Science 4 (2011) 4116–4123.
[78] A. Manor, E.A. Katz, B. Hirsch, E.A. Katz, T. Tromholt, F.C. Krebs, Origin of size effect on efficiency of organic photovoltaics, Journal of Applied Physics 109 (2011) 074508-1–074508-9.
[79] A. Cravino, P. Schilinsky, C.J. Brabec, Characterization of organic solar cells: the importance of device layout, Advanced Functional Materials 17 (2007) 3906–3910.
[80] M.O. Reese, S.A. Gevorgyan, M. Jørgensen, E. Bundgaard, S.R. Kurtz, D.S. Ginley, D. C. Olson, M.T. Lloyd, P. Morvillo, E.A. Katz, A. Elschner, O. Haillant, T.R. Currier, V. Shrotriya, M. Hermenau, M. Riede, R. Kirov, G. Trimmel, T. Rath, O. Inganäs, F. Zhang, M. Andersson, K. Tvingstedt, M. Lira-Cantu, D. Laird, C. McGuiness, S. Gowrisanker, M. Pannone, M. Xiao, J. Hauch, R. Steim, D.M. DeLongchamp, R. Rösch, H. Hoppe, N. Espinosa, A. Urbina, G. Yaman-Uzunoglu, J.B. Bonekamp, A.J. J.M. van Breemen, C. Girotto, E. Voroshazi, F.C. Krebs, Consensus stability testing protocols for organic photovoltaic materials and devices, Solar Energy Materials and Solar Cells 95 (2011) 1253–1267.
[81] H.J. Snaith, How should you measure your excitonic solar cells? Energy and Environmental Science 5 (2012) 6513–6520.
[82] V. Shrotriya, G. Li, Y. Yao, T. Moriarty, K. Emery, Y. Yang, Accurate measurement and characterization of organic solar cells, Advanced Functional Materials 16 (2006) 2016–2023.
[83] J.M. Kroon, M.M. Wienk, W.J.H. Verhees, J.C. Hummelen, Accurate efficiency determination and stability studies of conjugated polymer/fullerene solar cells, Thin Solid Films 403–404 (2002) 223–228.
[84] S. Ito, H. Matsui, K.i. Okada, S.i. Kusano, T. Kitamura, Y. Wada, S. Yanagida, Calibration of solar simulator for evaluation of dye-sensitized solar cells, Solar Energy Materials and Solar Cells 82 (2004) 421–429.
[85] G. Yu, J. Gao, J.C. Hummelen, F. Wudl, A.J. Heeger, Polymer photovoltaic cells—enhanced efficiencies via a network of internal donor-acceptor heterojunctions, Science 270 (1995) 1789–1791.
[86] G. Li, V. Shrotriya, J.S. Huang, Y. Yao, T. Moriarty, K. Emery, Y. Yang, High-efficiency solution processable polymer photovoltaic cells by self-organization of polymer blends, Nature Materials 4 (2005) 864–868.
[87] N. Espinosa, R. García-Valverde, A. Urbina, F. Lenzmann, M. Manceau, D. Angmo, F.C. Krebs, Life cycle assessment of ITO-free flexible polymer solar cells prepared by roll-to-roll coating and printing, Solar Energy Materials and Solar Cells 97 (2012) 3–13.
[88] F.C. Krebs, All solution roll-to-roll processed polymer solar cells free from indium-tin-oxide and vacuum coating steps, Organic Electronics 10 (2009) 761–768.
[89] R. Garca-Valverde, J.A. Cherni, A. Urbina, Life cycle analysis of organic photovoltaic technologies, Progress in Photovoltaics 18 (2010) 535–558.
[90] G. Dennler, M.C. Scharber, C.J. Brabec, Polymer-fullerene bulk-heterojunction solar cells, Advanced Materials 21 (2009) 1323–1338.
[91] N. Espinosa, M. Hösel, D. Angmo, F.C. Krebs, Solar cells with one-day energy payback for the factories of the future, Energy and Environmental Science 5 (2012) 5117–5132.
[92] D. Yue, P. Khatav, F. You, S.B. Darling, Deciphering the uncertainties in life cycle energy and environmental analysis of organic photovoltaics, Energy and Environmental Science 5 (2012) 9163–9172.
[93] N. Espinosa, R. García-Valverde, F.C. Krebs, Life-cycle analysis of product integrated polymer solar cells, Energy and Environmental Science 4 (2011) 1547–1557.
[94] C.J.M. Emmott, A. Urbina, J. Nelson, Environmental and economic assessment of ITO-free electrodes for organic solar cells, Solar Energy Materials and Solar Cells 97 (2012) 14–21.
[95] L.J.A. Koster, V.D. Mihailetchi, P.W.M. Blom, Ultimate efficiency of polymer/fullerene bulk heterojunction solar cells, Applied Physics Letters 88 (2006) 093511-1–093511-3.
[96] K.M. Coakley, M.D. McGehee, Conjugated polymer photovoltaic cells, Chemistry of Materials 16 (2004) 4533–4542.
[97] G. Dennler, M.C. Scharber, T. Ameri, P. Denk, K. Forberich, C. Waldauf C.J. Brabec, Design rules for donors in bulk-heterojunction tandem solar cells-towards 15% energy-conversion efficiency, Advanced Materials 20 (2008) 579–583.

Please cite this article as: M. Jørgensen, et al., The state of organic solar cells—A meta analysis, Solar Energy Materials and Solar Cells (2013), http://dx.doi.org/10.1016/j.solmat.2013.05.034